The University Of Sheffield.

Department of Civil and Structural Engineering

Application of Smoothed Particle Hydrodynamics Modelling to Turbulent Open Channel Flows over Rough Beds

Eslam Gabreil

Submitted for the degree
of Doctor of Philosophy

May (2017)

Abstract

In this study, 2D and 3D numerical models based on the Smoothed Particle Hydrodynamics (SPH) approach have been developed to simulate turbulent open channel flows over a fixed rough bed. Both models were then used to simulate free surface turbulent flow over a rough boundary, including the free surface dynamic behaviour. The numerical code is based on the open source code SPHysics (http://www.sphysics.org) and during this study significant improvements have been made to this code on the modelling of turbulence and rough bed treatment. A modified sub-particle-scale (SPS) eddy viscosity model is proposed to reflect the turbulence transfer mechanisms and drag force equations are included into the momentum equations to account for the existence of roughness elements on the bed and on sidewalls. The computed results of flow velocity, shear stress and free surface elevations have been compared with detailed laboratory measurements under different flow conditions. The comparison has demonstrated that the modified SPH models can accurately simulate the free surface flows over a fixed rough bed. It was found that the modified 3D model is more accurate than the modified 2D model in predicting the flow velocity, shear stress profiles and the dynamic behaviour of the free surface. The capabilities and limitations of each model to simulate such free surface flow are highlighted and discussed.

Keywords: SPHysics; free surface flow; ADV; rough bed; drag force; SPS eddy viscosity model; water surface dynamic behaviour;

Acknowledgement

The author would like to express sincere appreciation to Dr. Songdong Shao and Prof. Simon Tait for their outstanding supervision, guidance and friendly meetings during all the years of study. The author would also thank Mr. Ehsan Kazemi, Dr. Giulio Dolcetti and Dr. Andrew Nichols for their great advice and support. Also to be thanked are the Hydraulic Laboratory technicians at Bradford University for their technical support during the laboratory experiments.

Special thanks must also go to my wife, who provided support, comfort and patience during all the years of study.

Contents

Figures

Tables

Nomenclature

A_d	Drag area	(m^2)
A_r	Aspect ratio ($A_r = W_b / H$)	(-)
C_d	Drag coefficient	(-)
c_0	Speed of sound	(m/s)
C_s	Smagorinsky constant	(-)
D	Sphere diameter	(m)
dx, dy, dz	Streamwise, vertical and lateral computational particle size	(m)
F_{dx}	Streamwise drag force acting on the bed	(N)
F_{dz}	Lateral drag force acting on the bed	(N)
Fx_{wall}	Streamwise drag force acting on the sidewalls	(N)
Fy_{wall}	Vertical drag force acting on the sidewalls	(N)
F_r	Froude Number	(-)
f	Darcy-Weisbach friction factor	(-)
g	Acceleration due to gravity	(m/s^2)
H	Total uniform flow depth measured from roughness bottom to the water surface.	(m)
h_w	Flow depth measured from 4 mm below the roughness top to the water surface.	(m)
$\bar{h}_w$	Time-averaged water surface elevation	(m)
h'_w	Water surface fluctuation calculated as ($h'_w = h_w - \bar{h}_w$)	(m)
h_d	Bed roughness height	(m)
k_s	Hydraulic roughness	(m)

k^+	Dimensionless hydraulic roughness	(-)
κ	Von Karman constant ($\kappa = 0.41$)	(-)
l_x, l_y, l_z	Local streamwise, vertical and lateral eddy size	(m)
L_x, L_y, L_z	The largest streamwise, vertical and lateral eddy size	(m)
m	Mass flow rate	(kg)
N	Total number of time-series measurements	(-)
P	Fluid pressure	(Pa)
Q	Flow discharge	(m^3/s)
R	Correlation coefficient	(-)
Re	Flow Reynolds Number	(-)
S_0	Channel slope	(-)
t	Time	(sec)
T	Total time of measurements	(sec)
u	Instantaneous local streamwise velocity	(m/s)
u'	Instantaneous streamwise fluctuating velocity	(m/s)
u^*	Fluid shear velocity	(m/s)
U	Time-averaged streamwise velocity	(m/s)
$\overline{U}$	Depth-averaged streamwise velocity	(m/s)
U_{rms}	Local streamwise turbulent intensity	(m/s)
U_s	Secondary flow velocity	(m/s)
U_{wave}	Advection speed of water surface	(m/s)
U^+	Normalized time-averaged streamwise velocity	(-)
v	Instantaneous local vertical velocity	(m/s)
v'	Instantaneous vertical fluctuating velocity	(m/s)
V	Time-averaged vertical velocity	(m/s)
$\overline{V}$	Depth-averaged vertical velocity	(m/s)

V_{rms}	Local vertical turbulent intensity	(m/s)
v_t	Turbulent eddy viscosity	(m^2/s)
w	Instantaneous local lateral velocity	(m/s)
w'	Lateral fluctuating velocity	(m/s)
W	Time-averaged lateral velocity	(m/s)
$\overline{W}$	Depth-averaged lateral velocity	(m/s)
W_{rms}	Local lateral turbulent intensity	(m/s)
W_b	Channel width	(m)
x	Streamwise location	(m)
x_l	Streamwise spatial lag	(m)
y	Vertical location	(m)
y_0	Mean spheres elevation (datum 4 mm below the top of the spheres)	(m)
y^+	Normalized vertical location	(-)
z	Lateral location	(m)
ρ	Fluid density	(kg/m^3)
υ_0	Kinematic water viscosity	(m^2/s)
τ_b	The averaged measured bed shear stress ($\tau_b = \rho g h_w S_0$)	(N/m^2)
τ_{sps}	Sub-Particle-Scale shear stress (SPS)	(N/m^2)
τ_l	Time lag	(sec)
Π	Coles' wake strength parameter	(-)
Δt	Computational time step	(sec)

Abbreviations

ADV	Acoustic Doppler Velocimeter
ADVP	Acoustic Doppler Velocimetry Profiler
DNS	Direct Numerical Simulation
FSGD	Free Surface Gradient Detector
LDA	Laser Doppler Anemometry
LES	Large Eddy Simulation
LIF	Laser Induced Fluorescence
MPS	Moving Particle Semi-implicit
MSEP	Mean Square Error Percentage (%)
PDF	Probability Density Function
PIV	Particle image velocimetry
RANS	Reynolds-Averaged Navier-Stokes
rms	root mean square
SGS	Sub-Grid-Scale Model
SPH	Smoothed Particle Hydrodynamics
SPS	Sub-Particle-Scale Model
STD	Standard deviation
2D	Two dimensional
3D	Three dimensional

CHAPTER 1 **Introduction**

1.1 Introduction

Free surface flows in rivers, and man-made channels are of significant importance in the field of hydrodynamics and hydraulic engineering. These types of flows are often over rough surfaces sometimes with complex topographies and are often characterised with spatial and temporal deformations of the free surface. Most "practical" open channel flows are characterized by complex 3D turbulence and large-scale flow structures. These structures can be reflected in secondary currents which are generated by the anisotropy of turbulence caused by the channel shape and bed topography, and thus influencing the pattern of the boundary shear stress (Einstein and Li, 1958). These flow structures are vertical large scale structures that generate counter rotating cells over the channel cross-section. They are called secondary flows of Prandtl's second kind, and play a major role in flow dynamics (Nezu and Nakagawa, 1993). Between these rotating cells, regions of alternating upflow and downflow motion are formed that extend throughout the depth of the whole water column (Albayrak and Lemmin, 2011). They influence the whole depth flow field and are believed to affect the free surface flow pattern. It is also believed that water surface pattern may carry some information about the underlying turbulent flow structures. There have been very limited studies into the free surface dynamic behaviour and its relationship to the underlying turbulent flow due to the scaling difficulty in laboratory measurements and spatial resolution constraint in numerical simulation.

Numerical simulations on the basis of mesh-based approaches have widely been used for different free surface flows. The three popular numerical techniques which

have been used to deal with turbulent flows are Direct Numerical Simulation (DNS), Large Eddy Simulation (LES) and Reynolds-Averaged Navier-Stokes Simulation (RANS). In DNS, motions of all turbulent length scales are resolved via the original Navier-Stokes (N-S) equations and hence the turbulent closure problem is avoided. However, DNS simulations are highly computationally expensive and are currently constrained to relatively low Reynolds number flows over a simple geometry. To overcome these problems, LES simulations were developed based on the fact that large eddies contain most of the turbulent energy and are most effective in the momentum transfer and mixing processes. In LES simulations, turbulent eddies larger than the computational grid size are directly resolved, while eddies smaller than this grid size are modelled. This is obtained by applying a low-pass spatial filter on the variables of the original N-S equations resulting in additional stress terms that can be modelled by sub-grid-scale (SGS) models such as the Smagorinsky model. Although LES is computationally much cheaper than DNS, it still requires higher spatial resolution especially in regions close to solid boundaries. In some engineering applications it is not necessary to simulate the detailed instantaneous flow, and the mean flow properties are sufficient. This is the basic for RANS simulations in which all turbulent length scales are modelled as mean flow properties, leading to a significant reduction of computational time. RANS uses a time averaging procedure (Reynolds decomposition) to the original N-S equations for an incompressible fluid. This results in extra terms over the original N-S momentum equations referred to as Reynolds stresses caused by turbulent fluctuations as shown in Equations 1.1 and 1.2.

$$\rho\left(\frac{\partial U}{\partial t}+U\frac{\partial U}{\partial x}+V\frac{\partial U}{\partial y}+W\frac{\partial U}{\partial z}\right)=-\frac{\partial P}{\partial x}+\rho g_x+\mu\nabla^2 U-\rho\left(\frac{\partial}{\partial x}\overline{u'^2}+\frac{\partial}{\partial y}\overline{u'v'}+\frac{\partial}{\partial z}\overline{u'w'}\right)+F_x$$

$$\rho\left(\frac{\partial V}{\partial t}+U\frac{\partial V}{\partial x}+V\frac{\partial V}{\partial y}+W\frac{\partial V}{\partial z}\right)=-\frac{\partial P}{\partial y}+\rho g_y+\mu\nabla^2 V-\rho\left(\frac{\partial}{\partial x}\overline{u'v'}+\frac{\partial}{\partial y}\overline{v'^2}+\frac{\partial}{\partial z}\overline{v'w'}\right)+F_y \quad (1.1)$$

$$\rho\left(\frac{\partial W}{\partial t}+U\frac{\partial W}{\partial x}+V\frac{\partial W}{\partial y}+W\frac{\partial W}{\partial z}\right)=-\frac{\partial P}{\partial z}+\rho g_z+\mu\nabla^2 W-\rho\left(\frac{\partial}{\partial x}\overline{u'w'}+\frac{\partial}{\partial y}\overline{v'w'}+\frac{\partial}{\partial z}\overline{w'^2}\right)+F_z$$

$$\begin{bmatrix}\tau_{xx} & \tau_{xy} & \tau_{xz}\\ \tau_{yx} & \tau_{yy} & \tau_{yz}\\ \tau_{zx} & \tau_{zy} & \tau_{zz}\end{bmatrix}=-\rho\begin{bmatrix}\overline{u'^2} & \overline{u'v'} & \overline{u'w'}\\ \overline{u'v'} & \overline{v'^2} & \overline{v'w'}\\ \overline{u'w'} & \overline{v'w'} & \overline{w'^2}\end{bmatrix} \quad (1.2)$$

where x, y, z, U, V and W denote the streamwise, vertical and lateral directions and time-averaged velocities, respectively. P, ρ, μ and g are the fluid pressure, density, viscosity and gravitational acceleration, respectively. F_x, F_y and F_z represent the three components of drag force due to the existence of rough boundaries. The terms in equation 1.2 can be determined using different turbulence models such as mixing length model, two equations $k-\varepsilon$ model, and Reynolds stress model (RSM). However no model can be accepted to be universal for solving wide range of turbulent flow problems. The mixing length model was first proposed by Prandtl (1925), and it relates the shear stress to the local mean velocity gradient and an empirical mixing length l_m. This model is robust and simple but it cannot account for the transport and history effects of turbulence as it implies the assumption of local equilibrium of turbulence production and dispersion (Rodi, 2017). Also the mixing length l_m is difficult to be specified for flows with complex geometry. Due to its simplicity, the mixing length model is still used by different commercial programs to simulate the vertical turbulent transport in practical flow calculations (Rodi, 2017).

In the past decades, the two popular approaches in mesh-based method for tracking the free surfaces are the mark-and-cell (MAC) and volume-of-fluid (VOF) techniques. In these methods, the properties of the free surface flow are computed through the Navier-Stokes (N-S) equations over a stationary mesh, which gives rise to the problem of numerical diffusion due to the advection terms in the N-S equations (Shao *et al*, 2003). This can make the application of mesh-based approach to be challenging for free surface flows in which the water surface is specified on an arbitrarily moving boundary.

In recent years, the mesh-free Smoothed Particle Hydrodynamics (SPH) technique, which was first introduced by Gingold and Monaghan (1977) to solve the astrophysical problems, has been developed and successfully used for the simulation of a wide range of computational fluid dynamics (CFD) problems, such as wave breaking and overtopping (Monaghan and Kos, 1999), multi-phase flow with sharp material interface (Colagrossi and Landrini, 2003) and dam break generated flows (Gomez-Gesteira *et al*,. 2010). Unlike the mesh-based methods, SPH is a purely Lagrangian mesh-less technique in which the fluid domain is described by a set of particles carrying various physical properties, and these particles are moved according to governing equations. A kernel function is used to define the contribution of the neighbouring particles to the motion of the reference particle. Thus, all the terms in the governing equations are expressed as the interaction between the reference particle and its neighbours and no computational mesh is need. More advanced turbulence closure modelling techniques in SPH have been systemically reviewed by Violeau and Issa (2007) and used by Dalrymple and Rogers (2006) for wave impact on a coastal defence. Due to its capability and flexibility of simulating complex flow situations SPH has become a competitive alternative to the mesh-based methods.

Although SPH has been successfully used for the simulation of different fluid phenomena such as in coastal hydrodynamics, only a small number of researchers have applied this technique to open channel free surface laminar flows (Federico *et al.* 2012; Shakibaeinia & Jin, 2010 ; Meister *et al*. 2014). Recently, Dzebo *et al.* (2014) performed the SPH modelling of dam break flow through a narrow rough valley, in which two different methods of defining the terrain roughness have been used, i.e. a wall-particle eddy viscosity coefficient for the hydraulically smooth terrain and the elevation of mesh-node on the obstacles along the terrain valley for the hydraulically rough terrain. Besides, SPH modelling techniques have also been used for the simulation of hydraulic jumps as documented by Lopez *et al.* (2010), Chern and Syamsuri (2013) and De Padova *et al.* (2013), and various turbulent closure models were included in their SPH formulations. However, in all of these works, there was no detailed quantification of velocity and shear stress profiles for turbulent free surface flows over a fully rough bed, and also there was a lack of information on water surface behaviour and its relationship with the underlying turbulent flow structures. Since these types of flows always exist in natural rivers and man-made drainage channels, the motivation of this research is to develop a SPH modelling for the more numerous practical applications.

1.2 Aims & Objectives

The primary aim of this study is to develop SPH numerical models for turbulent free surface flows over a fixed rough bed. These models will be validated using a representative set of hydraulic data collected in a rectangular open channel with turbulent flows over a fixed rough bed. Therefore the objectives of this study are:

- To design laboratory experiments that are capable of measuring the flow velocities in the vertical and spanwise directions, and to measure the temporal change in water surface elevations in the streamwise and spanwise directions of a rectangular open channel flow over a fixed rough bed.

- Use these laboratory experiments to gather data for a range of steady uniform flow conditions which cover a range of Froude Numbers.

- To deliver a 2D SPH numerical model capable of modelling a 3D free surface turbulent flow over a fixed rough boundary and validate the results using the collected laboratory measurements.

- To extend the proposed 2D SPH model to 3D and validate the results using the collected laboratory measurements. The improvements of 2D and 3D numerical models will be made on the turbulence modelling and the treatment of the fixed rough boundary.

- The proposed 2D & 3D numerical models will then be used to examine the dynamic behaviour of the free surface and its interaction with the underlying flow structure.

1.3 Structure of the thesis

This thesis consists of seven chapters that are organised as follows:

Chapter 1 describes the significance of turbulent structures in open channel flow, the need for a numerical model that is capable in simulating such flow structures and free surface behaviour, and aims & objectives of this research. **Chapter 2** is the literature review which first of all covers the basic characteristics of 2D turbulence open channel flow followed by a detailed review on the characteristics of 3D turbulent flow in river channels. The chapter also demonstrates the techniques available which are used to measure the temporal change in the water surface elevations. An analysis of the interaction of the water surface and the underlying flow is also made. Finally, numerical modelling approaches based on the mesh free Smoothed Particle Hydrodynamic SPH technique and its applications to the free surface flows are described and discussed. **Chapter 3** describes the experimental program carried out in a hydraulic rectangular flume with a well-defined rough bed. Turbulent velocity and instantaneous water surface elevations measurements including the equipment and calibration process are reported. **Chapter 4** covers the 2D numerical model set up and the improvement made on the turbulence model and bed roughness treatment. The turbulent effect is accounted for by modifying an existing turbulence model, and a drag force term is included in the momentum equation to account for the resistance forces exerted by roughness elements. Finally, the computed time averaged streamwise velocity, shear stresses profiles and water surface behaviour are compared to the measured data, and result analysis are discussed. **Chapter 5** presents the 3D numerical model setup and the developments made on the 3D turbulence effect and rough bed treatment. The computed and measured time averaged streamwise velocity, shear stress profiles and lateral bed shear stress patterns are compared. This chapter also compares the dynamic behaviour of the computed and measured water surface

elevations. **Chapter 6** compares and discusses the difference between the proposed 2D and 3D SPH models in predicting the flow velocity, shear stresses and free surface behaviour. It also highlights the capabilities and limitations that both models have in simulating free surface flow over a fixed rough bed. **Chapter 7** concludes the discussions of the findings, the achievements of the work, and recommendations are suggested on the improvements that could be made on the models to more accurately simulate such free surface flows.

CHAPTER 2 **Literature Review**

2.1 Introduction

Flows with a free surface in civil engineering applications are mainly turbulent. These include flows in rectangular, trapezoidal, and partially-full circular channels. The study of turbulent flow structures for flows with a free surface is essential to understanding the fluid dynamics for such civil engineering applications. The following literature review focuses on analysing turbulent flow structures for both two and three-dimensional free surface flows. This is important as it highlights the significance of considering the dynamic nature of turbulent flows in the design and construction of different types of hydraulic structures. Section **2** of this review deals with quasi-2D turbulent flows and examines the existing universal laws, the effect of rough bed and free surface on such flows. This section also looks at how small turbulent eddies induced at the rough bed are transported towards the free surface. Section **3** examines 3D turbulent flow structures and looks at the spatial distributions of the three velocity components, the spatial distributions of the flow shear stress, the mechanism of the secondary flow generation and its pattern throughout the flow cross section. Section **4** has an analysis of water surface dynamic behaviour and its interaction with the underlying turbulent flow, while section 5 highlights the existing work on numerical simulation using the Smoothed Particle Hydrodynamics SPH technique. These sections are central to develop an understanding of the turbulent flow structures in free surface flows in rectangular channel.

2.2 Quasi-2D turbulent flow structures

2.2.1 Introduction

Although turbulent fluid flows occur across all three dimensions of space, a two-dimensional (quasi-2D) hydrodynamic model can be considered sensible when one of the directions is suppressed. The degree to which this suppression occurs is dependent on the intensity of the forces, such as frictional, rotational which can result in strong anisotropy in the turbulent flow. 2D turbulence is of importance to the study of fluid flow not only to help understand more complex flow structures, but also to help develop numerical turbulent models of generally straight open channel quasi-2D flows.

2.2.2 Universal velocity distribution law

The universal Law of the wall as described by Von Karman is generally represented by Equation (2.1) (Kahler *et al.* 2005). It offers a solution for calculating the time averaged velocity for quasi-2D flow in the wall region. It is valid for steady fully developed turbulent flows with high values of Reynolds Numbers to ensure negligible viscous effects.

$$U^+ = \frac{1}{\kappa} \ln y^+ + B \tag{2.1}$$

where $y^+ = yu^*/\upsilon_0$; $u^* = \sqrt{\tau_b/\rho}$; and $U^+ = U(y)/u^*$. In this case, U^+ represents the dimensionless velocity (that is, the time-averaged velocity $U(y)$ parallel to the channel wall as a function of the distance (y) from the wall divided by the frictional velocity u^*). On the other hand, y^+ denotes the wall coordinate and is the distance to the wall which is made dimensionless by use of the kinematic viscosity υ_0 and the friction velocity u^*. Finally, τ_b denotes the shear stress posed by the wall, ρ is the fluid density, κ is the Von Karman constant (κ = 0.41). B is a constant ($\approx$ 5.0 for

smooth walls) and for hydraulically rough flows is dependent on the wall roughness (Schlichting and Gersten, 2000).

Several studies show that velocity profiles in the near boundary regions follow the universally accepted log law (Ead *et al*. 2000; Abbs *et al*. 2007). The log law is largely representative of the law of the wall as shown in Equation (2.1), (Nezu and Nakagawa, 1993). Several authors offer different values for the Von Karman constant κ and the constant B for free surface flows over smooth walls as shown in Table 2.1. However, Nezu and Nakagawa (1993) suggest that the widely accepted values are those developed by Coles since they are valid for numerous velocity profiles.

Table 2.1 Typical values for constants in the Log-Law equation (2.1).

Study	κ	B
Coles (1968)	0.41	5.0
Nezu & Rodi (1986)	0.41	5.29
Brederode & Bradshaw (1974)	0.41	5.2
Graf & Altinakar (1998)	0.41	5.0

However, the universal law of the wall needs modification to cater for rough boundaries. This is achieved by adding a roughness shift, which causes a downward shift of the U^+ values on the vertical axis (a general reduction in velocity due to increased boundary resistance). The roughness shift term is subtracted from Equation (2.1) and is represented by ΔB.

$$\Delta B = \frac{1}{\kappa} \ln k^+ \tag{2.2}$$

Thus, the log law for flow over rough boundaries can be formulated as:

$$U^+ = \frac{1}{\kappa} Ln\left(\frac{y^+}{k^+}\right) + C \tag{2.3}$$

k^+ represents the normalized equivalent roughness height $= u^* k_s / \upsilon_0$, k_s = hydraulic roughness height, and C is a constant (≈ 8.5 for rough walls). The value of the roughness shift varies with the orientation, shape and density of roughness element surface (Pope, 2000). The universal law of the wall, simplified to its general log law form is a central part of the current study in turbulent flow structures. However, it has been shown recent studies that the law of the wall given in Equation (2.3) is valid only in the wall region. The deviation from the standard law of the wall is accounted by adding a wake function and thus, Equation (2.3) becomes.

$$U^+ = \frac{1}{\kappa} Ln\left(\frac{y^+}{k^+}\right) + C + w\left(\frac{y}{h}\right) \tag{2.4}$$

where, $w(y/h)$ is known as wake function given by Coles (1956) as:

$$w\left(\frac{y}{h}\right) = \frac{2\Pi}{\kappa} \sin^2\left(\frac{\pi y}{2h}\right) \tag{2.5}$$

where Π is Coles' wake strength parameter and h = water depth. Nezu and Rodi (1986) stated that Π increases with the Reynolds Number from zero and becomes constant $\Pi \approx 0.2$ for Re > 2000, whereas experimental study by Li *et al.* (1995) gives $\Pi \approx 0.3$ for Re > 10^5. Figure 2.1 illustrates the vertical distribution of the mean streamwise velocity. It shows a linear distribution ($U^+ = y^+$) in the viscous sublayer, the log law (Equation 2.1), and the wake function (Equation 2.5).

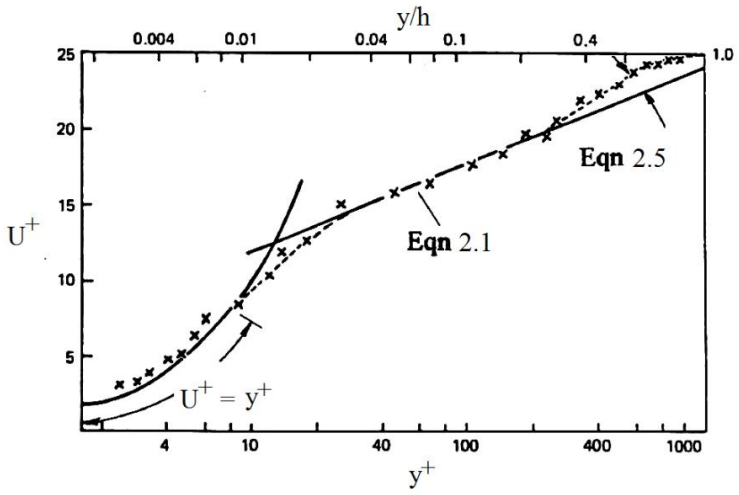

Figure 2.1 A typical mean velocity profile, (from Tritton 1988).

2.2.3 The effect of wall roughness

The effects of a rough wall on flows have been extensively studied. These effects are usually classified into three categories: Hydraulically smooth surface ($k^+ < 5$), Incompletely rough surface ($5 \le k^+ \le 70$), and Hydraulically rough surface ($k^+ > 70$). When the laminar sub-layer δ_v is larger than the surface texture, then the fluid flow over the laminar sublayer is not affected by the surface texture – smooth turbulent flow). However, with the roughness height greater than the depth of the laminar sub-layer, then the flow is affected by the surface texture. Figure 2.2 shows the effect of the bed roughness on the turbulence characteristics of different hydraulic flows in open structures.

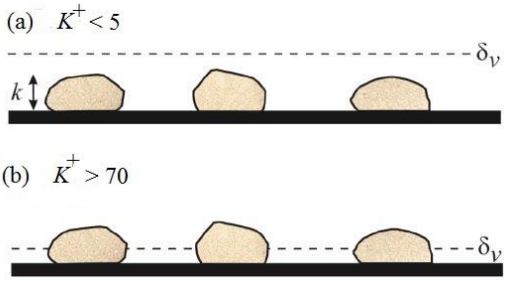

Figure 2.2 (a) Hydraulically smooth surface; (b) Hydraulically rough surface.

When dealing with hydraulically smooth surfaces, the position of the origin ($y = 0$) for the velocity profile at which ($U \approx 0.0$ m/s) can be easily determined. However, for hydraulically rough surfaces, the position of the origin can be set at a δ level, below the roughness crest. The value of δ should be obtained so that the averaged streamwise velocity distribution agrees well with the Log Law given in Equation (2.3). In experiments of fully developed turbulent flows over hemispherical roughness with diameter D, slightly different values of δ/D have been provided. According to Einstein and El-Samni (1949), the value of δ/D is 0.2, whereas Cheng and Clyde (1972) found that $\delta/D = 0.15$. Bunco and Partheniades (1971) determined $\delta/D = 0.27$. Grass (1971) obtained value of $\delta/D = 0.18$ in his gravel bed experiments, and $\delta/D = 0.25$ according to Nakagawa *et al*. (1975). Bayazit (1976) found $\delta/D = 0.35$ for his hemispherical bed, therefore, the value of δ/D could be within the range of 0.15 ~ 0.35 in order to fit the averaged streamwise velocity with the Log Law (Equation 2.3).

Chow (1959) classified the rough boundary into three types (see Figure 2.3): Isolated roughness flow (*k-type*) w/k > 4; wake-interference flow (*d-type*) w/k < 2; and quasi-smooth flow (transitional) 2 < w/k < 4. This classification is based on the assumption that the production of turbulence and flow energy dissipation are mainly because of the wakes formed behind the roughness elements. With roughness *k-type*, eddies which are generated in front and behind the roughness element have an influence on the flow above the crests of the roughness elements. Whereas with roughness *d-type*, the eddies are isolated by the roughness elements and they do not significantly affect the flow above the crests of the roughness elements (Perry *et al*. 1969).

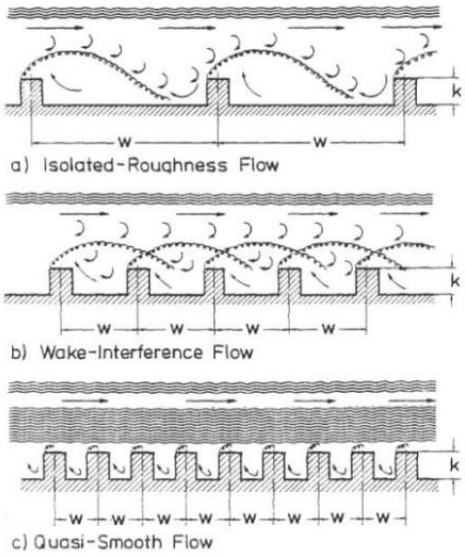

Figure 2.3 Types of rough surface flows: (a) *k-type*; (b) transitional; (c) *d-type*, Chow (1959).

Additionally, experimental observations have shown that the wall roughness effect changes with the flow submergence. Shamloo *et al.* (2001) performed an experimental study of fully developed turbulent flows over Styrofoam hemispheres for different flow submergences *h*/k ranged from 0.5 ~ 7.0. They concluded that the relative depth *h*/k was found to be an important parameter. With flows having relative depth *h*/k greater than 4, the effect of the roughness element is not felt at the surface, while with flows having relative depth *h*/k between 1.3 ~ 4, the surface waves started to appear. In the case of *h*/k between 1 ~ 1.3, the free shear layer from the roughness element causes the mixing throughout the whole flow depth. When the value of *h*/k is below 1, the top of roughness element is above the water surface elevation and strong backward flow was observed behind the roughness element. For all flow regimes, behind the roughness element there was a circulation zone with size of about twice the diameter of the hemisphere (see Figure 2.4).

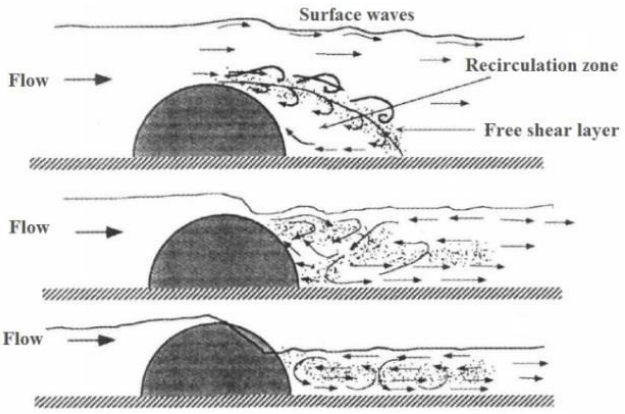

Figure 2.4 Definition sketch of different flow regimes, from Shamloo *et al.* (2001).

Similar experimental observations were found by Papanicolaou *et al.* (2010) who examined the interaction between isolated spheres (having diameter D = 55 mm) and the surrounding flow for a high relative submergence h/D = 3.5, and a low relative submergence h/D = 0.8. They concluded that for high relative submergence, a stagnation zone occurred behind the spheres but their effect was slightly reflected at the water surface. On the other hand, the effect of the spheres was felt at the free surface and a horseshoe vortex with counter-rotating limbs developed around the spheres for low relative submergence.

2.2.4 Friction factor (f) and hydraulic roughness (k_s)

In natural open channels, flows are always subject to resistance and energy dissipation due to roughness elements. Estimating the friction factor of this resistance is of great importance in natural open channels management because of its potentially significant impacts on channel conveyance (Järvelä, 2002). The friction factor is a measure of the effect of a rough boundary but it might not reflect the actual physical roughness size. The most frequently used formulas to estimate the friction factor in open channel flows are:

$$f = \frac{8gRS_0}{\overline{U}^2} \qquad \text{(Darcy – Weisbach)} \qquad (2.6)$$

$$\overline{U} = \frac{1}{n} R^{2/3} S_0^{1/2} \qquad \text{(Manning)} \qquad (2.7)$$

$$\overline{U} = C\sqrt{RS_0} \qquad \text{(Chezy)} \qquad (2.8)$$

where f, n, and C are the Darcy-Weisbach, Manning, and Chezy resistance factors, respectively; R is the hydraulic radius (given by the ratio of flow cross-sectional area to the wetted perimeter); $\overline{U}$ = mean cross sectional flow velocity; g = gravitational acceleration; and S_0 = channel slope. Later in 1939, Colebrook and White proposed the following semi-empirical formula to estimate the flow friction factor.

$$\frac{1}{\sqrt{f}} = -c_1 \log_{10}\left(\frac{k_s}{c_3 R} + \frac{c_2}{4\,\mathrm{Re}\sqrt{f}}\right) \qquad (2.9)$$

The above formula is often used for flows with Reynold Number Re higher than 25,000 (Yen, 2002). Some different values for c_1, c_2, and c_3 were suggested for different channel geometries in Table 2.2.

Table 2.2 Constants of Colebrook-White formula for steady uniform flow (from Yen, 1991).

Channel geometry	Reference	c_1	c_2	c_3	Remarks
Full circular pipe	Colebrook (1939)	2.0	14.83	2.52	
Wide channel	Keulegan (1938)	2.03	11.09	3.41	
Wide channel	Rouse (1946, p.214)	2.03	10.95	1.70	
Wide channel	Thijsse (1949)	2.03	12.2	3.033	
Wide channel	Sayre and Albertson (1961)	2.14	8.888	7.17	
Wide channel	Henderson (1966)	2.0	12.0	2.5	
Wide channel	Graf (1971, p. 305)	2.0	12.9	2.77	
Wide channel	Reinius (1961)	2.0	12.4	3.4	
Rectangular	Reinius (1961)	2.0	14.4	2.9	Width/depth = 4
Rectangular	Reinius (1961)	2.0	14.8	2.8	Width/depth = 4
Rectangular	Zegzhda (1938)	2.0	11.55	0	Dense sand

Determination of the hydraulic roughness k_s (which is also known as equivalent sand roughness) is a major problem for hydraulic engineers, especially when the roughness is irregular. This parameter is required for the calculation of a channel flow capacity and boundary shear stress so that the sediment transport and entrainment could be estimated. Traditionally, the mean particle diameter of a rough bed material is used to define k_s which parameterises the effect of this rough bed on the flow. In experimental studies, however, the hydraulic roughness k_s was found to be much larger than the actual physical size of the roughness element. According to Kamphuis (1974) (in his experiments with sand beds) $k_s \approx 4 \sim 5$ times the roughness element height. Bayazit (1976) found that $k_s \approx 5$ times the roughness element for his hemispherical bed. More recently, Christodoulou (2014) performed experimental study for flows in open channel with a slope of 16.5 % over different types of submerged artificial large-scale roughness elements. He reported that k_s is significantly larger than the physical height of the roughness element. For sharp-edged elements with height equal to width (baffle blocks, cubes and angles), $k_s \approx 10$ times the roughness element height, whereas for rounded-edged elements (cylinders and hemispheres), $k_s \approx 5$ times the roughness element height. The value of k_s can also be evaluated by fitting the vertical profile of the average streamwise velocity to the Log Law given in Equation (2.3). Also one can determine k_s from Colebrook and White formula using an estimated Darcy-Weisbach friction factor.

2.2.5 Reynolds decomposition

Turbulent eddies create fluctuations in velocity. As an example, the instantaneous longitudinal velocity u measured at a point in a laboratory flume is shown in Figure 2.5 below.

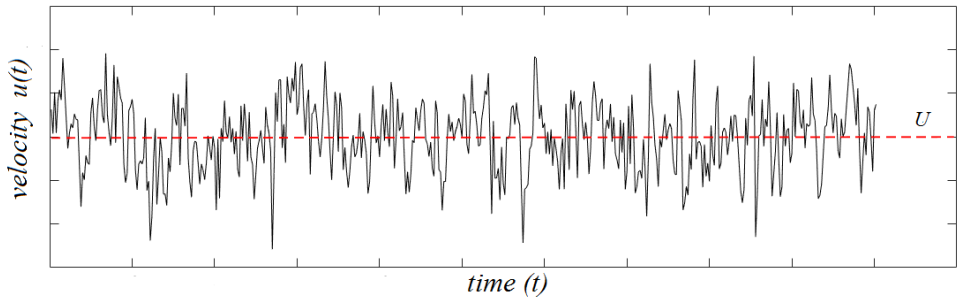

Figure 2.5 Time series velocity measured at a point.

To calculate the time-averaged velocity U and the turbulent component u', the flow is decomposed as follows:

$$U = \int_{t}^{t+T} u dt = \frac{1}{N}\sum_{i=1}^{N} u_i \tag{2.10}$$

where N is the total number of measurements. And the velocity time-series u at a point can be expressed as the sum of the time-averaged velocity U and the turbulent fluctuation of the velocity u'.

$$u = U + u' \tag{2.11}$$

This decomposition can be performed to other quantities such as, pressure, temperature and heat flux that are affected by the turbulent flow.

2.2.6 Turbulence intensity distributions

The turbulence intensity is generally defined as the ratio between the root mean square (rms) value of turbulent velocity fluctuations at a particular point over a specific period, i.e. $U_{rms} = \sqrt{\overline{u'^2}}$; $V_{rms} = \sqrt{\overline{v'^2}}$; $W_{rms} = \sqrt{\overline{w'^2}}$ to the shear velocity u^*. All the three components of turbulent intensities were first measured by Nakagawa *et al*. (1975) for open channel flows using a dual-sensor hot-film anemometer, while, Nezu and Rodi (1986) and Cardoso *et al*. (1989) used Laser Doppler Anemometry (LDA). Universal expressions for turbulence intensities, normalized with the friction velocity u^*, were later investigated for various values of Reynolds and Froude Numbers in smooth open channel flow. The following semi-empirical equations were provided by Nezu (1977a).

$$\frac{U_{rms}}{u^*} = 2.3\exp(\frac{-y}{h}) \tag{2.12}$$

$$\frac{V_{rms}}{u^*} = 1.27\exp(\frac{-y}{h}) \tag{2.13}$$

$$\frac{W_{rms}}{u^*} = 1.63\exp(\frac{-y}{h}) \tag{2.14}$$

Although the above three equations are useful for predicting the turbulence intensities in smooth open channel flows over the entire depth, they also can be used to approximate turbulent intensities over rough beds. In an experimental study by Carvalho *et al.* (2010), the vertical distributions of the streamwise and vertical turbulence intensities were determined using velocity profile data measured over rough bed as shown in Figure 2.6. These data were measured using two-component LDA technique (Laser Doppler Anemometer). It is worth noting that the experimental

measurements presented in Figure 2.6 (a) and (b) can well be approximated by Equations (2.12) and (2.13).

2.2.7 Reynolds shear stress

Reynolds stress term $-\rho\overline{u'v'}$ appearing in Equations (1.1) and (1.2) was first measured by McQuivey & Richardson (1969) in water flow over rough bed using a yawed hot-film sensor. Later, Nakagawa *et al*. (1975) used simultaneous measurements of u and v with the help of a dual-sensor hot-film probe to obtain the $-\overline{u'v'}$ value. It was shown that the data for $-\overline{u'v'}$ obtained from the hot-film and

LDA, coincides well with the linear distribution expressed in the following equation for steady, uniform free surface flow:

$$\frac{-\overline{u'v'}}{u^{*^2}} = \left(1 - \frac{y}{h}\right) \tag{2.15}$$

However, if the Reynolds shear stress distribution deviates from the above equation, the cause may be attributed to secondary flows and non-uniform and unsteady flow (Nezu and Nakagawa, 1993; Kironoto and Graf, 1995).

2.2.8 Drag force

A drag force is the resistance force generated by the interaction between a solid body and fluid flow. The mean drag force always acts in the direction opposite to the mean flow direction and it is generally given by resistance equation as:

$$F_d = \frac{1}{2}\rho A_d C_d U_d |U_d| \tag{2.16}$$

here, C_d = the drag coefficient; A_d = frontal area of the obstructing element; U_d = is the average flow velocity in the direct vicinity of the obstructing object; and F_d = drag force.

In the literature, the drag coefficient has been found to be dependent on the shape of the roughness element, blockage ratio, incoming flow direction and the Reynolds Number. Figure 2.7 shows the experimental data obtained by variety of researchers for smooth spheres. It generally shows the drag coefficient decreases as the Reynolds Number increases. For the range of Reynolds Numbers between $3\times10^3 \sim 3\times10^5$, C_d is almost constant with a value of approximately 0.5.

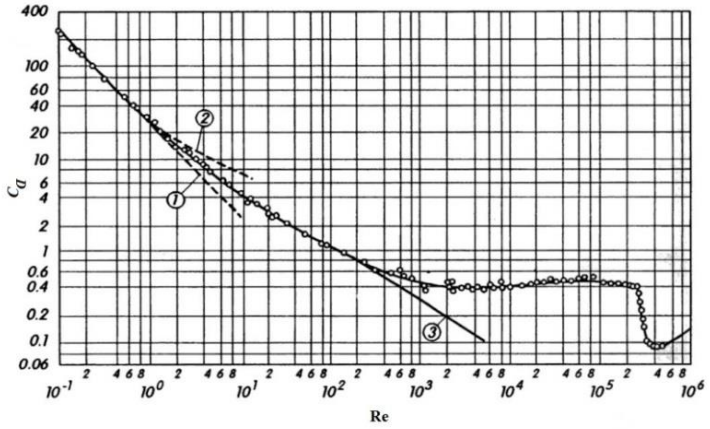

Figure 2.6 Dependency of the drag coefficient of smooth spheres on Reynolds Number (from Schlichting and Gersten, 2000), (curve 1 is $C_d = 24/\mathrm{Re}$; curve 2 is $C_d = 24/\mathrm{Re}\left[1+3\mathrm{Re}/16\right]$; and curve 3 is the numerical result after Fornberg, 1988).

In a more recent study, however, Schmeeckle *et al.* (2007) found that C_d is larger than the values obtained by other researchers. They performed experimental velocity and streamwise drag force measurements for three different types of bed roughness materials, i.e. a single sphere, a single cube and gravel particles. The examined flows were fully turbulent with Re ranged from 50000 ~ 200000, and mean streamwise velocity ranged from 0.2 ~ 0.9 m/s. The value of C_d for each bed roughness material was obtained as the gradient of linear trend of the measured streamwise drag force F_d and $0.5\rho A_d C_d U_d^2$ (see Figure 2.8). The linear regressions give drag coefficients of 0.76 for the spheres, 1.36 for the cubes, and 0.91 for the natural gravel particles.

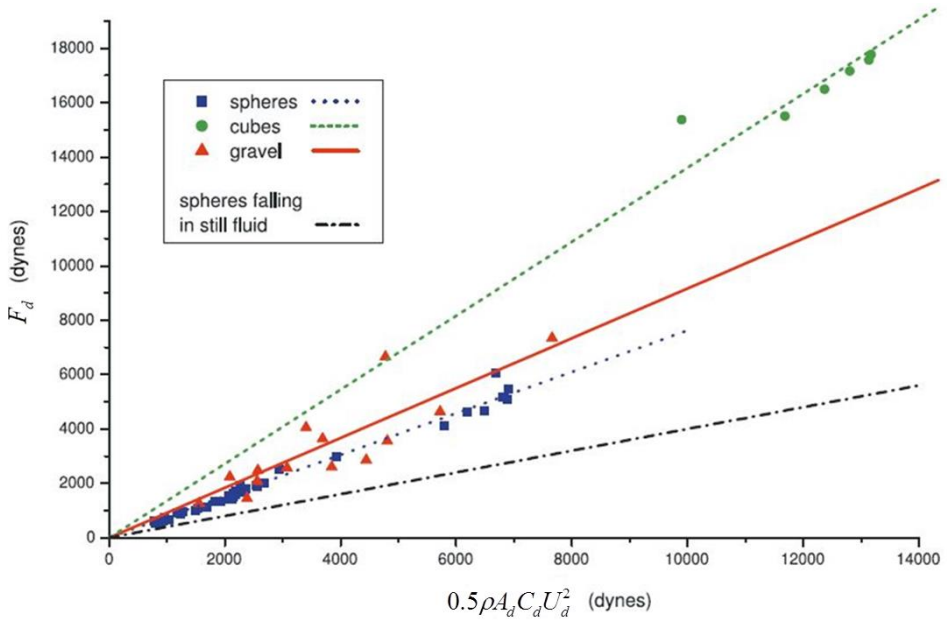

Figure 2.7 Mean streamwise drag force F_d versus $0.5\rho A_d C_d U_d^2$ for three different bed roughness materials, from Schmeeckle *et al.* (2007).

2.2.9 Free surface effect

The effect of a free surface on turbulent flow structures is very important for open channel flow calculation. Generally, it has been shown that turbulence structure is influenced by the presence of a free surface (Smutek, 1969; Nezu, 1977a; Nezu & Rodi, 1986). In fact, turbulent flows in open channels present two main regions as: inner or near boundary region and an outer region (away from the boundary) (Nezu and Nakagawa, 1993). Rodriguez and Garcia (2008) reported, **"**The characteristic that makes flow in open channels unique in terms of its outer structure is the presence of the free water surface**,** which acts as a confinement and defines a third surface-influenced layer where turbulence intensities and the turbulence length scale are modified**".** Some studies showed how the free water surface affects the turbulence in the regions just below the water surface. For example, a study by Nezu & Rodi (1986) who used LDA measurements to obtain the turbulence intensities along the water column indicates that the streamwise turbulence U_{rms}/u^* increases near the water

surface. They attributed this to the water surface fluctuations (surface waves). Another feature was experimentally observed by Smutek (1969), Nakagawa *et al.* (1975) and Komori *et al*. (1982), which is that the vertical velocity fluctuations v' are dampened by the free surface, which therefore, causes the turbulence intensity V_{rms}/u^* to decrease near the water surface ($y/h > 0.9$). Investigation of this effect is a great challenge for experimental and numerical simulations.

2.2.10 Mixing length theory

In 1925 Prandtl proposed a simple way of providing analytical turbulence closure for turbulent flows. He defined the mixing length l_m as the mean transverse distance through which a small mass of fluid would travel vertically from one layer of fluid (at y) to another before acquiring the velocity at the new layer (at $y + l_m$).

The gain or loss in velocity by the fluid mass travelling a distance l_m is expressed as (see Figure 2.9):

$$\Delta U = l_m \left(\frac{dU}{dy} \right) \tag{2.17}$$

Prandtl assumed that the turbulent fluctuation of u' and v' have same magnitude as mean velocity U, and thus equation (2.17) can be adjusted as:

$$(\Delta U)^2 = \overline{u'v'} = l_m^2 \left(\frac{dU}{dy} \right) \left| \frac{dU}{dy} \right| \tag{2.18}$$

Thus, a shear stress in turbulent flows can be obtained as:

$$\tau = \rho l_m^2 \left(\frac{dU}{dy} \right) \left| \frac{dU}{dy} \right| \tag{2.19}$$

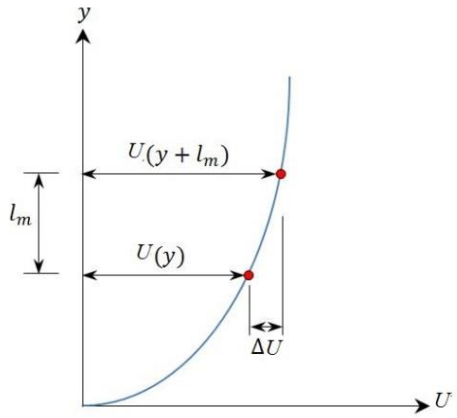

Figure 2.8 Mixing length theory.

The mixing length l_m describes the turbulent eddies size which transport momentum and other properties such as temperature within a fluid. A larger mixing length means that the fluid eddy length scale travels further and transferring momentum at a higher rate and so producing larger shear stresses. In open channel flow, the eddies size within a fluid are affected by both the bed and water surface boundaries, and hence l_m changes in the vertical direction. The best known empirical formula that calculates the mixing length in the vertical direction was reported by Nikuradse in 1950. This formula has been widely used for different free surface flows in pipes and open channels with a great success. It reads

$$\frac{l_m}{h} = 0.14 - 0.08(1-\xi)^2 - 0.06(1-\xi)^4 \equiv 0.14Ni(\xi) \qquad (2.20)$$

where $\xi = y/h$ and $Ni(\xi)$ = the introduced function which maps l_m along the flow depth. Later, Nezu and Rodi (1986) performed an experimental study of turbulent open channel flows over smooth bed with Reynolds Numbers ranged from 2.3×10^4 ~ 44×10^4. With Reynolds Stress obtained from Equation (2.15), and the velocity gradient dU/dy determined from the best spline fit through the data, the vertical distribution of the mixing length l_m was expressed as follows (see Figure 2.10):

$$\frac{l_m}{h} = \kappa\sqrt{1-\xi}\left[\frac{1}{\xi} + \pi\Pi\sin(\pi\xi)\right]^{-1} \tag{2.21}$$

In the near bed region (ξ < 0.25), l_m can be approximated by a linear ramp function $l_m \approx \kappa y$. The mid-depth values of l_m/h depends on the parameter Π, however, the measured data presented in Figure 2.10 do not directly confirm that l_m/h declines to zero as the free surface is approached because they show large scatter in the sub free surface region. Nezu and Rodi (1986) attributed this to the sensitivity of measuring the velocity gradient with great accuracy near the free surface. For flow region (ξ > 0.25), a constant value $l_m = \beta h$ is appropriate, where β depends on the Reynolds Number, it has the value of β = 0.12 for larger Reynolds Numbers (Nezu and Nakagawa, 1993). The application of the mixing length approach is very attractive because it is simple, computationally economical to apply, and it does not introduce any additional differential equations.

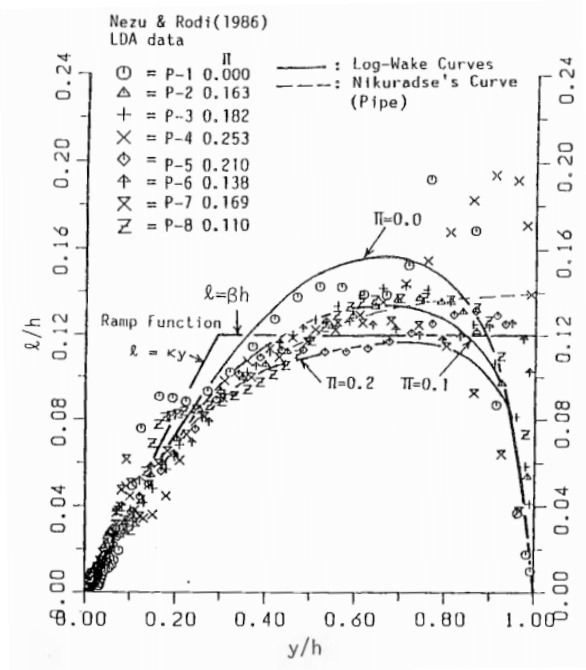

Figure 2.9 Vertical distribution of mixing length l_m/h in a turbulent open channel flows, (from Nezu and Nakagawa, 1993).

2.3 Three dimensional turbulent open-channel flow structures

2.3.1 Introduction

All turbulent flow structures in the natural environment are inherently a three-dimensional (3D) turbulence flow structure. In these types of flows, smaller structures are produced from larger structures, intense energy dissipations and random vorticity (Mathieu and Scot, 2000). In studying 3D turbulence flow structures in open channels, it is imperative to consider secondary currents, lateral and vertical streamwise velocity distributions, bed shear stress distributions and secondary flow patterns as these all reflect how momentum and energy are re-distributed. This will be the central concern of this section with a view of establishing the formation and character of such features within open channel flows.

2.3.2 Secondary flow in straight open-channel flow

Prandtl (1952) identifies two major types of secondary flows –skew induced streamwise vorticity and those observed in straight non-circular channels. The second category of secondary currents relates to the turbulence that leads to the formation of structures such as sand ridges (Yang *et al.*, 2012). Although the primary source for secondary currents has been considered to be 'corners', recent research proves that such currents can also be a result of slight perturbation of the channel bed (Nezu & Rodi, 1986; Nezu & Nakagawa, 1993; Wang and Cheng, 2005; Blanckaert *et al.*, (2010); Albayrak & Lemmin, 2011). These studies determined that spanwise changes in bed roughness and topography potentially lead to secondary currents that are not corner-induced. An imbalance in the cross sectional view of the boundary shear stress also leads to secondary currents (Nezu & Rodi, 1986). The lateral variation in the turbulent velocities drives secondary currents. Additionally, many studies showed that the boundary plays an important role in the formation of the secondary currents.

Rodriguez and Garcia (2008) conducted experimental study in a wide channel with a rough bed and smooth vertical sidewalls, and they observed multicellular flow structures generated over the channel cross section. The formation of these multicellular structures was attributed to the difference in the roughness scale between the gravel bed and the smooth glass sidewalls. This agrees with the experimental finding of Nino & Garcia (1996) and Cooper & Tait (2008) who observed longitudinal streaks with low and high velocities existing over smooth and rough beds. They reported that the variation in bed roughness is the primary source of the secondary flows. According to Yang *et al.* (2012), the deformation of bed deposits that are mobile can amplify secondary flow until an instance where equilibrium is achieved between the secondary flow and the lateral variation in sediment transport. Additionally, when the transverse distribution of the bed shear stress is non-uniform, secondary flow is generated. As long as flow is perturbed, non-uniform roughness of the bed and secondary flow reinforce each other. Secondary flow mechanism occurs in such a way that it moves from the region of low bed shear stress (or lower streamwise velocity) to high bed shear stress (or higher streamwise velocity). The propagation of secondary currents is also aided by the transportation of sediment by the near boundary secondary flow. The near bed region, and not the main flow region, causes secondary currents. Yang *et al.* (2012) conclude that apart from causing turbulence, the boundary is essentially the source of secondary currents. The significant debate surrounding the formation of secondary currents suggests that knowledge gaps still exist.

2.3.3 Mean velocity distributions

Many experimental studies have been carried out to measure the mean velocities distribution in straight open channel flows. Mclelland *et al.* (1999) performed mean

velocities distribution analyses for a rectangular open channel flow. Their experimental set up is shown in Figure 2.11. Two types of sediment materials (fine gravel and coarse sand) were placed as strips at the channel bottom. The flow was seeded using water-based paint particles (< 10 μm diameter). Two-component, laser Doppler anemometer (LDA) velocity measurements were recorded over one half of the flume for 180 s and at an average sampling frequency of 160 Hz. The sampling grid was spaced at 0.005 and 0.0075 m in the vertical and lateral directions, respectively.

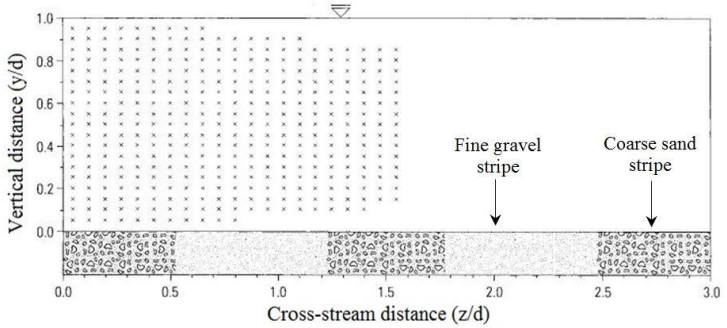

Figure 2.10 Cross-section view of 0.3 m wide channel; water depth d = 0.1 m; cross-sectional mean flow velocity U_m = 0.399 m/s; and flow Re = 45300, from Mclelland *et al.* (1999).

Figure 2.12 presents the local mean streamwise and vertical velocities measured at each grid point over the half flume cross section. The local mean streamwise and vertical velocities have been normalized by the cross sectional mean flow velocity U_m. The region of high streamwise velocity appears in the centre of the channel and is depressed to a level below the free surface, which is a phenomeno known as 'velocity dip'. Towards the bottom corner, the isovels of streamwise velocity become increasingly distorted, show 3D features and the position of the maximum streamwise velocity occurs deeper below the free surface. This corner influence has also been reported by (Naot & Rodi, 1982; Nezu & Nakagawa, 1984; Nezu & Nakagawa, 1993). Near the flume bed, the streamwise flow velocity increases towards the centre,

showing a small variation with respect to the change in bed material. Figure 2.12b shows upflow and downflow in the mean vertical flow velocities. The strongest upflow occurs near the side-wall above y/d ≈ 0.3, and also near the flume bed at the interface between the side-wall coarse sand strip and the fine gravel strip. In contrast, the greatest downflow was observed at the channel centre over the coarse sand trip. There is also a small region of strong downflow in the bottom flume corner. The maximum and minimum measured mean vertical flow velocity was about $0.03U_m$. During their experiment the LDA instrument was not able to measure the spanwise velocity, instead it was estimated from the continuity equation for an incompressible fluid which is expressed as:

$$\frac{\partial U}{\partial x}+\frac{\partial V}{\partial y}+\frac{\partial W}{\partial z}=0 \tag{2.22}$$

For uniform steady flow, $\partial U/\partial x = 0.0$ and $\partial W/\partial z = -\partial V/\partial y$. By integrating both sides the mean spanwise velocity at a given location can be determined as:

$$W_{(y,z)} = -\int_0^z \left(\frac{\partial V}{\partial y}\right) dz \tag{2.23}$$

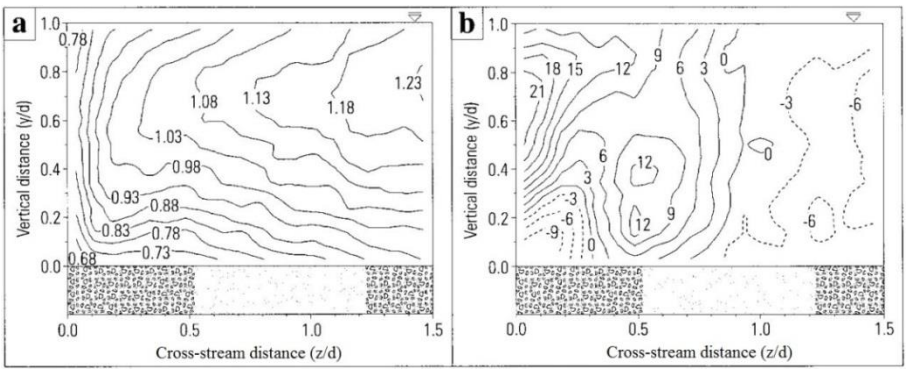

Figure 2.11 Contour plot of (a) Normalized streamwise velocity U/U_m ; (b) Normalized vertical velocity $10^3 \times V/U_m$, from Mclelland *et al.* (1999).

Wang and Cheng (2005) conducted similar experiments with a wider rectangular channel. The experiment was designed to incorporate alternate smooth and rough strips longitudinally aligned in the open channel. The width of the smooth and rough strips was λ=75 mm while the width of the two rough strips attached to the sidewall was only 37.5 mm each. The flow velocities were measured over the half of cross section using 2D-Laser Doppler Anemometry (LDA). The sampling period was taken as 200 s and at an average sampling rate of 75 Hz. In the central region of the channel the measurements were only collected from y/h = 0.13 ~ 0.8 and the measuring grid points were spaced 5 mm apart. Near the side wall, more measuring points were added with vertical spacing of 2 or 3 mm (see Figure 2.13).

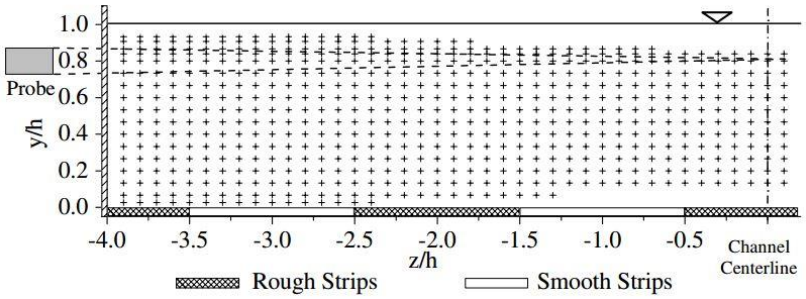

Figure 2.12 Half cross-section view of 0.6 m wide channel; water depth *h* = 0.075 m; mean streamwise velocity in the central region U_m = 0.449 m/s; and flow Re = 42000, from Wang and Cheng (2005).

The contour plots of the normalized average streamwise and vertical velocities over the half cross section are presented in Figure 2.14. Figure 2.14(a) clearly illustrates the strong influence of the side wall on the streamwise flow velocity distribution within a lateral distance of around 1.0*h* from the sidewall. In this zone, the maximum streanwise velocity is located below the water surface. In region between z/λ = –2.0 ~ 0.0, the undulation in the average streamwise velocity is in phase with the lateral variation in bed texture. In the upper region of the flow, higher streamwise velocity occurs above the rough strips, while lower streamwise velocity above the smooth

strips. However, the velocity dip phenomenon was not clearly observed in the central zone of the flume. In contrast, the streamwise velocity near the bed and above the smooth strips is higher than that above rough strips. Figure 2.14(b) clearly demonstrates upflows and downflows in the average vertical flow velocity which correspond to the undulation of the streamwise velocity. Upflow occurs above smooth strips whereas downflow appears in regions above rough strips.

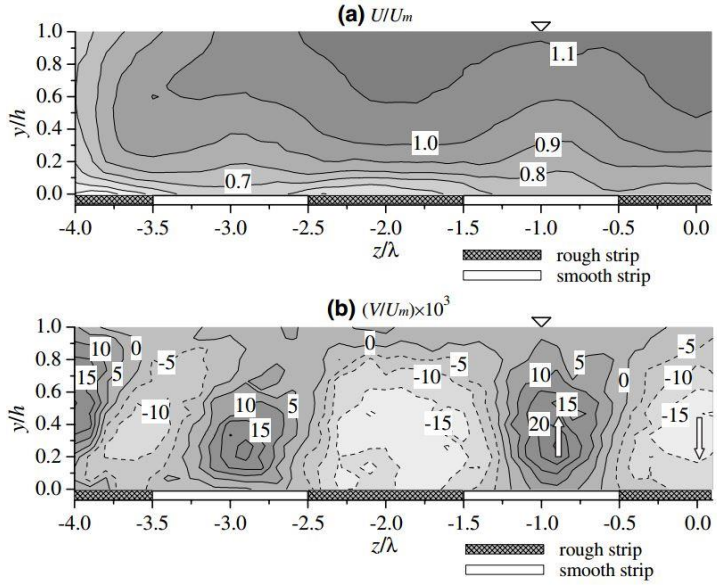

Figure 2.13 Contour maps of (a) normalized average streamwise velocity U/U_m ; (b) normalized average vertical velocity $(V/U_m)\times 10^3$, from Wang and Cheng (2005).

Figure 2.15 plots the mean streamwise vertical profiles at different lateral locations (from $z/\lambda = 0.0 \sim -1.0$). Two profiles were plotted together, one over smooth bed and the other over rough bed, and they have same lateral location measured from the strip interface (at $z/\lambda = -0.5$). One can note that the two profiles become more linear as the lateral distance from the strip interface decreases, and the velocity gradient in the lower region of the flow is much steeper over rough bed. At the strip interface ($z/\lambda = -0.5$), the mean streamwise velocity distribution coincides well with that given in Equation (2.3). Similar findings were also observed by Nakagawa *et al.* (1981).

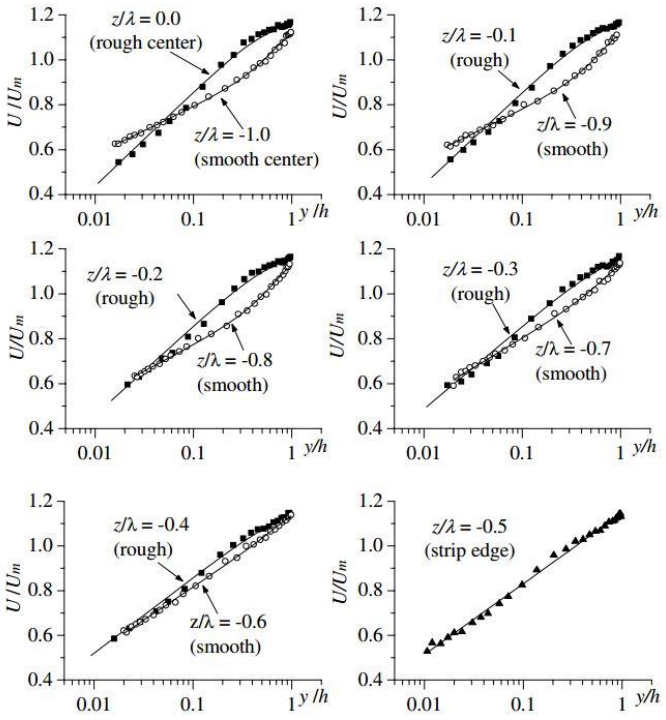

Figure 2.14 Vertical profiles of mean streamwise velocity, Scattered points represent measured data; solid black lines are obtained from Equation (2.24), from Wang and Cheng (2005).

Moving laterally further from the strip interface the velocity profiles deviates from the classic Log Law due to the presence of the cellular secondary flow. Wang and Cheng (2005) accounted for this effect by modifying the classical Log Law to:

$$\frac{U_{(y,z)}}{\overline{u^*}} = \ln\left(\frac{y}{y_0}\right) + \left[\delta_1 \ln\left(\frac{y}{y_0}\right) + D + \delta_2 \sin^2(\pi y/2h)\right]\cos(\pi z/\lambda) \qquad (2.24)$$

where, $\overline{u^*}$ = the mean shear velocity in the central zone; δ_1, δ_2 and D are constants and equal to 0.3,− 0.8 and ,− 1.7, respectively. The above equation was derived by introducing some empirical parameters to the classical Log Law to account for the curvature of the measured velocity profiles induced by the secondary flow (Wang and Cheng, 2005). The spanwise velocity was obtained from the continuity equation as shown earlier by (Mclelland *et al.*, 1999). Moreover, Vermaas *et al.* (2011) conducted an experimental study to examine the lateral transfer of the streamwise momentum

with respect to the lateral variation in bed materials. The experimental set up was developed as shown in Figure 2.16. The right half of the flume bed was covered by stones having size of 7.6 mm 9.3 mm, and the left half of the channel was covered by 6 mm thick polished wooden plates to form a smooth bed. Effectively, the level of the rough and smooth beds was equal. An Acoustic Doppler Velocimeter (ADV) was used to measure the three components of velocity. At every measuring point, the velocity was recorded over 180 s and at sampling rate of 25 Hz. Four flow regions were examined as demonstrated in Table 2.3.

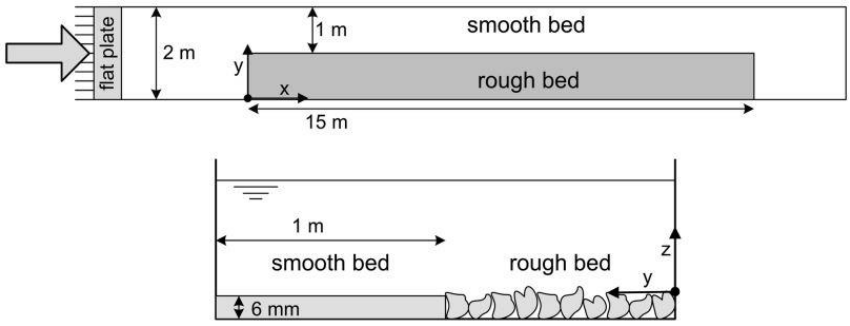

Figure 2.15 Flume configuration, from Vermaas *et al.* (2011).

Table 2.3 List of flow conditions, from Vermaas *et al* (2011).

Case	Method	Discharge ($m^3 s^{-1}$)	Water Depth (m)	$Re = \frac{U \cdot R}{\upsilon}$
E08	Flume experiment	0.040	0.081	17×10^3
E11	Flume experiment	0.040	0.110	18×10^3
E15	Flume experiment	0.100	0.151	41×10^3
E22	Flume experiment	0.100	0.222	39×10^3

Figure 2.17 presents the contour maps of the average streamwise velocity distribution at x = 12.5 m. For the four flow conditions in Table 2.3, lateral variation in the mean streamwise velocity was observed. Near bed streamwise velocity appears to be higher over the smooth bed than that over rough bed, and strong downflow occurs at a location where the near bed streamwise velocity abruptly changes.

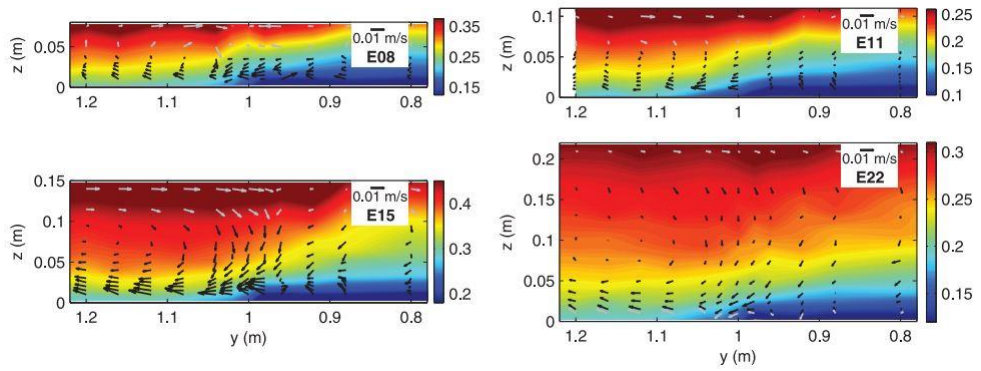

Figure 2.16 Contour map of the mean streamwise velocity at x = 12.5 m, from Vermaas *et al.* (2011).

2.3.4 Velocity-dip phenomenon

The velocity dip phenomenon is defined as the location where the maximum main velocity appears below the free surface. It has been widely reported that this phenomenon occurs if the aspect ratio of the flume width to flow depth, ($Ar = W_b/H$), is less than a certain value. For example, Vanoni (1941) argued that for wide open channel flows where the aspect ratio $Ar > 5$, there always exist a central zone where the velocity dip does not appear. The velocity dip phenomenon always appears in regions close the sidewall even if the aspect ratio is large enough (Yang *et al.*, 2004; Luo & Lü 2006; Hu *et al.*, 2008). The velocity dip phenomenon essentially represents a deviation from the Log Law (Equation 2.3). It is observable in both rivers and open channel flows. It generally relates to the secondary currents that occur in 3D open channel flows. Nezu and Nakagawa (1993) reported that this phenomenon is due to the presence of secondary flows which transport low momentum fluid from the near side wall towards the centre, and high momentum fluid moving from the water surface towards the channel bed. Yang *et al.* (2004) offered a dip-modified log law from the experimental data in uniform open channel flows over smooth bed (see Equation 2.25). The velocity dip phenomenon in this new law is predicted by the term $\ln(1-y/h)$, and α being the dip-correction parameter defined as $\alpha = 1.3e^{-z/h}$,

where z = the spanwise distance measured from the sidewall to the centre of the channel.

$$\frac{U_{(y,z)}}{u^*} = \frac{1}{\kappa}\ln\left(\frac{y}{y_0}\right) + \left(\frac{\alpha}{\kappa}\right)\ln\left(1-\frac{y}{h}\right) \tag{2.25}$$

The dip-modified log law was found to be able to describe the dip phenomenon, and to approximately estimate the streamwise velocity in regions from the near bed to slightly below the water surface, and laterally from the sidewall to the central of the flume. The advantages that the dip-modified log law have over other velocity laws are: (a) it is capable of estimating the velocity near sidewalls; (b) it is capable in simulating the velocity-dip phenomenon in the sidewall and central regions of the open channel flows; (c) it is simple to use and compares well with the measurements (Yang *et al.*, 2004). However, Kundu and Ghoshal (2012) stated that the above dip-modified log law can correctly predict the velocity-dip location but it deviates from the measured data in the upper region of the flow (y/h > 0.2). They proposed an analytical equation called "the total-dip-modified-log-wake-law" that can predict the velocity throughout the flow depth and locate the dip-velocity position correctly. This equation reads.

$$\frac{U_{(y)}}{u^*} = \frac{1}{\kappa}\ln\left(\frac{y}{y_0}\right) + \frac{\lambda}{\kappa}\ln\left(1-\frac{y}{h}\right) + \frac{2\Pi}{\kappa}\left(3\left(\frac{y}{h}\right)^2 - 2\left(\frac{y}{h}\right)^3\right) - \frac{4\Pi}{\kappa}\left(\frac{y}{h}\right)^3 \tag{2.26}$$

here, λ is the dip-correction parameter $=\left(h/y_{Dip}\right)-1$; $y_{Dip}=$ the position of the maximum velocity; and the value of Π increases with the increase of λ.

2.3.5 Bed shear stress distribution

The lateral Reynolds shear stress distribution for Mclelland *et al.* (1999) is shown in Figure 2.18. Generally, Figure 2.18(a) demonstrates that the shear stress is larger near the bed and declines as the free surface and the sidewall are approached.

Negative shear stress occurs in a small zone next to the sidewall and just below the water surface. The lateral boundary shear stress was approximated from Reynolds stress $\tau = -\rho\overline{u'v'}$ in region $y/d < 0.3$ and is shown in Figure 2.18(b). The dashed line corresponds to the averaged boundary shear stress τ_b which was estimated from $\tau_b = \rho g d S_0$, where d and S_0 are the flow depth and channel slope, respectively. The boundary shear stress distribution is undulating and has a strong relationship with the bed grain size. It increases rapidly from a low value at the sidewall to a peak value of 16.0 % greater than the τ_b value over the centre of the coarse strip. Then it decreases to a value of 18.0 % less than τ_b over the fine gravel strip. The maximum boundary shear stress occurs at the channel centreline with value of 27.0 % greater than τ_b. Over the strips interface, the boundary shear stress has value very close to τ_b. It was expected that the undulation of the bed shear stress is due to the change of near-bed streamwise velocity gradient ($dU/dz \neq 0$).

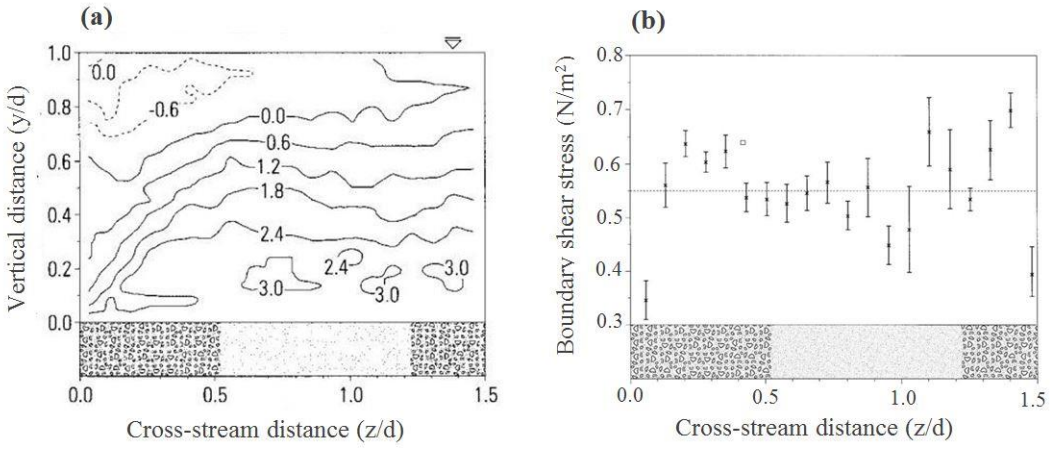

Figure 2.17 (a) Contour map of normalized Reynolds stress $-\rho\overline{u'v'}/U_m^2$; (b) Bed shear stress τ, Dashed horizontal line is the mean bed stress $\tau_b = \rho g d S_0$, from Mclelland *et al.* (1999).

Wang and Cheng (2005) observed a similar shear stress pattern. Their result revealed that regions with rough strips experience high bed shear stress and low bed shear stress occurs over smoother strips (see Figure 2.19).

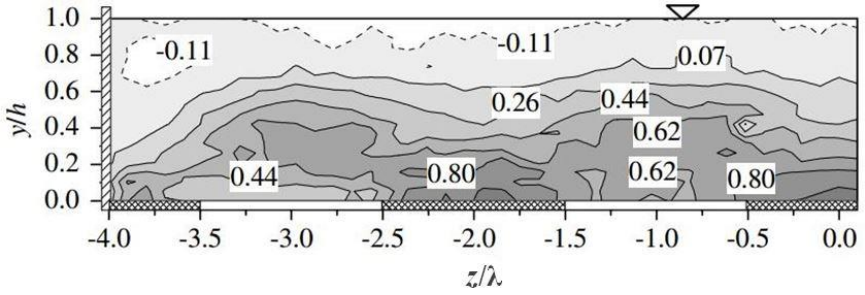

Figure 2.18 Contour map of normalized Reynolds stress $-\overline{u'v'}/ghS_0$, from Wang and Cheng (2005).

The vertical profiles of the shear stress at different spanwise locations are presented in Figure 2.20. Near the bed (*y/h < 0.2*), higher shear stress occur above the rough strips whereas over the smooth strips, the shear stress becomes smaller. In the upper flow portion (*y/h > 0.2*), the shear stress becomes higher above the smooth strips and lower over the rough strips. The vertical shear stress profile is linear at the strip edge ($z/\lambda = -0.5$) but it deviates as laterally moving farther from the strip edge. Wang and Cheng (2005) described this deviation by fitting the experimental data to the following Equation.

$$\frac{-\overline{u'v'}}{\overline{u*^2}} = \alpha_3\left(1-\frac{y}{h}\right)+\alpha_4\left(1-\frac{y}{h}\right)\frac{y}{h}\sin^2(\pi y/h) \qquad (2.27)$$

where, $\alpha_3 = 1+0.18\cos(\pi z\lambda)$ and $\alpha_4 = 1-1.44\cos(\pi z\lambda)$.

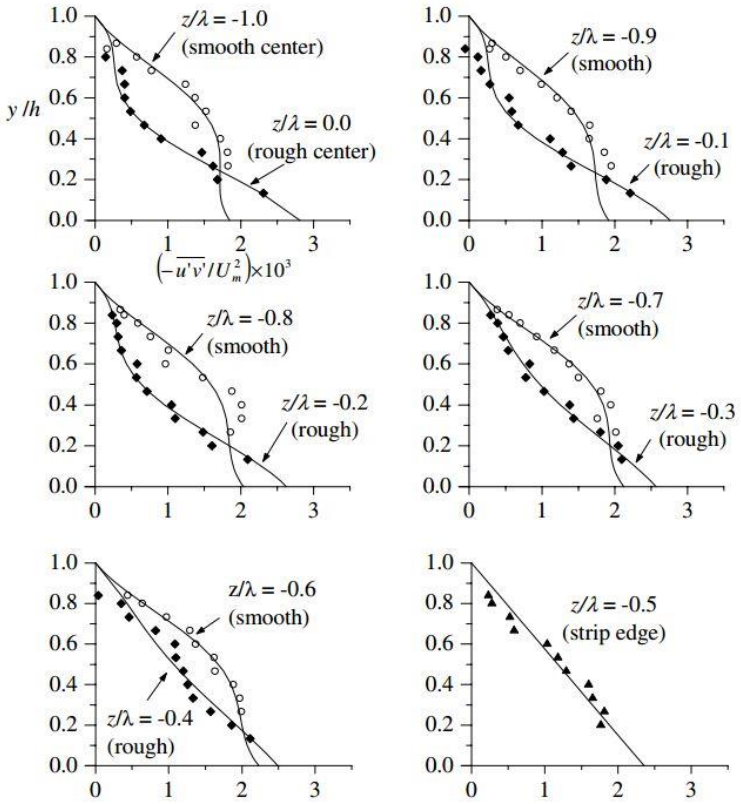

Figure 2.19 Vertical profiles of normalized Reynold stress $(-\overline{u'v'}/U_m^2)\times10^3$, Scattered points represent measured data; solid lines are obtained from Equation (2.28), from Wang and Cheng (2005).

Having said that in the presence of the secondary flows, the Reynolds Stress deviates from the linear equation given in Equation (2.15). However, Yang *et al.* (2012) proposed an equation to predict the Reynolds stress vertical profile which is affected by the secondary flows as follows.

$$\frac{-\overline{u'v'}}{u_*^2}=\left(1-\frac{y}{h}\right)+\frac{UV}{u_*^2} \tag{2.28}$$

The above equation indicates that in the upflow regions ($V>0$), Reynolds Stress becomes higher than the linear distribution, whereas in the downflow regions ($V<0$), Reynolds Stress becomes less than the linear distribution. Also the boundary shear stress at different spanwise locations were determined by extrapolating the corresponding $-\overline{u'v'}$ profiles to the bed surface. Figure 2.21 illustrates the spanwise

variation of the bed shear stress which can be expressed by a cosine function as follows.

$$\frac{\overline{u_*^2}}{u_*^2} = 1 + 0.18\cos\left(\frac{\pi z}{\lambda}\right) \tag{2.29}$$

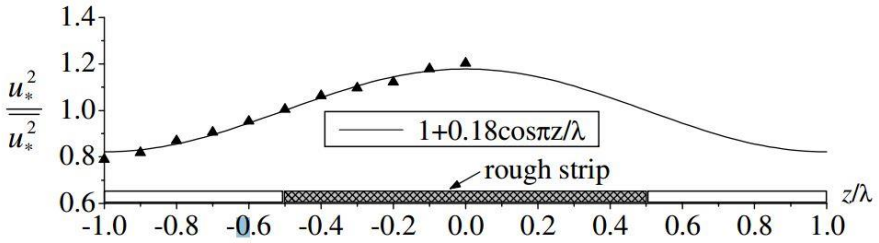

Figure 2.20 Bed shear stress distribution obtained from the measurements of $-\overline{u'v'}$, from Wang and Cheng (2005).

2.3.6 Secondary flow pattern

Inherent features of open channel flows are significantly modified whenever secondary flows occur. In Mclelland *et al.* (1999), a plot of the half cross section velocity vectors is shown in Figure 2.22. The plot clearly highlights the existence of the secondary flow circulations. This circulation pattern consists of two counter-rotating flow cells (4 cells across the flume width). They define the lower small cell as the 'bottom vortex' whereas the upper cell as the 'free surface vortex'. The free surface vortex has a size that is approximately equal to the flow depth, while the bottom one has approximately the half size of that. The motion of both cells draws strong downward flow into the corner causing the bulge in the streamwise isovels (see Figure 2.22a). Near the water surface, the upper vortex transports low momentum fluid from the sidewall towards the centre, producing the velocity-dip phenomenon.

In the centre of the flume, fluid with high momentum is transported by the downflow from the free surface toward the bed. This downflow then moves laterally towards the sidewall, meeting the bottom vortex. The two vortices are then turned upward over the fine-gravel strip (Mclelland *et al*, 1999).

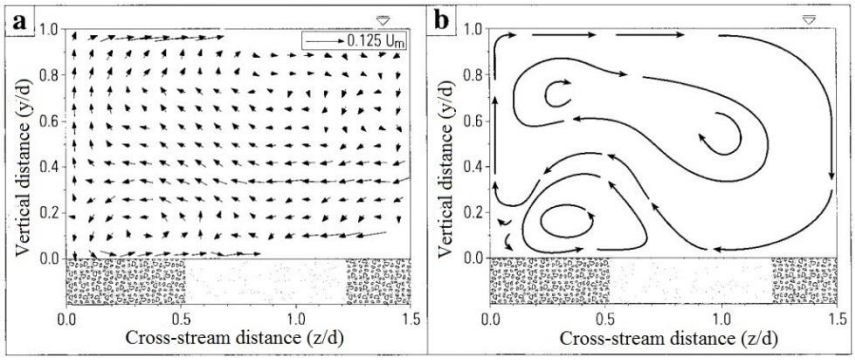

Figure 2.21 (a) Vector plot of secondary flow pattern; (b) Schematic view of inferred secondary flow pattern, (Mclelland *et al.*, 1999).

In Wang and Cheng (2005), the generation of artificial secondary flows demonstrates the effect of perturbations due to the bed configuration that induces secondary currents. Additionally, the study discusses the relationship between Reynolds shear stress and secondary flow. The analysis shows that secondary flow alters the flow structure such that it differs from the quasi-2D flow and causes the primary velocity to deviate from the classical Log-Law. Additionally, a relationship between secondary flows and bed shear stress has been established. The results show that higher bed shear stresses are always associated with downflows, and lower bed shear stresses occur at the region with upflows. This is consistent with the Nezu and Nakagawa's (1993) experimental observations as summarized in Table 2.4.

Table 2.4 Summary of turbulent flow structures in upflow and downflow regions, (from Nezu and Nakagawa 1993).

Type	Upflow Region ($V > 0$)	Downflow Region ($V < 0$)
Mean streamwise velocity	Low	High
Bed shear stress	Low	High
Turbulence intensity farther from the bed	High	Low
Reynolds shear stress farther from the bed	High	Low
Suspended load	High	Low
Bed load	Low	High
On water surface	Boil lines, divergence	Foam lines, divergence
River bed form	Ridges	Troughs
Bed roughness	Fine sand, smooth bed strips	Coarse sand, rough bed strips

The secondary flow patterns visualized by Wang and Cheng (2005) are shown in Figure 2.23.

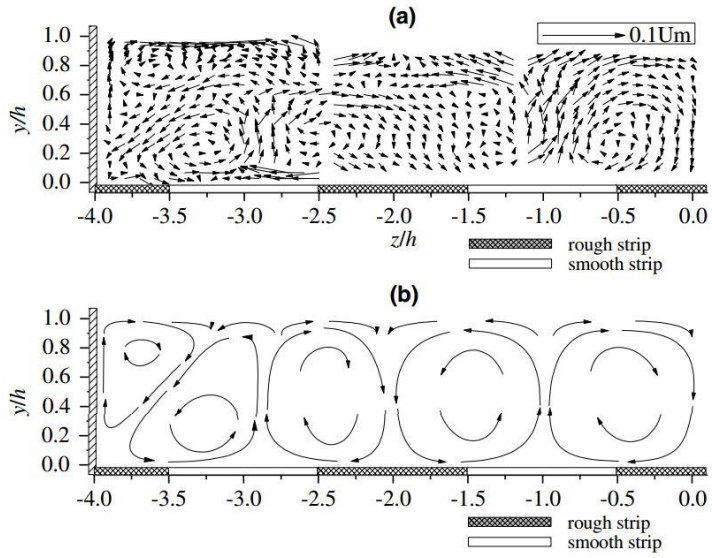

Figure 2.22 (a) Vector view of secondary flow pattern; (b) Simplified secondary flow pattern, from Wang and Cheng (2005).

Blanckaert *et al.* (2010) carried out experimental study in a 9.0 m long and 1.3 m wide straight channel. The sidewalls were vertical and smooth, and the bed roughness was

artificially formed using quasi-uniform sand grains having a diameter of 2 mm. Three flow conditions were chosen to examine the effect that the flow shallowness has on the secondary flow patterns and bed shear stresses (see Table 2.5). The three velocity components were measured using an Acoustic Doppler Velocity Profiler (ADVP) at a frequency of 31.25 Hz during 180 s. At least 36 vertical velocity profiles and 30 spanwise velocity profiles from n = 0.59 m ~ – 0.5 m were recorded. The symbols s, z and n donate the streamwise, vertical and spanwise directions, respectively.

Table 2.5 Flow condition properties (Blanckaert *et al.*, 2010).

Experiment	*b (m)*	*b/h*	$U_m\ (ms^{-1})$	*Re*	*Fr*	S_0	k^+
I	1.3	11.9	0.4	44000	0.39	0.00068	50
II	1.3	8.1	0.43	69000	0.34	0.00062	56
III	1.3	6.2	0.38	80000	0.27	0.00041	51

Figures 2.24, 2.25 and 2.26 illustrate the flow patterns of some hydrodynamic variables for experiments I, II and III listed in Table 2.5, respectively. In all three experiments, the secondary flows exist throughout the entire channel width. These secondary flows are scaled with water depth resulting in 12, 8 and 6 circulating cells for experiments I, II and III, respectively. Regions of upflow and downflow associated with lower and higher streamwise velocities, and also with lower and higher bed shear stresses, respectively. Momentum transport by the secondary flows results in lateral variability of the flow: about $0.2u^{*2}$ ~ $0.3u^{*2}$ in the bed shear stress and 10 ~ 15 % in the streamwise velocities. All of these findings are consistent with experimental observations of (Tominaga *et al.*, 1989; Nezu and Naagawa, 1993; Rodriguez and Garcia, 2008). Tamburrino and Gulliver (1999) suggested that the number of upflow and downflow regions could be calculated from the aspect ratio as:

Upflow regions = odd integer close to $\frac{A_r}{2 \to 3} + 1$ (2.30)

Downflow regions = even integer close to $\frac{A_r}{2 \to 3}$ (2.31)

It can be seen from the Figures 2.24 ~ 2.26 the number of the upflow and downflow regions agrees with the above two equations.

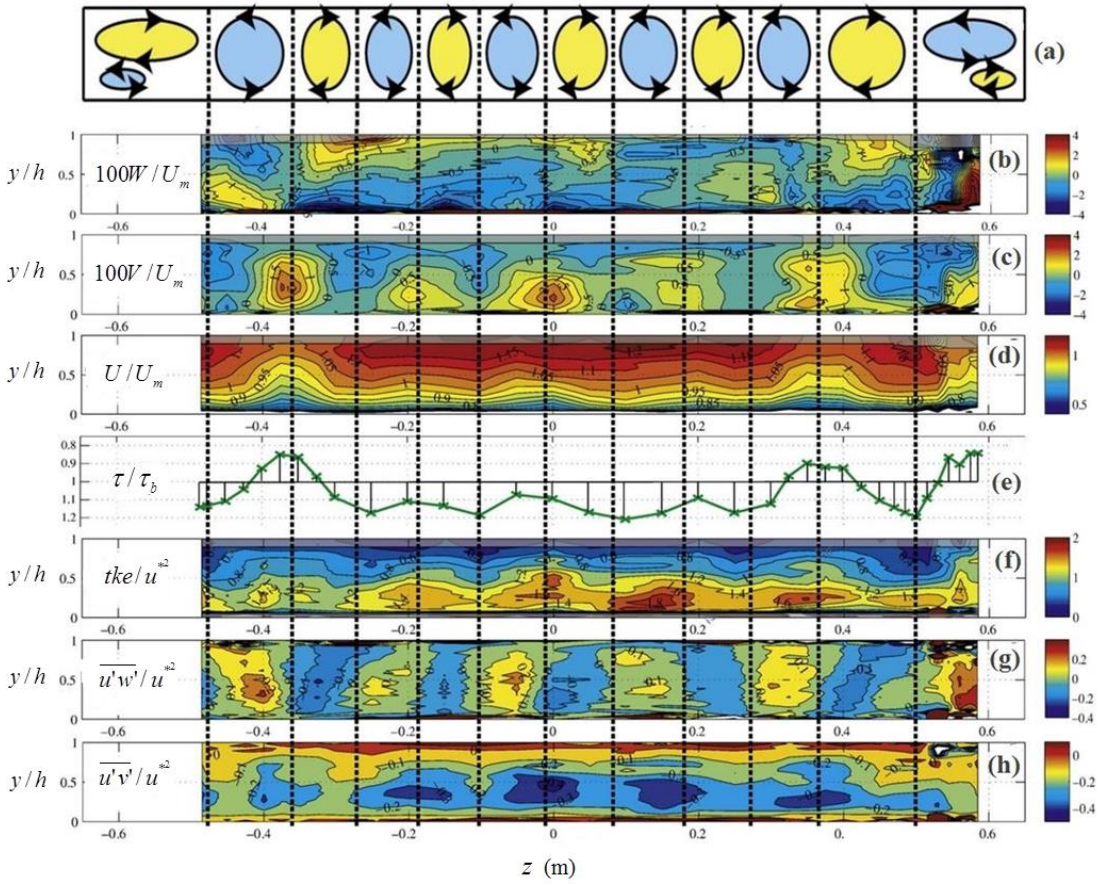

Figure 2.23 Patterns of some hydrodynamic variables for experiment I (a) **Schematic plot of secondary flow patterns;** (b) **Dimensionless spanwise velocity** $\left(100W/U_m\right)$**;** (c) **Dimensionless vertical velocity** $\left(100V/U_m\right)$**;** (d) **Dimensionless streamwise velocity** $\left(U/U_m\right)$**;** (e) **Dimensionless bed shear stress** $\left(\tau/\tau_b\right)$**;** (f) **Dimensionless turbulent kinetic energy** $\left(tke/u^{*2}\right)$**;** (g) **Dimensionless turbulent shear stress** $\left(\overline{u'w'}/u^{*2}\right)$**;** (h) **Dimensionless turbulent shear stress** $\left(\overline{u'v'}/u^{*2}\right)$**, (from Blanckaert *et al.*, 2010).**

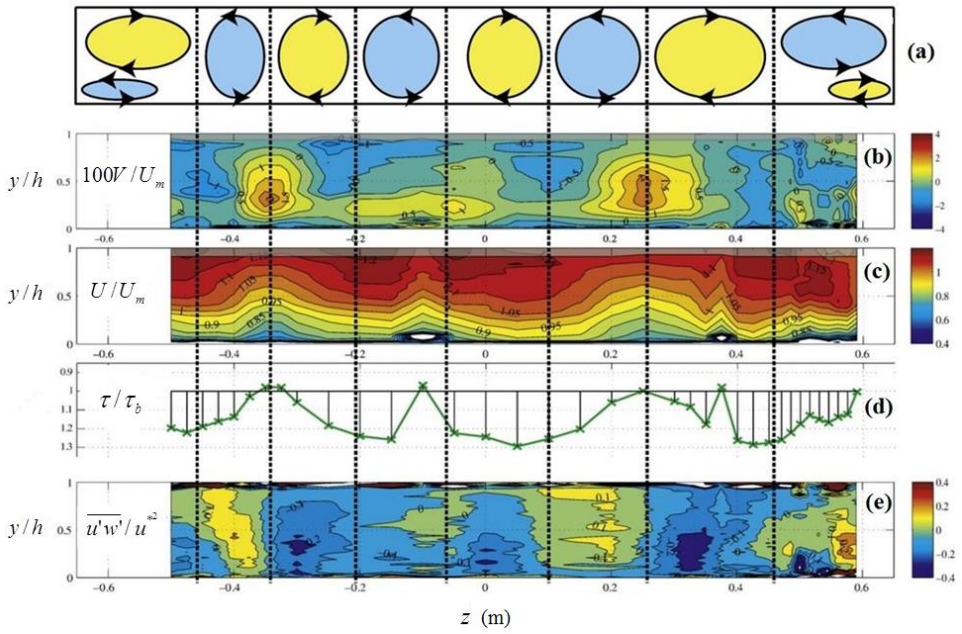

Figure 2.24 Patterns of some hydrodynamic variables for experiment II: (a) Schematic plot of secondary flow patterns; (b) Dimensionless vertical velocity $\left(100V/U_m\right)$; (c) Dimensionless streamwise velocity $\left(U/U_m\right)$; (d) Dimensionless bed shear stress $\left(\tau/\tau_b\right)$; (e) Dimensionless turbulent shear stress $\left(\overline{u'w'}/u^{*2}\right)$, (from Blanckaert *et al.*, 2010).

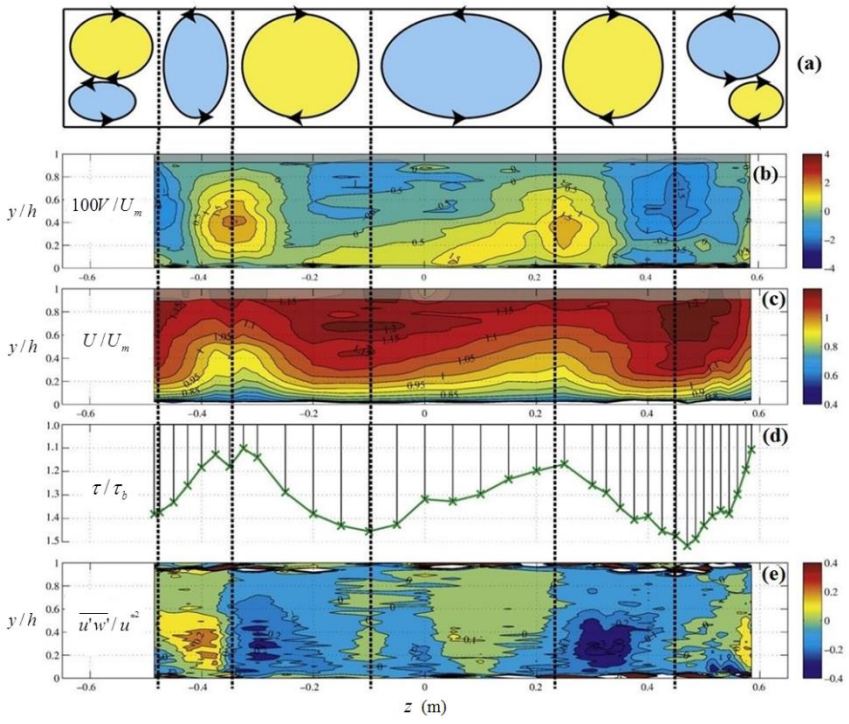

Figure 2.25 Patterns of some hydrodynamic variables for experiment III: (a) **Schematic plot of secondary flow patterns;** (b) **Dimensionless vertical velocity $\left(100V/U_m\right)$;** (c) **Dimensionless streamwise velocity $\left(U/U_m\right)$;** (d) **Dimensionless bed shear stress $\left(\tau/\tau_b\right)$;** (e) **Dimensionless turbulent shear stress $\left(\overline{u'w'}/u^{*2}\right)$, (from Blanckaert *et al.*, 2010).**

Albayrak and Lemmin (2011) defined the secondary flow phenomenon as the component of flow that occurs perpendicular to the channel axis. Of particular concerns to their study were the effect that the aspect ratio has on the dimensions of secondary flow cells, and the relationship between the secondary flow cells and the surface velocity. Their experiment was conducted in 2.45 m wide and 27.0 m long straight channel. The bed material consists of mixed gravel with size between 10 ~ 20 mm giving an average gravel size of $d_{50} \approx 15$ mm. The channel slope was set to zero so that the flow is in a state called moving equilibrium. In this case, both flow depth and shear stress change slowly in the longitudinal direction, and this change can be ignored. Three sets of experiments were investigated (see Table 2.6). In the cross section of the channel, the three velocity components were measured with an Acoustic Doppler Velocimetry Profiler (ADVP) for a period of at least 3 minutes at each location. Spanwise spacing of 20 % of the flow depth is used which can sufficiently resolve secondary flows. A sensor based on the hot-film principle was used to obtain the bed shear stress. The measurements of water surface velocities were made by a 2D Large Scale Particle Image Velocimetry (LSPIV) for a sampling duration of 3 minutes.

Table 2.6 Hydraulic parameters for the three experiments (Albayrak and Lemmin, 2011).

Exp.	Q (m^3/s)	h (m)	U (m/s)	U_{max} (m/s)	u^* (m/s)	Re	Fr	b/h	d_{50}
(1)	0.185	0.195	0.39	0.54	0.0283	76900	0.2856	12.25	1.5
(2)	0.168	0.16	0.43	0.60	0.0322	68500	0.3432	15	1.5
(3)	0.10	0.12	0.36	0.51	0.0265	43500	0.3318	20	1.5

The contour plots of the hydrodynamic variables for experiment (2) are shown in Figure 2.27. The contour map of the streamwise velocity exhibits oscillation in the spanwise direction. The maximum streamwise velocity appears at approximately

y = 0.9h and *z = 2h*, and the difference between the minimum and maximum values is around 10.0 %. Lower streamwise velocities occur in the upflow zones where the contour lines bulge towards the free surface, while higher streamwise velocities correspond to downflow zones where the contour lines are deflected towards the bed. The contour maps of the mean spanwise and vertical velocities clearly indicate the existing of the secondary flows with a maximum velocity approximately equal to 2.0 % of the maximum streamwise velocity. Near the sidewall, free surface and bottom vortices exist. The free surface vortex extends to a distance of *z = 1.75h*. This is close to the value which is reported by Nezu and Nakagawa (1993) that for large aspect ratio, the free surface vortex reaches up to *z = 2h*. The lateral spacing between upflow and downflow zones across the channel width varies between 1.5*h* ~ 2*h*. This gives a total number of 14 cells which agrees with equations suggested by (Tamburrino and Gulliver, 1999). Figure 2.27(e) shows the contour map of the normalized Reynolds Stress being undulated in the spanwise direction. In the upper region of the flow, the Reynolds Stress is higher in upflow regions, but it becomes less in downflow regions. This was pointed out previously by Wang and Cheng, (2005). The normalized bed shear stress shown in Figure 2.27(f) reveals an undulation with an amplitude of $0.2\tau_b \sim 0.3\tau_b$ which agrees with those values reported by (Nezu & Nakagawa, 1993; Mclelland *et al.*, 1999; Blanckaert *et al.*, 2010). The undulation of the bed shear stress in the spanwise direction can influence the mobility of the sediment particles which leads to the formation of the bed forms (Albayrak & Lemmin, 2011). For experiments (1) and (3), only the mean streamwise velocities were plotted in Figure 2.28 in order to investigate the influence that the aspect ratio has on the secondary flow patterns.

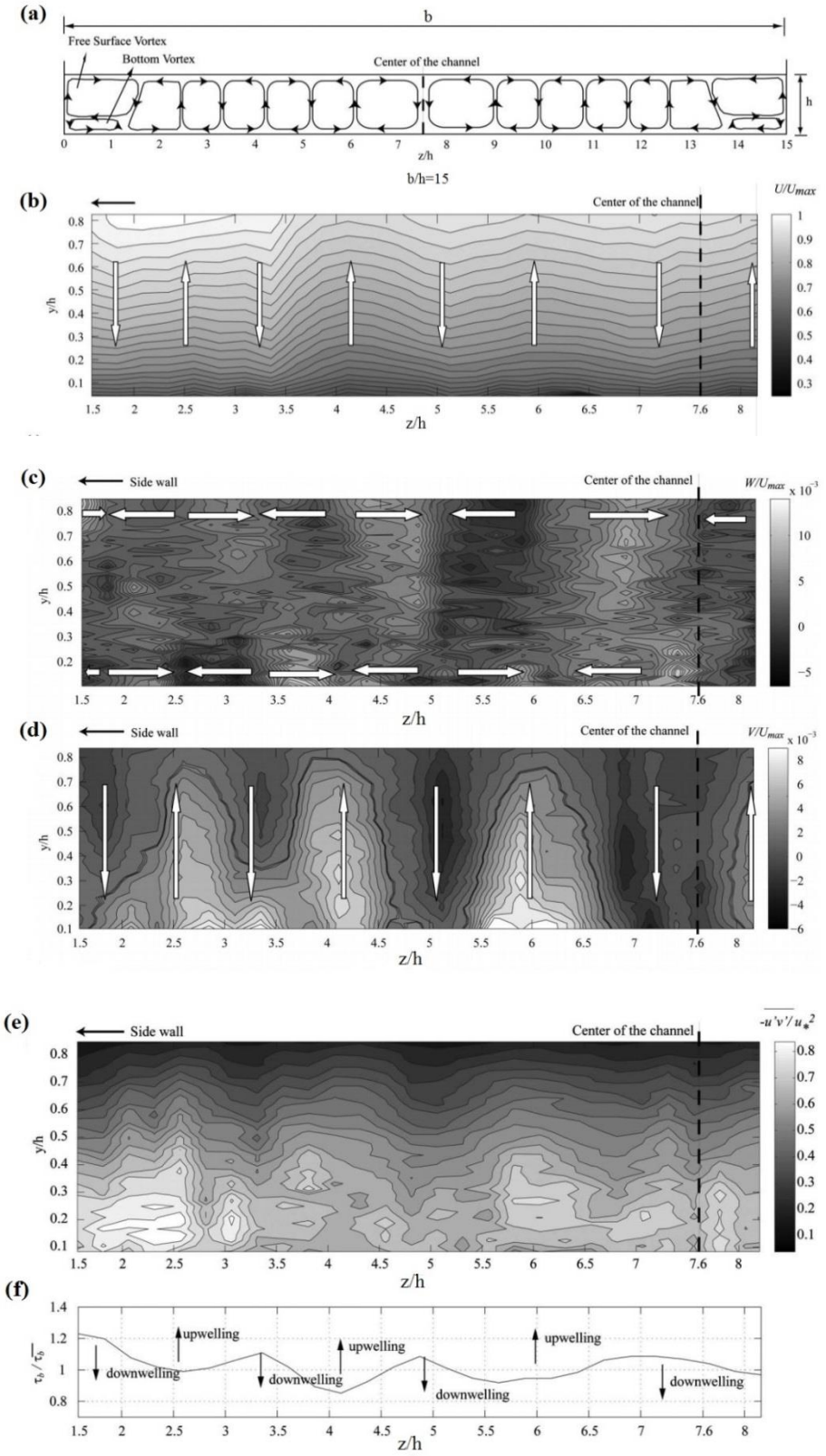

Figure 2.26 Contour lines of (a) Secondary flow patterns; (b) Normalized mean streamwise velocity ($U/U_{\max}$); (c) Normalized mean spanwise velocity ($W/U_{\max}$); (d) Normalized mean vertical velocity ($V/U_{\max}$); (e) Normalized Reynolds Stress ($-\overline{u'v'}/u^{*2}$); (f) Normalized bed shear stress ($\tau_b/\overline{\tau_b}$), (for Exp. 2), (from Albayrak and Lemmin, 2011).

Figures 2.28(a) shows that there are a number of 12 cells exist for experiment (1) which also agrees with Tamburrino and Gulliver's equations. However, Figure 2.28(c) reveals that there are 22 cells exist in the channel cross section. According to Tamburrino and Gulliver (1999), the number of cells should be equal to 20 cells. This could be due to the aspect ratio of the roughness over water depth being less than that in experiment (1) and (2). Additionally, the size of the free surface vortex in the spanwise direction becomes larger as the aspect ratio increases. For experiment (1), the free surface vortex extends to around $z = 1.5h$ and it reaches approximately $z = 1.85h$ for experiment (3). The comparison between the three experiments indicates that the aspect ratio directly controls both the number of the secondary cells and the size of the free surface vortex (Albayrak and Lemmin, 2011). Moreover, the comparisons between the mean surface streamwise velocity and the mean streamwise velocity measured in the water column for experiments (1), (2) and (3) are shown in Figures 2.29 ~ 2.31, respectively. A lateral variation in the mean surface streamwise velocities can be observed. The difference between the maximum and minimum velocities is around 10 % ~ 15 %. Higher mean surface streamwise velocity steaks correspond to the downflow regions, whereas lower values were observed in the upflow regions. These higher and lower streamwise velocity steaks were also reported by Tamburrino & Gulliver (2007). The spanwise distance between these steaks varies between $1.5h$ ~ $2h$ which correlates very well with the size of the secondary flow cells. Therefore, the pattern of the mean surface velocity could be explained by multicellular secondary flows in the water column (Albayrak & Lemmin, 2011).

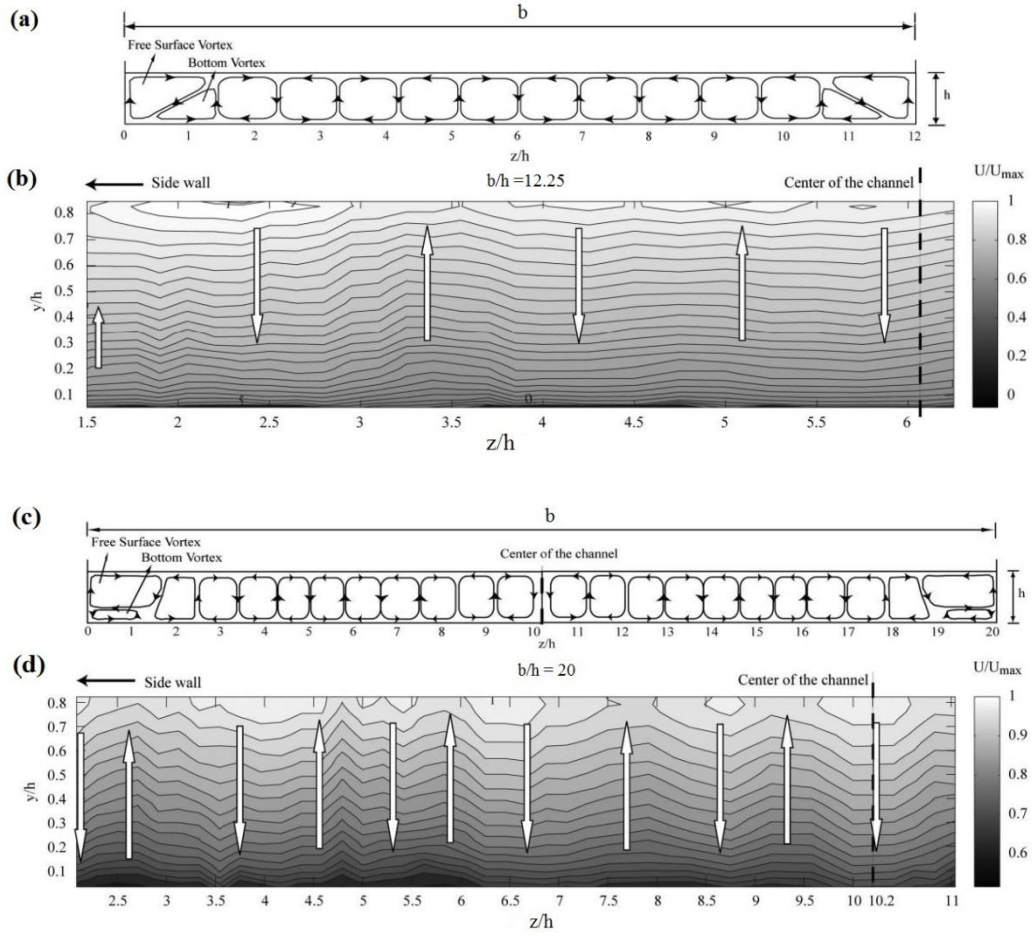

Figure 2.27 Contour lines of (a) Secondary flow patterns (Exp. 1); (b) Normalized mean streamwise velocity ($U/U_{\max}$) (Exp. 1); (c) Secondary flow patterns (Exp. 3); (d) Normalized mean streamwise velocity ($U/U_{\max}$) (Exp. 3) (from Albayrak and Lemmin, 2011).

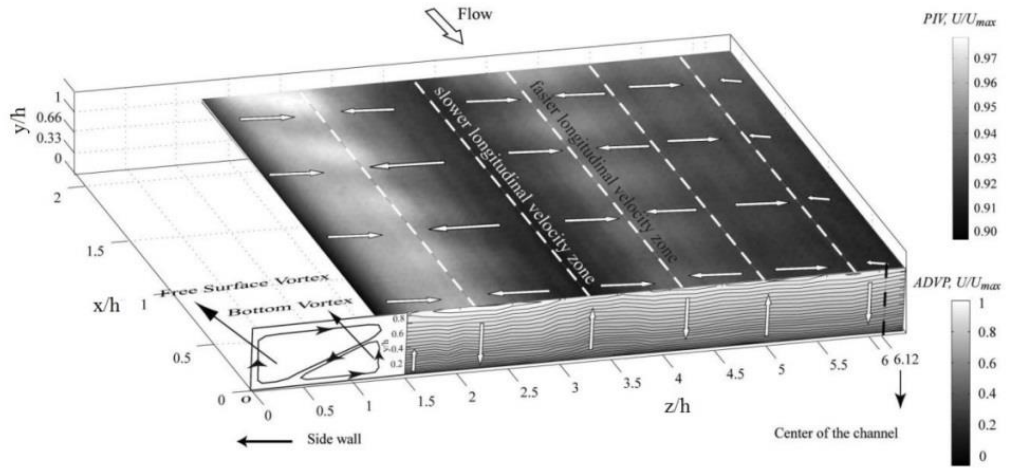

Figure 2.28 Mean patterns of the normalized streamwise surface velocity measured by PIV and the normalized streamwise velocity over the flow depth measured by ADVP (Exp. 1) (from Albayrak and Lemmin, 2011).

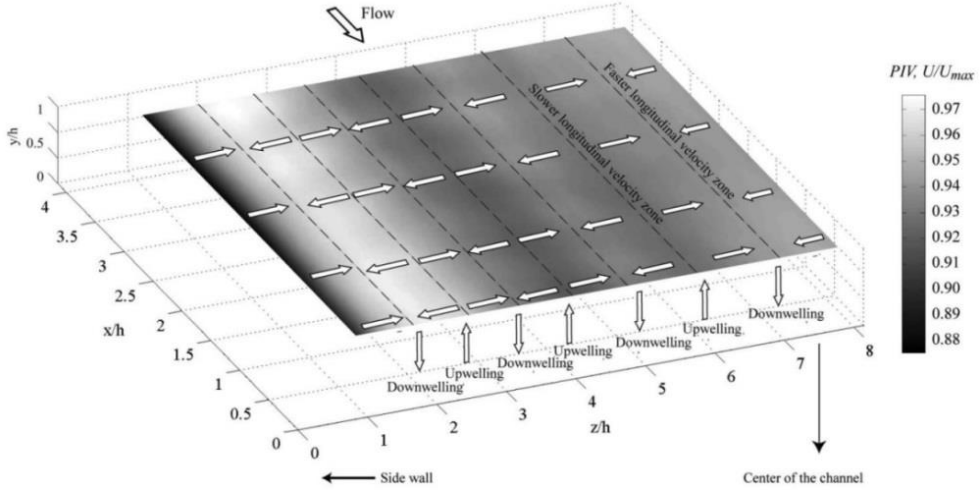

Figure 2.29 Mean patterns of the normalized streamwise surface velocity measured by PIV and the corresponding upwellings and downwellings in the water column (Exp. 2) (from Albayrak and Lemmin, 2011).

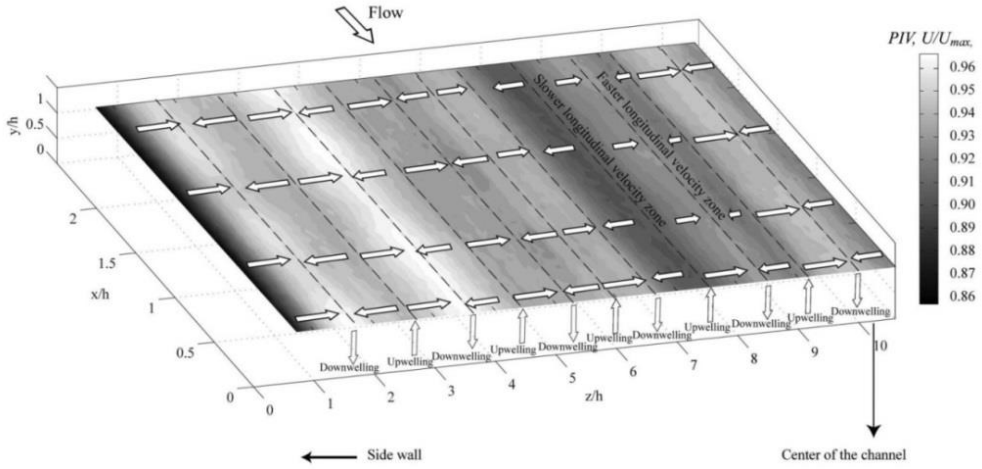

Figure 2.30 Mean patterns of the normalized streamwise surface velocity measured by PIV, and the normalized streamwise velocity in the water column measured by ADVP (Exp. 3) (from Albayrak and Lemmin, 2011).

2.4 Water surface dynamic behaviour

2.4.1 Introduction

When a fluid flows over a solid boundary, the fluid-air interface is often observed to be wrinkled. Whilst in open channel flows with the absence of the wind, the vertical velocities must disappear at the surface and while turbulent eddies can never die

inside the flow; they must end perpendicularly at the free surface. This causes temporal changes in water surface elevations above these vortices (Smolentsev & Miraghaie, 2005; Savelsberg & Van de Water, 2009). The following sections outline the techniques used to measure free surface elevations, and the interaction between the water surfaces with the underlying flow properties for open channel flows.

2.4.2 Water surface elevations measurements

Water surface dynamic behaviour studies require the measurement of the instantaneous elevations of water depth and the instantaneous velocities of the underlying flow. Several techniques have been used to provide a means of measuring these instantaneous. Dabiri (2003) used a combination of a Particle Image Velocimetry (PIV) and Free Surface Gradient Detector (FSGD) to study the interaction between a free surface and a vertical shear layer, generated by a surface-piercing splitter plate. Their experimental set up for the PIV and FSGD is shown in Figure 2.32. The general measurement technique of FSGD is based on the simultaneous two-component slope colour-encoding scheme which is originally developed by (Zhang and Cox, 1994). The FSGD was mounted on the free surface directly over the measuring area to measure the instantaneous water elevations, while the PIV generates a horizontal laser light sheet 1mm below the water surface to measure the instantaneous streamwise and snapwise velocity components. The PIV and FSGD acquire data simultaneously, thus both devices were synchronized by placing the FSGD pulse between the two PIV pulses as shown in Figure 2.32(c). Some work has been carried out using stereoscopic measurement to measure two-dimensional water surface variations in an asymmetric open channel trench (Tsubaki and Fujita, 2005). The basic principle of stereoscopic measurement is to compare two or more images of the same location recorded at the same time by

high-resolution cameras from different angles. The accuracy of this type of free surface measurement depends on two important procedures; first is to calibrate the camera parameters as accurate as possible and second to match the target points in each recorded image as closely as possible. Savelsberg and Van de Water (2006) used a novel technique called 'laser scanning' to measure the space time water surface gradient field along a line L_s as shown in Figure 2.33. The principle of this technique is based on the refraction of a laser beam. A laser beam is perpendicularly sent through a transparent bottom of a water-channel towards the water surface. The laser beam is refracted onto a translucent screen, and the laser spot is then imaged onto a position sensitive device (PSD) using two strong lenses. The registered signals can then be converted easily to time-dependent water surface gradient. For this, spectra and correlation functions can be obtained.

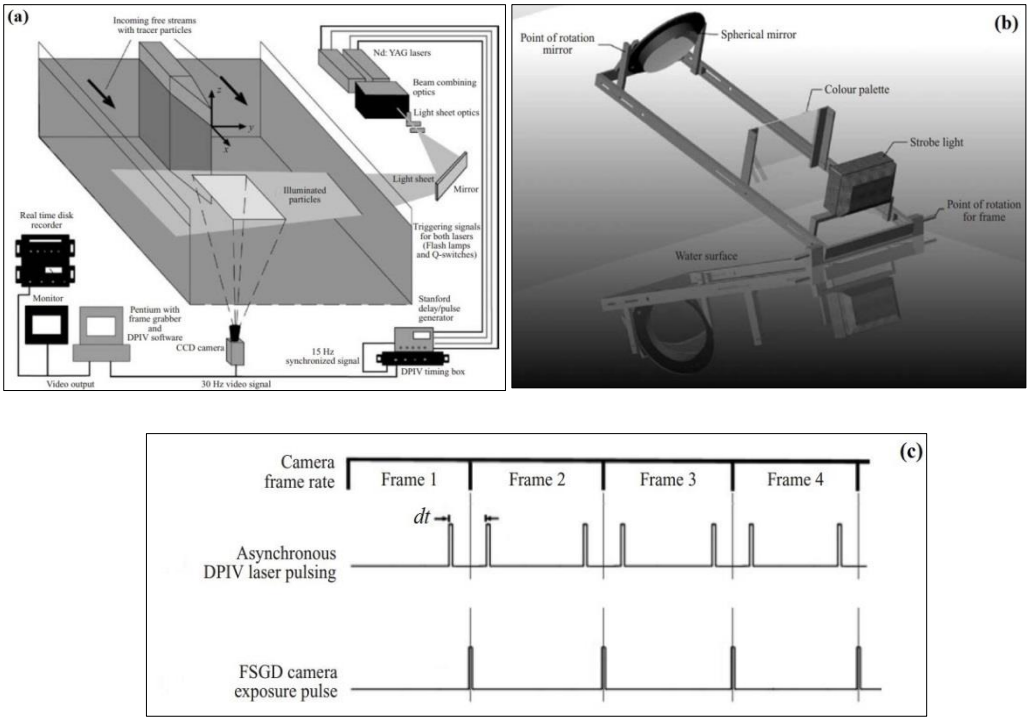

Figure 2.31 (a) DPIV experimental setup; (b) FSGD experimental setup; (c) DPIV and FSGD Time synchronization , (from Dabiri, 2003).

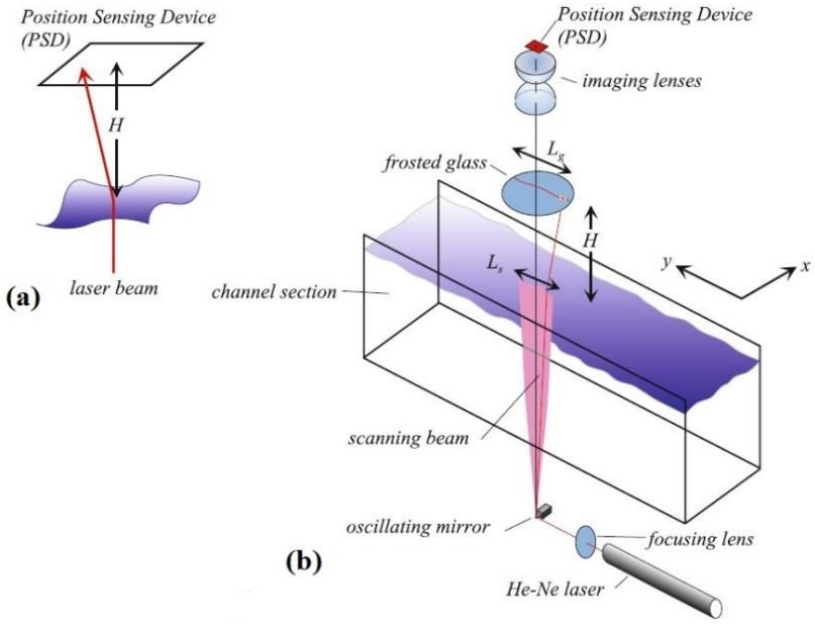

Figure 2.32 (a) A Position Sensing Device (PSD) has a surface area of 2 × 2 cm^2 located at height *H* measured from the undisturbed water surface; (b) Experimental setup of the laser scanning technique, (from Savelsberg and Van de Water, 2006).

Cooper *et al.* (2006) and Nichols *et al.* (2012) used an acoustic device which remotely measures the temporal change in water surface elevations at different locations as shown in Figure 2.34. The principle of this technique is that an acoustic wave is sent from ultrasonic transducer, this wave then is reflected from the water surface towards a microphone located at some distance away. Due to the time taken from the acoustic wave to travel from the ultrasonic transducer to the microphone, the received signal will likely has a difference in phase comparing to the transmitted signal. If the water surface is stationary then the difference in phase is constant. When the water surface is moved vertically then the difference in phase is changed. This change in phase describes in an accurate manner the water surface fluctuations. From this, the RMS wave height can be measured.

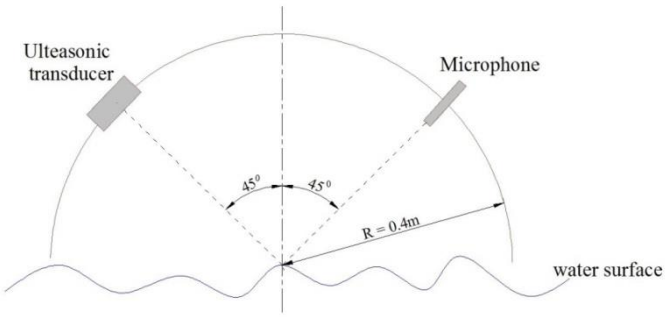

Figure 2.33 Experimental setup for the acoustical measurements (from Nichols *et al.*, 2012).

Another experimental set up detailing the use of conductance wave probes in determining water surface elevations. A conductance wave probe is composed of two thin wires which are stretched perpendicular to the water surface and partly submerged in the water. An electric current is generated using wave monitor module, and the resultant voltage between these wires relates directly to the water level between the two wires (see Figure 2.35). These probes are appropriate for conditions when the flow velocity is relatively low. Thinner wires are required to avoid generating large vortices that may have significant impact on the measurements.

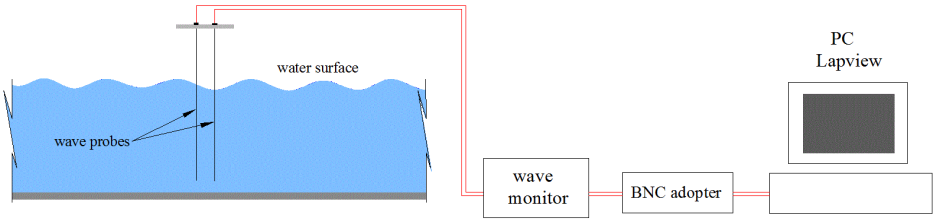

Figure 2.34 Experimental setup for conductance wave probes.

The advantage of using acoustic instruments is that, they can collect measurement without being submerged into water, unlike the conductance wave probes. However, conductance wave probes are easily to set up and calibrated, they can also be operated at different frequencies to avoid mutual interaction between two or more closely spaced probes. Generally, conductance wave probes provide high dynamic accuracy.

In more recent work by Nichols *et al.* (2016), a laser induced fluorescence technique (LIF) was used to measure the temporal change of water surface elevations in shallow turbulent flows over gravel bed. The equipment and set-up of this technique are illustrated in Figure 2.36. The principle of this technique is briefly described as follows: the laser sheet with a thickness of approximately 3.0 mm illuminates a streamwise distance 0.22 m along the centre of the flume. The LIF camera which provides an image area of 1600 × 600 pixels is focused on the laser sheet, and is synchronized with the laser pulses. The position of the air water interface was then captured by the camera at sampling frequency of 26.9 Hz. A rhodamine WT dye is added to the flow to better define the free surface in the recorded images. The free surface profile is obtained by detecting the threshold between the non-illuminated air and the illuminated flow in each column of pixels (Nichols *et al.*, 2016).

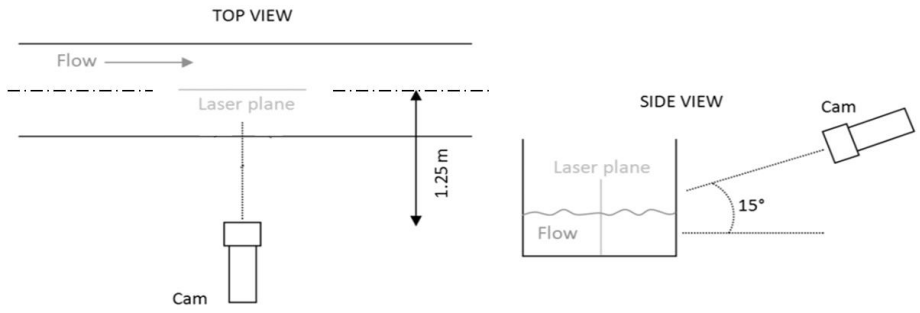

Figure 2.35 LIF Camera and laser sheet arrangement for flow visualization,(from Nicholas *et al*, 2016)

2.4.3 Interaction between water surface and underlying flow

A few experimental studies have been conducted and reported in the literature on understanding the linkage between the dynamic behaviour of the water surface and the turbulent flow structures underneath it (Smolentsev & Miraghaie, 2005; Cooper *at al*., 2006; Savelsberg *et al.*, 2006; Savelsberg & Van de Water, 2009; Fujita *et al*., 2011;

Horoshenkov *et al*., 2013; Krynkin *et al.*, 2014). Kumar *et al.* (1998) performed an experimental investigation of the characteristics of free surface turbulent in horizontal glass channel flow with Reynolds Number ranging from 2800 ~ 8800. Their results indicated that the persistent structure of the water-air interface can be classified into three types: upwelling, downwellings and spiral eddies. The upwellings were found to be related to the bursts originating from the channel bed and eddies are observed to be formed at the edge of these upwellings. These eddies often merge if they are rotating in the same direction, and they form pairs if are rotating in opposite direction. Kumar *et al.* (1998) also investigated the behaviours of the flow field in the sub surface region using PIV measurements. By comparing the spatial variation of the spanwise gradient of the vertical velocity time series with the measured upflows and downflows on the free surface, they observed that upwelling zones were associated with positive spanwise gradient in the vertical velocity, while downwelling zones are characterised by a negative lateral gradient in the vertical velocity. By examining the flow field in a vertical plane, they showed that bursting events generate upwellings on the free surface and these upwellings then generate spiral eddies and downwellings. Statistical analyses of Dabiri (2003) have shown that the free surface deformation is strongly correlated with near surface vorticity field with a correlation coefficient of about 0.7 ~ 0.8. Smolentsev and Miraghaie (2005) performed an experimental study from different flow conditions ranging from weak to strong turbulence in very wide open channel. They observed that three types of disturbances are always presented on the free surface at the same time: capillary waves, gravity waves and turbulent waves. Examples of capillary-gravity waves are those commonly observed at the surface of the ocean, which are generated due to turbulent wind, while turbulent waves are believed to be generated due to the interactions between bulk flow and water surface. The turbulent waves were found by Smolentsev and Miraghaie (2005) to be the most

dominate type, having a characteristic size of approximately half the mean flow depth. An interesting feature has also been observed on the free surface is that these turbulent waves has celerity very close to the average flow velocity, while the speed of capillary and gravity waves were different. This feature was also observed by Fujita *et al.* (2011) who stated that the water surface waves travel with velocity close to the mean flow velocity. Savelsberg and Van de Water (2009) reported that although there are several appealing relations between subsurface flow field and water surface gradient, the water surface of fully developed turbulent flow exhibits a dynamic behaviour of its own. They attributed this to the large eddies of subsurface turbulent flow exciting random gravity and capillary waves which move in all directions across the water surface. This is illustrated in Figure 2.37 which shows the spectra of the water surface deformation for one flow condition with mean flow velocity $U = 0.25$ m/s. The dashed-line in Figure 2.37(*b*) corresponds to $\omega = -kU$, while the solid-lines represent the Doppler-shifted dispersion relation of capillary-gravity waves as $\omega = \left(gk + \sigma k^3/\rho\right)^{1/2} \pm kU$, where σ and ρ are water surface tension and water density, respectively.

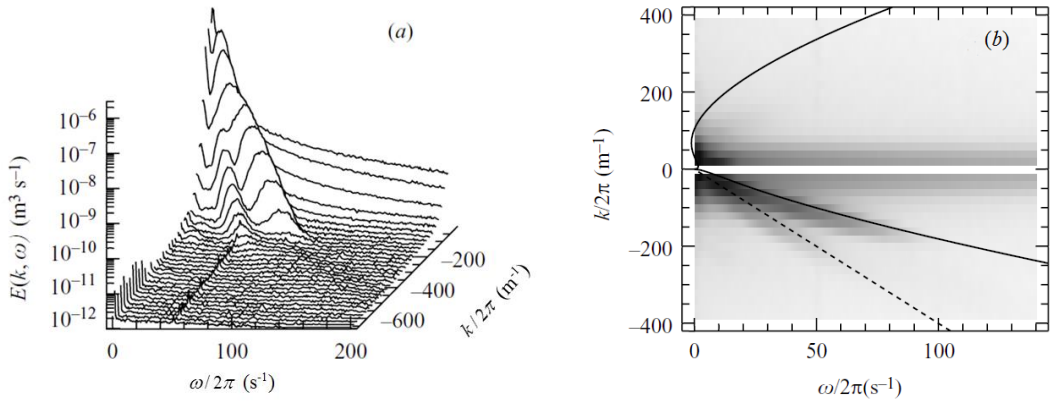

Figure 2.36 (a) Longitudinal spectra $E(k,\omega)$ of free surface; (b) corresponding shading plot, (from Savelsberg and Van de Water, 2009).

Fujita *et al.* (2011) showed that there is a strong correlation between the vertical velocity components and the boil vortices on the surface that are not due to the gravity waves. Albayrak and Lemmin (2011) performed velocity field analysis on the surface in order to detect such flow structures as vortices, swirling and the effect of upwellings and downwellings on the surface. Figure 2.38 shows the streamline map of the surface vorticity calculated as $\omega_{xz} = (dw/dx) - (du/dz)$. Several vortex pairs are observed mainly in the upflow regions where the average streamwise velocity is low, and size of these vortices was found to range from $0.3h \sim 1.0h$.

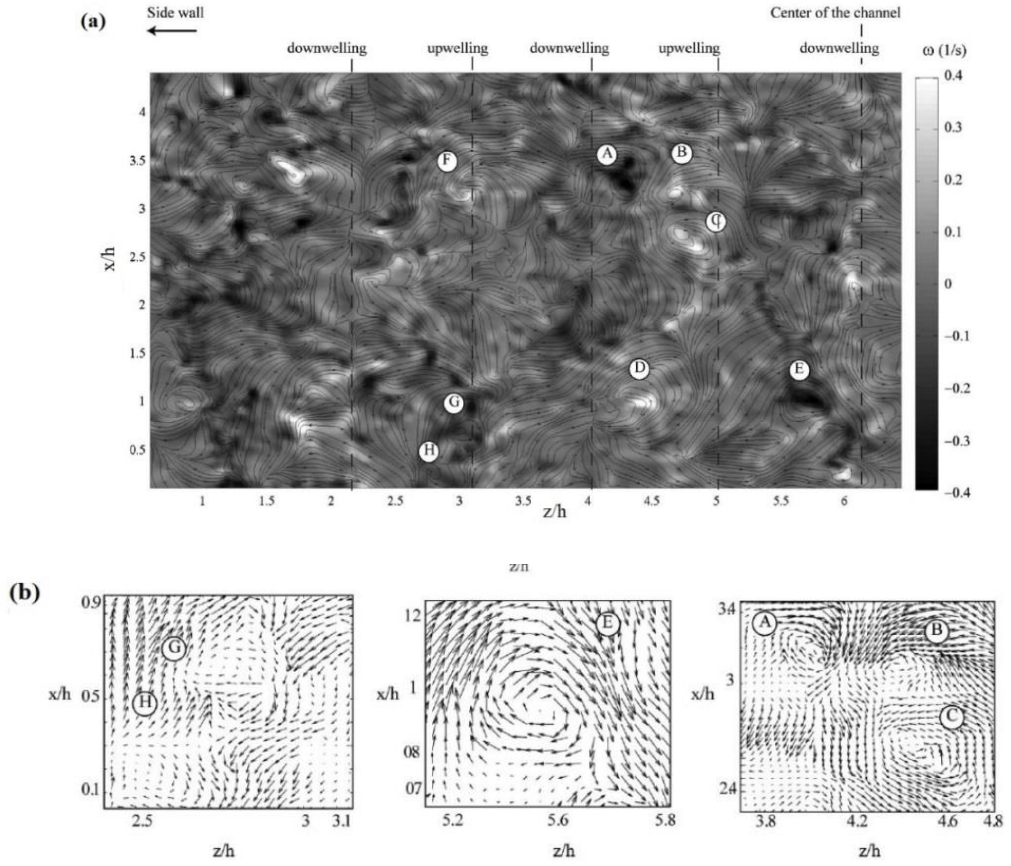

Figure 2.37 (a) Vorticity map with streamline field; (b) vectors of the instantaneous surface velocities for experiment 1 (from Albayrak and Lemmin, 2011).

Horoshenkov *et al.* (2013) experimentally studied the free surface dynamic behaviour and its interactions with the underlying turbulence of shallow open channel flows over a gravel bed. A number of sixteen flow conditions were investigated and their hydraulic parameters are listed in Table 2.7. These experiments were carried out in a 12.0 m long and 0.46 m wide rectangular open channel. The temporal change in water surface elevations was measured using conductance wave probes in the central of the channel at different streamwise positions starting from 9.5 m away from the inlet. The signals recorded at probe pairs spaced by a distance of 0 mm, 30 mm, 50 mm, and 70 mm were cross correlated to obtain the extreme values (minimum or maximum) which occurs at time lag τ. These extreme values were then presented as a function of the distance $x = V \times \tau$ for flow conditions 1, 4, and 7 (see Figure 2.39).

Table 2.7 Hydraulic parameters, from Horoshenkov *et al.* (2013).

Condition	Bed Slope	Depth, D, (mm)	Velocity, V, (m/s)	Re	Equivalent Roughness, k_s, (mm)	Relative Submergence D/k_s	rms Elevation σ, (mm)
1	0.004	40	0.29	12000	19.0	2.10	0.34
2	0.004	50	0.35	19000	17.4	2.87	0.40
3	0.004	60	0.41	26000	15.1	3.97	0.45
4	0.004	70	0.45	32000	14.1	4.96	0.57
5	0.004	80	0.50	43000	13.3	6.03	0.74
6	0.004	90	0.53	52000	12.9	7.00	0.86
7	0.004	100	0.57	66000	11.8	8.46	0.97
8	0.003	50	0.26	14000	29.2	1.71	0.36
9	0.003	60	0.31	19000	24.3	2.47	0.43
10	0.003	70	0.35	26000	22.2	3.16	0.50
11	0.003	80	0.40	35000	18.3	4.36	0.58
12	0.003	90	0.45	43000	14.7	6.11	0.67
13	0.002	60	0.22	13000	39.7	1.51	0.23
14	0.002	70	0.25	18000	34.6	2.02	0.36
15	0.002	80	0.29	23000	26.3	3.04	0.43
16	0.001	70	0.17	12000	40.3	1.74	0.11

The positions of the extreme value (round markers in Figure 2.39) were found to be close to the actual streamwise positions. This finding supports that the free surface roughness patterns are strongly controlled by bulk flow properties and are not due to the gravity waves.

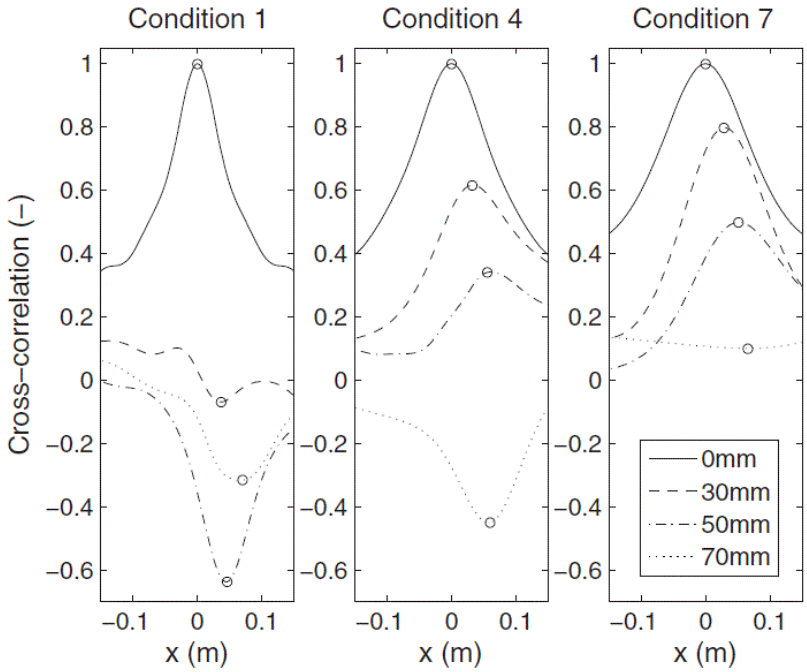

Figure 2.38 The temporal cross correlation for conditions 1, 4 and 7, (from Horoshenkov *et al.* 2013).

Horoshenkov *et al.* (2013) also showed that the free surface roughness patterns can be described by the following analytical formula:

$$W(\rho) = e^{-(\rho^2/\sigma_w^2)} \cos(2\pi\rho/L_0) \tag{2.32}$$

where W = the correlation coefficient and ρ is the spatial lag (spatial separation). Both L_0 and σ_w carry a clear physical sense. L_0 describes the characteristic period in the water surface pattern, and σ_w corresponds to the spatial radius of the correlation that describes the dissipation rate of the turbulent structures in the flow. Horoshenkov *et al.* (2013) established physical connections between the water surface patterns and the bulk flow hydraulic parameters by linking the correlation parameters σ_w and L_0 with the corresponding hydraulic parameters. Figure 2.40 shows a nonlinear relationship between the normalized characteristic spatial period L_0/k_s and the ratio of the depth averaged main velocity to the shear velocity V/U_*. The Figure generally reveals that value of L_0 carries information on the shape of the vertical profile of the main

velocity and the roughness on the bed for a number of flow conditions (Horoshenkov *et al.*, 2013).

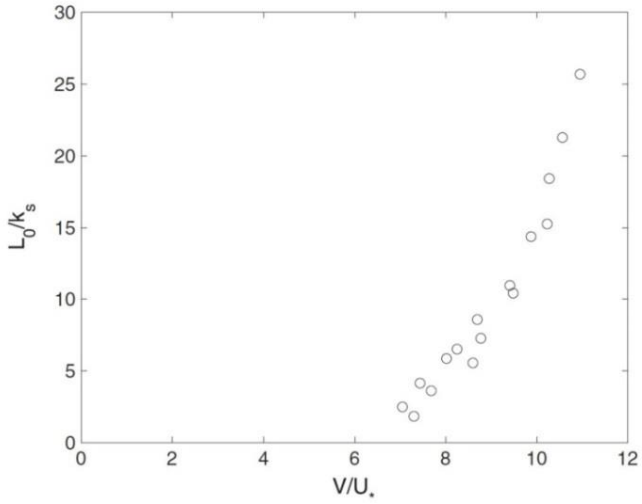

Figure 2.39 The relation between the normalized characteristic spatial period and the normalized depth average velocity, (from Horoshenkov *et al.*, 2013).

The normalized spatial radius of the correlation σ_w/k_s was found to be almost linearly dependent on Reynold Number VD/υ as shown in Figure 2.41.

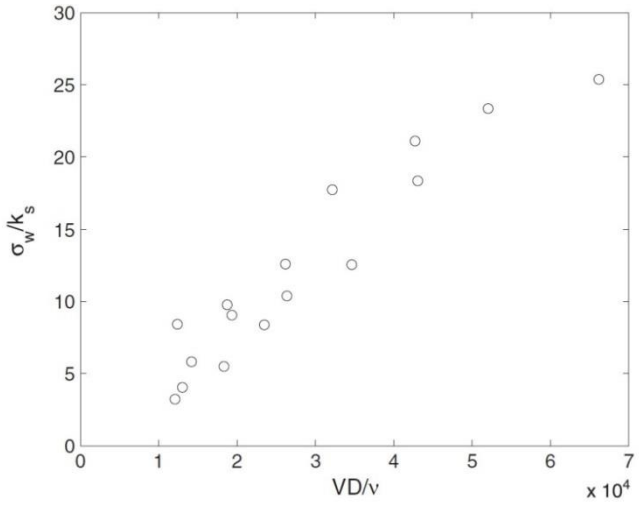

Figure 2.40 The relationship between the normalized spatial correlation radius and the flow Reynolds Number, (from Horoshenkov *et al.*, 2013).

Nichols *et al*. (2016) determined the free surface profile for flow conditions 1, 3, and 6 listed in Table 2.7 using LIF technique which was demonstrated earlier. Their results are plotted in Figure 2.42 which presents the instantaneous water surface elevations over streamwise spatial of 0.2 m and time of 6.0 sec. The greyscale represents the value of the normalized deviate which was calculated as $h'_i \Big/ \sqrt{\overline{h'^2_i}}$, where i is the streamwise position, and h'_i is the instantaneous fluctuating component of the free surface elevation at position i. The white-dashed lines correspond to the surface velocity which was measured by transit of a floating tracer. An interesting feature can be observed that the water surface fluctuating between position and negative elevations over space and time. Similar water surface pattern was in fact reported by Fujita *et al*. (2011). Another interesting phenomena can be observed is that as the flow velocity increases from condition 1 ~ 6, the spatial period of the oscillatory also increases. This finding matches well with the spatial periods measured by Horoshenkov *et al*. (2013). By comparing the gradient of the white-dashed lines and the water surface spatial patterns in Figure 2.42, it can be said that these patterns are moving with a velocity close to that of the surface velocity (Nichols *et al.*, 2016).

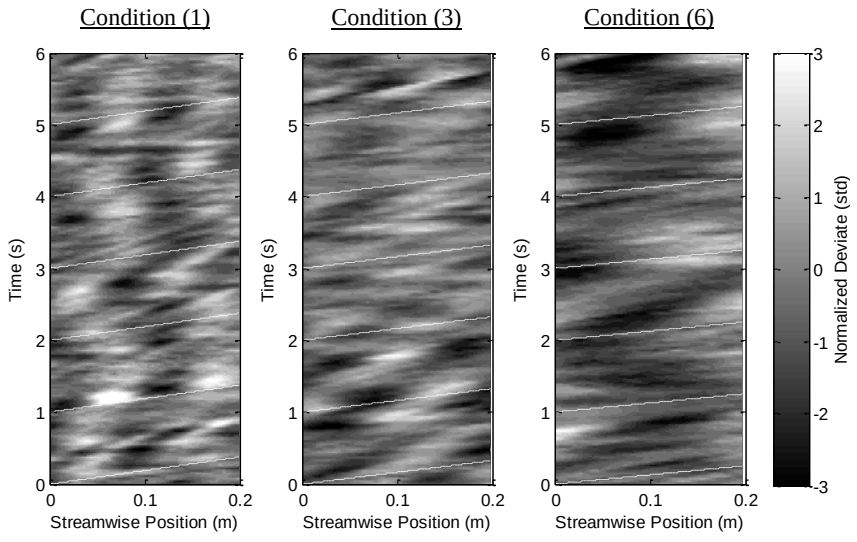

Figure 2.41 Water surface dynamic patterns for flow conditions 1, 3, and 6, (from Nicholas *et al*., 2016).

2.5 Numerical model: Smoothed Particle Hydrodynamics (SPH)

2.5.1 Background

Numerical simulations are used as a very valuable tool in the field of hydrodynamics and hydraulic engineering to solve complex problems. They have the advantage of disclosing details of flow structures without the spatio-temporal limitations of laboratory instruments. Thus they can provide an economical and fixable tool to study flows of practical interest. In numerical simulations, the physical governing equations are described into two main approaches. The first one is the mesh-based approach in which the fluid domain is decomposed into a fixed grid. Examples of this approach are Finite Volume (FV), Finite element (FE) and Finite difference (FD). These techniques have been successfully and widely used to solve various engineering problem for several decades. However, simulating complex flows with large deformations is limited and difficult with these methods due to numerical diffusion originating from the advection terms in the N-S equations (Shao *et al*, 2003). The second is the mesh-free approach in which the fluid domain is decomposed into moving points of space commonly called "particles". The Finite points (Onate *et al*, 1996), Free mesh (Yagawa & Yamada, 1996), and Moving Particle Semi-implicit (MPS) techniques all belong to mesh-free approaches. Such techniques are inherently well suited for the simulation of flows with complex boundaries. In recent years, the most popular Lagrangian mesh-free method to have been used is Smoothed Particle Hydrodynamics (SPH). Although the SPH method has been widely used in coastal hydrodynamics, using this method for the simulation of open channel flow problems has received little attention. Therefore, this study presents an investigation into the feasibility of using the SPH method for the simulation of turbulent free surface flows over rough bed.

2.5.2 Smoothed Particle Hydrodynamics (SPH)

The SPH technique, originally formulated by Gingold and Monaghan (1977) and Lucy (1977), initially focussed on the provision of solutions to astrophysics problems related to the formation and eventual evolution of galaxies (Li and Liu, 2004). It finds wide use in solving applied mechanics problems due to its advantage of using a discretization method that is using a set of particles in the approximation of a continuum. The most compelling advantage that attracts the application of the SPH method is its inherent ability to use the set of particles to predict the behaviour of highly strained motions without the need for grids or meshes (Violeau, 2012). Due to its meshless nature, SPH can handle complex solid boundaries and can also define free surface flows without the typical problems of grid-based methods that they need to be coupled with a suitable technique such as volume of fluid (VOF) to capture the air-water interface. Effective application of this technique requires an understanding of the requisite equations of fluid motion, the significance of kernels and the wide variety of options related to the application of SPH technique. The following section embarks on a description of the SPH process.

2.5.3 Fundamentals of SPH

SPH relies on an interpolation technique that expresses a function in the form of its values in a set of points which are disordered (Monaghan, 1992). The interpolation of a given function $A(\mathbf{r})$ in the SPH context is defined as

$$A(\mathbf{r}) = \int A(\mathbf{r}')W(\mathbf{r}-\mathbf{r}', h)d\mathbf{r}' \tag{2.33}$$

The integration occurs over the entire space where W represents the interpolating kernel, $\mathbf{r}$ is the vector position and h is called the smoothing length and the radius of the influence domain = $2h$. A kernel is introduced in the SPH method to avoid

singularities since it serves as the smoothing interpolation field (Li & Liu, 2004). The interpolating kernel has the following characteristics.

$$\int W(\mathbf{r}-\mathbf{r}',h)d\mathbf{r}'=1 \tag{2.34}$$

$$\lim_{h\to 0} W(\mathbf{r}-\mathbf{r}',h)=\delta(\mathbf{r}-\mathbf{r}') \tag{2.35}$$

According to Monaghan (1992), the limit is that of the integral interpolant that corresponds to the kernel. This then simplifies the complications posed by singularities. In the SPH framework, a reference particle a interacts with the neighbouring particle b within its kernel influence domain by a weighting function $W(|\mathbf{r}_{ab}|,h)$, where $|\mathbf{r}_{ab}|=|\mathbf{r}_a-\mathbf{r}_b|$ is distance between particle a and b. In the SPH approximation, the value of any vector quantity or physical scalar A of a desired particle a and its gradient ∇A can be estimated by using the following discretized summation equations that are carried out for all particles b located inside the influence domain.

$$A(\mathbf{r}_a)=\sum_b \frac{m_b}{\rho_b}A(\mathbf{r}_b)W_{ab} \tag{2.36}$$

$$\nabla A(\mathbf{r}_a)=\sum_b \frac{m_b}{\rho_b}(A(\mathbf{r}_a)-A(\mathbf{r}_b))\nabla_a W_{ab} \tag{2.37}$$

where m_b and ρ_b are the mass and density of the neighbouring particles *b*; $A(\mathbf{r}_a)$ and $A(\mathbf{r}_b)$ represent the values of the quantity A at point $\mathbf{r}_a$ and $\mathbf{r}_b$, respectively*;* $\nabla A(\mathbf{r}_a)$ = the gradient of the quantity A at a point $\mathbf{r}_a$; and $\nabla_a W_{ab}$ = the gradient of the kernel function at the desired particle *a.*

Although the summation occurs over all particles in the set, *W* is chosen so that it tapers rapidly for $|\mathbf{r}_a-\mathbf{r}_b|\geq h$. The implication of this is that only a small number of the particles contribute to the outcome.

2.5.4 Governing equations and SPH formulations

In SPH, the following mass and momentum conservation equations of the incompressible Newtonian fluids are solved:

$$\frac{D\rho}{Dt} + \nabla.\mathbf{u} = 0 \tag{2.38}$$

$$\frac{D\mathbf{u}}{Dt} = -\frac{1}{\rho}\nabla P + \mathbf{g} + \upsilon_0 \nabla^2 \mathbf{u} \tag{2.39}$$

where $\mathbf{u}$ = particle velocity vector; ρ = density; P = pressure; $\mathbf{g}$ = gravitational acceleration; υ_0 = kinematic viscosity; and t = time. The notation D/Dt is used to denote the Lagrangian or material derivative. So the fluid particle movement is computed by the following equation, where $\mathbf{r}$ is particle position vector.

$$\frac{D\mathbf{r}}{Dt} = \mathbf{u} \tag{2.40}$$

By applying the SPH discretization outlined in the previous section to mass conservation equation (2.38), the changing rate of density of particle *a* with respect to its neighbouring particles *b* can be computed as:

$$\frac{D\rho_a}{Dt} = \sum_b m_b \mathbf{u}_{ab} \nabla_a W_{ab} \tag{2.41}$$

where $\mathbf{u}_{ab} = \mathbf{u}_a - \mathbf{u}_b$.

Similarly, all terms in the momentum Equation (2.39) can be transformed into SPH forms. The following anti-symmetric form of pressure gradient of a reference particle *a* is the most commonly used as it ensures the conservation of linear and angular momentum Monaghan (1989).

$$\left(-\frac{1}{\rho}\nabla P\right)_a = -\sum_b m_b \left(\frac{P_b}{\rho_b^2} + \frac{P_a}{\rho_a^2}\right)\nabla_a W_{ab} \tag{2.42}$$

Lo and Shao (2002) simplified the viscous stress term $\upsilon_0 \nabla^2 \mathbf{u}$ to the following SPH formulation:

$$\left(\upsilon_0 \nabla^2 \mathbf{u}\right)_a = \sum_b m_b \left(\frac{4\upsilon_0 \mathbf{r}_{ab} . \nabla_a W_{ab}}{\left(\rho_a + \rho_b\right)\left|\mathbf{r}_{ab}\right|^2} \right) \mathbf{u}_{ab} \tag{2.43}$$

So in SPH notation, the momentum Equation (2.39) for a reference particle *a* can be written as:

$$\frac{D\mathbf{u}_a}{Dt} = -\sum_b m_b \left(\frac{P_b}{\rho_b^2} + \frac{P_a}{\rho_a^2} \right) \nabla_a W_{ab} + \mathbf{g} + \sum_b m_b \left(\frac{4\upsilon_0 \mathbf{r}_{ab} . \nabla_a W_{ab}}{\left(\rho_a + \rho_b\right)\left|\mathbf{r}_{ab}\right|^2} \right) \mathbf{u}_{ab} \tag{2.44}$$

To close the system of the governing equations for slightly compressible fluid flow, the following equation of state is employed to determine the fluid pressure (Monaghan *et al.* 1999).

$$P = B\left[\left(\frac{\rho}{\rho_0}\right)^{\gamma} - 1 \right] \tag{2.45}$$

where $B = c_0^2 \rho_0 / \gamma$; c_0 is the sound speed at the reference density; ρ_0 = 1000 kg/m^3 is the reference density (usually taken as the fluid density at the water surface); $\gamma = 7.0$ is the polytrophic constant; the -1 term in the above equation is to achieve zero pressure at the free surface. It should be noted that using a value corresponding to the actual value of sound speed in water requires very small time steps in order to achieve numerical stability based on the Courant-Fredrich-Levy condition. However, it was suggested by Monaghan (1994) that the minimum speed of sound should be around 10 times larger than the maximum flow velocity. This keeps the change in density to within less than 1.0 %, and therefore no major deviations are introduced.

In an SPH computation, with regard to Equation (2.40), the fluid particles are actually moved using the XSPH variant as proposed by Monaghan and Kos (1999), as follows:

$$\frac{D\mathbf{r}_a}{Dt} = \mathbf{u}_a + \varepsilon \sum_b m_b \frac{\mathbf{u}_{ba}}{\rho_{ab}} W_{ab} \tag{2.46}$$

where $\varepsilon = \text{constant}$ $(0 \le \varepsilon \le 1)$ and a value of 0.5 is often used; and $\rho_{ab} = (\rho_a + \rho_b)/2$. The idea behind XSPH variant is that a fluid particle *a* moves with speed that is close to the average speed of its neighbouring particles *b* depending on the coefficient ε. The main advantage of using this method in coastal hydrodynamics is to prevent fluid particles from penetrating each other, and thus keep the simulations to be stable. However, this technique may not be useful for fully turbulent free surface flows over rough boundary where the flow is significantly influenced by the roughness on the bed.

2.5.5 SPHysics code

SPHysics code (http://www.sphysics.org) is a free open-source SPH code that was released in 2007 and developed jointly by researchers at the Johns Hopkins University (U.S.A.), the University of Vigo (Spain), the University of Manchester (U.K.) and the University of Roma La Sapienza (Italy). The code is based on Large Eddy Simulation (LES) and it used the concept of weakly compressible SPH approach to solve the Navier-Stokes equations with different add-on features such as boundary treatment, turbulence closure, and viscosity formulation. It is programmed in FORTRAN language, and developed specifically for the free-surface hydrodynamics (Gómez-Gesteira *et al*., 2012). SPHysics code has been used to simulate different phenomena including dam breaks, breaking waves, floating and sliding objects and wave impact on a structures. In this code, a variety of features are available to choose various compiling options (see Table 2.8), and a user manual is also provided.

Table 2.8 Compiling options available in SPHysics.

Dimensions	- 2D - 3D
Kernel functions	- Gaussian - Quadratic - Cubic Spline - Wendland
Time-stepping schemes	- Predictor-Corrector algorithm - Verlet algorithm - Symplectic algorithm - Beeman algorithm
Density filter	- Shepard filter - Moving Least Squares filter (MLS)
Viscosity treatment	- Artificial Viscosity - Laminar Viscosity - Sub-Particle Scale (SPS) Turbulence Model
Boundary conditions	- Dynamic boundaries - Repulsive forces - Periodic open boundaries
Operating system & compilers	- Windows: Compaq Visual Fortran - Linux: GPL gfortran and Intel fortran compiler - Mac: GPL gfortran

This code has mainly been developed to motivate other researchers to work with SPH model more easily and to provide contributions to SPHysics code. The source code and the installation are demonstrated in details in the **Appendix** file provided with this thesis.

2.5.6 Time-stepping schemes

In SPHysics, four different time integration schemes are implemented, the Predictor-Corrector (Monaghan, 1989), the Verlet algorithm (Verlet, 1967), the Symplectic algorithm (Leimkhuler, 1997) and Beeman algorithm (Beeman, 1976). The Predictor-corrector solution has been mostly used due to its being explicit in time integration and straightforward to implement.

Besides, it is also second order integration solution, by which particle velocities, densities, positions, and pressure are computed as follows.

$$\mathbf{F}_a = \frac{D\mathbf{u}_a}{Dt} \tag{2.47}$$

$$D_a = \frac{D\rho_a}{Dt} \tag{2.48}$$

$$\mathbf{U}_a = \frac{D\mathbf{r}_a}{Dt} \tag{2.49}$$

here $\mathbf{F}_a$; D_a; and $\mathbf{U}_a$ are the right hand side terms of the conservation of momentum, mass, and particle movement Equations, respectively. The solution procedure of predictor-corrector algorithm is to predict particle velocities, positions, and densities at the first half time step $t+0.5$ using $\mathbf{F}_a$, D_a , and $\mathbf{U}_a$ at initial time t as follows.

$$\begin{aligned}
\mathbf{u}_a^{t+0.5} &= \mathbf{u}_a^t + 0.5\Delta t\mathbf{F}_a^t \\
\mathbf{r}_a^{t+0.5} &= \mathbf{r}_a^t + 0.5\Delta t\mathbf{U}_a^t \qquad \text{(prediction step)} \\
\rho_a^{t+0.5} &= \rho_a^t + 0.5\Delta t D_a^t
\end{aligned} \tag{2.50}$$

The pressure now can be determined using equation 2.45. The predicted variables are then corrected at the second half time step $t+0.5$ as follows.

$$\begin{aligned}
\mathbf{u}_a^{t+0.5} &= \mathbf{u}_a^t + 0.5\Delta t\mathbf{F}_a^{t+0.5} \\
\mathbf{r}_a^{t+0.5} &= \mathbf{r}_a^t + 0.5\Delta t\mathbf{U}_a^{t+0.5} \qquad \text{(correction step)} \\
\rho_a^{t+0.5} &= \rho_a^t + 0.5\Delta t D_a^{t+0.5}
\end{aligned} \tag{2.51}$$

Finally, the particle velocities, positions, densities, and pressure at the end of time step $t+1$ are calculated as following.

$$\mathbf{u}_a^{t+1} = 2\mathbf{u}_a^{t+0.5} - \mathbf{u}_a^t$$

$$\mathbf{r}_a^{t+1} = 2\mathbf{r}_a^{t+0.5} - \mathbf{r}_a^t \tag{2.52}$$

$$\rho_a^{t+1} = 2\rho_a^{t+0.5} - \rho_a^t$$

To achieve numerical particles stability, a variable time step Δt is controlled by the Courant–Friedrich–Levy (CFL), the forcing term, and viscosity conditions (Monaghan, 1989). According to Monaghan and Kos (1999), the variable time step Δt is determined as follows:

$$\Delta t = C_{CFL}.\min(\Delta t_f, \Delta t_{cv})$$

$$\Delta t_f = \min_a \sqrt{h/|f_a|} \tag{2.53}$$

$$\Delta t_{cv} = \min_a \frac{h}{c_0 + \max_a \left| \frac{h\mathbf{u}_{ab}.\mathbf{r}_{ab}}{\mathbf{r}_{ab}^2} \right|}$$

where C_{CFL} is a constant being $(0.1 < C_{CFL} < 0.5)$; Δt_f is based on the force per unit mass $|f_a|$; and Δt_{cv} is based on the combination of CFL and viscosity conditions.

2.5.7 Density reinitialization

In applications of Smoothed Particle Hydrodynamics for slightly compressible flow (where the flow pressure is computed by Equation 2.45 using an artificial sound speed), the fluid particles can exhibit large oscillations in the pressure field. Researchers have overcome this problem by preforming a filter over the density of fluid particles normally every 20 ~ 30 time steps to smooth out the density and pressure noise. Two different density filter methods are available for users in SHPysics code. One is called the Shepard filter (Shepard,1968) and the other is Moving Least Squares (MLS) developed by (Dilts, 1999).

2.5.8 Kernel functions

The advantage posed by the SPH method is that kernels can be calculated through a table or sub-routine. A kernel function defines the width of the influence domain and must satisfy the requirement that it behaves as a delta function as the smoothing length h tends to zero. Thus the dimensional influence of the neighbouring particles is determined. Within SPHysics, the user is able to choose from one of the kernel functions listed in Table 2.8. Although there are many kernels, the cubic spline kernel function is advantageous. This is because of its large compact support where only closer particles have large contributions to the reference particle (Monaghan, 1992). It takes on the form:

$$W(\mathbf{r}_{ab},h)=\alpha_D\begin{cases}1-\frac{3}{2}q^2+\frac{3}{4}q^3 & \text{if} \quad 0\le q\le 1.0\\ \frac{1}{4}(2-q)^3 & \text{if} \quad 1.0<q\le 2.0\\ 0.0 & \text{if} \quad q>2.0\end{cases} \tag{2.54}$$

where $\alpha_D=10/7\pi h^2$ in 2D simulations and $\alpha_D=1/\pi h^3$ in 3D simulations; $q=\mathbf{r}_{ab}/h$. Figure 2.43 presents the shape of the cubic spline kernel function and its derivative.

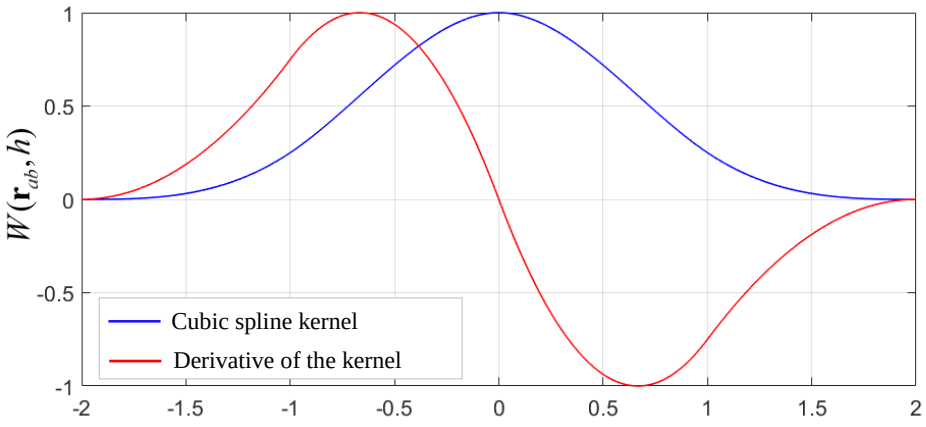

Figure 2.42 Cubic spline kernel and its derivative.

2.5.9 Solid boundary conditions

In SPH, the wall boundaries are treated mainly to ensure that fluid particles cannot penetrate the walls, also the no-slip fluid condition should be satisfied. Different wall treatments have been implemented in SPH applications, for example Ghost particles (Randles and Petscheck, 1991), Repulsive particles (Monaghan, 1992) and Dynamic particles (Dalrymple and Knio, 2001). In SPHysics, two different choices of solid boundary are available for users, the Repulsive particles and the dynamic particles. The dynamic wall particles treatment is advantageous mainly because of its computational simplicity, since the wall particles are computed inside the same loop as the fluid particles, thus the computational time is reduced.

The repulsion mechanism of the dynamic particles is that when a fluid particle approaches a wall (when distance between wall particles and fluid particles becomes less than $2h$), the wall particles density increases according to Equation (2.41) and followed by an increase of pressure according to the equation of state (Equation 2.45), thus the pressure term in the momentum equation exerts force on the fluid pressure. No-slip condition is implemented by assigning zero velocity to the wall particles. These particles are placed in two layers in staggered pattern with spacing equal to the initial fluid particle size (see Figure 2.44).

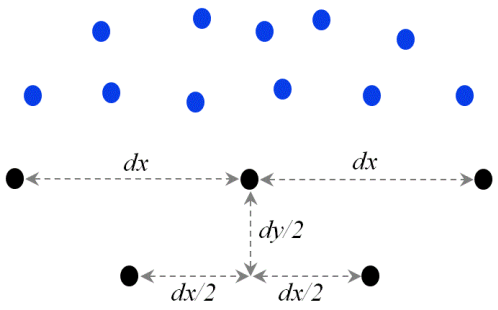

Figure 2.43 Sketch of the interaction between fluid particles (blue circles), a set of fixed wall particles (black circles) and *dx, dy* are the initial particle spacing in streamwise and vertical directions.

2.5.10 Inflow & outflow boundaries treatment

The treatment of inflow and outflow boundaries in SPH is the key for the successful simulation of open channel flow problems. In recent years, different inflow and outflow boundaries have been implemented. For example, Lee *et al*. (2008) used a periodic open boundary by which the fluid particles that leave the computational domain through the outflow boundary are instantly re-inserted at the inflow boundary, and the fluid particles close to one open lateral boundary interact with the fluid particles close to the complementary open lateral boundary on the other side of the computational domain. They implemented this boundary treatment to simulate 2D laminar flows (Re = 20 and 100) around a bluff body located between two flat plates. Their results were only compared with other numerical results obtained by FV method. This boundary treatment is demonstrated in Figure 2.45 where a fluid particle ***i*** (the red particle) lies near the right open boundary and its influence domain (or kernel support) is continued through the left open boundary so that fluid particles interact near left open boundary within the extended influence domain. This periodic boundary treatment is simple and straightforward to implement and it has a good performance in boundaries of symmetrical geometry. However, this boundary treatment is not suitable for applications in which the fluid volume leaving the computational domain does not have the same fluid volume that needs to be generated to enter the computational domain at the same time (Shakibaeinia *et al*. 2011). Later, Shakibaeinia and Jin (2010) performed a different inflow and outflow boundaries technique. In their technique, the fluid particles leaving and entering the computational domain are added to and subtracted from an additional type of particles called ’storage particles’.

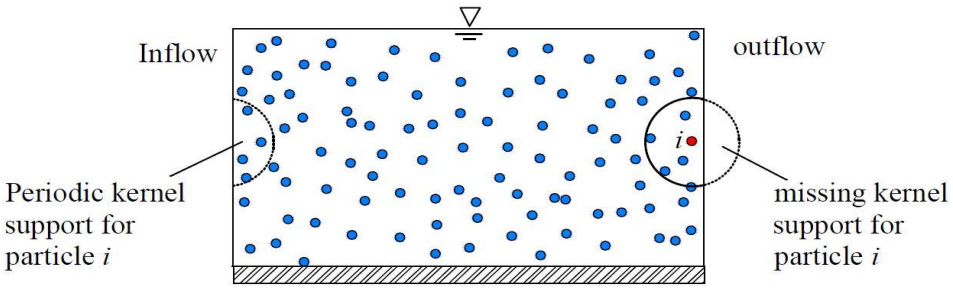

Figure 2.44 Periodic lateral boundaries:

These storage particles have no physical properties but they provide the model the capacity to subtract and add particles to the computational domain without limitation. When the fluid particles leave the solution domain, their physical properties are removed, and new physical properties are added to the fluid particles entering the computational domain depending on the type of inflow boundary conditions (see Figure 2.46). Shakibaeinia and Jin (2010) implemented this technique to validate their results using an experimental measurement of a hydraulic jump conducted by (Gomez, 2007), and both results were in good agreement in terms of the jump toe position.

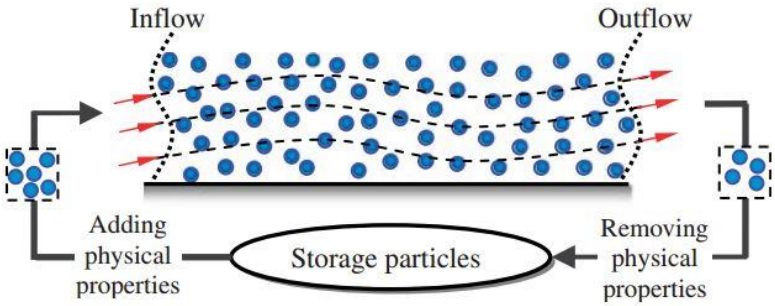

Figure 2.45 A sketch of inflow/outflow treatment proposed by Shakibaeinia and Jin (2010).

Federico *et al*. (2012) used another inflow and out flow boundaries treatment. In their model, two additional sets of boundary particles called inflow and outflow particles are defined in order to simulate different open channel flows. The width of the region

covered by these particles is at least equal to the kernel radius. The main advantage of their model is that different inflow and outflow conditions can be assigned. Figure 2.47 presents the initial sketch of their computational domain and boundaries treatment. At the inflow region, the desired pressure and velocity conditions are imposed to the inflow particles and water depths time series are determined by increasing or decreasing the number of particles in the vertical direction. They used this technique to simulate three different hydraulic test cases: laminar open channel flow, hydraulic jump and flash-flood impacting on a bridge. The latter case was chosen to test the capability of their proposed model to simulate more complex flow. In laminar open channel flow and flash-flood impacting on bridge test cases, the fluid properties that cross the outflow region, they become outflow particles and their physical properties are frozen (stay constant in time). Conversely, in the hydraulic jump test case, a specific outflow condition was imposed to force subcritical outflow. For the laminar open channel flow case, their mean streamwise velocity was only compared with an analytical solution. In the case of hydraulic jump, the averaged flow velocity profiles in the downstream were compared against the experimental finding of Hornung *et al*. (1995). Their comparison of mean streamwise velocity profiles in laminar open channel flow is presented in the following section.

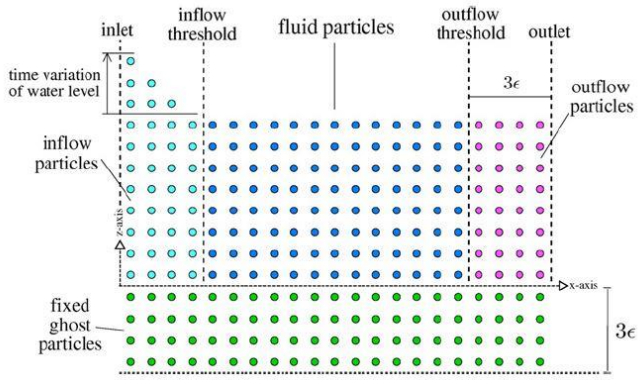

Figure 2.46 Initial sketch of computational domain and boundaries treatments Fedrico *et al.* (2012).

2.5.11 SPH model applications to open channel flow

Federico *et al.* (2012) performed 2D weakly compressible SPH modelling (WCSPH) of viscous free surface flow in the laminar regime, using range of Reynolds Number *Re* from 10 ~ 200 presented of the order $O(10^2)$. The sound speed was set to the minimum value $(c_0 = 10U_{\max})$ as recommended by Monaghan (1994), and the particle size was shown as $dx = h/125$, where h = the average flow depth. Figure 2.48 illustrates the elementary fluid domain. At each time step the analytical velocity and pressure profiles were imposed on inflow particles.

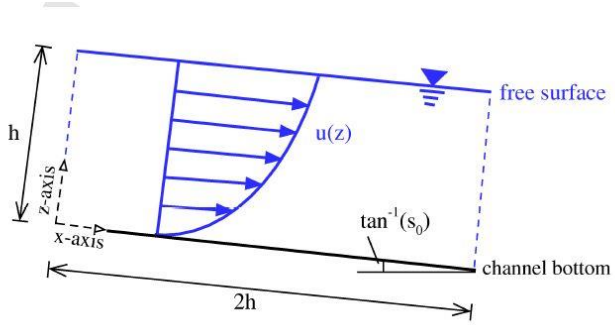

Figure 2.47 Sketch of the elementary fluid domain (S_0 =0.001), h = total water depth and channel length = 2h, Federico *et al.* (2012).

Figure 2.49 and 2.50 show the main velocity distribution for *Re* = 10.0 and *Re* = 100.0, respectively. It is apparent that the flow developed in almost parallel layers with a reasonable ordered particle distribution. The main velocity vertical profiles at $x = h$ for different *Re* were compared against the analytical solution defined as $u(z) = gS_0(2hz - z^2)/2\upsilon_0$ and are shown in Figure 2.51. A good agreement has been achieved between the analytical and numerical profiles, and the mean square error stays below 3.5 %. They concluded that SPH technique has the capability to simulate laminar open channel flows.

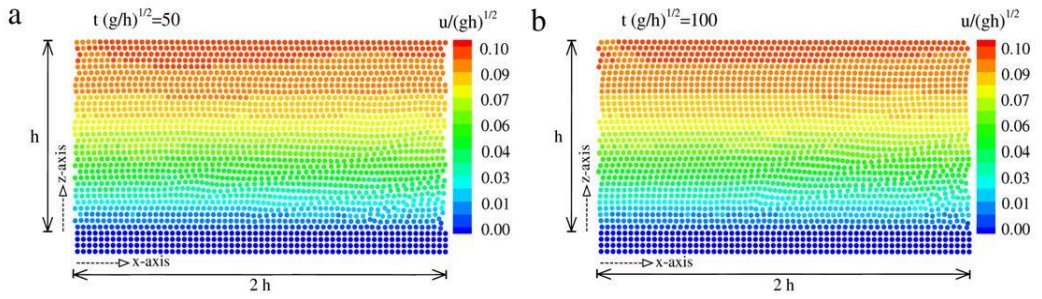

Figure 2.48 Main velocity field at (a) $t(g/h)^{1/2}=50$ and (b) $t(g/h)^{1/2}=100$ [*Re* = 10] Federico *et al.* (2012).

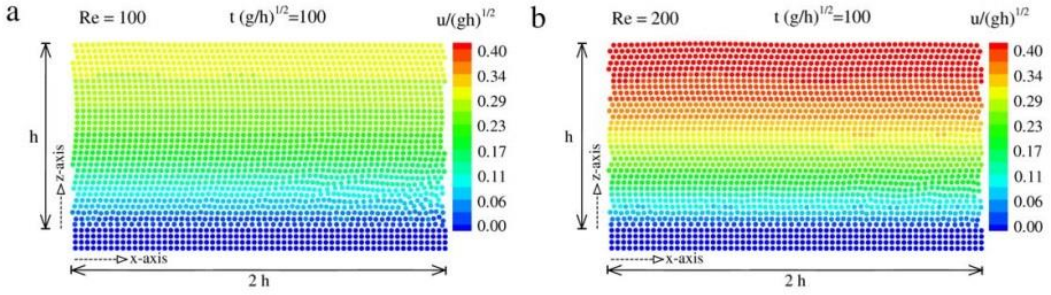

Figure 2.49 Main velocity field at (a) $t(g/h)^{1/2}$ = 100 , *Re* = 100 and (b) $t(g/h)^{1/2}$ =100 , [*Re* = 200] Federico *et al.* (2012).

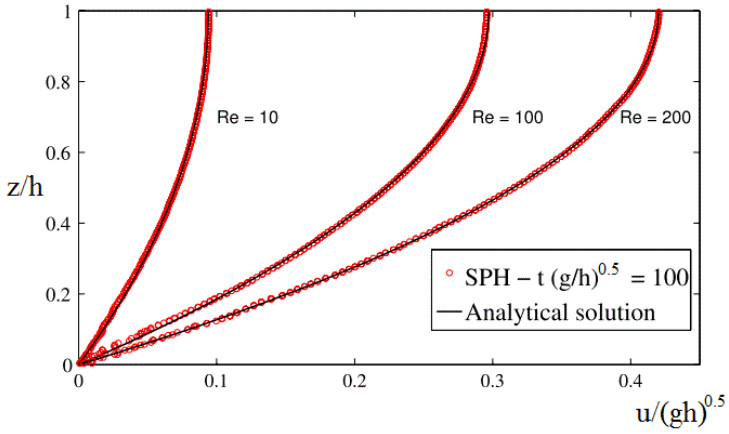

Figure 2.50 Comparisons between SPH and analytical results at $t(g/h)^{0.5}$, Federico *et al.* (2012).

More recently, Meister *et al.* (2014) performed the same numerical technique for the steady laminar open channel flows with different water viscosities; high viscous flow ($\upsilon_0 > 10^{-2}\,\mathrm{m^2/s}$) and low viscous flow ($\upsilon_0 = 10^{-6}\,\mathrm{m^2/s}$). For high viscous flow, the fluid

block of height $L_y = L_x / 2 = 0.29\,\text{m}$ driven by a bed slop $S_0 = 0.001$ were used. While for low viscous flow, $L_y = L_x / 2 = 0.03\,\text{m}$, a bed slop $S_0 = 10^{-5}$, and a resolution of 59 particles along the channel height were used. The analytical solution of the main velocity and the corresponding pressure distribution were initially imposed. Their results demonstrated that for the high viscous flow, the streamwise velocity agreed well with the analytical solution. However, when the viscosity was reduced to the actual value of water, the predicted velocities gradually deviated from the analytical solution as time increases. They also found that close to bottom boundary, there were some fluid particles moving with different velocities opposite to the flow direction (see Figure 2.52).

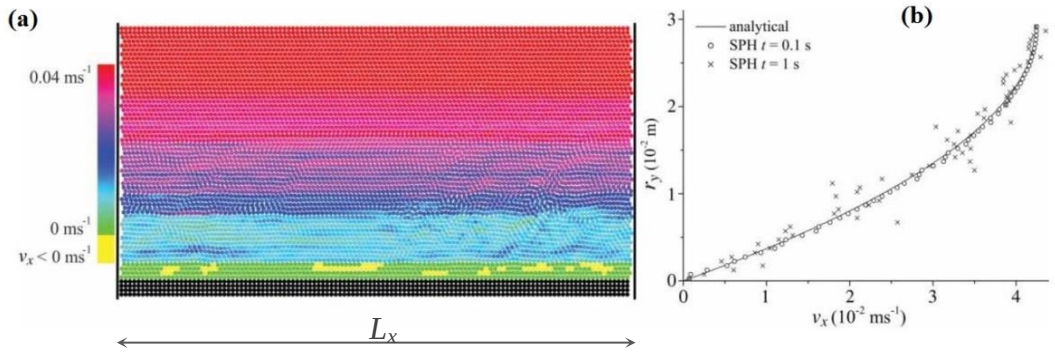

Figure 2.51 (a) Main velocity v_x distribution, (b) deviation of the main velocity profile, (*Re* = 798), Meister *et al.* (2014).

Moreover, Tan *et al*. (2015) performed Incompressible SPH technique (ISPH) to simulate open channel turbulent flows over a smooth bed. The numerical channel length of 1.2 m and water depths range from 0.1 m ~ 0.4 m were selected. To achieve balance between computational accuracy and efficiency, the initial computational particle size was selected as 0.005 m. This giving a resolution of 20 ~ 80 particles located along the water depth to minimize the channel bed boundary effect. The flow viscosity was taken as $\upsilon_0 = 10^{-6}\,\text{m}^2/\text{s}$ and Reynold Number approximately reaching 150,000 so the flows were fully turbulent. The particle velocity contour of flow depth

0.4 m is shown in Figure 2.53(a). It demonstrates a disordered and random particles motion, with large particle mixing near the interface of different velocity layers. To examine the ISPH turbulent flow model in more detail, the vertical profiles of the computed streamwise velocity for flow depth d = 0.1, 0.2 and 0.4 m were compared with the analytical profiles of Cheng (2007), defined as $U/U_{\max} = (y/d)^{1/m}$. The comparisons in Figure 2.53(b) indicate that the velocity trend in the upper region is quite promising, however, the error becomes larger near the channel bed as the flow depth becomes shallower (Tan *et al*., 2015). They attributed this to the artificial boundary drag forces which were numerically generated from imposing the nonslip velocity condition on the solid boundary. Similar issues were reported by Koshizuka *et al*. (1998) who use the Moving Particle Semi-implicit (MPS) method to study a plunging wave over a slope. They concluded that the movement of the fluid particles near the solid bed was strongly influenced by the solid boundary and this could be described by an artificial drag force.

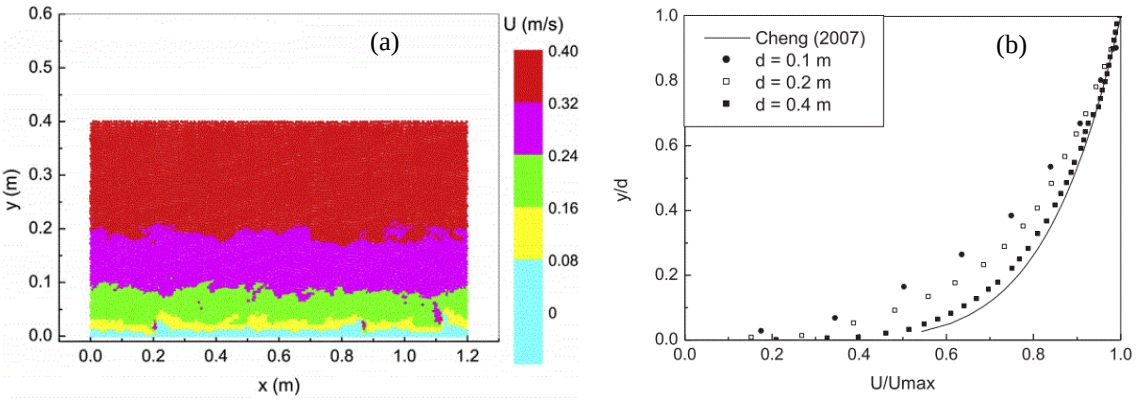

Figure 2.52 (a) Computed particle velocity contour for d = 0.4 m , (b) computed vertical velocity profiles for flow depth 0.1, 0.2 and 0.4 m, Tan *et al*. (2015).

2.5.12 Rough bed surface treatment

There is quite a limited literature on the use of SPH for describing the wall roughness in free surface flows. This is a key issue since a hydraulically rough surface exists for most practical engineering hydraulics applications. Gotoh and Sakai (1999) treated the bed roughness by incorporating a drag force term into the momentum equation for a plunging wave interaction with porous bed. Khayyer and Gotoh (2010) implemented similar treatment for dam break flow over a frictional bed. Generally their results of particles snapshots provided a good match with the measured data. Cleary & Prakash (2004) simulated the historical St Francis dam collapse using real topography which was defined by boundary particles with an interpolation length in the range of 10 m for coarse resolution simulations. The predictions were found to be reasonably consistent with the observed flood time scales. Roubtsova & Kahawita (2006) modelled the well-known Vaiont disaster in Italy 1963, where the topography of the valley was treated by particles and imposing slip boundary condition. Although the slip boundary and water levels were not known with a high precision, the simulated results fairly agreed with the sequence of events. More recently, Dzebo *et al.* (2014) performed the SPH modelling of dam break flow through a narrow rough valley. The aim of their study was to show the differences between using a hydraulically smooth terrain (where only the roughness coefficient was considered to account for the drag) and a hydraulically rough terrain (where both the roughness coefficient and form drag were considered to account for the drag due to roughness elements). For a hydraulically smooth surface, two coefficients of eddy viscosity were specified. One for particle-particle (**avis**) and another for particle-wall (**bvis**) interactions. The following equation is used to compute the turbulent viscosity between particles:

$$v_a = \mathbf{avis} d^2 \frac{|\mathbf{u}|}{l_a} \tag{2.55}$$

The following equation is used to compute the turbulent viscosity between the wall and particles:

$$v_b = \mathbf{bvis} d^2 \frac{|\mathbf{u}|}{l_b} \tag{2.56}$$

where d = particle size; $\mathbf{u}$ = particle velocity; l_a = space between particles; and l_b is the space between the particle and the boundary. For a hydraulic rough surface, the terrain roughness was defined by elevating the grid-nodes resulting in pyramid-shaped elements. The computed results were compared both with measurements on a physical model and results obtained from 2D-FV model. The comparison of the water surface level show that the SPH results obtained by either way of defining the roughness terrain agreed better than the FV model.

2.5.13 Water surface computation

In mesh free methods, the free surface can be easily and accurately tracked without numerical diffusion. Since no particles exist in the outer zone of the water surface, the density of a fluid particle drops abruptly on the surface. Different techniques have been developed in the SPH literature. According to the Incompressible SPH approach (ISPH), the free surface particle is recognized by using the density ratio. A particle is identified as free surface particle if its density is less than a certain value. Koshizuka *et al.* (1998) proposed the following condition for free surface particles recognition of the ISPH technique.

$$\rho_i \leq \beta \rho_0 \tag{2.57}$$

where ρ_i = free surface particle density; ρ_0 = initial particle density; and β = a constant parameter taken between 0.8 ~ 0.99. However, this technique may not be suitable for weakly compressible SPH approach since a small noise in the pressure

field may exist near the surface. Moreover, other researchers have numerically computed the water surface elevations using Tis Isat model (Petkovšek *et al*, 2010; Dzebo *et al*, 2012, 2013b; Dzebo *et al*, 2014). The Tis Isat model calculates water depth h_{dep} at any chosen point using the following two equations:

$$h_{dep} = d^2 \sum_b W(\mathbf{r}_{obs} - \mathbf{r}_b) \qquad \text{for 2D-simulation} \qquad (2.58)$$

$$h_{dep} = d^3 \sum_b W(\mathbf{r}_{obs} - \mathbf{r}_b) \qquad \text{for 3D-simulation} \qquad (2.59)$$

where $\mathbf{r}_{obs}$ is the location of the observed point where the water position is to be determined, W the kernel function. Figure 2.54 shows the computation of water position with the 2D Tis Isat model. Fluid particles within a *2h* distance from the observed point (red particles in Figure 2.54a) affect the water elevation at the observed point. The influence of the kernel function (Figure 2.54b) for each fluid particle located within 2*h* distance from the observed point is obtained using the cubic spline kernel shown in Equation (2.54).

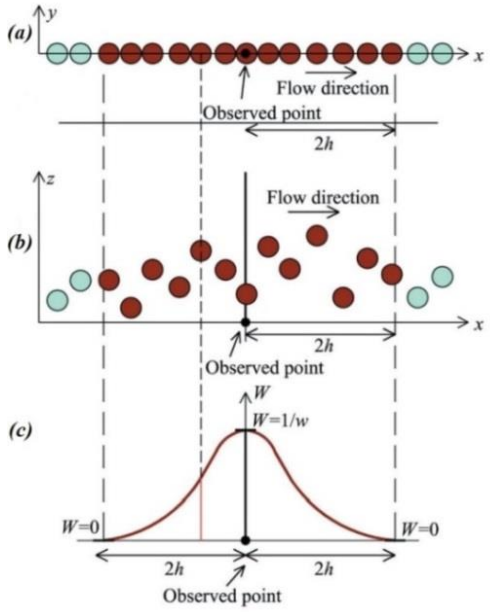

Figure 2.53 Computation of water elevation with 2D Tis Isat model (a) top view of the free surface with the observed point; (b) side view of the free surface with the observed point (c) Kernel influence (Equation 2.55), from Dzebo *et al,* 2013b.

Lee *et al*. (2008) and Farhadi *et al*. (2016) used another technique called particle divergence to compute the water surface level. This divergence in the SPH formulation is defined as:

$$\nabla.\mathbf{r} = \sum_b \frac{m_b}{\rho_b} \mathbf{r}_{ab}.\nabla_a W_{ab} \tag{2.60}$$

In a 2D model, the divergence $\nabla.\mathbf{r}$ is equal to 2.0 when the kernel is fully supported (far enough away from the free surface boundary). Near the water surface the kernel is truncated due to the insufficient number of neighboring particles, and thus the divergence $\nabla.\mathbf{r}$ becomes smaller than 2.0. This feature is implemented to recognize the free surface particles. Lee *et al*. (2008) and Farhadi *et al*. (2016) suggested that a threshold criterion ranged from 1.2 ~ 1.5 can be used to determine which particle belongs to the water surface. Most of the free surface particles are accurately detected and some of them could not be detected. This is because the free surface particles that could not be detected have a pressure very close to zero. The defect is acceptable, and it could be further minimized by kernel correction techniques (Lee *et al*., 2008; Farhadi *et al*., 2016).

2.6 Literature review conclusions

This chapter has outlined the pertinent data related to turbulent flow structures in flows with a free surface. Starting with definitions and explanations of the concepts of quasi-2D turbulence flow structures, the review endeavoured to also provide an adequate analysis of the correct state of knowledge on the 3D turbulence flow structure generation, evolution and the influence of the bed roughness in turbulent open channel flow common in rivers.

Several experimental studies have been conducted in open channels and showed that turbulence flow structures are initiated at the bed and grow upwards with the flow depth. In near bed regions, shear stresses were found to be larger over rougher bed surfaces. Smoothing the bed surface reduces boundary shear stresses and hence alters the turbulence structures flow. Spanwise variation in near bed turbulence flow structures leads to secondary flows that move from low streamwise velocity or (low bed shear stress) region to high streamwise velocity or (high shear stress). Additionally, secondary flow patterns were found to be significantly influenced by the roughness distributions, roughness shape, and flow submergence ratio. Smaller flow structures generated near the bed are transferred by the mean flow velocity until they combine to form large flow structures and occupy the entire water depth. These flow structures considerably wrinkle the water surface by creating surface features such as splats and boils by upwellings and eddies by downwellings. Although, some fundamental understanding of the turbulence flow structures effect on free surface flow was provided, knowledge gaps exist in the study of the linkage between the water surface and the turbulence flow structures beneath the surface. It is essential that the outlined knowledge gaps be filled by future research on the turbulent flow structures for flow with a free surface.

Finally, the chapter has also reviewed the existing literature on the use of a numerical model based on the Smoothed Particle Hydrodynamic (SPH) for simulating open channel flows. SPH finds numerous applications related to fluid mechanics. It is capable of handling complex problems related to beach surface disruption by ocean waves and motion of elastic and rigid bodies. The SPH method is of invaluable application in studying the effects of waves on coastal structures, the study of dam spillways and simulations of low Reynolds Number free surface water flows.

Although in the last decades the SPH modelling has been widely used to simulate different free surface flows, few researchers have used the SPH for the simulation of turbulent open channel flows. This is because of the difficulty to treat the inflow and outflow boundaries in SPH. They only used analytical solutions to validate their computations under specified laminar flow conditions.

As for open channel turbulent flows over rough beds, almost no work has ever been reported in the literature of using SPH models to simulate bed roughness in turbulent flows. Additionally, the SPH model has only been used to examine the dynamic behaviour of the water surface in coastal hydrodynamic problems. Therefore, it is worth to investigate the capability of this model for simulating free surface turbulent flow over rough beds. In this case, the improvements of the 2D and 3D SPH models will be made on turbulence modelling to address the shear stress, and new treatments of rough beds will be developed to account for the drag forces due to roughness elements. Also the improved models will then be used to examine the dynamic behaviours of the water surface and its interactions with the flow structures underneath.

This work will pave the way for researchers to implement the SPH technique in open channel flows with more complex geometries, rough boundaries, and to extract more details on the flow structures and water surface behaviour, since these details are currently difficult to be obtained by the grid-based methods.

CHAPTER 3 Experimental Study

3.1 Aims of the experiments

The aim of these experiments is to measure the flow velocity components in streamwise, vertical and lateral directions over a fixed uniform rough bed for a range of flow conditions. It was also the intention to measure the temporal change in water surface elevations at different locations in the streamwise and lateral directions. These measurements will then be used to support the development of the SPH approach for use in open channel shallow, turbulent free surface flows. This will allow examination of the underlying flow patterns and the water surface spatial pattern.

3.2 Hydraulic flume setup

3.2.1 The hydraulic flume

Measurements were carried out in an 0.459 m wide and 12.6 m long rectangular open channel flume including the recirculation water system as shown in Figure 3.1. At the upstream end the hydraulic flume is supported on a fixed pivot joint and on a pivot joint attached to an adjustable jack at the downstream end. The sidewalls of the fume were composed of glass to enable flow observation.

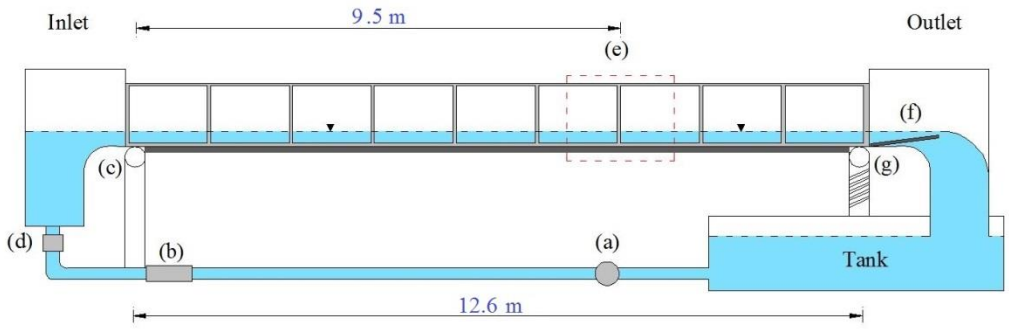

Figure 3.1 Side view of the hydraulic flume: (a) pump, (b) flowmeter, (c) fixed pivot joint, (d) adjustable valve, (e) measurement section, (f) adjustable plate, (g) adjustable jack.

3.2.2 Bed roughness material

To form a well-defined rough bed surface, the channel bottom was covered by two layers of smooth plastic spheres with diameter of D = 25.0 mm and density of 1400 kg/m^3, which were arranged in a hexagonal pattern as shown in Figure 3.2.

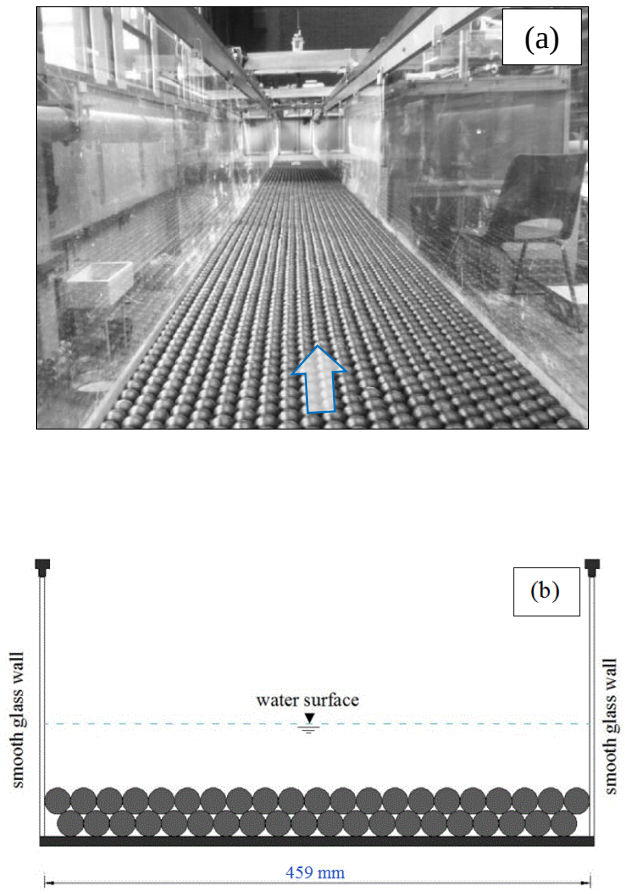

Figure 3.2 (a) Photograph of the flume taken from the inlet; (b) cross sectional view of the flume included the spheres.

3.3 Experimental flow conditions

In this study, a total number of eight hydraulic flow conditions were selected using a wide range of water depths and bed slopes that would provide a range of Froude Number, as shown in Table 3.1. Also these flow conditions were selected to

investigate the influence of rough bed elements on velocity and shear stress profiles as well as on water surface patterns of the turbulent flows. The experimental Re Numbers ranged approximately 11000 ~ 43000 so all the flows were fully turbulent.

Table 3.1 Summary of the experimental flow conditions.

Flow condition (-)	Uniform flow depth h_w (mm)	Mean velocity $\overline{U}$ (m/s)	Shear velocity u^* (m/s)	Flow rate Q (m^3/s)	Bed slope S_0 (-)	Reynolds Number Re (-)	Froude Number F_r (-)	Hydraulic roughness k_s (mm)
1	40	0.28	0.039	0.008	0.004	11200	0.447	35.0
2	50	0.35	0.044	0.011	0.004	17000	0.499	35.0
3	60	0.26	0.034	0.010	0.002	13200	0.339	30.0
4	70	0.33	0.037	0.013	0.002	23100	0.398	28.0
5	70	0.36	0.045	0.016	0.003	30800	0.434	30.0
6	80	0.42	0.048	0.021	0.003	33600	0.474	28.0
7	90	0.47	0.051	0.024	0.003	42300	0.500	26.0
8	100	0.43	0.044	0.023	0.002	43000	0.434	22.0

Shear velocity describes the gradient of the velocity profile near the boundary of the flow (< 20% of the total flow depth) and was calculated as $u^* = \sqrt{gh_wS_0}$, where g = 9.81 m/s^2. Reynolds Number Re was calculated from: $\overline{U}h_w/\upsilon_0$ and Froude Number $F_r = \overline{U}/\sqrt{gh_w}$. The hydraulic roughness k_s was determined by fitting the average streamwise velocity measured in the centreline of the flume to the Log Law for rough bed turbulent flows given by Equation 2.3.

3.4 Flow velocity measurement & analysis

Firstly, the preparations for the velocity measurement were carried out as follows:

- The water was seeded with a polymer powder type (Plascoat Talisman 30) which is normally used for coating metals. This material acts as seeding

particles with a diameter of around 150 μm, and also was neutrally buoyant and so followed the flow path representatively. The specific gravity of these particles is 0.99, which is sufficient to maintain particles suspended in the water for several hours (Vlaskamp, 2011). This material provides adequate return signal strength for an Acoustic Doppler Velocimeter (ADV).

- For each flow condition, the bed slope of the flume was controlled by using an adjustable jack located in the outlet end.
- The uniform flow depth h_w was measured with three point gauges located before, beyond and within the measurement section at locations 4.5 m, 11.0 m and 9.5 m measured from the inlet, respectively.
- The zero datum was taken as the mean hemisphere elevation (4.0 mm below the top of the spheres), from which the uniform flow depth h_w is measured.
- In the measurement section, a 3D side-looking Acoustic Doppler Velocimetry (ADV) probe was mounted on a scaled mechanical frame. This allows the instrument to measure the flow velocity components in the vertical and lateral directions. The size of the sampling volume is 6 mm (diameter) and 6 mm (height), and is located 5 cm away from the tip of the ADV transmitter.

Secondly, the experiments were started by switching on the pump and carefully adjusting the flow rate by an adjustable valve located in the flume inlet pipe. The uniform flow was then established using the adjustable plate located in the outlet. The maximum deviation between the flow depths measured by the three point gauges stayed below 1.5 % of the flow depths used. This indicates that the water surface slope was almost equal to the bed slope for all flow conditions. The flow rate was

determined using a calibrated orifice plate located in the inlet pipe. For each flow condition, the flow was running for at least one hour before measurements were taken. This is to allow equilibrium conditions to be established. The measurement section is located 9.5 m away from the inlet, which is believed to be more than sufficient to allow stable flow condition to establish. This length was estimated based on the relation $L \approx h_w(76 - 0.0001\mathrm{Re}/F_r)$ proposed by Kirkgöz and Ardiclioglu (1997) for turbulent free surface flows over a smooth bed.

Thirdly, the ADV velocity measurements were taken in the following three steps:

Step I: for the eight flow conditions listed in Table 3.1, velocity measurements were taken in the vertical direction at the flume centreline within the measurement section.

Step II: based on the fact that near-bed secondary flow always moves from regions with lower bed shear stress to the regions with higher bed shear stress, the lateral distribution of bed shear stress along one half of the flume cross section was measured from the side wall (z= 0.0 mm) towards the centreline of the flume (z= 230 mm) using lateral spacing of Δz=10.0 mm. The bed shear stress was approximated from the Reynold stress $\tau = -\rho\overline{u'v'}$ at vertical location y = 12.0 mm from the zero datum. These measurements were only taken for conditions 2 and 8 as they represent the shallower and deeper flow conditions, and thus different secondary flow patterns are expected to occur. The normalized lateral distribution of bed shear stress for conditions 2 and 8 are presented in Figure 3.3. They reveal an undulation with an amplitude of 20% ~ 50% of the mean bed shear stress ($\tau_b = \rho u^{*2}$). The lateral distributions of the bed shear stress suggest a number of 10 and 6 cells exist across

the flow cross section for condition 2 (shallower) and condition 8 (deeper), respectively. These numbers agrees well with both Equation (2.30) and (2.31) provided by Tamburrino and Gulliver (1999). The size of these cells varies approximately between $0.6h_w$ ~ $1.2h_w$ and become smaller as moving towards the flume centreline.

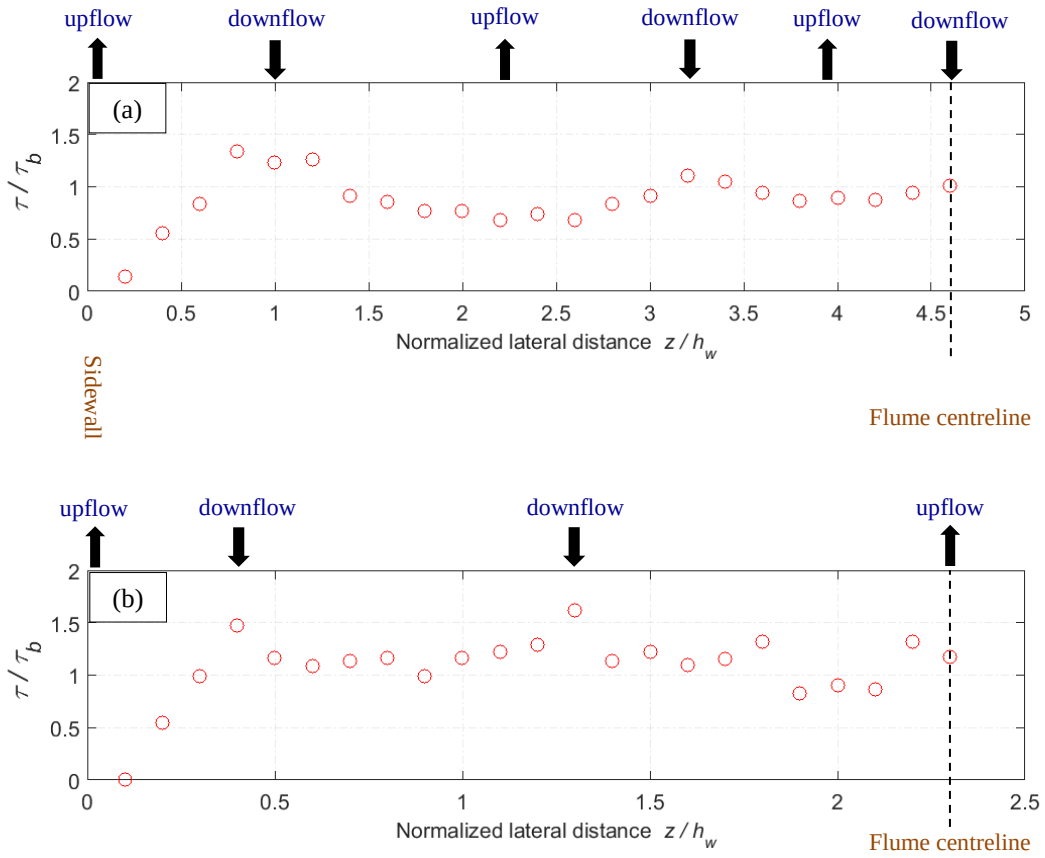

Figure 3.3 Lateral distribution of bed shear stress measured from the side wall towards the centreline of the flume for (a) flow condition 2 (shallower); (b) flow condition 8 (deeper).

Step III: velocity measurements were taken in the vertical direction at the upflow and downflow regions as showed in Figure 3.3. For flow condition 2, vertical resolution of $\Delta y = 3\,\text{mm}$ was used for $y / h_w \le 0.42$ and $\Delta y = 5\,\text{mm}$ was used for $0.42 < y / h_w \le 1$ giving a number of 10 vertical locations. While for flow condition 8, vertical spacing

of $\Delta y = 2$ mm was used for $y/h_w \le 0.2$, $\Delta y = 5$mm for $0.2 < y/h_w \le 0.5$, and $\Delta y = 10$ mm for $0.5 < y/h_w \le 1$, giving a number of 17 vertical locations.

For each single location, the velocity was measured using a sampling rate of 100 Hz and a sampling duration of 300 s. This sampling duration was chosen as it was long enough to provide time-converged velocity measurements. Throughout all measurements, the signal to noise ratio SNR and the signal correlation value were maintained around 20.0 dB and 80 %, respectively.

Figure 3.4 and 3.5 present the vertical profiles of time-averaged streamwise velocity and normalized Reynold Stress for conditions 2 and 8, respectively. Generally, flow condition 2 experiences low lateral variation in the streamwise velocity which suggests that the secondary flows are weaker than that in flow condition 8. The bed shear stress gradually increases from minimum at the side wall to a peak value of $1.4\tau_b$ at $z/h_w = 1.0$ and $1.5\tau_b$ at $z/h_w = 0.4$ for condition 2 and 8, respectively. This suggests that the strongest secondary flow cell occurs near the side wall such that it transports high flow momentum from the free surface towards the channel bed resulting in the increase in bed shear stress. In condition 8 which has aspect ratio of *Ar*= 4.6, the velocity dip can be clearly observed at $z/h_w = 0.4$. Although the flow condition 2 has aspect ratio of *Ar*= 9.2 that is much larger than the critical value (*Ar*= 5), the velocity dip phenomena can also be observed at $z/h_w = 1.0$. The maximum velocity occurs at around y/h_w = 0.7 for both flow conditions.

To check the accuracy in achieving uniform steady flow conditions, velocity measurement taken in **Step I** were used to calculate the streamwise and vertical turbulent intensity profiles. The obtained results were then compared with the semi-

empirical curves Equation (2.12) and Equation (2.13) as shown in Figure 3.6. It is apparent that all measured profiles almost follow the analytical curves, such that they decrease from the bed towards the water surface with almost same gradient.

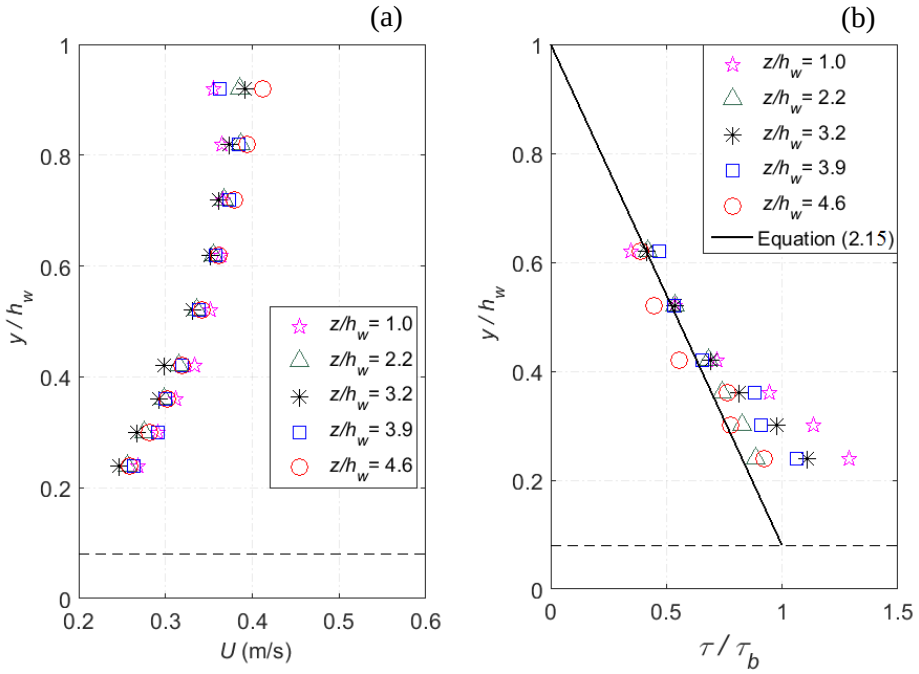

Figure 3.4 Vertical profiles of (a) time-averaged streamwise velocity; (b) Normalized Reynolds Stress for flow condition (2); black-dashed lines are the top of the sphere.

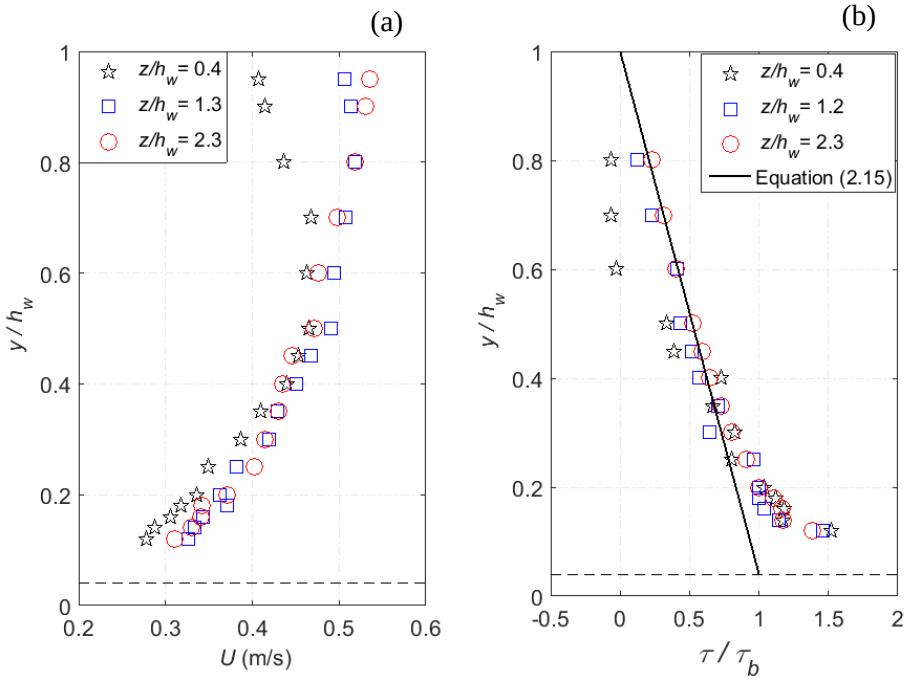

Figure 3.5 Vertical profiles of (a) time-averaged streamwise velocity; (b) Normalized Reynolds Stress for flow condition (8); black-dashed lines are the top of the sphere.

However, for condition 4, the streamwise and vertical turbulent intensity profiles become more concave with smaller values than the analytical curves. This deviation indicates that a precise uniform flow was probably not achieved for this flow condition due to flow deceleration along the channel (Kironoto & Graf, 1995; Yang & Chow, 2008).

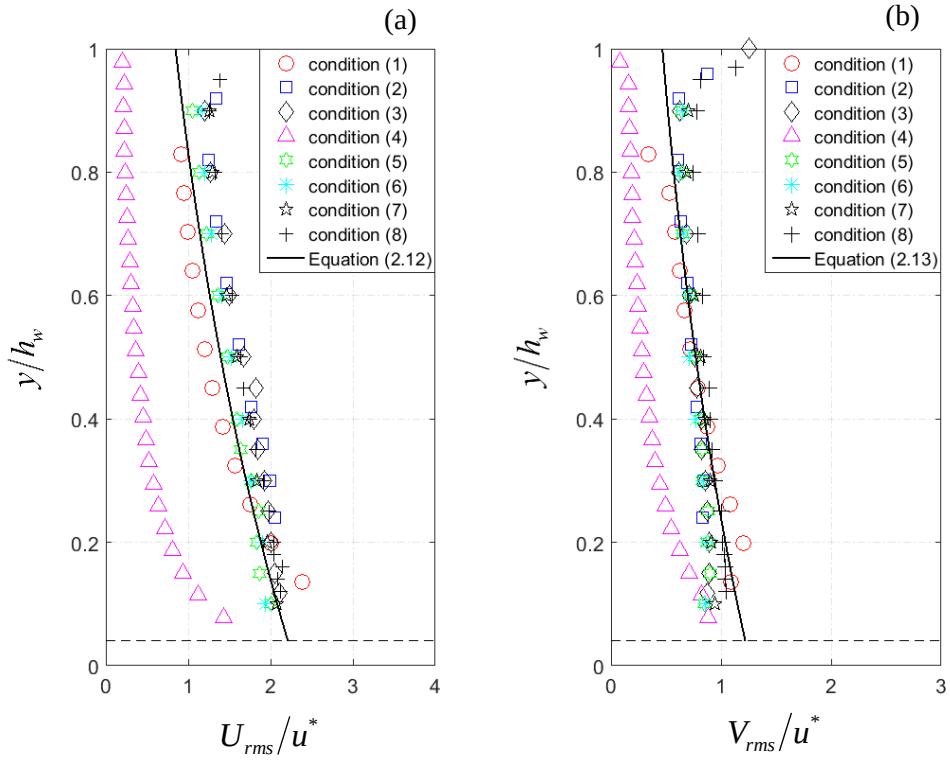

Figure 3.6 (a) Normalized streamwise turbulent intensity profiles; (b) Normalized vertical turbulent intensity profiles for conditions 1 ~ 8; black-dashed lines are the top of the sphere.

Figure 3.7 presents the Reynolds Stress profiles for all measured conditions compared with the analytical solution. It can be said that all measured profiles can be approximated by Equation (2.15) that they diminish gradually towards the water surface indicating uniform flow conditions. They slightly differ from Equation (2.15) which might be due to the secondary currents in the examined flows that has not been accounted for in the analytical solution. However, it can be seen once again the shear

stress profile for condition 4 becomes more concave in region y/h_w < 0.4 due to flow being decelerated (Kironoto and Graf, 1995). Given that uniform flow condition was not precisely achieved for condition 4, it was no longer used in the rest of this thesis.

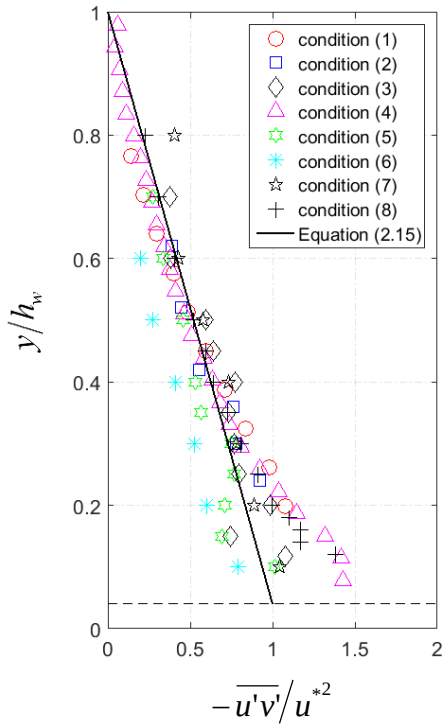

Figure 3.7 Normalized Reynolds Stress profiles for conditions 1 ~ 8 compared with analytical solution.

3.5 Water surface measurement

The temporal changes in the water surface were measured using the conductance wave probe technique. For this experiment, a tinned copper wire of 0.25 mm in diameter was adopted. The wave probes consisted of two thin wires, which were laterally separated by a distance of 13.0 mm.

3.5.1 Wave probes installation

An array of eight conductance wave probes were installed along the flume centreline starting from 9.0 m from the inlet (the black circles in Figure 3.8) in order to measure the instantaneous free surface elevations at different streamwise locations. And two lateral arrays of eight conductance wave probes each (the grey circles in Figure 3.8) were installed in one half of the flume cross section to measure the instantaneous water surface elevations in the lateral direction. The two lateral arrays are separated by a streamwise distance of 300.3 mm to ensure uniformity of free surface measurement, and also to allow the ADV probe to take velocity measurement between the two arrays. The positions of the streamwise probes were selected in order to obtain unique numbers of spatial separation. Whereas the positions of the lateral conductance wave probes are corresponding to lateral regions of low and high bed shear stresses (where the velocity measurements were taken in the vertical direction). At the bottom of the flume, the upper layer spheres were drilled with a 1.0 mm diameter holes, and each probe was carefully attached into these holes. The drilled spheres then were fixed into the spheres using strong glue. At the top, each wave probe was connected to a screw system enabling the wire to be vertically held under tension without causing plastic deformation (see Figure 3.9). The overall error in the probe positions between the two lateral arrays was 2.5 %.

All the probes then were connected to wave monitor modules provided by Churchill Controls (2003). For each wave monitor module output, a 10 Hz low-pass filter was used to eliminate high frequency noise. The wave monitor modules provided analogue voltage signals between ±10 V, which were tuned to cover flow depths ranging from 30 mm to 130 mm. Each wave monitor module allows a maximum number of eight wave probes to be simultaneously operated.

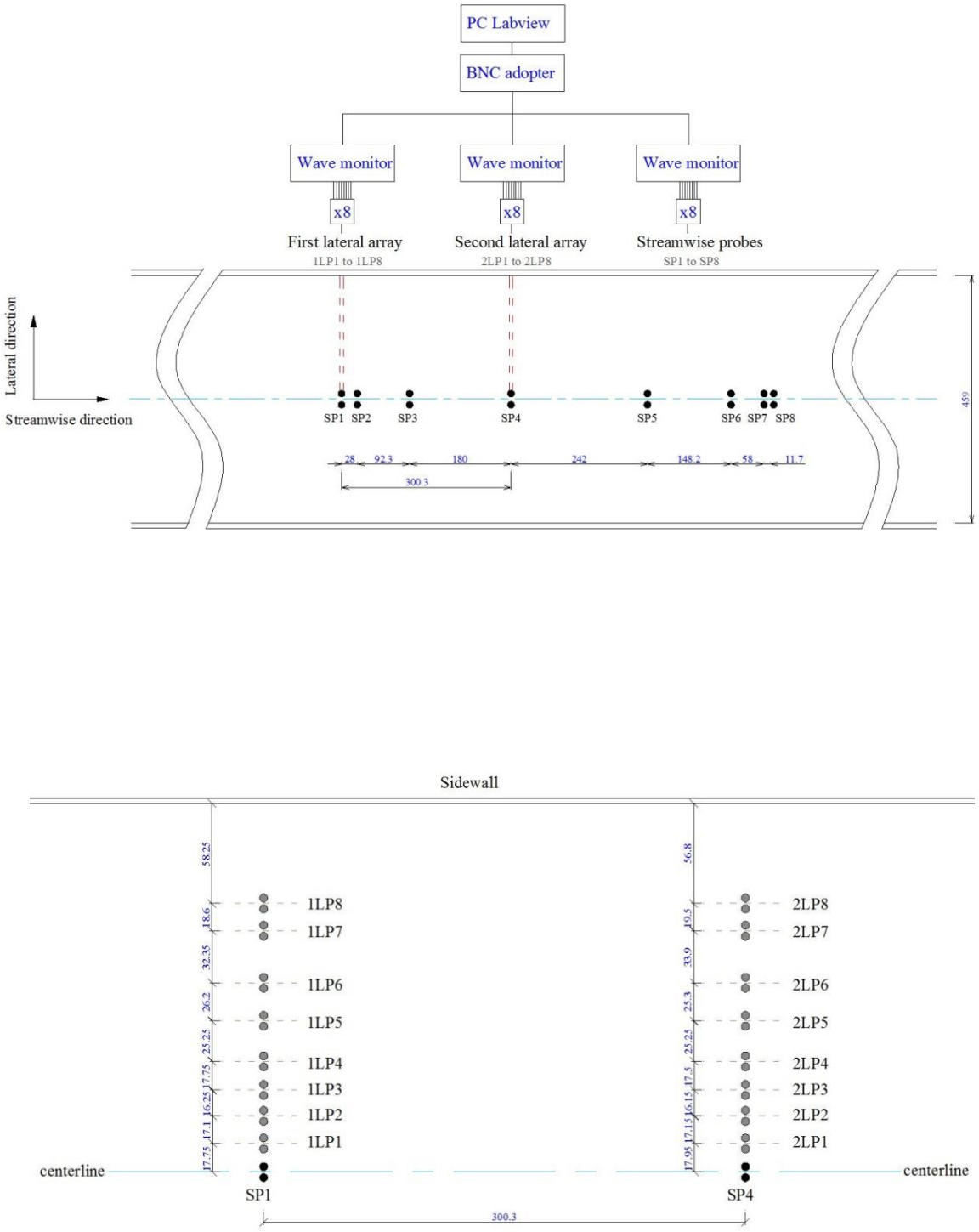

Figure 3.8 Top view of laboratory wave probe equipment and positions schematics within the measurement section (All dimensions in mm).

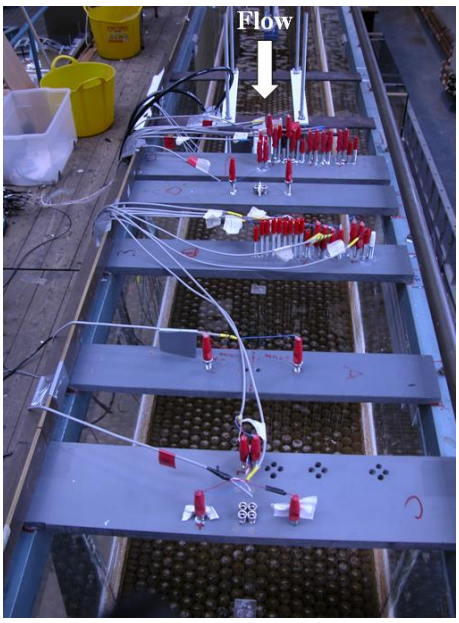

Figure 3.9 Photograph of the arrays of conductance wave probes.

3.5.2 Calibration

All the installed wave probes were simultaneously calibrated and the process of this calibration is as follows. The flume was set to a slope of S_0 = 0.0, and both inlet and outlet ends were carefully blocked to ensure that water cannot leak from the flume. The water in the flume tank was then pumped into the flume until a desired water depth was achieved. When the water in the flume settled down (horizontal water surface) after half an hour, the voltage readings of the wave probes were recorded at 100 Hz for a period of 1800 s by the use of a LabView program. This procedure was repeated for a number of six flow depths ranged from 30 mm to 130 mm, so that a linear trend between the water depth and voltage was achieved for each wave probe. This linear relationship then was used to convert the time-dependent voltage recorded on a wave probe into time-dependent water elevations. During the calibration process, the maximum change in water temperature remains below 1.0 %. The wave probes were regularly cleaned and calibrated every time before starting the measurements. It was found that the calibration constants changed to within 2.0 % throughout the whole

measurements. Figure 3.10 presents the voltage to water depth calibration for all wave probes. A linear relationship has been achieved for the all streamwise probes. For the first lateral array, it can be seen that only 1LP1 and 3LP1 differ from the rest of the probes, but their relationships become much better in the second lateral array. Generally the voltage to water depth calibration of the most probes show a good regression line that can be expressed as $h_w = 7.14V + 70.71$.

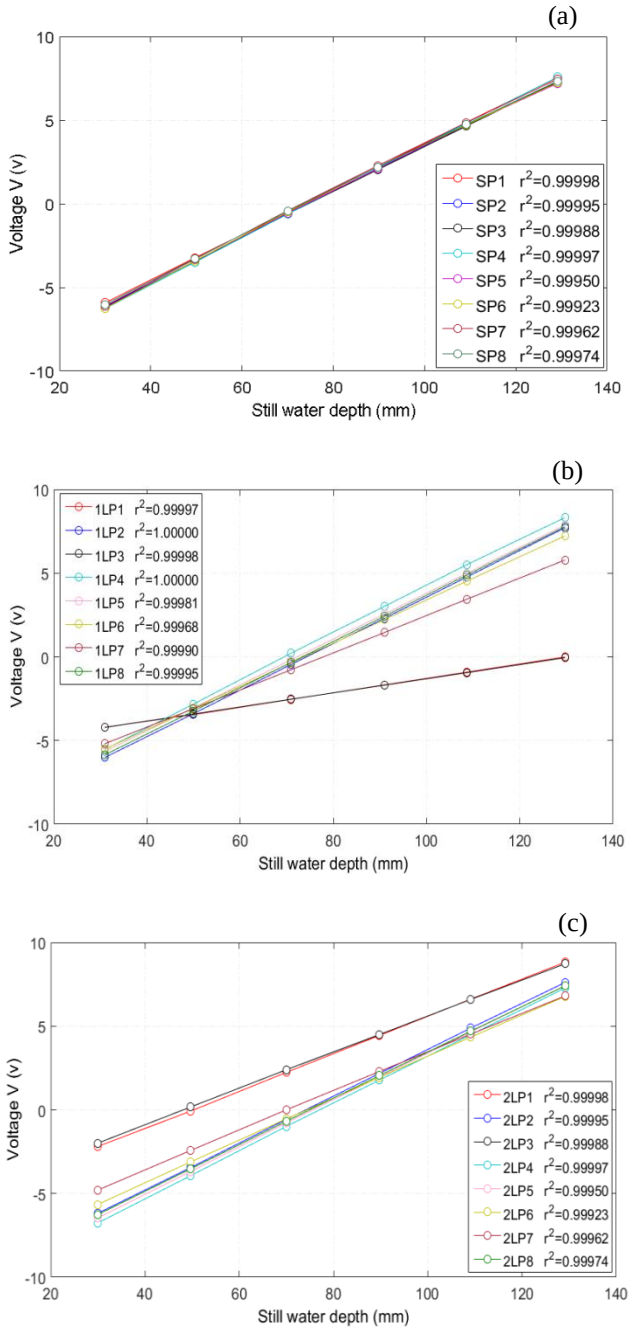

Figure 3.10 Wave probe voltage to water depth calibration of (a) Streamwise probes (SP1 ~ SP8); (b) first lateral array (1LP1 ~ 8LP8); (c) second lateral array (2LP1 ~ 2LP8).

3.5.3 Water surface data collection

Before water surface measurements were taken, the uniform steady flow condition was first achieved and then was allowed to run for at least one hour. This is to ensure that accurate temporal water surface behaviour is captured. These measurements were only taken for conditions 1, 2, 5 and 8, which are characteristic of all the examined flow conditions in Table 3.1. The voltage signals of all probes were recorded at a sampling frequency of 100 Hz and a sampling time of 1800 s. A digital thermometer was used to measure water temperature before and after taking water surface measurements. This is to ensure constant water viscosity throughout the measurements. For all flow conditions the water temperature change was within 5.0 %.

Figure 3.11 shows the Probability density function (PDF) obtained for the wave probe signals in flow conditions 1, 2, 5 and 8. The solid red lines presented in Figure 3.11 correspond to the best match with Gaussian function as, $\mathrm{PDF}(h'_w) = e^{-(\frac{h'_w}{2\sigma^2})} / \sigma\sqrt{2\pi}$, where h'_w and σ are the water surface fluctuations and its standard deviation (STD), respectively. It can be seen that the behaviour of the PDF closely follows a Gaussian distribution. The error in σ value obtained from the above Gaussian function and from wave probe statistics remains below 2.0 % for the four flow conditions. Also the value of σ was found to increase as the flow depth increases from condition 1 ~ 8. These observations agree well with the experimental findings reported by Horoshenkov *et al*. (2013) and Nichols *et al*. (2016) who measured the water surface fluctuations using conductance wave probes and image based Laser Induced Fluorescence (LIF), respectively.

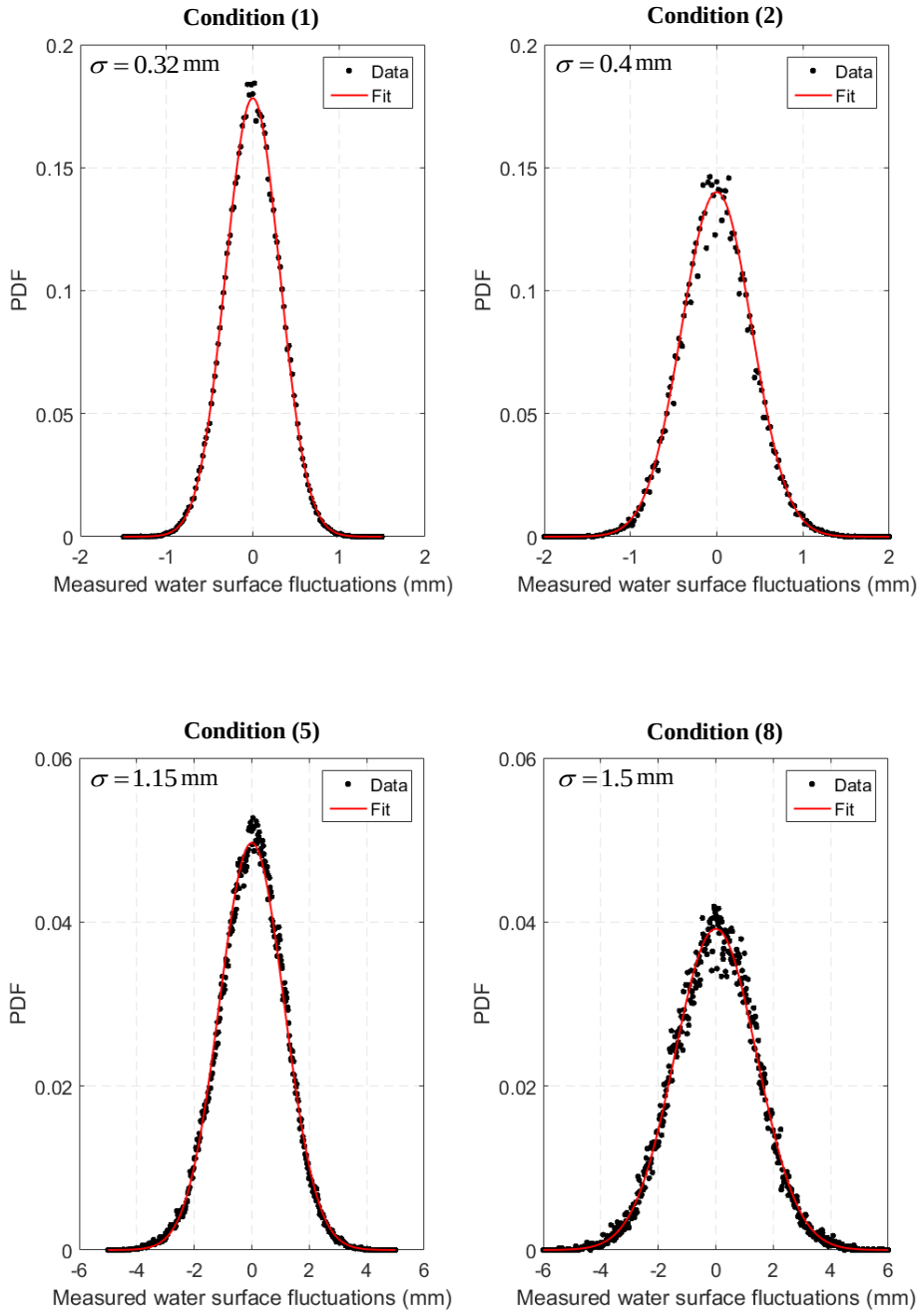

Figure 3.11 Probability density function (PDF) of the measured water surface fluctuations for flow conditions 1, 2, 5 and 8 in Table 3.1.

3.6 Experimental study conclusions

This chapter has presented the experimental study carried out in a rectangular open channel flow over rough bed. Smooth plastic spheres of diameter D = 25.0 mm have been used to generate rough boundary at the bottom of the channel while the sidewalls of the flume are made of smooth glass. A 3D side-looking Acoustic Doppler

Velocimetry (ADV) has been used to measure the velocity components in the vertical and lateral directions over one half of the flume cross section and within the measurement section. Firstly, velocity measurements were taken in the vertical direction at the flume centreline for all flow conditions listed in Table 3.1. Secondary, the bed shear stresses along the lateral direction were measured for flow condition 2 (shallower) and flow condition 8 (deeper), resulting in regions of low and high magnitudes. Thirdly, velocity measurements were taken in the vertical direction above these regions. The zero datum of the whole measurement was taken 4.0 mm below the top of the spheres, which corresponds the mean hemisphere elevation. The bed shear stress, which was approximated from the Reynold Stress measured in regions $y/h_w < 0.25$, it exhibits undulations in the lateral direction with magnitude of $20\% \sim 50\%$ of the mean value. This finding supports the existence of secondary flows, that are moving from zones with lower bed shear stress (upflow) to zones with higher bed shear stress (downflow). The lateral profiles of the time-averaged velocity and Reynolds Stress show little variations in flow condition 2, which suggests a weak secondary flow. As the aspect ratio decreases the secondary flow becomes stronger with less number of cells a cross the flume width. The velocity-dip phenomena was observed in the near side wall region for both flow conditions, that occurs approximately at $y/h_w \approx 0.7$.

Finally, the instantaneous water surface elevations have been measured in the streamwise and lateral directions using conductive wave probes for the four flow conditions 1, 2, 5 and 8 listed in Table 3.1. In the calibration process, a linear trend with a fit value of $r^2 = 0.99$ has been achieved between voltage and water depth for the most wave probes. The probability density function (PDF) has shown that the measured water surface elevations for the four flow conditions have a Gaussian

distribution. The standard deviation of the measured water surface fluctuations was observed to increase as the flow condition becomes deeper.

The measured data of flow velocity, shear stress and water surface levels will be used to support the development of the 2D and 3D SPH numerical models which are demonstrated in the following chapters.

CHAPTER 4 2D SPH Numerical Model

4.1 Investigation of 2D SPH numerical models

In the present study, the weekly compressible SPH open source code 2DSPHysics (http://www.sphysics.org) was first used to help develop a computational code able to investigate free surface flows over a rough bed, and validate the numerical results using careful laboratory measurements of flow velocity and water surface already collected for a rectangular channel described in Chapter 3.

4.2 Model setup and computational parameters

Since the flow in the present study is considered as uniform steady flow and the main objective is to investigate the turbulence model and treatment of rough bed boundary, the periodic open boundary provided by SPHysics, (Gómez-Gesteira *et al*., 2012), was implemented. The principle of this boundary treatment has been described in detail in section 2.5.10. To account for sufficient numerical accuracy and low CPU load simultaneously, the numerical flume was taken as 0.2 m long as shown in Figure 4.1. The flume length was selected based on the experimental observation of the characteristic period of the free surface pattern L_0 given in Equation 2.32. It was found in the conducted experiment that the value of L_0 varies between $1.5 \sim 2.0\,h_w$ for different flow conditions. Thus the minimum numerical flume length for the free surface pattern to be visualized in flow condition 8 (the deepest) is 0.2 m. The initial computational particle size *dx* was selected as 0.0015 m for all the flow conditions, giving a range of 4000 ~ 9000 particles involved in the model computations. The CFL stability number was taken as 0.15 and the computational time step was automatically adjusted to follow the Courant stability requirement (Gómez-Gesteira *et*

al., 2012). SPH kernel range can take some values between 1.0 *dx* ~ 2.0 *dx*, in this computation, it was found that *h* = 1.5 *dx* provides the most optimum results. Since the flow is assumed to be slightly compressed by the use of an artificial speed of sound c_0, a value of c_0 = 60 m/s was used for all flow conditions to maintain a constant flow depth for a long time up to 100 s ~ 130 s. The real water viscosity ($\upsilon_0 = 10^6$ m^2/s) was used and the MLS filter was applied every 30 time steps to smooth out the density and pressure fluctuations. To be dimensionally consistent with the experiment, the reference level y_0 was considered to be 4.0 mm below the top of the roughness elements (the red dashed-line in Figure 4.1), from which the uniform flow depth h_w is measured.

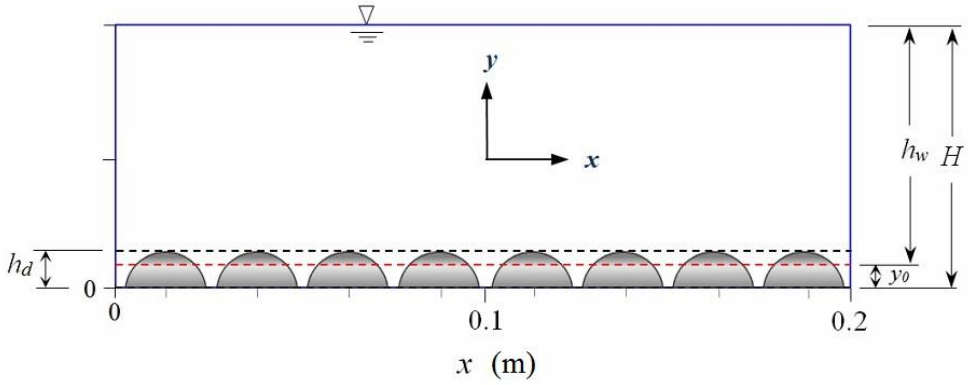

Figure 4.1 Sketch of numerical flume with rough bed elements (h_d is the roughness height = y_0 + 4 mm).

To improve the model capacity to address the turbulence effect, a corrected sub-particle-scale (SPS) eddy viscosity model is included, in which the fixed Smagorinsky model constant is replaced by a mixing length formulation. On the other hand, to account for the bed roughness effect, a drag force term is added to the momentum equation as a source to compute the resistance shear stress. These developments of the code are described in more details in the following sections.

4.2.1 Turbulence closure in 2DSPHysics

Since this model is to be applied to fully-turbulent open channel flows, a turbulence model is required to close the system of the momentum equation. In 2DSPHysics, the flow turbulent stress is modelled by using the eddy viscosity based sub-particle scale (SPS) model initially described by Gotoh *et al.* (2001) combined with the momentum Equation (2.39). The sub-particle-scale turbulent stress $\vec{\tau}$ is based on the eddy viscosity assumption as follows:

$$\frac{\vec{\tau}_{ij}}{\rho} = 2\nu_t S_{ij} - \frac{2}{3}k\delta_{ij} - \frac{2}{3}C_I\Delta^2\delta_{ij}\left|S_{ij}\right|^2 \tag{4.1}$$

where *i* and *j* denote the 2D coordinate components. $\vec{\tau}_{ij}$ is the SPS shear stress component; $\nu_t = \left(C_s\Delta\right)^2|S|$ is the turbulent eddy viscosity, where C_s is the Smagorinsky constant, $\Delta = \sqrt{dx^2 + dy^2}/2$, is the characteristic length scale of eddies (filter size) and $|S| = \sqrt{2S_{ij}S_{ij}}$ is the local strain rate; $S_{ij} = \frac{1}{2}\left(\frac{du}{dy} + \frac{dv}{dx}\right)$ is the SPS strain tensor; $k = \nu_t\left(\frac{du}{dx} + \frac{dv}{dy}\right)$ is the SPS turbulence kinetic energy; δ_{ij} is Kronecker's delta; and C_I is a constant typically, 0.0066. In most SPH applications C_s is regarded as a constant being 0.1 ~ 0.2.

Although this benchmark formulation has been successfully used up to date in quite a few coastal applications, very limited predictions have been reported on simulating turbulence levels in shallower open channel flow. In this model tests on laboratory shallow rough bed open channel flows, it was found that the value of $C_s\Delta$ has a significant influence on the streamwise flow velocity profiles. For example,

increasing $C_s\Delta$ resulted in a decrease in both the streamwise velocity and its profile gradient dU/dy. This might be due to the effect of more numerical dissipation, or perhaps due to the fact that $C_s\Delta$ acts as a spatial filter size and as this becomes larger, the model is not able to resolve the smaller physical turbulent length scales.

To obtain the best match between the measured and computed time-averaged streamwise velocity profiles, different values of C_s were set for each flow condition listed in Table 3.1. An analysis has been made on the relationship between $C_s\Delta$ and the uniform flow depth h_w, channel slope S_0, Re Number and shear velocity u^*, and the results are presented in Figure 4.2. It shows that $C_s\Delta$ has a positive correlation with the flow depth and channel bed slope but appears to be independent of the Reynolds Numbers. A strong positive correlation has been found between $C_s\Delta$ and the shear velocity u^*, which indicates that the product $C_s\Delta$ carries information on the near bed streamwise velocity gradient. If dividing by Δ, the C_s values of the present study were found to be 0.6 ~ 3.5 for free surface flows over a rough bed. This value is significantly larger than the common C_s value typically used in other SPH applications, for example, in coastal hydrodynamics a value of 0.1 ~ 0.2 is recommended. This could be attributed to the different flow mechanisms at the physical boundaries. In many coastal applications, the flow is unsteady and transient and thus it is much less influenced by the rough bed, while in this model a much longer simulation time was needed, and the flow was strongly influenced by the roughness elements on the bed.

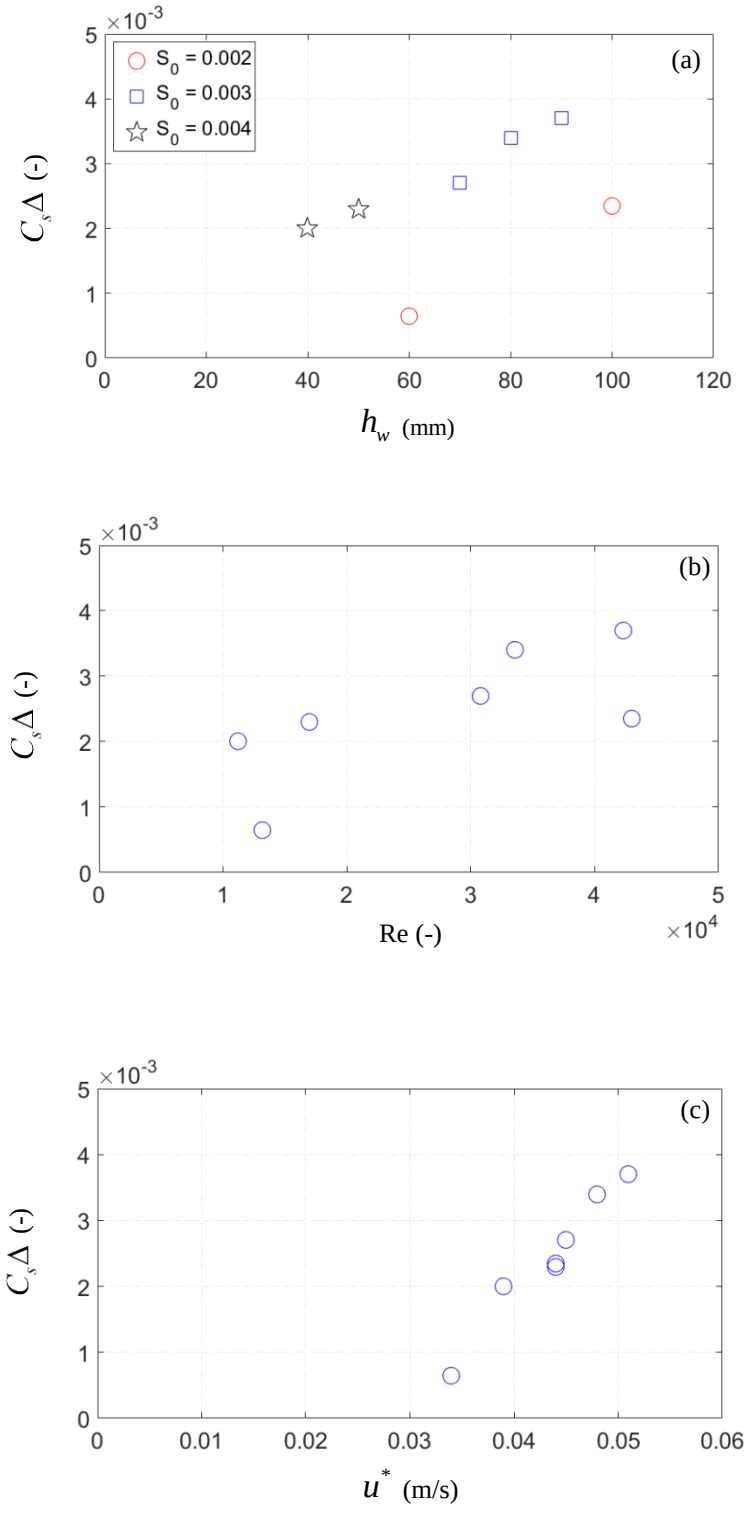

Figure 4.2 Relations between $C_s\Delta$ and (a) uniform flow depth h_w and channel slope S_0 ; (b) Re Number; and (c) shear velocity u^* for flow conditions listed in Table 3.1.

However, the obtained values of C_s have been found to provide total turbulent shear stresses much smaller than the measured ones. More detailed analysis about this finding is given later in section 4.5. Because of the failure to predict the total turbulent shear stress it was therefore decided to use the classic mixing length approach given by Equation 2.19 to modify the SPS model of Gotoh *et al.* (2001), by replacing the product of $C_s\Delta$ with a mixing length formulation, which was hoped to predict more realistic turbulent shear stress for open channel flows as it allows the use of a function that depends on the distance from the bed boundary. The vertical distribution of the mixing length l_m which describes the turbulent eddies' size needs to be defined. Among the numerous expressions to determine l_m, the most popular one was proposed by Nezu & Nakagawa (1993), and was further applied in open channel flows (Stansby, 2003). It is defined as follows:

$$l_m = \begin{cases} \kappa y & \text{for} \quad 0 \le y/H \le \lambda/\kappa \\ \\ \lambda H & \text{for} \quad \lambda/\kappa < y/H \le 1.0 \end{cases} \tag{4.2}$$

where y is the vertical distance measured from the zero velocity level to the water surface; H represents the total water depth measured from the bottom of the roughness at (y = 0) to the water surface; λ is a constant, typically 0.09. By adopting this approach, a better representation of the effect of the flow mechanisms over the rough bed open channel would be expected, since the model coefficient now depends on the local flow conditions and the size of the flow structures to internally transfer momentum within the fluid.

4.2.2 Treatment of bed roughness

In the present study, the bottom wall was treated using the dynamic particles approach (Dalrymple and Knio, 2001), to prevent the inner fluid particles from penetrating the wall. This is because of its computational simplicity, as all of the wall particles are computed inside the same loop as the inner fluid particles. However, this boundary treatment has been found to behave like a hydraulically smooth bed and it cannot adequately reflect the frictional force generated by roughness elements such as spherical gravel. To enable the model to be compatible with the experiments performed for a hydraulically rough bed, the drag force due to the existence of the roughness elements on the channel bottom must be accounted for. This can be quantified by the drag force formula in Equation (2.16).

The determination of the drag coefficient C_d is a key factor in the simulation of flow over bed obstacles. Although different values of C_d have been experimentally found for the spherical beds, a constant value of $C_d = 0.8$ that is close to the value measured experimentally by Schmeeckle *et al.* (2007) for spheres in a bed and was used throughout this numerical model. In the physical experiment, the reference area A_d in Equation (2.16) is usually taken as the obstacle front area perpendicular to the flow direction, whereas the reference velocity U_d is related to the average streamwise flow velocity acting on that area. In this numerical model, the drag area of the bed roughness element is visualized in Figure 4.3.

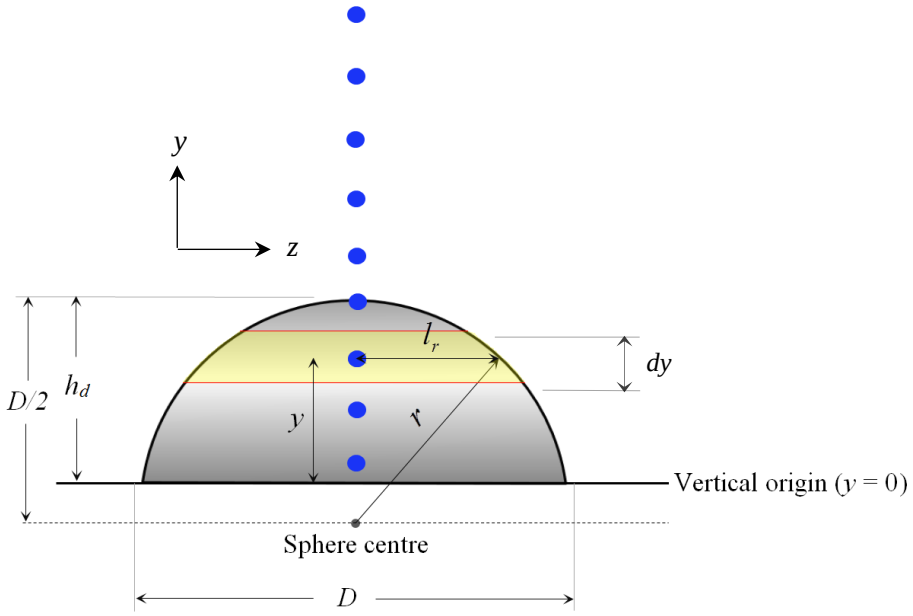

Figure 4.3 Schematic view of drag area (blue circles: fluid particles).

It shows that the front drag area A_d is not constant for a spherical shape, and it decreases towards the top of the sphere, resulting in a decrease in the drag force F_d. Thus Equation (2.16) becomes a function of the vertical distance *y* by following Figure 4.3, in which the yellow highlighted drag area $(A_d)_y$ for each fluid particle within the roughness height h_d is mathematically determined as $(A_d)_y = dy \times 2l_r$, where l_r is the length of the half chord and is calculated as $l_r = \sqrt{r^2 - (y + r - h_d)^2}$, where $r = D/2$. By replacing the average streamwise velocity U_d and the drag area A_d in Equation (2.16) with $(U_d)_y$ and $(A_d)_y$, the drag force of a fluid particle at a level *y* could be computed by the following equation:

$$(F_d)_y = \frac{1}{2}\rho (A_d)_y C_d (U_d)_y^2 \tag{4.3}$$

It should be noted that the drag force $(F_d)_y$ needs to be computed per unit volume of fluid in order to be dimensionally consistent with the momentum equation. In 2D

model, the volume over which this drag force acts is equal to $dx \times dy \times 1$ (where dx is the initial particle spacing), thus Equation (4.3) computationally becomes:

$$\frac{(F_d)_y}{dx \times dy \times 1} = \frac{\rho C_d (2 l_r dy)(U_d)_y^2}{2 dx dy} = \frac{\rho C_d l_r (U_d)_y^2}{dx} \tag{4.4}$$

The position of the vertical origin (y = 0) for the velocity profile at which $U \approx 0.0$ was set at h_d below the roughness crest. In the literature, it was experimentally found that the value of h_d can be in the range of $0.15D$ ~ $0.35D$ in order to obtain the best agreement between the averaged streamwise velocity profile and the log-law (see section 2.2.3). To numerically investigate this, the current numerical simulations were performed under four different values of $h_d = 0.24D$, $0.28D$, $0.32D$ and $0.4D$ for each flow condition. It has been found that a value of $h_d = 0.32D$ was suitable for the deeper flow conditions 6 ~ 8 and $0.4D$ for the shallower flow conditions 1 ~ 5. This actually makes physical sense in that shallower flows experience proportionately higher flow resistance and therefore needs a larger roughness height to generate this higher flow resistance. This also can be observed in the experimentally measured values of the hydraulic roughness k_s listed in Table 3.1, which shows that k_s generally decreases as the flow depth increases. This means that h_d is a dynamic parameter, depending on not only the absolute value of bed roughness height but also on the corresponding flow depth.

4.3 Velocity profiles and analysis

The 2D SPH numerical model was run for the seven flow conditions listed in Table 3.1 until time t exceeded 120.0 s and using a time output of 0.02 s. For each flow condition, the experimental depth-averaged streamwise velocity $\overline{U}$ listed in Table 3.1 was used as a feeding velocity of the fluid particles at the beginning of the

computation. From the numerical observations, it was found that stable flow conditions were achieved after 100.0 s for flow conditions 6, 7 and 8 (deeper), but much earlier (80.0 s) for the other flow conditions 1 ~ 5 (shallower), as shown in Figure 4.4. This indicated that different initial feeding velocities can influence the timing of reaching the final steady state, but it has little effect on the terminal stable velocity value. Also, an initial feeding velocity that is closer to the final stable one can make the evolution process much quicker by using the present periodic boundary for flow circulation. The computed data beyond simulation time of t = 100 s is believed to have no longer been influenced by the initial model setup, and therefore only these data were used in further analysis.

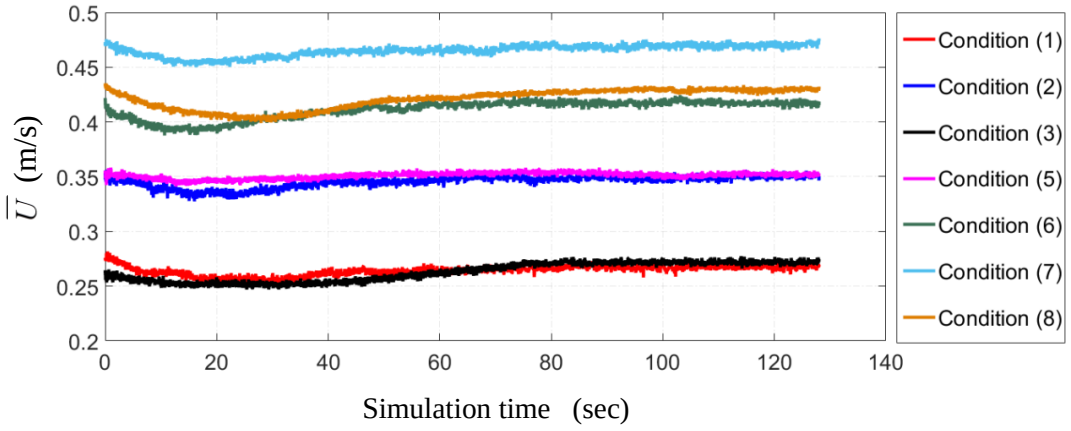

Figure 4.4 Time variation of the computed depth-averaged velocity for flow conditions 1 ~ 8.

To check the time convergence of the model, the depth averaged velocity data in Figure 4.4 from simulation time t = 100 ~ 130 s were used to calculate the standard deviation (STD) of increasing period as a percentage of STD over 30 s. The results are plotted in Figure 5.4 and show that the standard deviation settles down to within ± 2.0 % from approximately t = 20 ~ 30 s for all simulated flow conditions. The time t = 20 s corresponds to the minimum required averaging period to provide

representative computed time-averaged quantities. Therefore all the time averaged quantities were obtained over t = 20 s.

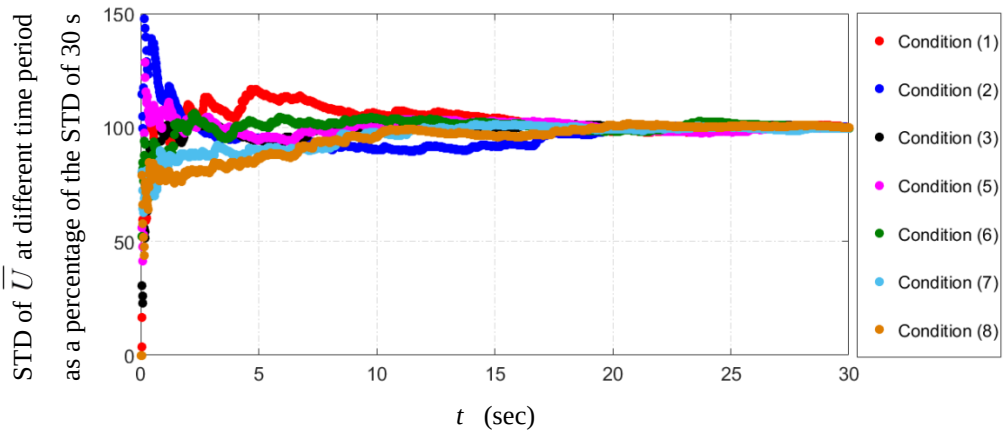

Figure 4.5 Settling time of standard deviation of the computed depth-averaged velocity for increasing period.

Figure 4.6 presents the contour maps of time-averaged pressure for flow conditions 1 ~ 8. Their contours demonstrate a nicely hydrostatic distribution pattern without significant fluctuations, due to the efficient use of the MLS density filter and the selected speed of sound. The vertical profiles of the pressure for each flow condition exhibit a linear distribution that can be approximated by $P = \rho g H$, which indicates uniform stable flow conditions.

To validate the SPH results for rough bed free surface turbulent flows, the computed time averaged streamwise velocity profiles at steady state are compared with the experimental measurements taken in the centreline of the flume demonstrated in Chapter 3. The comparisons in Figure 4.7 demonstrate a good agreement among the different data sets across the range of flow conditions. It is promising to note that these streamwise velocity profiles have been obtained without imposing any analytical solutions for the inflow/inner fluid regions, but rather they have evolved through the

influence of the new drag force and turbulence models under the action of gravity in the SPH computations.

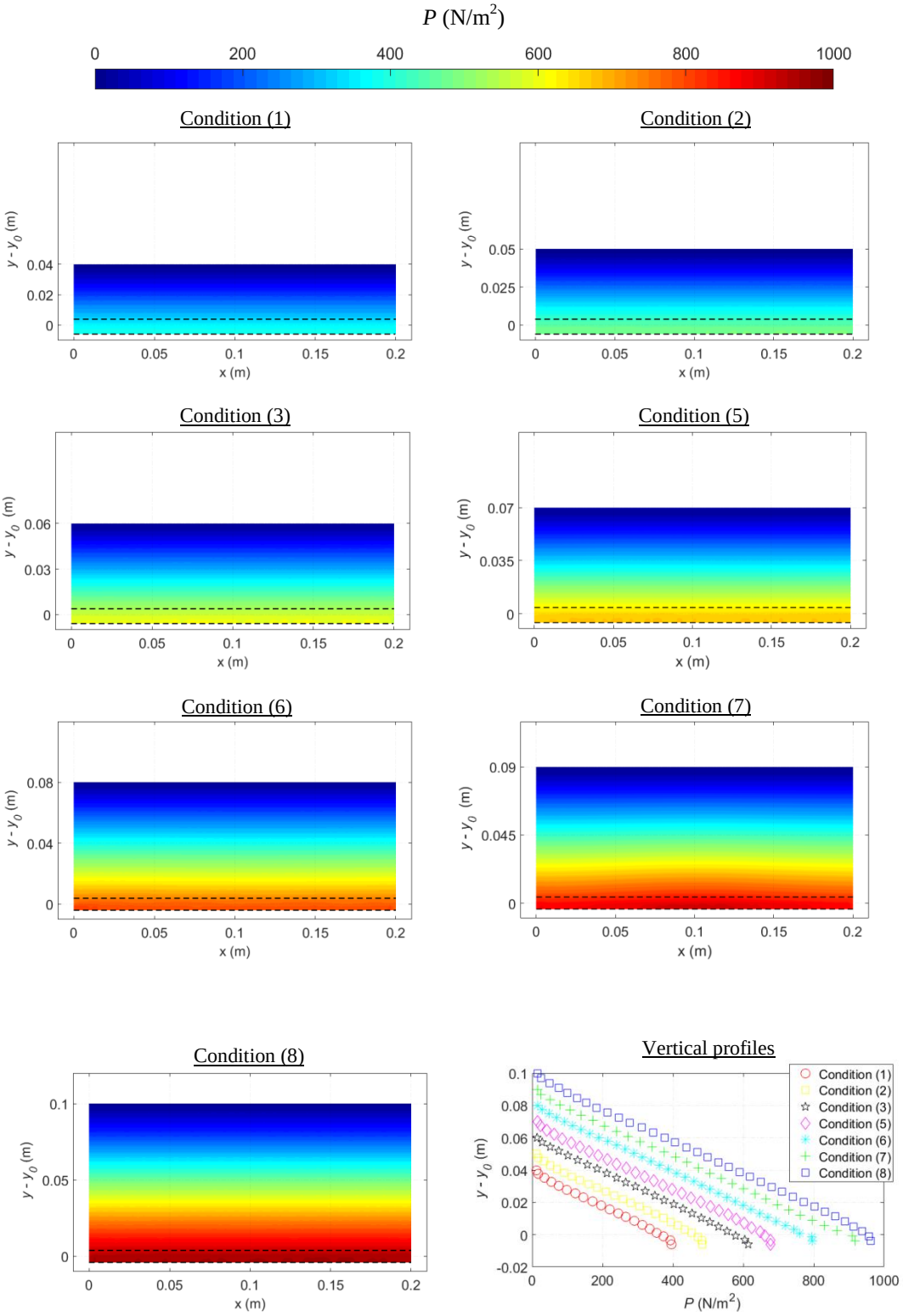

Figure 4.6 Time-averaged pressure contours and vertical profiles computed by SPH model for flow conditions 1 ~ 8, (dash lines: roughness top and bottom).

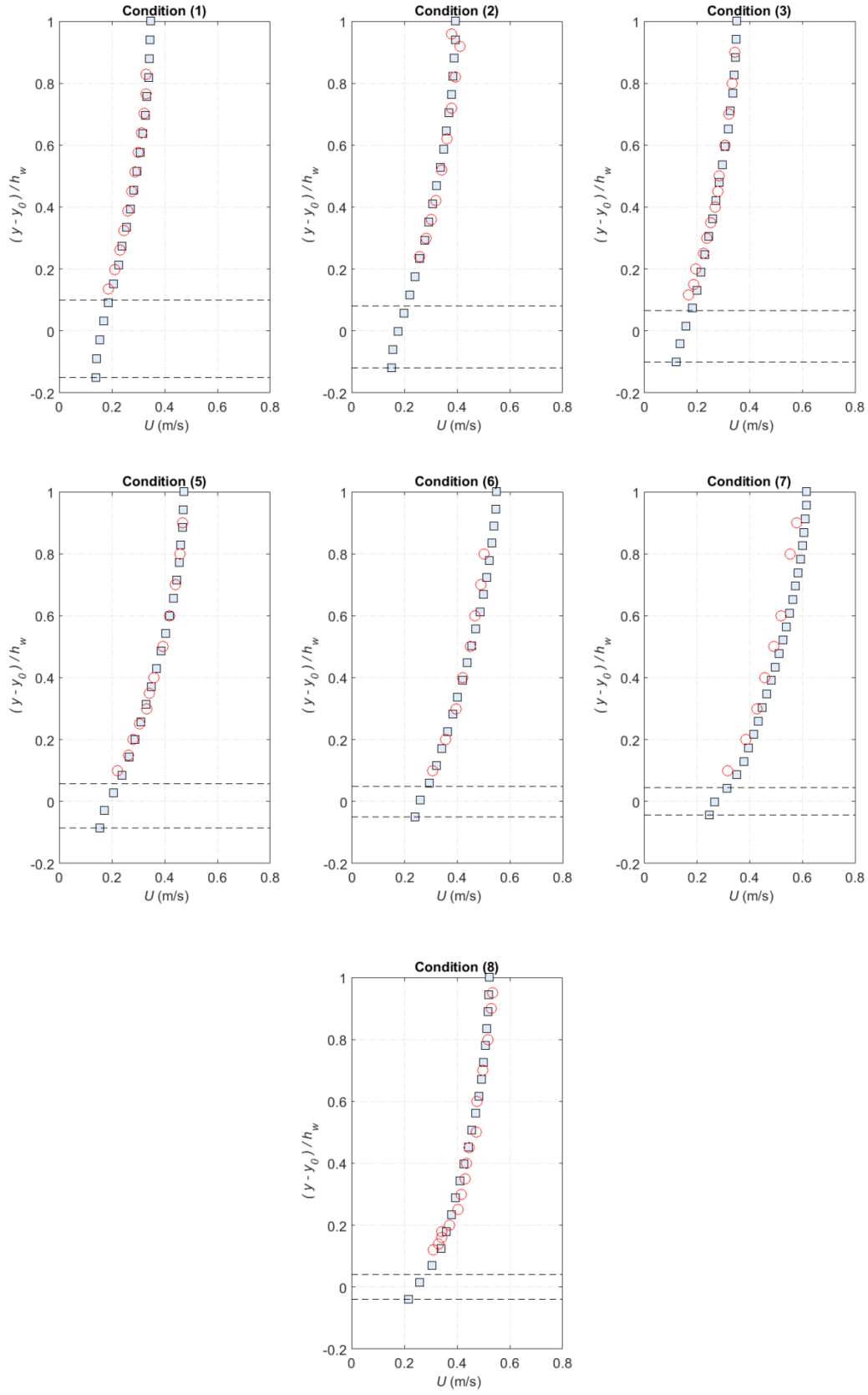

Figure 4.7 Comparisons of time-averaged streamwise velocity profiles between experimental data and 2D SPH results (circles: exp data; squares: SPH; dashed lines correspond to roughness top and bottom).

To quantify the accuracy of SPH computations, the mean square error percentage (MSEP) between the experimental and numerical streamwise velocity profiles and their gradient dU/dy are calculated as follows.

$$\text{MSEP} = \left(\frac{U^{Exp} - U^{Num}}{U^{Exp}} \right)^2 \times 100 \tag{4.5}$$

where, U^{Exp} and U^{Num} are the experimental and numerical time-averaged streamwise velocities, respectively. Among all examined flow conditions, it was found that the variation in U^{Exp} at every vertical location falls within ± 5%. Due to these measurement uncertainties, the experimental velocity gradient was determined from a best fit spline curve through the data. Figure 4.8 presents the MSEP of U and dU/dy that are calculated at every experimental vertical location for all flow conditions. It is apparent that in the upper flow region approximately $0.25 \le (y - y_0)/h_w \le 1.0$, the MSEP in U remains less than 0.5 % for all flow conditions. Similarly, the lowest error in *dU/dy* is observed in the middle region of the flow $0.25 \le (y - y_0)/h_w \le 0.7$, whereas in the near bed region, $0 \le (y - y_0)/h_w \le 0.25$, the MSEP in U and *dU/dy* becomes larger, reaching up to 2.5 % and 12.0 %, respectively. This is probably due to the kernel truncation errors near the bed boundary, where the SPH velocity gradient is calculated, or some kinds of experimental measurement errors may also exist. The largest errors in *dU/dy* take place in the free surface region $0.8 \le (y - y_0)/h_w \le 1.0$. This could be attributed to that the adopted mixing length model (Equation 4.2) which assumes that the turbulent eddies' size is constant ($l_m = \lambda H$) near the free surface, while in real flow, the turbulent eddies must decline near the surface. The kernel truncation near the free surface boundary could also lead to an error in velocity gradient.

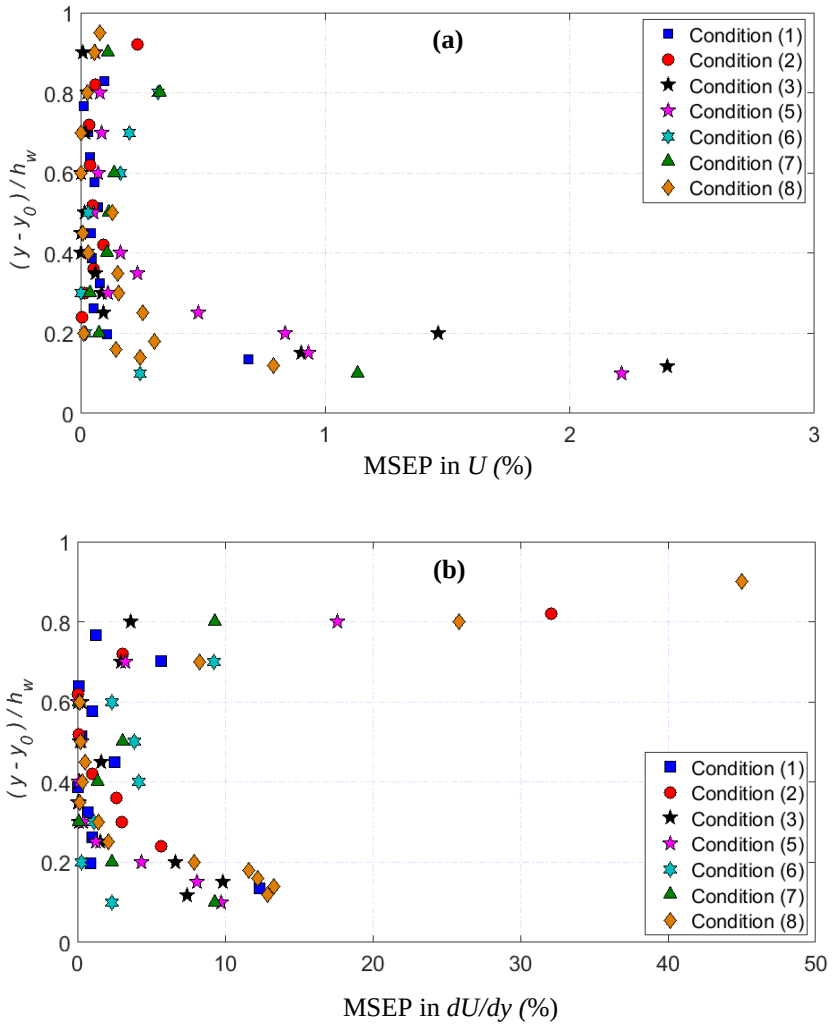

Figure 4.8 Mean square error percentage (MSEP) of (a) the streamwise velocity, (b) the streamwise velocity gradient at every experimental vertical location for condition 1~ 8.

To demonstrate the variations of particle velocities in the *u* component with respect to the flow depth, and also to check the stability of the numerical simulation, the time-averaged steamwise velocity from the bottom of the spheres to the water surface is plotted in Figure 4.9, for flow conditions 1 ~ 8. In general, Figure 4.9 reveals a systematic increase in the streamwise velocities through the flow depth. Although XSPH has been ignored in the model, the flow still developed in almost parallel layers indicating that the fluid particles are quite uniformly distributed. This is due to the

inclusion of the turbulence model and drag force equation, which dampened the numerical noise in the particle field.

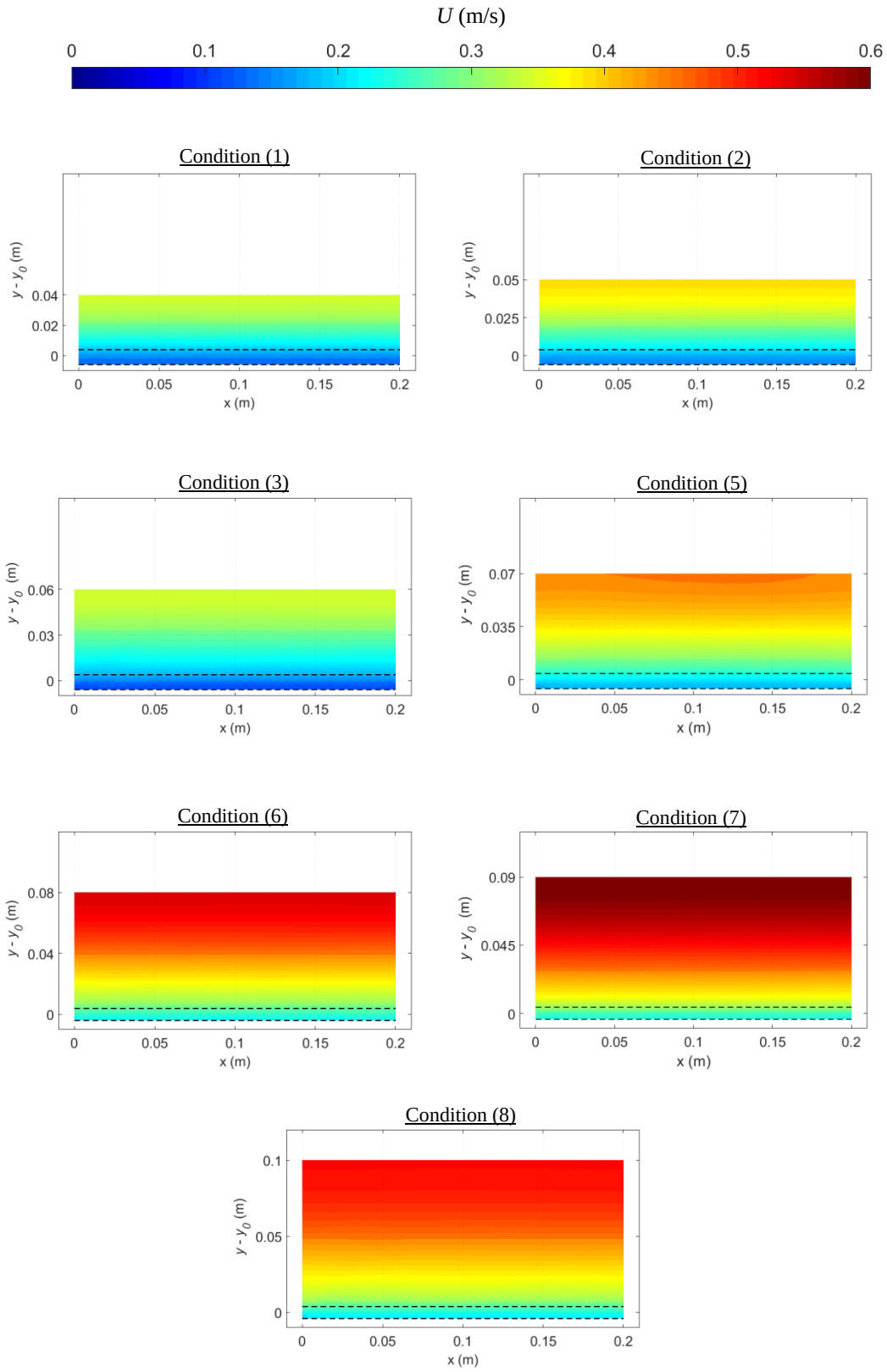

Figure 4.9 Time-averaged streamwise velocity contours computed by SPH model for flow conditions 1 ~ 8, (dash lines: roughness top and bottom).

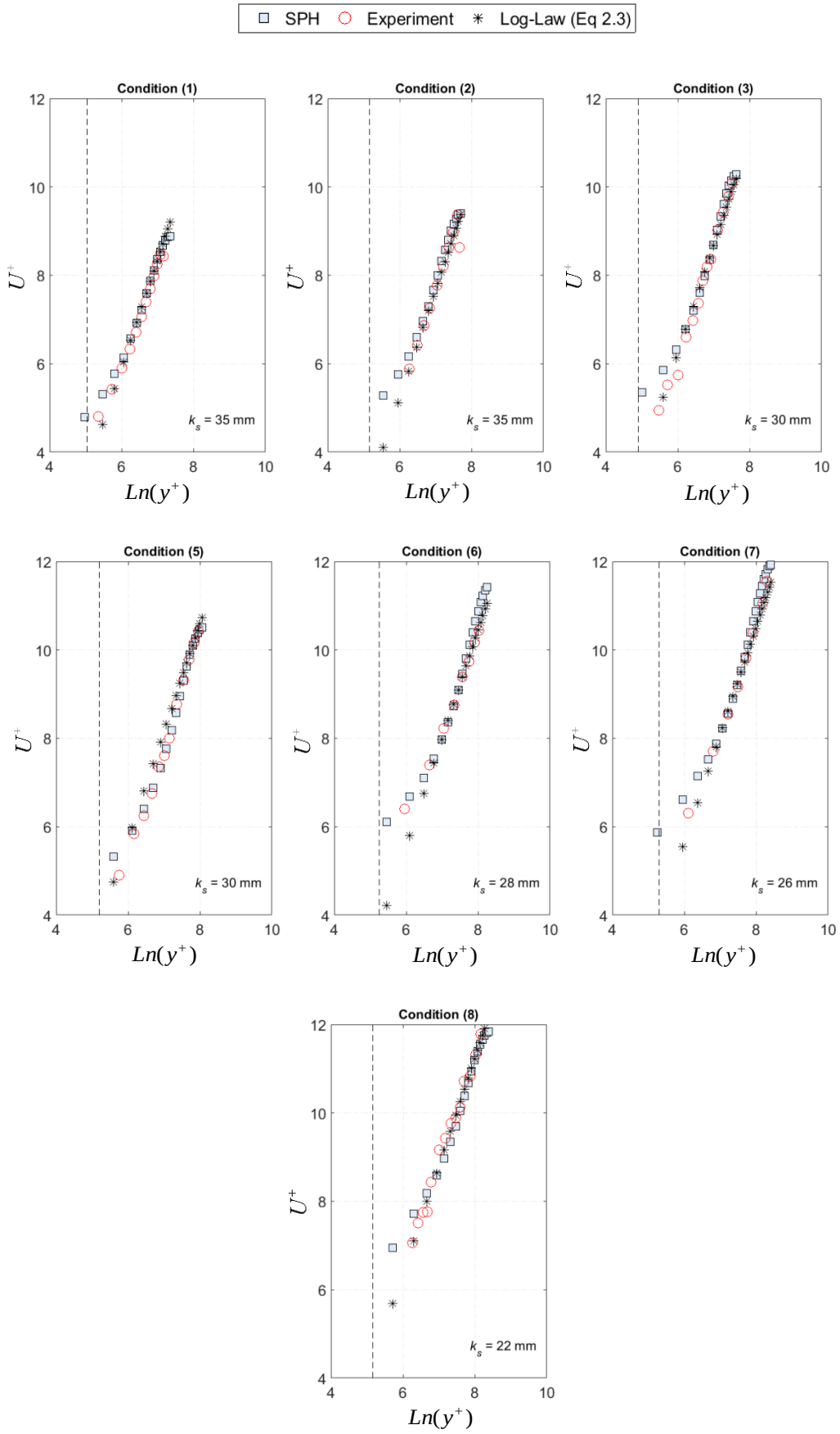

Figure 4.10 Comparison of Experimental, SPH and Log Law time-averaged streamwise velocity profiles (dashed-lines: top of spheres).

Moreover, the SPH and experimental velocity profiles were compared with the log law given by Equation (2.3), in order to examine the accuracy of the numerical model in predicting the shear velocity u^*. The comparison in Figure 4.10 generally shows a satisfactory match among each other across the seven flow conditions. The percentage of the relative error between the predicted and measured shear velocity was calculated as $100\times\left|u^*_{measured}-u^*_{predicted}\right|\Big/u^*_{measured}$. It was found that the maximum error among the seven flow conditions remains less than 6.0 % as presented in Table 4.1. This shows the robustness of the SPH technique in simulating such complicated free surface flows.

Table 4.1 Error in the shear velocity u^*.

Flow condition	(1)	(2)	(3)	(5)	(6)	(7)	(8)
Error in u^* *(%).*	2.5	2.0	6.0	2.0	1.5	4.0	2.3

4.4 Shear stress profiles and analysis

The calculations of shear stress in free surface flows are very important for the prediction of flow structure and the estimation of pollutant mixing and sediment transport. Although the SPH modelling approach has been applied to a limited number of open channel free surface flows, there is almost no quantitative work reported on the shear stress profiles due to the complexity of the problem. Here the SPH computed shear stress is compared with the experimental data, and the analytical solution which is given by the following formula:

$$\tau_{(y-y_0)}=\tau_b(1-\frac{y-h_d}{H-h_d}) \tag{4.6}$$

The compared shear stresses are all normalized by the shear stress on the bed surface defined as the top of the roughness elements $\tau_b=\rho g S_0(H-h_d)$ and are shown in Figure 4.11.

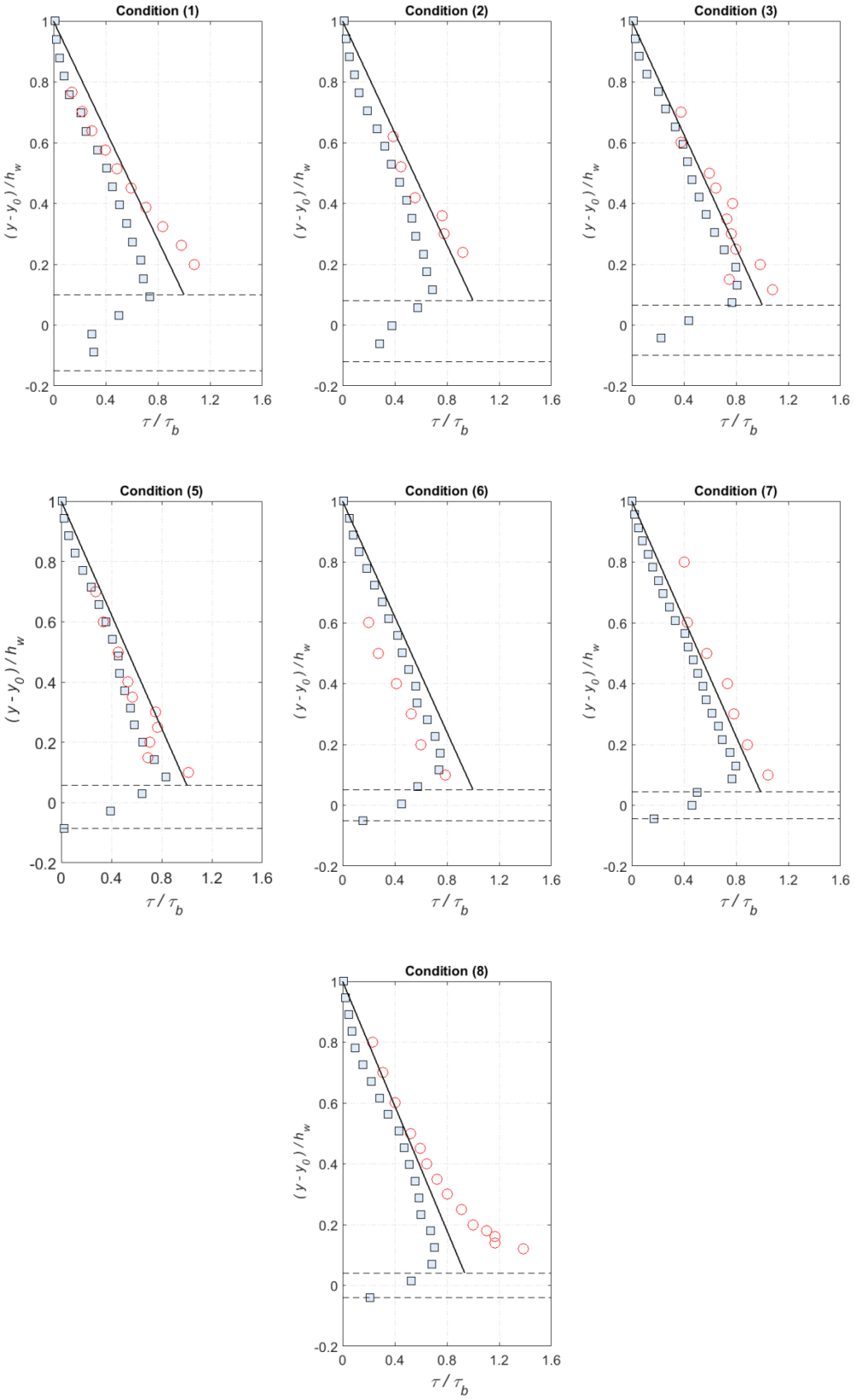

Figure 4.11 Comparisons of time-averaged shear stress profiles between experimental, analytical and SPH results (circles: exp data; squares: SPH; solid black lines: analytical (equation 4.6); dash lines: roughness top and bottom).

Although there are small errors found in regions close to the channel bed due to SPH kernel truncation errors and measurement uncertainties, the SPH predicted shear stresses are in satisfactory agreement with the experimental data and the analytical solutions. It is also worth noting that some larger discrepancies are observed between the SPH results and experimental data for flow condition (8) somewhere above the roughness crest. This could be attributed to the flow condition in the laboratory experiments in which precise uniform flow condition was not achieved due to slight spatial flow decelerations along the flume (see also Figure 3.7).

Furthermore, the time-averaged contour fields of the computed shear stress are plotted in Figure 4.12 for the flow conditions 1 ~ 8. In general, the shear stress distributions reveal a gradual decrease towards the water surface, and the contour lines are in very good order without obvious numerical noise. This provided the evidence that the SPH computations were stable and the numerical scheme was sound. Although the maximum velocity gradient occurs at the top of spheres, the plots reveal that the maximum shear stress occurs at around 12 % ~ 20 % of the flow depth. This is due to the mixing length distribution used in the wall region ($l_m = \kappa y$) which dampens the near wall streamwise velocity gradient.

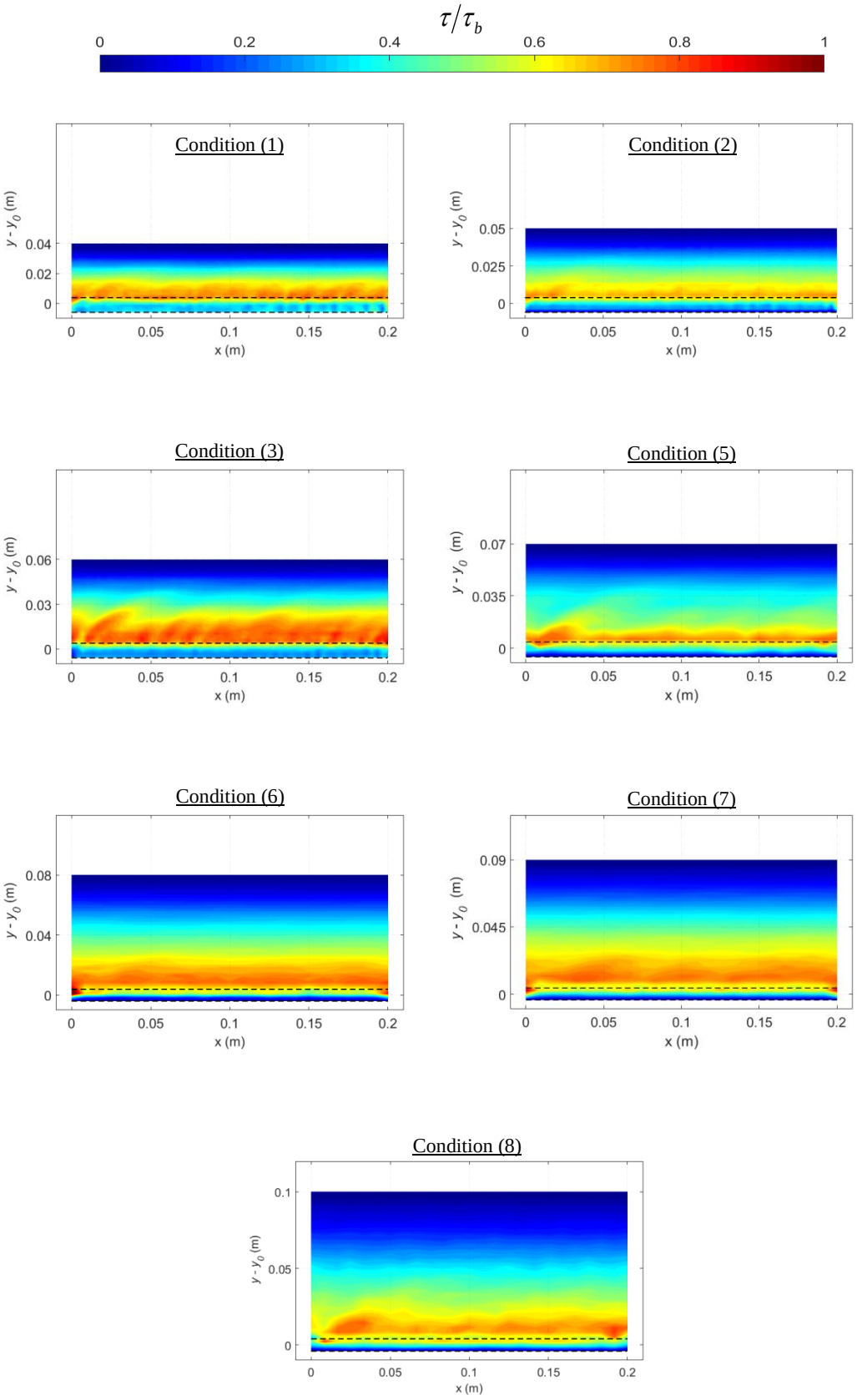

Figure 4.12 Time-averaged normalized shear stress contours computed by SPH model for flow condition 1 ~ 8, (dash lines: roughness top and bottom).

4.5 Sensitivity analysis of model results

To check the convergence of SPH computations in the spatial domain, and further evaluate the use of mixing length model for the flow turbulence, the following two sensitivity tests were carried out. Figures 4.13 (a) and (b) present the SPH computed flow velocity profiles and shear stresses based on the mixing length model Equation (4.2) for the two different particle spacing, i.e. dx = 1.5 mm (original run) and 2.0 mm (new run), for the flow conditions (3) and (6), respectively. These two cases represent the relatively shallower and deeper water conditions in the laboratory experiments. Both Figure 4.13 (a) and (b) show generally good convergence behaviour in view of the overlapping of two SPH curves. However, there are some deviations for the two SPH shear stresses computed above the roughness crest region, especially for the shallower flow condition (3). The numerical results using a coarser particle spacing dx = 2.0 mm generated somewhat smaller shear stress values, although good overlapping behaviours have been observed for most of the upper part of the flow region. This could be attributed to the complexity in modelling shallow rough bed flows, in which a more stringent spatial resolution might be needed near the roughness elements to fully account for their effect.

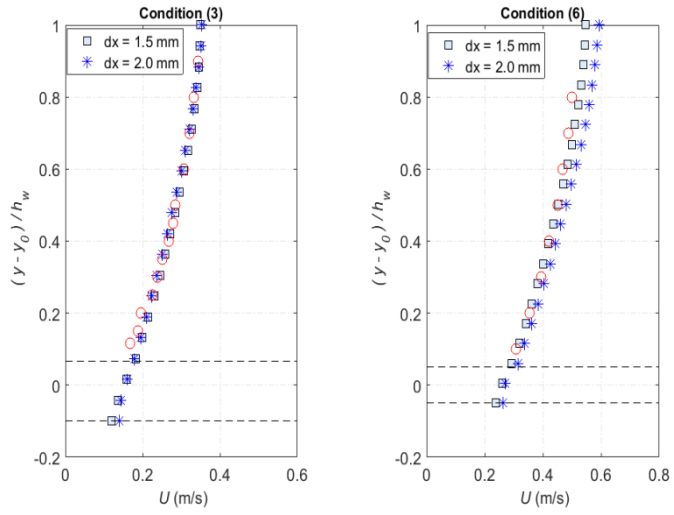

Figure 4.13 (a) Comparisons between experimental (red circles) and SPH time-averaged velocity profiles for two different particle sizes.

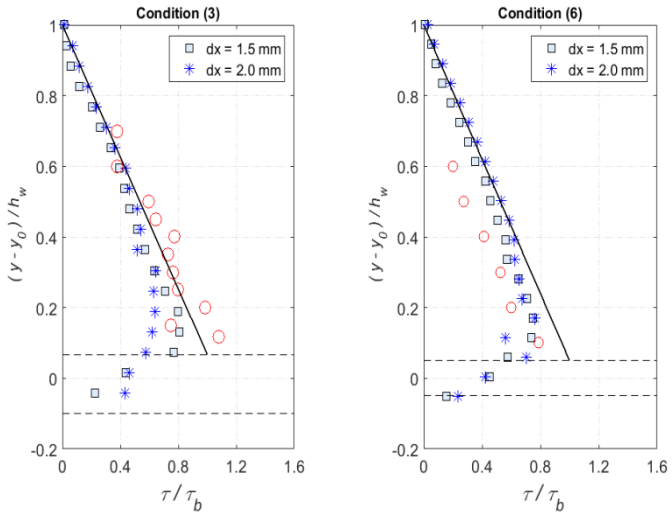

Figure 4.13 (b) Comparisons between experimental (red circles), analytical Equation (4.6) (black solid lines) and SPH time-averaged shear stress profiles for two different particle sizes.

Furthermore, another sensitivity test has been carried out to investigate the possible reasons why the original SPS turbulence model of Gotoh *et al*. (2001) as represented in Equation (4.1) could not provide the satisfactory results in the present case studies. The shear stresses computed from Equation (4.1) were found to be much smaller than the experimental observations. This could be attributed to that the computational particle size used in the model is much larger than many of actual turbulent scales. Also, the coefficient of equation parameters such as C_s were commonly calibrated in the unsteady and transient flow applications, such as for coastal waves, but it is not clear whether it can still perform well or not in a uniform, steady and long-time simulation of open channel flow. The current numerical model uses some numerical schemes such as the density filter and kernel averaging which may also have dampened the resolved turbulent scale in the flow. Another reason might be attributed to the effect of 3D flow which is not accounted for in the current 2D model. Besides, the effect of rough bed was microscopically modelled using the drag equation as described in section 4.4.2, which means that the flow dispersion is neglected and this may have resulted in insufficient turbulent damping mechanism flow.

To numerically prove this, the original SPS turbulence model predictions of the velocity and shear stress profiles for the two different particle sizes are shown in Figure 4.14 (a) and (b), respectively, again for the shallower and deeper flow conditions (3) and (6). It is shown from Figure 4.14 (a) that due to the insufficient turbulence damping mechanism, the SPH computations predicted a much faster flow velocity than the experimental ones, although the two SPH velocities are almost converged even for the different particle sizes. On the other hand, Figure 4.14 (b) demonstrated that not only the turbulence shear stress values have been underestimated by several orders (compared with Figure 4.13 (b)), but also the convergence behaviour of numerical computations degraded as well. This is due to the fact that the turbulent eddy viscosity ν_t in Equation (4.1) is explicitly dependent on the particle size, so much more obvious discrepancies in the shear stress profiles have been found around the roughness areas. In comparison, these differences are very small if the mixing length model of Equation (4.2) is used, which is evidenced by the comparisons as shown in Figure 4.13 (b).

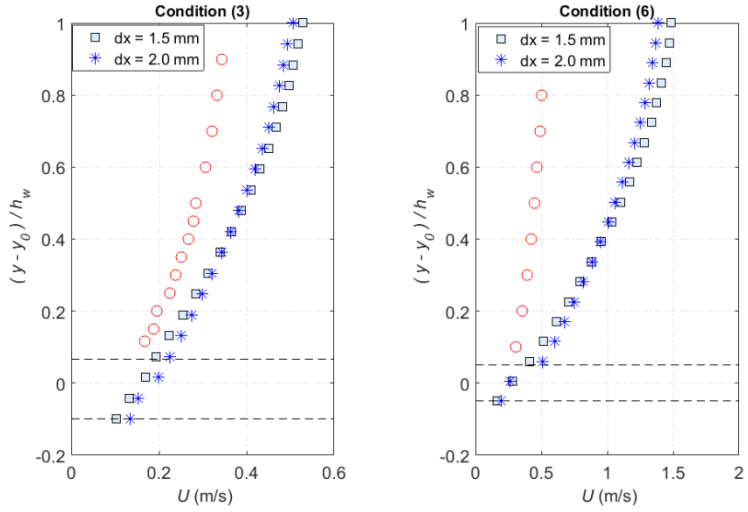

Figure 4.14 (a) Comparisons between experimental (red circles) and SPH time-averaged velocity profiles for two different particle sizes using original SPS turbulence model of Gotoh *et al.* (2001).

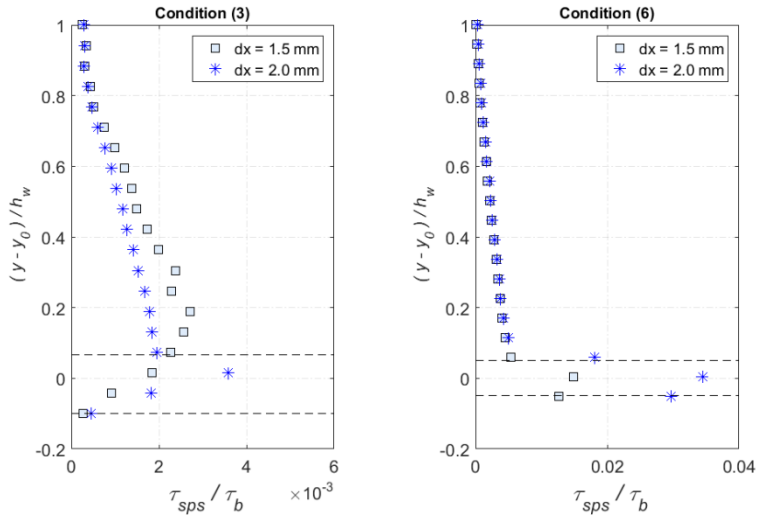

Figure 4.14 (b) Comparisons between two SPH time-averaged shear stress profiles for two different particle sizes using original SPS turbulence model of Gotoh *et al.* (2001).

Since SPH is meshless, fully Lagragian and has the potential to handle complex boundaries without introducing numerical diffusions, it is also worth to use this technique to attempt to simulate the dynamic behaviour of the free surface and its interaction with the underlying flow.

4.6 Water surface dynamic behaviour and analysis

4.6.1 Water surface identification

As well as studying the time average water surface position, the dynamics of the predicted water surface was also studied. The water surface elevations were extracted from the SPH particles data using the principle of the divergence of particle position which is given by Equation (2.60). In this work a threshold criterion of 1.4, which gives the highest standard deviation of the time series of the water surface, was used (see Figure 4.15). This value is also within the range 1.2 ~ 1.5 used by other SPH researchers (Lee *et al*., 2008; Farhadi *et al*., 2016).

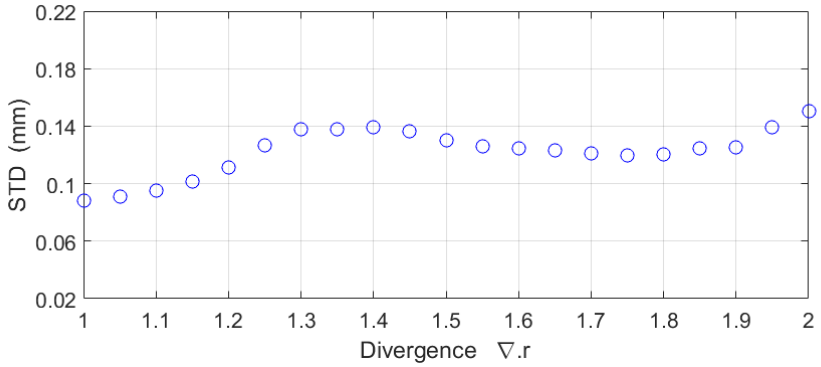

Figure 4.15 Standard deviation (STD) of the time series of the water surface computed for different values of $\nabla.\mathbf{r}$ for condition 2.

The instantaneous water surface elevations at a desired streamwise location x were computed as follows. First several vertical locations were defined below and above the initial water surface level by using a spacing of Δy = 0.02 mm. At each of these locations, the particle divergence $\nabla.\mathbf{r}$ in Equation (2.60) was computed for each time output t = 0.02 s, at a frequency of (1/0.02) 50Hz. Then the vertical location corresponding to the value closest to $\nabla.\mathbf{r}$ = 1.4 was considered as the instantaneous water surface. This process was performed over time t = 10.0 s resulting in a total of 10/0.02 = 500 sets of time series. This means that the flow has circulated more than 14 times throughout the numerical channel, which is believed to be sufficiently long to capture any spatial pattern on the free surface. The instantaneous water surface elevations were computed between streamwise location x = 0.02 m and x = 0.18 m using a resolution of Δx = 2.5 mm. By following this procedure, the experimentally and numerically time-averaged water surface elevations $\overline{h}_w$ are plotted in Figure 4.16 for a comparison. It shows that the predicted water levels are very close to the experimental data. However, as the flow depth increases from condition 1 ~ 8, the deviations between the numerical and experimental water levels become slightly larger. Nevertheless, the maximum deviation between experimental and numerical water surface levels stays below 5 mm, which is 5.0 % of the uniform flow depth.

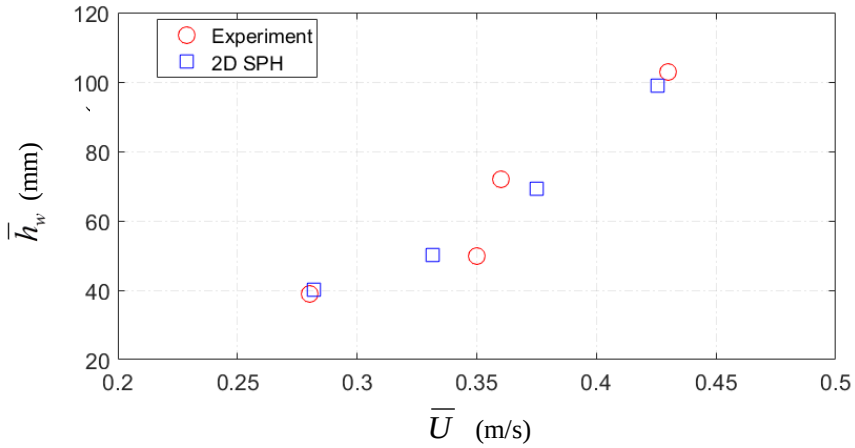

Figure 4.16 Comparisons of time-averaged water surface level vs depth averaged velocity between experimental and 2D SPH results for flow conditions 1, 2, 5, and 8.

Also, it was found that the probability density function (PDF) of the computed water surface fluctuations approximately follows Gaussian distribution (see Figure 4.17). This agrees well with the PDF distribution of the experimentally measured data. The solid red lines in Figure 4.17 correspond to the best match with Gaussian function as, $\mathrm{PDF}(h'_w) = e^{-(\frac{h'_w}{2\sigma^2})} / \sigma\sqrt{2\pi}$. However, it should be noted that the standard deviation σ of the computed water surface fluctuations are relatively smaller compared with the experiments, and they do not appear to systematically vary for each flow condition as presented in Table 4.2. This could be attributed to that some numerical parameters and schemes used, such as particle size dx, sound speed c_0, density filter and kernel averaging, may have dampened the fluctuations of water surface particles. Also, the numerical water surface fluctuations were computed based on 2D SPH model in which the fluid particles can only move in the streamwise and vertical directions, whereas in the experiment the shape of water surface is also affected by the underlying 3D flow structures and thus more accurate water surface fluctuations are expected.

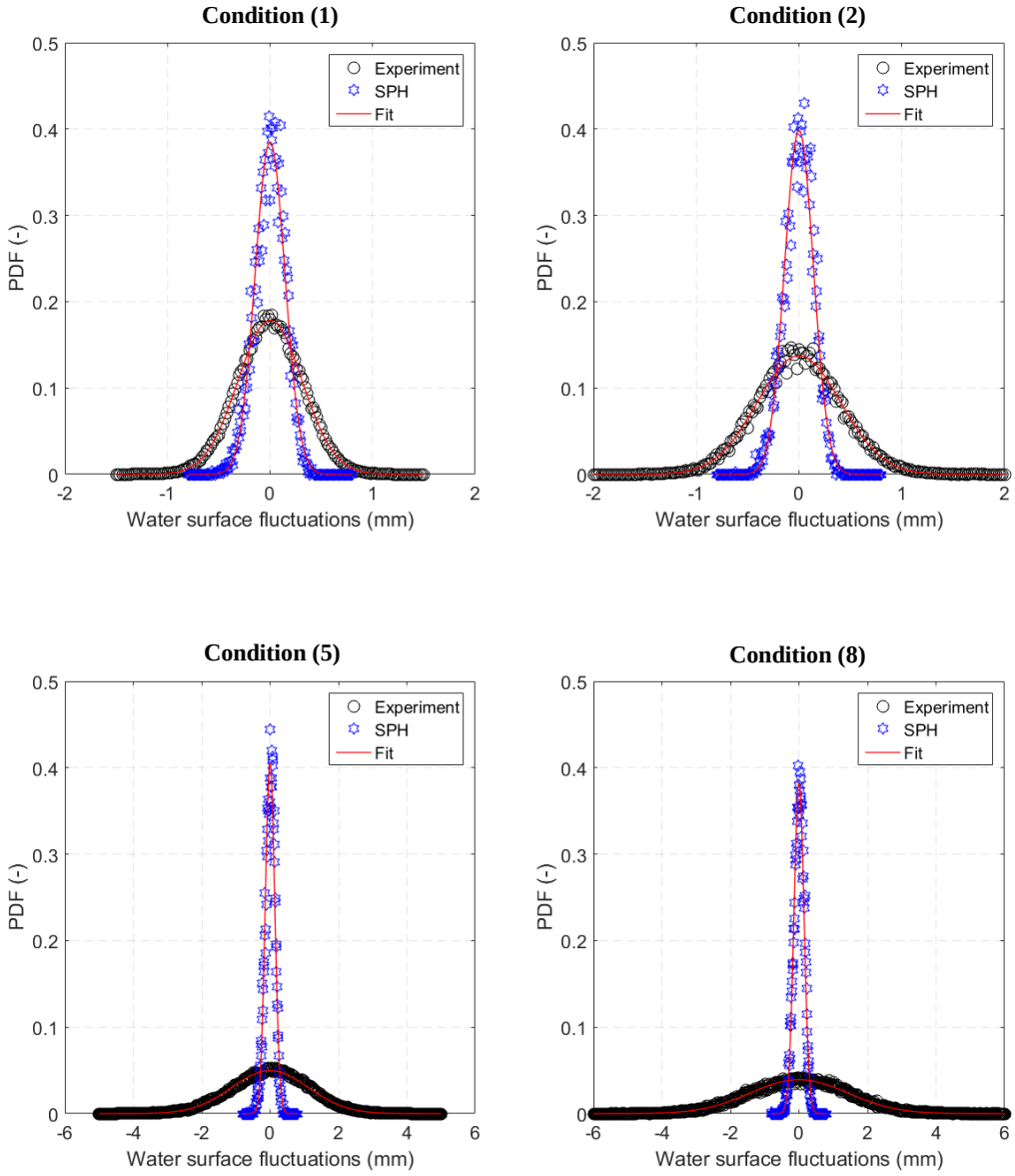

Figure 4.17 Probability density function (PDF) of the computed and measured water surface fluctuations for flow conditions 1, 2, 5 and 8 in Table 3.1.

Table 4.2 Standard deviation of the water surface fluctuations.

Flow condition	**(1)**	**(2)**	**(5)**	**(8)**
Measured water surface STD (mm).	0.32	0.40	1.15	1.50
Computed water surface STD (mm).	0.145	0.140	0.140	0.145

4.6.2 Water surface pattern

In order to investigate the dynamic behaviour of the water surface, the spatial-temporal field of the experimental and numerical instantaneous water surface fluctuations h'_w for flow conditions (1), (2), (5), and (8) are plotted in Figure 4.18. The experimental plots show the water surface fluctuations of the first four streamwise wave probes SP1 ~ SP4 located at 0.0 m, 0.028 m, 0.1203 m and 0.3003 m, respectively. The black-dashed lines in Figure 4.18 correspond to the depth averaged streamwise velocities $\overline{U}$ listed in Table 3.1. Figure 4.18 shows that the numerical plots demonstrate an interesting feature that the water surface is fluctuating between the positive and negative elevations travelling with almost same orientation angles over the space and time. This feature is more clearly captured in the case of shallower flow conditions (1) and (2), where the water surface pattern is more highly influenced by the proposed bed roughness. Despite the limited number of measurement locations, these experimental dynamic features were also detected by the four streamwise probes and the pattern yields almost the same orientation angle. Although the numerical flume length is only 0.2 m due to the CPU constraint, the results show that the spatial period of the water surface oscillations agrees well with the study of Horoshenkov *et al*. (2013) and Nichols *et al*. (2016). It is possible to estimate the celerity of the water surface patterns in Figure 4.18, and it was found that the gradient of these patterns approximately represents the depth-averaged flow velocity $\overline{U}$. Similar findings were also reported in the experimental study of Fujita *et al.* (2011), who revealed that the water surface pattern travels with celerity nearly close to the near-surface velocity.

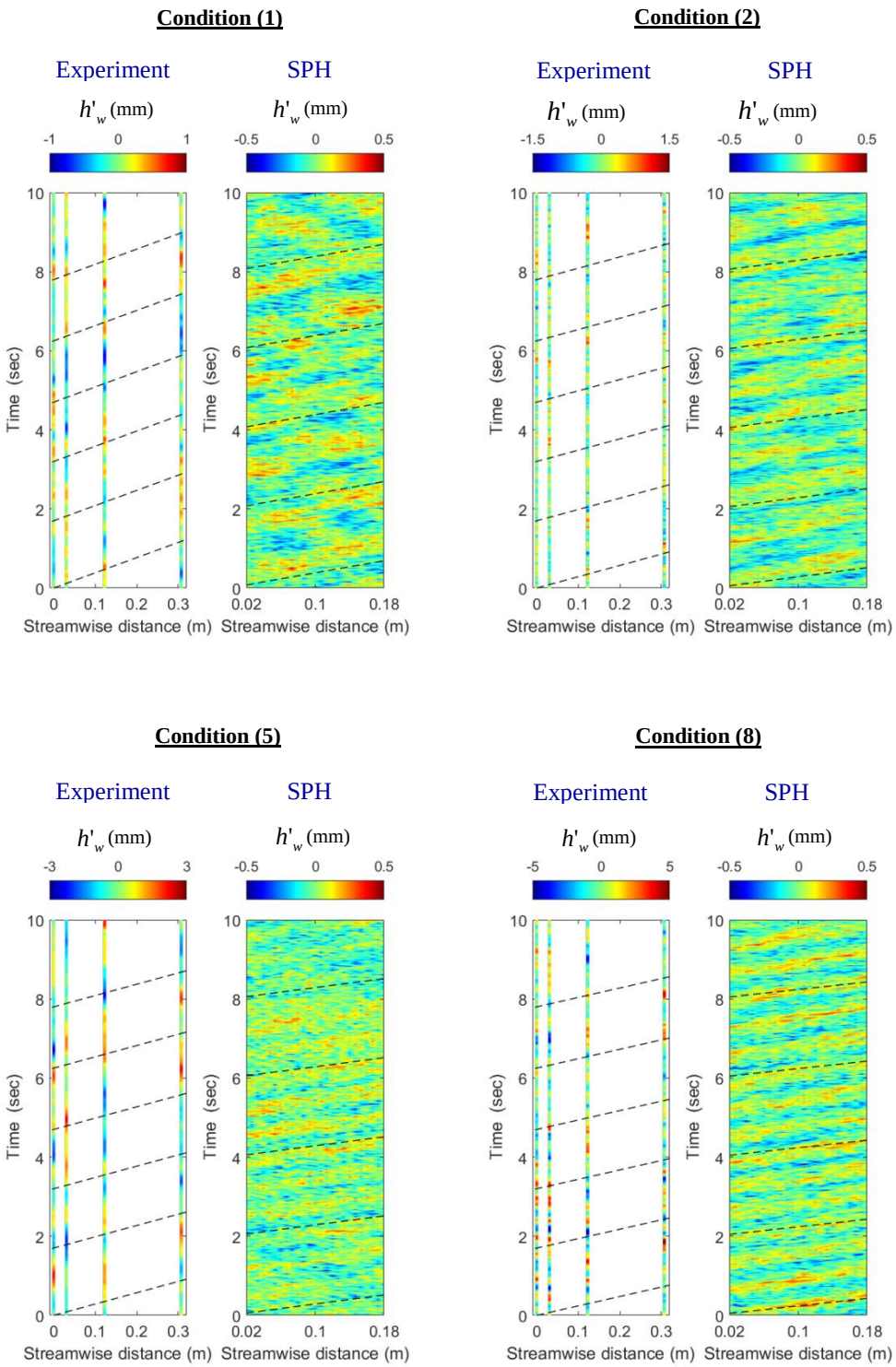

Figure 4.18 Comparisons of water surface dynamic patterns between experimental data and numerical results for flow conditions (1), (2), (5) and (8) in Table 3.1.

Here, all of these numerical findings were obtained using a SPH computational particle size of 0.0015 m, but the numerical model can well capture the flow

information much more refined than this scale. Also the sampling frequency used in this numerical model is 50 Hz, and water surface spatial pattern could be more clearly visualized when a larger sampling frequency is used. This observation provides evidence of the potential of the SPH particle modelling approach in free surface flow applications.

4.6.3 Correlation characteristics of the water surface pattern

As shown in the previous section, the free surface pattern is continuously changing over space and time, so it is necessary to examine its spatial dynamic behaviour by the use of a spatial correlation function which estimates the amplitude of the coherence and variance in water surface fluctuations at different locations. The measured and computed time-series of water surface fluctuations at different streamwise locations are cross-correlated to obtain the extreme value using the following equation:

$$R(\tau_l) = \frac{\sum \left(h_m(t) - \bar{h}_m\right)\left(h_n(t+\tau_l) - \bar{h}_n\right)}{\sqrt{\sum \left(h_m(t) - \bar{h}_m\right)^2}\sqrt{\sum \left(h_n(t+\tau_l) - \bar{h}_n\right)^2}} \tag{4.7}$$

where $R(\tau)$ is the temporal cross correlation function; $h_m(t)$ and $h_n(t)$ are the time-series data at streamwise locations m and n, which are separated by a spatial distance ρ_x; $\bar{h}_m$ and $\bar{h}_n$ are the time-averaged values; and τ_l is the time lag which corresponds to the time taken for the water surface wave to move between location m and n. To examine the advection speed of the free surface pattern more accurately, the temporally cross correlation function $R(\tau_l)$ was presented as the function of a spatial lag $x_l = \overline{U} \times \tau_l$. For the experimental data, the first three probes SP1 ~ SP3 were cross-correlated giving a number of four unique probe pairs as follows: SP1,1 (ρ_x = 0 mm), SP1,2 (ρ_x = 28 mm), SP2,3 (ρ_x = 92.3 mm), and SP1,3 (ρ_x = 120.3 mm).

Meanwhile, for the SPH computations, more steamwise locations were cross-correlated, giving nine unique streamwise spatial locations at ρ_x = 0.0 mm, 7.5 mm, 15 mm, 22.5 mm, 30 mm, 37.5 mm, 45 mm, 52.5 mm, and 60 mm, respectively. The results from the above procedures are plotted in Figure 4.19, which shows the experimental and numerical temporal cross-correlation functions against the spatial lag x_l for flow conditions (1), (2), (5) and (8). The red circle markers indicate the positions of the extreme values (maximum or minimum) of the experimental temporal cross-correlation function, whereas the blue square markers represent the positions of the extreme values of the numerical ones. Horoshenkov *et al*. (2013) performed similar experimental studies and showed that the extreme value of the temporal cross-correlation between two streamwise locations occurs at a spatial lag $x_l = \overline{U} \times \tau_l$. Similarly, the positions of the numerical SPH blue squares were also found to be very close to their streamwise spatial locations. It was estimated that the speed of the computed free surface patterns for the shallower flow condition (1) and (2) is approximately 25.0 % and 27.0 % slower than their depth averaged values, respectively. Whereas the computed free surface patterns of the deeper flow conditions (5) and (8) exhibit velocities that are 11.0 % and 6.0 % faster than their depth averaged values, respectively. An interesting finding here is that both the experimental and numerical correlations took almost a similar form in that they start from positive correlation of 1.0 and then flip their signs at a certain spatial lag x_l, and as this spatial lag increases their correlations become positive again with a value smaller than 1.0. This agrees well with the results of Nichols *et al*. (2016), which explains the physical mechanism behind the change of sign.

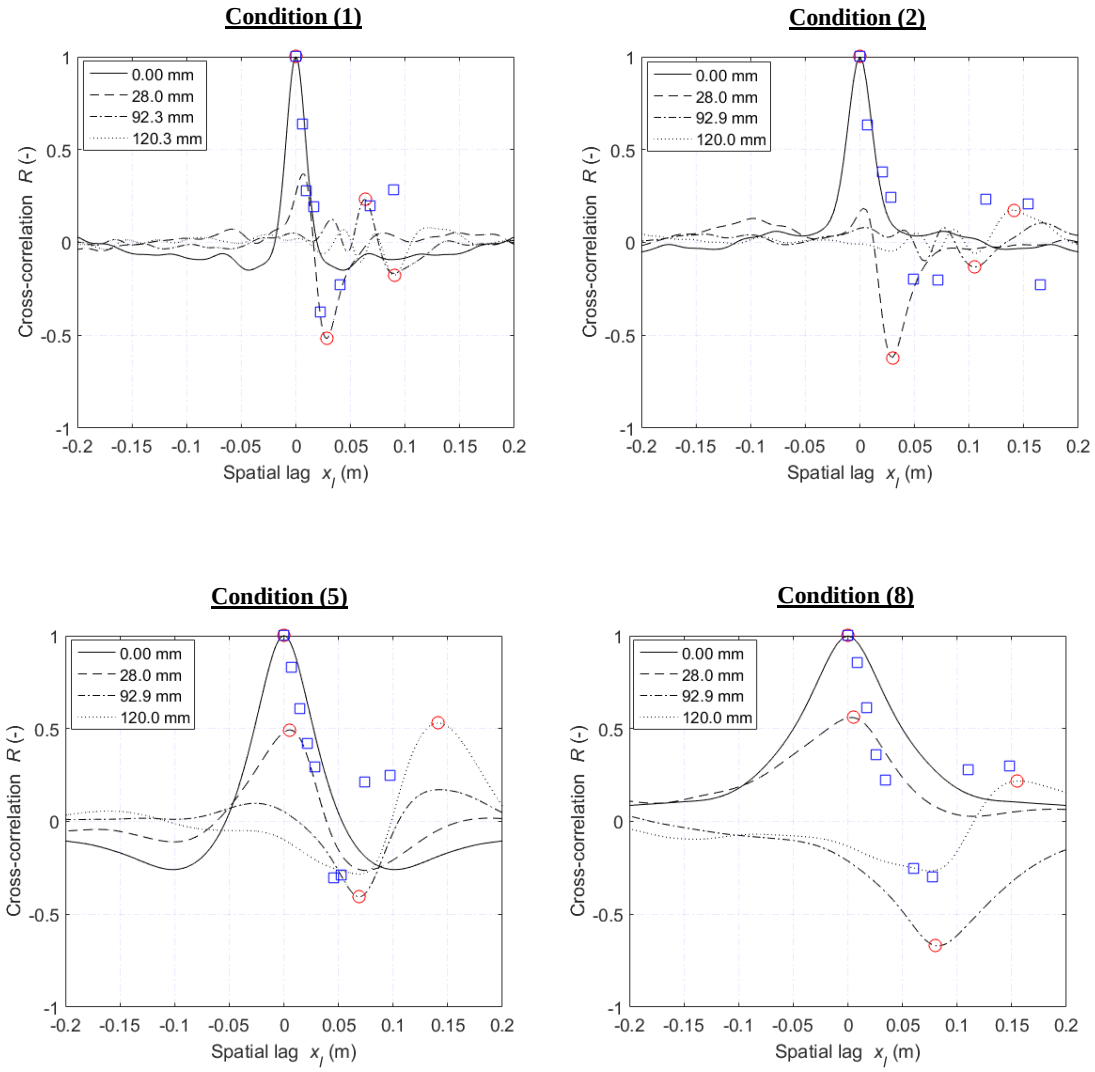

Figure 4.19 The experimental (red circles) and numerical SPH (blue squares) temporal cross-correlations for flow conditions (1), (2), (5) and (8) in Table 3.1.

The results in Figures 4.18 and 4.19 provide evidence that the SPH model is able to simulate the spatial and temporal patterns of the free surface although the ability to predict the instantaneous extreme elevation values is limited by the particle spacing of the SPH model.

4.6.4 Influence of free surface pattern on the underlying vertical flow velocity

The previous section has shown that the free surface roughness has an advecting spatial pattern that is strongly correlated to the bulk flow velocity. It is believed that the dynamic behaviour of these free surface patterns may also influence the sub-surface flow velocity field. The aim of this section is to use the SPH data of flow velocities to examine the degree to which the sub-surface flow velocity might be affected by the free surface dynamic behaviour. In this case the behaviour of the spatial correlation of the vertical velocity fluctuation over the flow depth will be investigated. This spatial correlation is calculated at different vertical locations from the bed $y/H = 0.0$ to the water surface $y/H = 1.0$. At each of vertical location, several streamwise locations equally separated by a spatial distance 5 mm were cross correlated to obtain the extreme values using the following equation.

$$R(\tau_l) = \frac{\sum \left(V_m(t) - \overline{V}_m\right)\left(V_n(t+\tau_l) - \overline{V}_n\right)}{\sqrt{\sum \left(V_m(t) - \overline{V}_m\right)^2}\sqrt{\sum \left(V_n(t+\tau_l) - \overline{V}_n\right)^2}} \tag{4.8}$$

where $V_m(t)$ and $V_n(t)$ are the time-series vertical velocity at streamwise locations m and n, which are separated by a spatial distance ρ_x; $\overline{V}_m$ and $\overline{V}_n$ are the time-averaged values; and τ_l is the time lag at which the two time series show the extreme value of their temporal cross-correlation $R(\tau_l)$. The results are plotted in Figure 4.20 which shows the continuous variation of the spatial correlation of the vertical velocity fluctuation throughout the flow depth. The first streamwise location (at zero spatial lag) has a correlation of unity which corresponds to the vertical velocity time series correlated against itself. It can be seen that a general decay in the spatial correlation is pronounced.

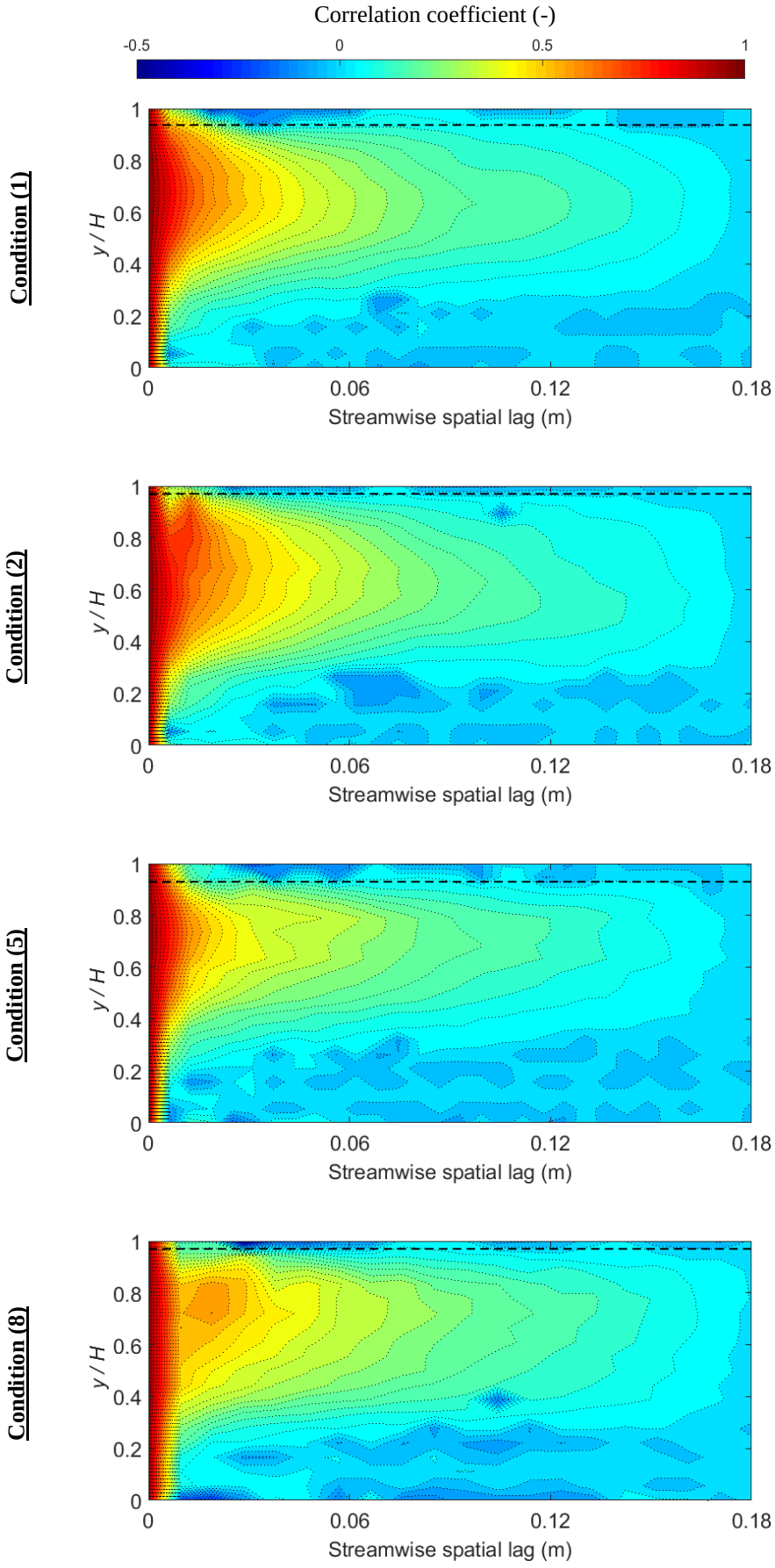

Figure 4.20 Computed spatial correlation function of the vertical velocity fluctuation over the flow depth for flow conditions (1), (2), (5) and (8) in Table 3.1.

In the middle region of the flow approximately between ($0.35 \le y/H \le 0.85$), the correlation behaviour exhibits almost liner trend reaching zero correlation at around 0.18 m streamwise spatial lag. It is also apparent that the effect of the inclusion of bed roughness which causing the spatial correlation to bulge towards the main flow region. Close to the free surface, the spatial correlation shows an oscillatory behaviour, whose spatial period seems to reasonably agree with that of the water surface presented in the previous section (see Figure 4.19). This finding would suggest a clear linkage, such that the water surface is being disturbed by the vertical velocity field in the sub surface layer. It is possible to estimate the influential depth of the water surface (the dashed-black lines in Figure 4.20 which correspond to the location of the deepest zero correlation values). It was found that the influential depth experienced down to a depth of approximately $y/H = 0.93$ for the examined flow conditions 1, 2, 5 and 8. It should be noted that no experimental measurement has been conducted to support this finding, and the accuracy of the influential depth is indeed depends on the values of some numerical parameters such as the computational particle size and sound speed.

4.7 2D SPH model conclusions

This chapter has presented the numerical model used to study shallow free surface flow over rough bed. The numerical program is based on the open source code 2DSPHysics (http://www.sphysics.org). Significant improvements were made on the turbulence modelling and rough bed treatment within the code. A modified sub-particle-scale (SPS) eddy viscosity model is proposed to reflect the turbulence transfer mechanisms in free surface flow and a drag force equation is included into the momentum equation as a source term to account for the effect of rough bed. The inflow/outflow boundary was treated using the periodic open boundary provided by

SPHysics, (Gómez-Gesteira *et al*., 2012). The computed streamwise velocity and shear stress have been validated against the laboratory measurements described in the previous Chapter. In the upper flow region, the MSEP between the measured and computed streamwise velocity stays below 0.5 %, while this error becomes larger near the bed region reaching approximately 2.5 %. The lowest MSEP in the velocity gradient dU/dy was found to be less than 5.0 % occurring in the middle region of the flow. Besides, the proposed 2D model was able to predict the shear velocity with a maximum error of 6.0 %. The sensitivity analysis using different particle size and turbulence closure techniques have shown that the original SPS turbulence model using a fixed Smagorinsky constant predicted much smaller and inconsistent shear stresses as compared with the experimental observations, while the new turbulence model using the mixing length approach could well achieve convergence between the simulated and observed values. The modified numerical model was also shown to be capable of predicting the average water depth and simulating the spatial pattern of water surface fluctuations. The spatial correlation analysis has shown that both the measured and computed free surface fluctuations exhibit an oscillatory component. The relative error between the estimated celerity of the free surface fluctuations and the depth averaged velocity was found to systematically increase as the flow depth becomes shallower. The computed spatial correlation of the vertical velocity has also revealed that the dynamic behaviour of the water surface appears to affect the sub-surface velocity field of free surface turbulent flows down to a depth of $y/H = 0.93$.

Implementation of 3D SPH numerical model would allow for more information on the underlying flow structure and water surface pattern to be disclosed, and hence a better understanding on the linkages between the underlying flow and free surface pattern throughout the flow cross section could be addressed. It was therefore decided to continue with the development of a 3D free surface code incorporating the new turbulence closure and the rough boundary treatment.

CHAPTER 5 3D SPH Numerical Model

5.1 Aim of 3D SPH numerical model

This chapter aims to modify the newly developed 2D SPH code and make it suitable for 3D free surface flows. Therefore the code will be significantly improved by including a suitable 3D turbulence model to simulate the turbulence transfer mechanisms found over the cross sectional area of a free surface channel flow. A new rough boundary treatment will also be developed, based on the concept developed in the previous chapter and included code to account for the existence of 3D roughness elements on the channel bed and on both side walls. Simulations using the newly developed 3D SPH numerical model are only performed for flow conditions 1, 2, 5 and 8 listed in Table 3.1. These flow conditions were chosen since they represent shallower and deeper conditions and thus different patterns of secondary flows and free surface could be observed. Prediction of the turbulent flow velocities and shear stresses will be compared with the flow velocity measurements taken for condition 2 (shallower) and condition 8 (deeper) described in Chapter 3. The numerical results of water surface patterns will be compared to those measured for flow conditions 1, 2, 5 and 8. This is to examine whether the improvements made on this model can simulate this type of flow adequately.

5.2 Model setup and computational parameters

To be dimensionally consistent with the experiment, the numerical flume width was taken as 0.46 m wide for the four flow conditions. To provide sufficient numerical accuracy and low CPU load simultaneously, the numerical flume length was considered to be three times the total flow depth as sketched in Figure 5.1. This length is believed to be sufficient enough to numerically visualize spatial stable

patterns of secondary flow, bed shear stress and water surface. The initial particle size was selected as 0.0015 m for flow conditions 1 and 2, and 0.0025 m for conditions 5 and 8, respectively. This provides a range of 80,0000 ~ 98,0000 particles involved in the computation domain. The selection of particle size is to ensure enough resolution within the bed roughness elements and also to minimize the kernel truncation near the boundaries. Similar to 2D model, a cubic spline kernel was adopted with a kernel size of h = 1.5dx. The real water viscosity ($\upsilon_0 = 10^{-6}\,\mathrm{m}^2/\mathrm{s}$) was used and the MLS filter was applied every 30 time steps to smooth out the density and pressure fluctuations. The computational time step was automatically adjusted to follow the Courant stability requirement (Gómez-Gesteira *et al*., 2012). To reduce the CPU time and meet the requirement for achieving flow stability, a speed of sound c_0 = 20 m/s was used throughout this computation. This value is approximately 3 times larger than the minimum requirement ($c_{0(\min)} = 10U_{\max}$) as suggested by Monaghan (1994). The XSPH variant was found to result in numerical dissipation and therefore it was turned off by assigning zero value to ε in equation 2.46.

Similar to the proposed 2D model, the reference level y_0 was taken 4.0 mm below the top of the spheres (the red dashed-line in Figure 5.1), from which the mean flow depth h_w is measured. In this 3D model, a value of $h_d = 0.32D$ was used for flow conditions 1 and 2 (shallower), and $h_d = 0.24D$ was used for flow conditions 5 and 8 (deeper). Since the flow is 3D, it is expected that smaller values of h_d , as compared to those values used in 2D model , can provide a better match with the experimental velocity profiles. Both $h_d = 0.24D$ and $h_d = 0.32D$ are within the range widely reported in the literature (Einstein & El-Samni, 1949; Bunco & Partheniades, 1971; Grass, 1971; Cheng & Clyde, 1972 ;Nakagawa *et al*., 1975; Bayazit, 1976).

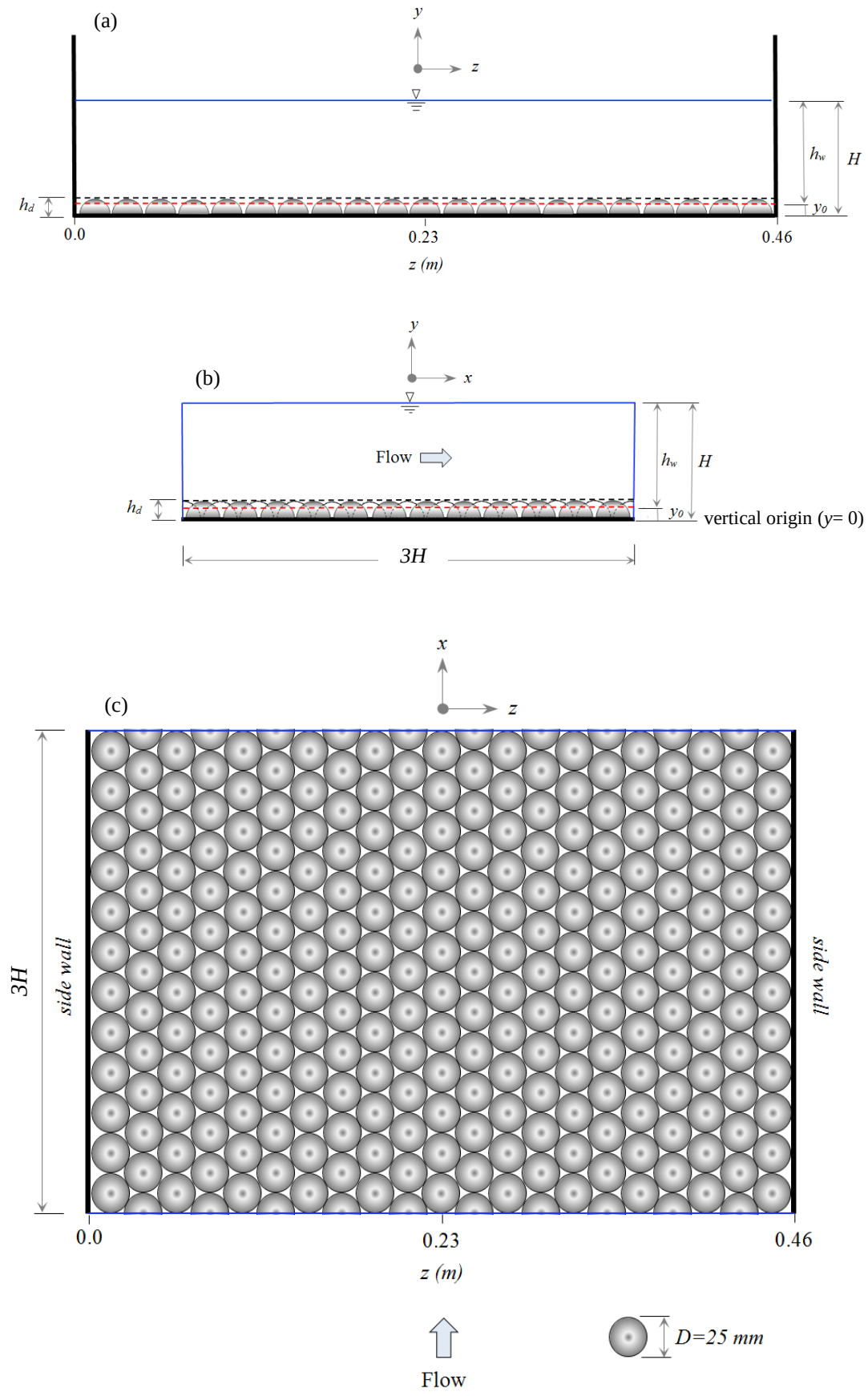

Figure 5.1 A sketch of 3D numerical model domain including bed roughness elements; (a) cross sectional view; (b) longitudinal view; (c) top view.

The following section demonstrates in details the improvement made on the turbulence modelling to address the 3D turbulent effect throughout the channel cross section.

5.2.1 Turbulence Closure in 3DSPHysics

Similar to 2DSPHysics, the flow turbulence shear stress is modelled by using eddy viscosity sub-particle scale (SPS) as.

$$\frac{\vec{\tau}_{ij}}{\rho} = 2\nu_t S_{ij} - \frac{2}{3}k\delta_{ij} - \frac{2}{3}C_I\Delta^2\delta_{ij}\left|S_{ij}\right|^2 \tag{5.1}$$

here, the turbulence eddy viscosity $\nu_t = (C_s\Delta)^2|S|$; $\Delta = \sqrt{dx^2+dy^2+dz^2}/3$ is the filter width; C_s is the Smagorinsky constant originally taken as 0.12; k is the SPS turbulent kinetic energy $k = \nu_t\left(\frac{du}{dx}+\frac{dv}{dy}+\frac{dw}{dz}\right)$; C_I is a constant, typically 0.0066; δ_{ij} = Kronecker's delta (δ_{ij} =1 when $i=j$ and δ_{ij} = 0 when $i\neq j$); and the local strain rate $|S|$ is defined as follows:

$$|S| = \sqrt{2\left(\frac{du^2}{dx}+\frac{dv^2}{dy}+\frac{dw^2}{dz}\right)+\left(\frac{du}{dz}+\frac{dw}{dx}\right)^2+\left(\frac{du}{dy}+\frac{dv}{dx}\right)^2+\left(\frac{dv}{dz}+\frac{dw}{dy}\right)^2} \tag{5.2}$$

S_{ij} is the SPS strain rate tensor which is defined as:

$$S_{xy} = 0.5\left(\frac{du}{dy}+\frac{dv}{dx}\right)$$

$$S_{xz} = 0.5\left(\frac{du}{dz}+\frac{dw}{dx}\right) \tag{5.3}$$

$$S_{yz} = 0.5\left(\frac{dv}{dz}+\frac{dw}{dy}\right)$$

In this 3D numerical simulation of free surface flows, it was found that the original SPS turbulent model using Smagorinsky constant still provides a much smaller shear stress compared to the experimental data. The results will be compared and discussed with the 2D SPS turbulent model in the following chapter.

Czernuszenko and Rylov (2000) proposed a simple analytical model based on the generalisation of Prandtl's mixing length approach that could be used to obtain the mean velocity and shear stress distributions in 3D non-homogeneous turbulent flows. This simple model was implemented in the current 3D SPH model by modifying the original SPS model (Equation 5.1). Thus the fixed product $C_s\Delta$ in the turbulent eddy viscosity was replaced by a mixing length which represent the turbulent eddies scale. In 3D flows, the turbulence eddy has three different length scales in streamwise, vertical and spanwise directions referred to as l_x, l_y and l_z, respectively. And it is assumed that the magnitudes of the largest turbulent eddies are L_x, L_y and L_z. The vertical size of the largest turbulent eddy L_y cannot be larger than the total flow depth H, and thus it is assumed to be equal to H. It is also assumed that the turbulent length scales in the streamwise and vertical directions are equal everywhere in the flume. Yalin (1992) reported that "if the bed friction-effect is sufficiently strong, then the lateral size of the largest eddies is much smaller than the channel width". Therefore, L_z is considered to be half smaller than that in vertical direction. So the largest turbulent eddies size used in the current numerical simulation are $L_x : L_y : L_z = 1:1:0.5$ and $L_x = L_y = H$. Now the distribution of mixing length in streamwise, vertical and lateral directions over the flume cross section needs to be specified. The cross sectional flow area of the flume can be divided into two zones, called the middle zone and edge zones (see Figure 5.2).

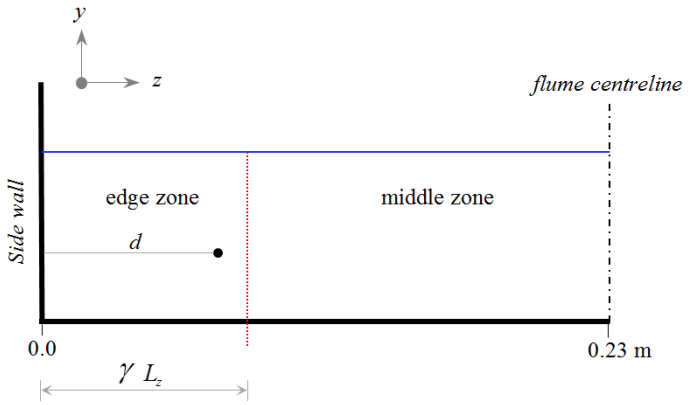

Figure 5.2 A sketch of half flume cross section.

In the middle zone (assumed to be hydraulically far away from both vertical side walls), the mixing length is only influenced by the rough bed and water surface, thus Equation (2.21) can be applied in this zone to compute mixing length in vertical and lateral directions. Whereas in the edge zone (hydraulically close to both vertical side walls), the mixing length is also influenced by both vertical walls, and the three component of mixing length l_x, l_y and l_z are assumed to vanish at each wall. Thus both Equations (2.20) and (2.21) can be applied in this zone to calculate mixing length in vertical and lateral directions. All the above produces to the following multiplicative equations:

$$l_y = \begin{cases} Ni(d/\gamma L_z) \times L_y \kappa \sqrt{1-y/H} \left(\frac{H}{y} + \pi \Pi \sin(\pi y/H) \right)^{-1} & \text{if} \quad \frac{d}{\gamma L_z} < 1.0 \\ L_y \kappa \sqrt{1-y/H} \left(\frac{H}{y} + \pi \Pi \sin(\pi y/H) \right)^{-1} & \text{else} \end{cases} \tag{5.4}$$

$$l_z = \begin{cases} Ni(d/\gamma L_z) \times L_z \kappa \sqrt{1-y/H} \left(\frac{H}{y} + \pi \Pi \sin(\pi y/H) \right)^{-1} & \text{if} \quad \frac{d}{\gamma L_z} < 1.0 \\ L_z \kappa \sqrt{1-y/H} \left(\frac{H}{y} + \pi \Pi \sin(\pi y/H) \right)^{-1} & \text{else} \end{cases} \tag{5.5}$$

where d = is the lateral distance measured from the size wall; Π was taken as 0.2 as recommended by Nezu and Rodi (1986) for flows with Re > 2000. The width of the edge zone is assumed to depend on the largest size of the lateral turbulent eddies with coefficient, i.e. to be equal to γL_z (see Figure 5.2). The coefficient γ controls the influence of the side wall on the flow. When γ is larger, the edge zones are larger, mixing lengths are smaller and velocities become greater there. Czernuszenko and Rylov (2000) reported that a value of γ between 0.25 ~ 1.0 can provide the best agreement between the measured and calculated main velocity distributions. They also concluded that in order to keep the pressure gradient in the streamwise direction close to zero, a value of γ=0.6 is recommended.

In the current simulations, γ was chosen as 0.5 which was found to provide reasonable match between the computed and measured bed shear stress distribution for flow conditions 2 and 8. Figure 5.3 shows the contour map of the normalized vertical mixing length distribution over the half cross sectional area of the flow. It can be seen that the mixing length vanishes at the bed, side walls and free surface boundaries. In the middle zone and near bed region $(y/H < 0.25)$, the mixing length is approximated by a damping function $(l_y = \kappa y)$. Smaller mixing length means that the flow momentum transfers over smaller distance, and thus the main flow velocity gradient dU/dy is higher due to the interaction with the solid boundary. The maximum mixing length occurs in the main region of the flow (far away from boundaries) approximately around $y/H = 0.7$. Figure 5.4 presents the vertical profiles of mixing length within the edge zone, and shows that the mixing length is being dampened by Equation (2.20) as the side wall becomes closer.

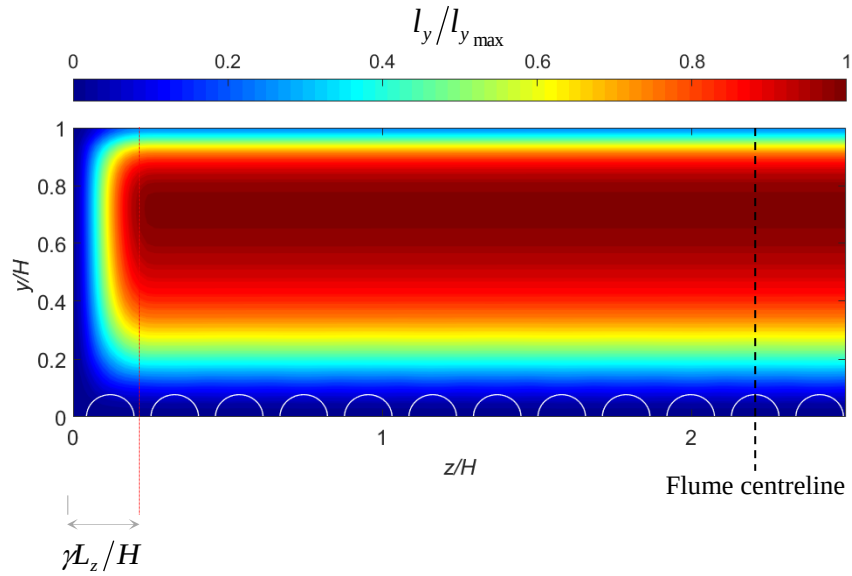

Figure 5.3 Contour plot of normalized vertical mixing length distribution over the half cross sectional flow area.

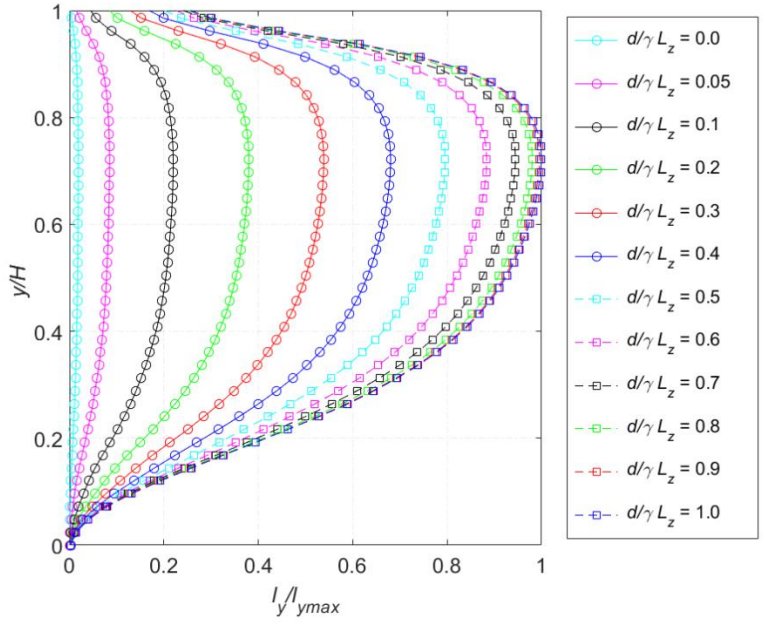

Figure 5.4 Normalized vertical mixing length distribution within the edge zone.

Czernuszenko and Rylov (2000) generalized the following formulate to calculate the turbulent stresses in 3D non-isotropic flows.

$$\frac{\tau_{ij}}{\rho} = 0.5(l_i^2 + l_j^2)\left(\frac{dU}{dy}\right)\left|\frac{dU}{dy}\right| \tag{5.6}$$

It is easy to notice that different turbulent mixing length scales can be specified in different directions by the term $0.5(l_i^2 + l_j^2)$ in Equation (5.6). When the mixing length in the streamwise and the vertical directions are equal, then Equation 5.6 turns into the original Prandtl's MLH (Equation 2.19). To modify the SPS turbulence model (Equation 5.1), the fixed product $C_s\Delta$ in the turbulent eddy viscosity ν_t is replaced by the term $0.5(l_i^2 + l_j^2)$ given in Equation (5.6). In this case, the combination of two different turbulent length scales in different directions is introduced rather than using only a fixed constant value. Thus the Modified-SPS shear stress $\vec{\tau}_{xy}$, $\vec{\tau}_{xz}$ and $\vec{\tau}_{yz}$ could now be computed as:

$$\frac{\vec{\tau}_{xy}}{\rho} = 0.5(l_x^2 + l_y^2)\left(\frac{du}{dy} + \frac{dv}{dx}\right)|S|$$

$$\frac{\vec{\tau}_{xz}}{\rho} = 0.5(l_x^2 + l_z^2)\left(\frac{du}{dz} + \frac{dw}{dx}\right)|S| \qquad (5.7)$$

$$\frac{\vec{\tau}_{yz}}{\rho} = 0.5(l_y^2 + l_z^2)\left(\frac{dv}{dz} + \frac{dw}{dy}\right)|S|$$

5.2.2 Treatment of Channel Roughness

In 3D turbulent open channel flow, the flow is not only influenced by the existing of the roughness element on the channel bed, but it is also influenced by the vertical side walls. This section aims to develop a new treatment of rough boundary to account for the drag forces due to the roughness element on both types of boundary.

5.2.2.1 Treatment of roughness element on the channel bed

To prevent the inner fluid particles from penetrating the bottom and side wall boundaries, the dynamic SPH particles approach (Dalrymple and Knio, 2001) has been implemented. It has been found that this boundary treatment behaves as a

hydraulically smooth bed, and it does not adequately exert a frictional effect on the flow. In the conducted experiments using spheres with diameter of 25 mm, the channel bed is indeed classified as a hydraulically rough surface, as the hydraulic roughness is constant as the flow Reynolds Number increases. Therefore, the frictional forces on the channel bed have to be accounted for.

In the current numerical simulation, the bed drag force was quantified using the classic drag formula given in Equation (2.16) and added to the momentum equation. It should be noted that, in 3D flow over rough bed the drag force acts in the streamwise, vertical and lateral directions. The lift force was neglected here due to being very small and it is believed to have no significant influence on the flow. The vertical drag forces were only computed on the sidewalls where high vertical velocities occur due to the interaction between the flow and sidewall corners. The drag area of the bed roughness element in the current numerical simulation is sketched in Figure 5.5.

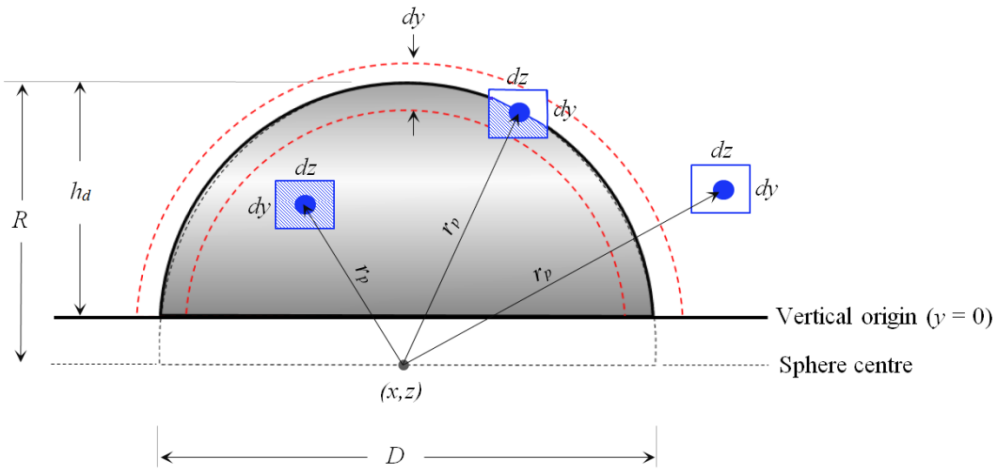

Figure 5.5 $yz-$**view of the total drag area of a single roughness element (blue circles: fluid particles).**

Figure 5.5 shows the cross sectional view of a single roughness element (sphere) in $yz-$view. The grey highlighted area is the total drag area perpendicular to the flow direction. The centre of the sphere in 3D space is located at *x* and *z* coordinates. The blue circles represent the numerical fluid particles, and each has coordinates x_p, y_p, z_p and is located at a distance r_p away from the centre of the sphere. The variable drag area A_d in Equation (2.16) needs to be defined in order to calculate the drag force of each fluid particle. It is necessary to be dimensionally consistent with the momentum equation, thus the drag area of a fluid particle has to be calculated per unit volume of fluid. The volume over which this drag force acts is equal to $dx \times dy \times dz$ (where dx, dy and dz are initial particle spacings in streamwise, vertical and lateral directions, respectively). By following Figure 5.5, the front drag area of each fluid particle per unit volume of fluid can be taken as $A_d = dydz$ in the $yz-$view. However, A_d of each fluid particle varies depending on the distance r_p. From Figure 5.5, r_p can be calculated as $r_p = \sqrt{\Delta x^2 + \Delta y^2 + \Delta z^2}$, where $\Delta x = x - x_p$, $\Delta z = z - z_p$ and $\Delta y = R - h_d + y_p$.

To be more accurate in calculating A_d for each fluid particle in 3D space, the roughness element in Figure 5.5 is divided into three regions as follows:

(a) Fully-submerged region, if $r_p < (R - dy/2)$.

(b) Partially-submerged region (between the red-dashed lines in Figure 5.5), if $(R - dy/2) \le r_p \le (R + dy/2)$.

(c) Fully outside the roughness element, if $r_p > (R + dy/2)$.

By taking into account the shape of the roughness element, A_d can be calculated in any regions as $A_d = \eta dydz$, where η is the shape factor. When a fluid particle is

located in the fully-submerged region, then $\eta = 1$ and $A_d = dydz$. If the fluid particle is located in the fully-outside the roughness element zone, then $\eta = 0.0$ and $A_d = 0.0$ (no drag forces). Now if the fluid particle is located within the partially-submerged region, then η should mathematically be calculated as shown in Figure 5.6.

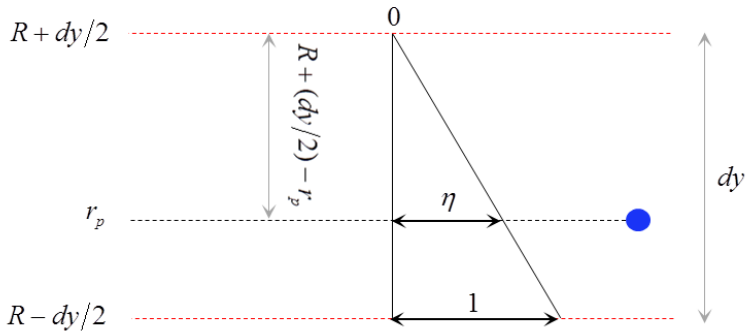

Figure 5.6 Schematic view of the calculation of the shape factor within the partially-submerged region (blue circle: fluid particle).

From Figure 5.6, the shape factor of a fluid located within the partially-submerged region can be calculated as $\eta = (R + (dy/2) - r_p)/dy$. The streamwise drag force of a fluid particle at a distance r_p can now be computed as:

$$(F_{dx})_{r_p} = \frac{1}{2}\rho C_d (\eta_{r_p} dydz) U_d |U_d| \tag{5.8}$$

Where C_d is the drag coefficient taken as $C_d = 0.8$; and U_d is the mean streamwise velocity of a fluid particle. To add this to the momentum Equation (2.39), $(F_{dx})_{r_p}$ needs to be computed per unit volume of the fluid as:

$$\frac{(F_{dx})_{r_p}}{dxdydz} = \frac{0.5\rho C_d (\eta_{r_p} dydz) U_d |U_d|}{dxdydz} \tag{5.9}$$

The drag force in the lateral direction ($xy-$view) needs to be considered in the current numerical simulation. It should be noted that the cross sectional total drag areas (the grey highlighted area is Figure 5.5) in $yz-$view and $xy-$view are identical. But A_d

in $xy-$view is equal to $A_d = \eta dydx$. Thus the lateral drag force of a fluid particle per unit volume of fluid can be computed as:

$$\frac{(F_{dz})_{r_p}}{dxdydz} = \frac{0.5\rho C_d(\eta_{r_p} dydx)W_d|W_d|}{dxdydz} \tag{5.10}$$

W_d is the average lateral velocity of a fluid particle. Equations (5.9) and (5.10) were coded in SPH form and added to the momentum equations in streamwise and lateral directions. The streamwise and lateral drag forces were computed for each single sphere element located on the channel bed at (*x*,*z*) coordinates (see Figure 5.1(c)). To check the accuracy of the proposed rough bed treatment, the results computed from Equations (5.9) and (5.10) are plotted in Figures 5.7, which shows the time-averaged and time-variation of the streamwise and lateral drag forces in $xz-$view for flow condition 8. As might be expected, the maximum value of F_{dx} occurs in the middle of each single sphere element (when a fluid particle is fully-submerged in the sphere), and it decreases as moving towards the sphere edge. It is also apparent that F_{dx} decreases as the side wall becomes closer due to the decrease in streamwise velocity. The maximum value of F_{dz} is approximately 4.0 % of the streamwise drag force and it occurs in regions close to both side walls. The positive and negative signs of F_{dz} show that high momentum flow moving from the flume centre towards the side wall corners, which indicates that strong near bed secondary flow exists. Figures 5.8 (a) and (b) present the cross sectional view ($yz-$view) of F_{dx} and F_{dy} at streamwise distance $x = 0.15\,\text{m}$. Figures 5.8 (a) shows that the maximum streamwise drag force is located in the middle of each sphere element, and it decreases towards the sphere edge due to the drag area A_d being decreased as well. This effect is also shown in Figure 5.8(c) which presents the longitudinal view ($xy-$view) of F_{dx} at $z = 0.23\,\text{m}$.

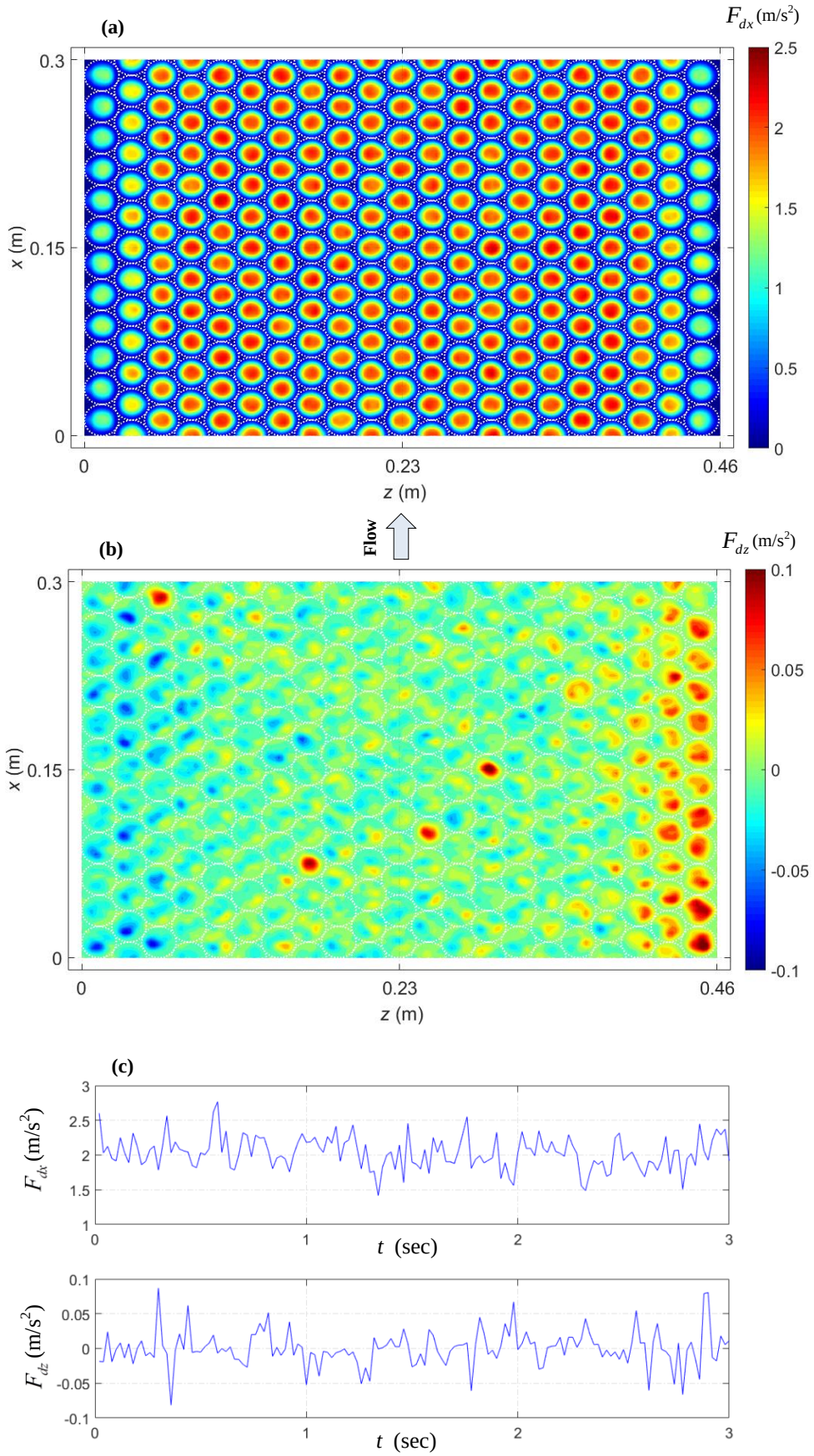

Figure 5.7 Contour maps of computed time-averaged of (a) streamwise drag force; (b) lateral drag force in $xz-$ view and (c) time-variation of streamwise and lateral drag forces at flume centreline for flow condition 8 (white-doted circles: physical sphere size).

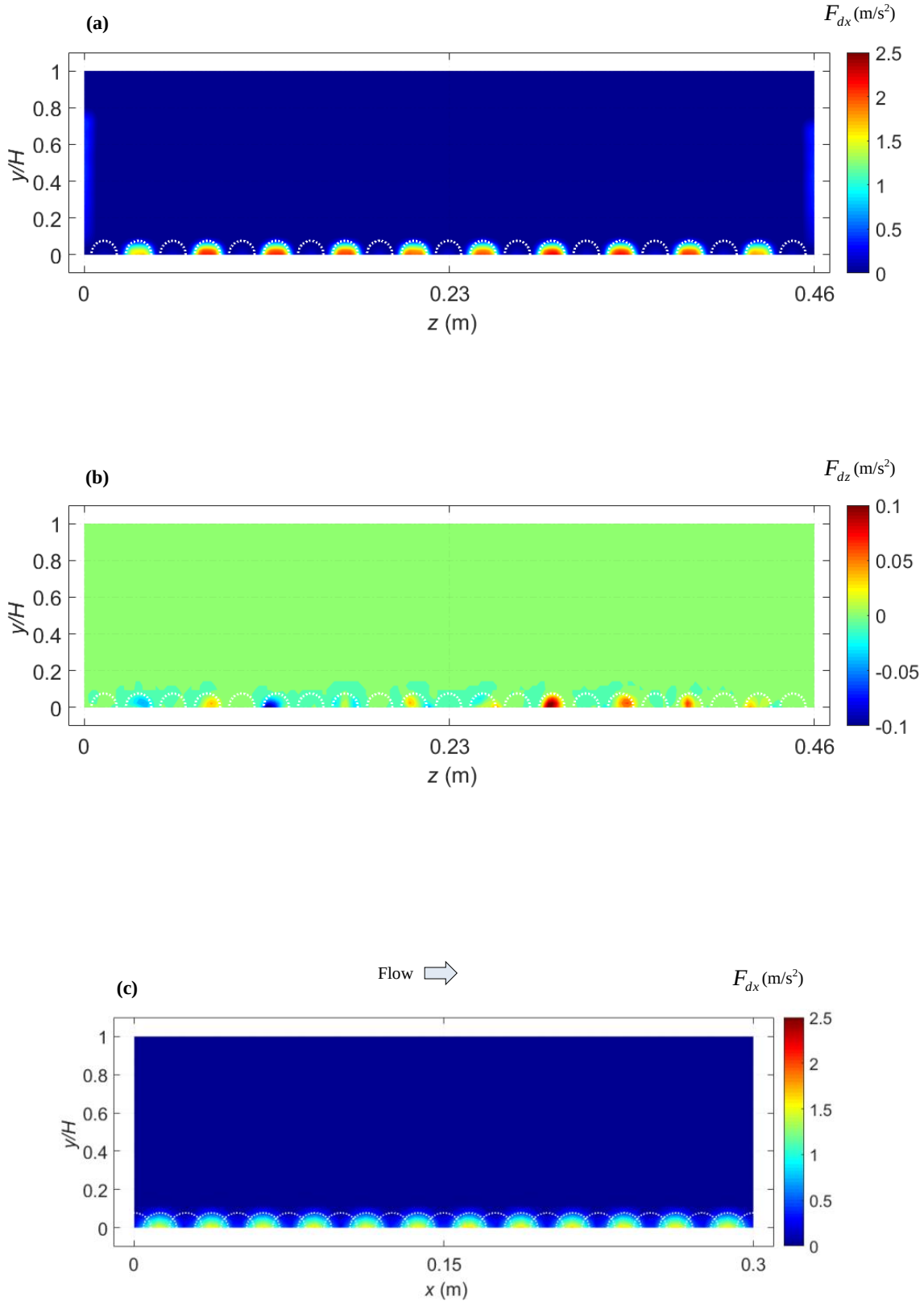

Figure 5.8 Contour maps of computed time-averaged of (a) streamwise drag force in $yz-$ view; (b) lateral drag force in $yz-$ view and (c) streamwise drag force in $xy-$ view for flow condition 8 (white-doted circles: physical sphere size).

5.2.2.2 Drag forces on the vertical side walls

The overall mean bed shear stress for uniform steady open channel flow is often obtained from $\tau = \rho g R S_0$, where R is the hydraulic radius which can be calculated as $R = HW_b/(2H + W_b)$, W_b is the flume width and H is the total flow depth. Einstein (1942) proposed that the shear forces exerted on the channel bed could be separated from those exerted on the sidewalls. He separated the flow into three sub-flow regions one corresponds to the flume bed and two correspond to sidewalls as shown in Figure 5.9.

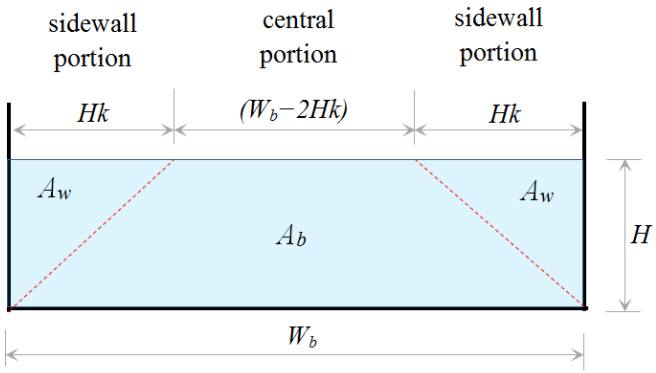

Figure 5.9 Flow cross sectional areas.

Each region has its own flow properties. Yang and Lim (1997) derived that the slope of the division lines (the red-dashed lines in Figure 5.9) can be expressed as:

$$k^3 + (2H/W_b)k - 2 = 0 \qquad (5.11)$$

where k is the ratio between the bed and wall shear velocities $(k = u^*_{bed}/u^*_{wall})$. The average shear stress for the bed and sidewall can be separately calculated as $\tau_{bed} = \rho g R_b S_0$ and $\tau_{wall} = \rho g R_w S_0$, where $R_b = A_b/W_b$ and $R_w = A_w/H$. From Figure 5.9, the area of each portion can be mathematically obtained as $A_b = HW_b - kH^2$ and $A_w = kH^2/2$.

The ratio between the total drag forces exerted on the bed and sidewall can be derived as follows.

$$k^2 = \tau_{bed}/\tau_{wall} = (F_{bed}/A_b)/(F_{wall}/A_w) \tag{5.12}$$

where F_{bed} and F_{wall} are the total drag forces acting on the channel bed and sidewall, respectively. F_{bed} represents the streamwise drag force (the most dominant force) which was calculated in the previous section given by Equation (5.9). The drag force F_{wall} acts in the streamwise and vertical directions referred to as Fx_{wall} and Fy_{wall}, respectively. Fx_{wall} and Fy_{wall} are computed for each a fluid particle located very close to the side walls within a layer of h_d as:

$$Fx_{wall} = \left(\frac{A_w}{A_b k^2}\right)\frac{0.5\rho C_d dydz U_d |U_d|}{dxdydz}$$

$$Fy_{wall} = \left(\frac{A_w}{A_b k^2}\right)\frac{0.5\rho C_d dxdz V_d |V_d|}{dxdydz} \qquad \text{if} \quad \frac{z}{h_d} < 1.0 \tag{5.13}$$

where V_d is the average vertical velocity of a fluid particle. For a given flow condition, Equations 5.9 ~ 5.13 can be used to compute the drag forces acting on the bed and both sidewalls.

5.3 Results and analysis

The 3D SPH numerical model was run for flow condition 1, 2, 5, and 8 listed in Table 3.1 until time *t* exceeded 6.0 s and using an output time of 0.02 s. To reduce the time of simulation and to reach the stable flow quicker, an analytical solution based on the power law $U = U_{\max}(y/H)^{(1/m)}$ was initially imposed within the fluid block for each flow condition. It should be noted that nothing has been imposed on the

inflow/outflow, bottom and side wall boundaries, instead the turbulent flow has been developed by the influence of the proposed 3D turbulence model and drag force equations demonstrated earlier. The value of m in the power law equation was determined from the best fit with the experimental time averaged streamwise velocity profiles at the flume centreline as $m = 2.8$, 3.0, 3.2, and 3.8 for flow condition 1, 2, 5 and 8, respectively. The values of m were found to be very close to the equation $m\sqrt{f} = 1.0$ provided by Cheng (2007), where f is the friction factor obtained from equation (2.6). It was observed that stable lateral bed shear stress has been achieved at t = 3.0 s after the flow was initialized for the four flow conditions. This allows for 3.0 s of data gathering that could be said to have no longer been under the influence of the initial model setup. It was also necessary to check the time convergence of the computed depth averaged streamwise velocity $\overline{U}$ from t = 3.0 s ~ 6.0 s. Figure 5.10 presents the standard deviation (STD) of the computed depth averaged velocity of increasing period as a percentage of the STD of 3.0 s. It is apparent that the STD of $\overline{U}$ settles down to within ± 2.0 % after time t = 2.0 s for the four flow conditions.

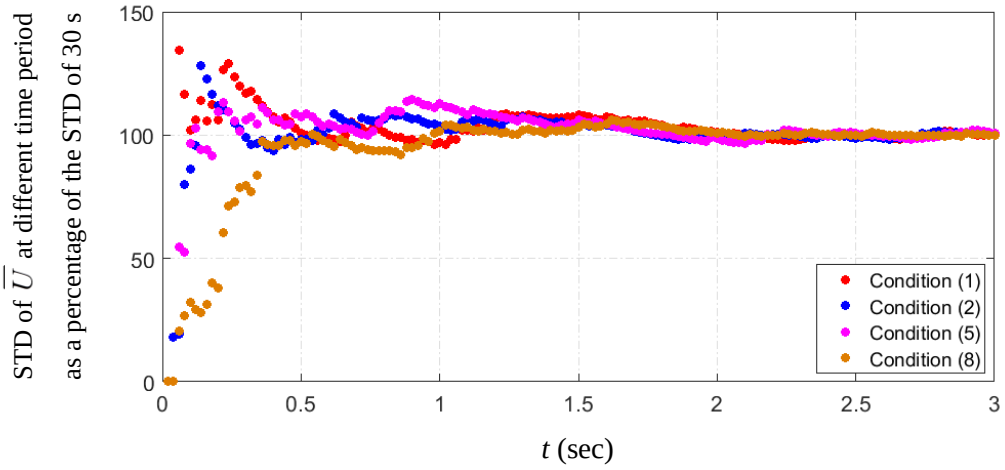

Figure 5.10 Settling time of standard deviation of the computed depth-averaged velocity for increasing period.

5.3.1 Flow pattern in the longitudinal direction

The spatial patterns of the time averaged streamwise velocity in the longitudinal direction at the flume centreline were computed and plotted in Figure 5.11 for the four simulated flow conditions 1, 2, 5 and 8. These contour plots exhibit smooth patterns that are developed in almost parallel layers, which indeed indicates that the fluid particles distribution is quite orderly without any obvious persistent numerical noise in the particle field.

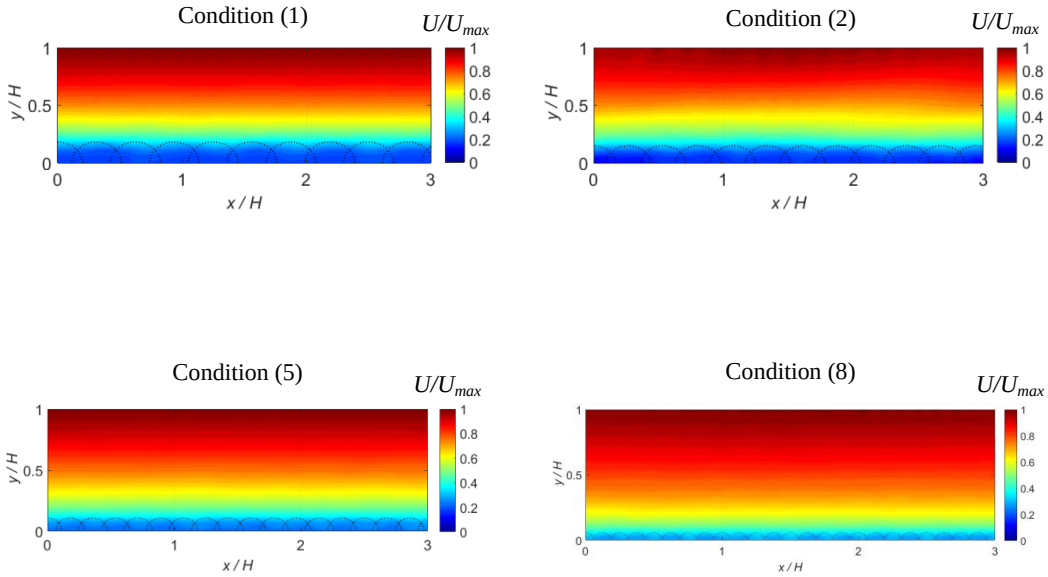

Figure 5.11 Longitudinal contours of the computed time-averaged streamwise velocity at the flume centreline for flow conditions 1, 2, 5 and 8.

The contour plots of the time averaged pressure in the longitudinal direction presented in Figure 5.12 reveal smooth patterns such that they decrease almost linearly from the bed towards the free surface without significant noise.

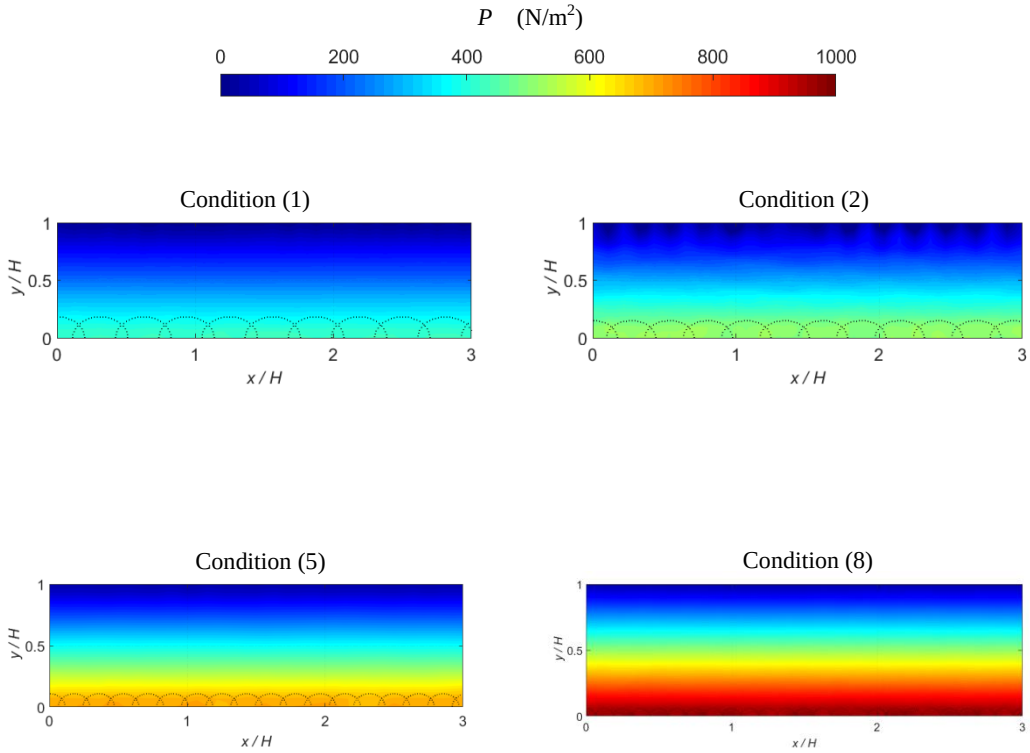

Figure 5.12 Longitudinal contours of the computed time-averaged pressure at the flume centreline for flow conditions 1, 2, 5 and 8.

Figure 5.13 presents a comparison of the measured and computed time averaged streamwise velocity profiles at the flume centreline for the four conditions. The computed profiles here were obtained by spatially averaging the contours shown in Figure 5.11 along the longitudinal direction. Both the measured and computed profiles reveal a satisfactory agreement in the upper region of the flow, while the computed velocities were slightly under predicted near the bed region for the four flow conditions. To more clearly demonstrate this, the mean square error percentage (MSEP) of the velocity and its gradient at every experimental vertical location were quantified and shown in Figure 5.14.

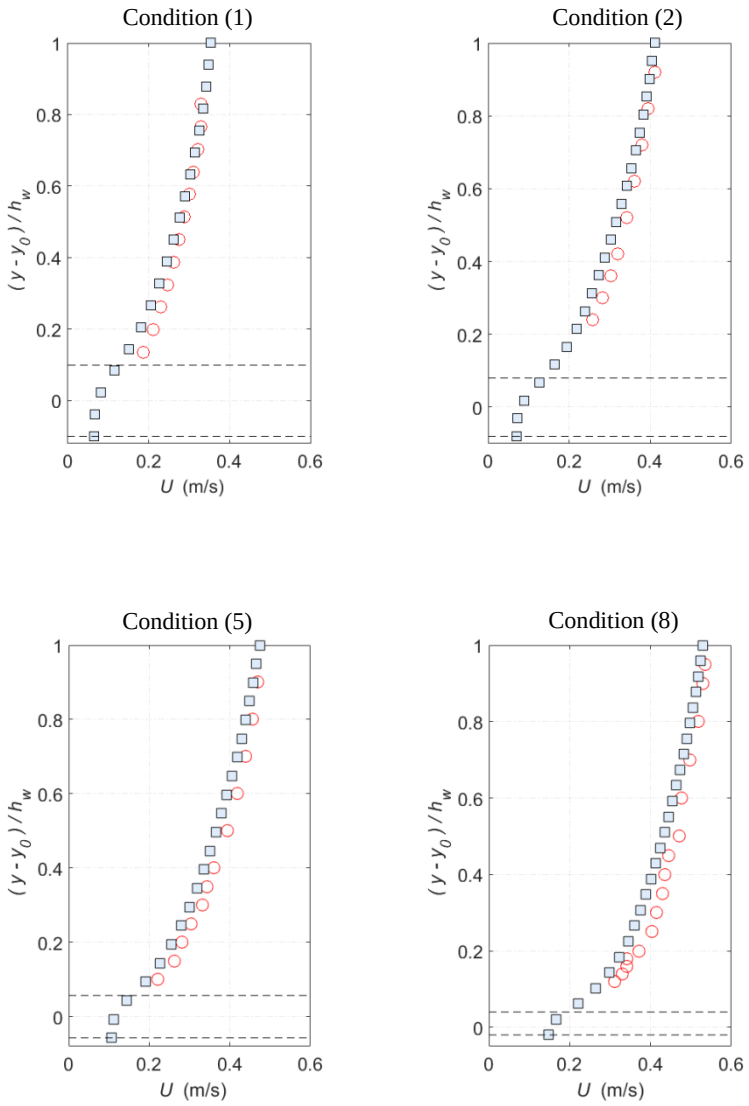

Figure 5.13 Comparisons of time averaged streamwise velocity profiles at the flume centreline for condition 1, 2, 5 and 8, (circles: exp data; squares: SPH; dash lines: roughness top and bottom).

It generally shows that the MSEP in the velocity increases approximately from 0.2 % at $(y-y_0)/h_w \approx 0.6$ to 4.5 % near the bed. These errors are larger for the shallower flow conditions (1) and (2), which may suggest that the roughness height used for these two conditions ($h_d = 0.32D$) is slightly bigger. This is also evidenced by the MSEP in dU/dy which shows that flow conditions (1) and (2) experience larger error reaching approximately 17.0 % in the middle region of the flow. A slightly smaller value of h_d would provide better agreement and minimizes these errors. To

numerically support this, the model was run for flow condition (1) using a smaller roughness height of $h_d = 0.30D$ (6.0 % smaller).

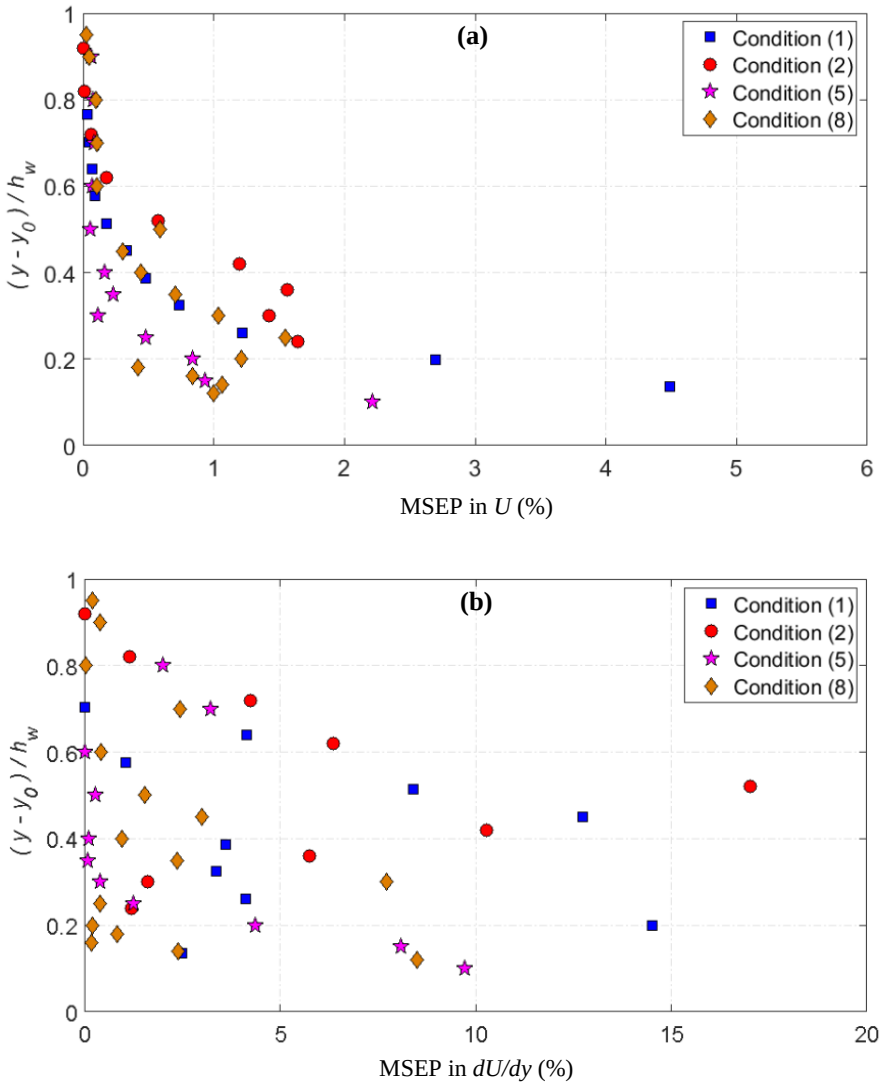

Figure 5.14 Mean square error percentage (MSEP) of (a) the streamwise velocity, (b) the streamwise velocity gradient for condition 1, 2, 5 and 8.

The MSEP in the velocity and its gradient using two different values of roughness height were calculated at every experimental vertical location and are presented in Figure 5.15. It is apparent that when $h_d = 0.30D$ was used, the maximum errors in U and dU/dy have been minimized to less than 1.5 % and 10.0 %, respectively. The agreement between the predicted and measured velocity profiles becomes better in the upper part of the flow approximately $0.4 \geq (y - y_0)/h_w \leq 1$.

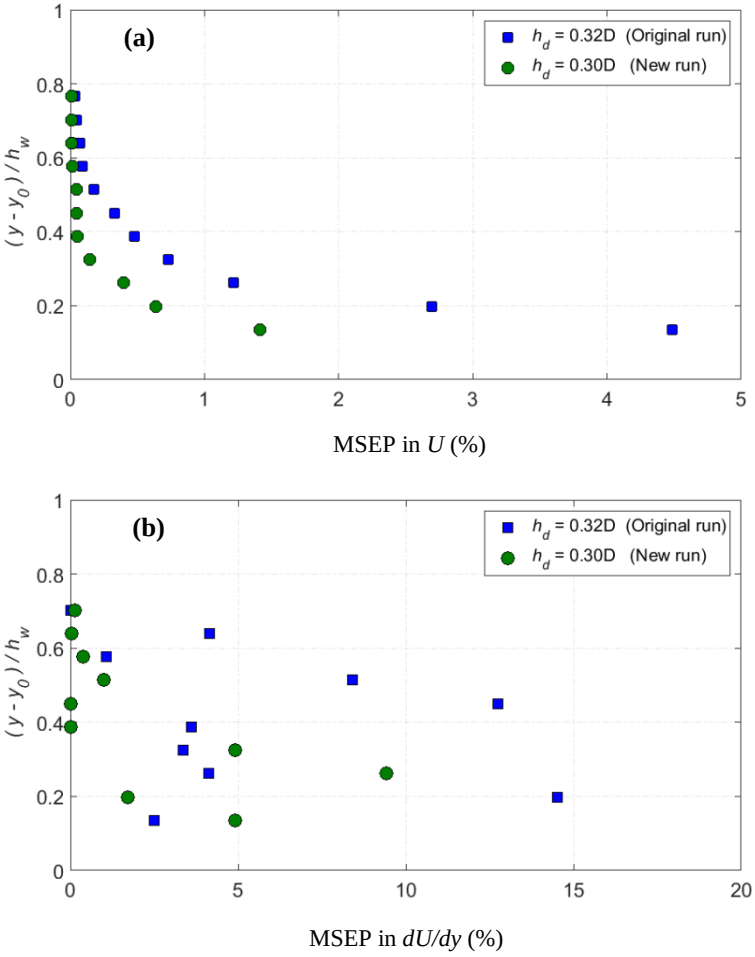

Figure 5.15 Mean square error percentage (MSEP) of (a) the streamwise velocity, (b) the streamwise velocity gradient using two different roughness heights for condition 1.

The spatial pattern of the shear stresses throughout the flow depth presented in Figure 5.16 reveals gradual decrease towards the free surface. The greatest shear stress occurs just above the top of the spheres and it slightly varies in the streamwise direction. This spatial variation might be attributed to the effect of secondary flows. Unlike the proposed 2D model, a better agreement between the computed, measured and the analytical shear stress profiles has been achieved as shown in Figure 5.17. Flow condition 8 (the deepest) experiences the largest deviation between the measured and predicted bed shear stress (about 16.0 % of τ_b). This was previously attributed to measurement uncertainties that the flow condition was slightly non-uniform.

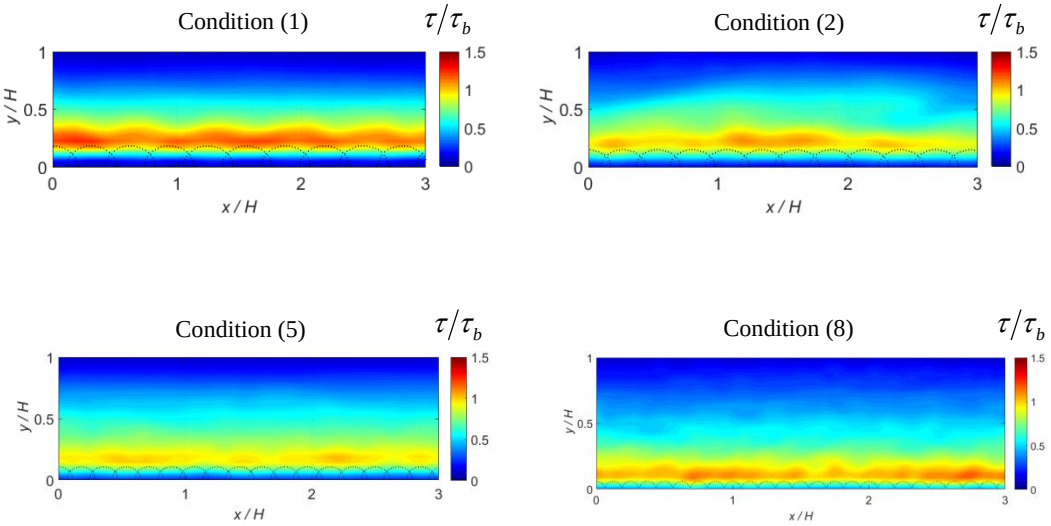

Figure 5.16 Longitudinal contours of the computed time-averaged shear stress at the flume centreline for flow conditions 1, 2, 5 and 8.

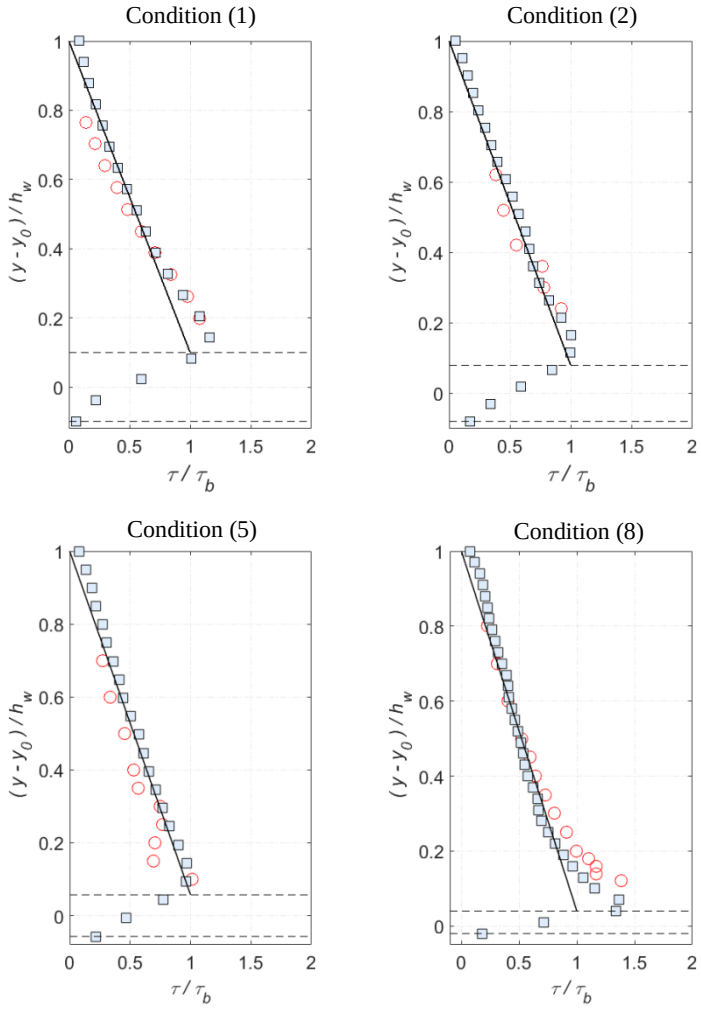

Figure 5.17 Comparisons of time averaged shear stress profiles at the flume centreline for condition 1, 2, 5 and 8, (circles: exp data; squares: SPH; solid black lines: analytical (equation 4.6); dash lines: roughness top and bottom).

5.3.2 Sensitivity analysis of the 3D SPH model

The aim of this analysis is to check the convergence of the newly developed 3D SPH model in the spatial domain using two different particle size for condition 1 and 5. Figures 5.18 (a) and (b) present the computed time averaged streamwise velocity and shear stress based on the new 3D mixing length model for two different particle size, i.e. dx = 1.5 mm (original run) and 2.0 mm (new run) for condition 2, and dx = 2.5 mm (original run) and 3.0 mm (new run) for condition 5, respectively. The selection of these particle size guarantees that at least 20 particles exist along the vertical direction. Figures 5.18 (a) and (b) generally reveal good overlapping behaviours along the flow depth for the two different particle size, indicating the convergence of the numerical model. However, when larger particle size is used for the two conditions, the shear stress values slightly deceases by approximately 10 % of τ_b in region just above the roughness top. This could be due to that more spatial resolution might be needed near the roughness interface to obtain more accurate velocity gradient.

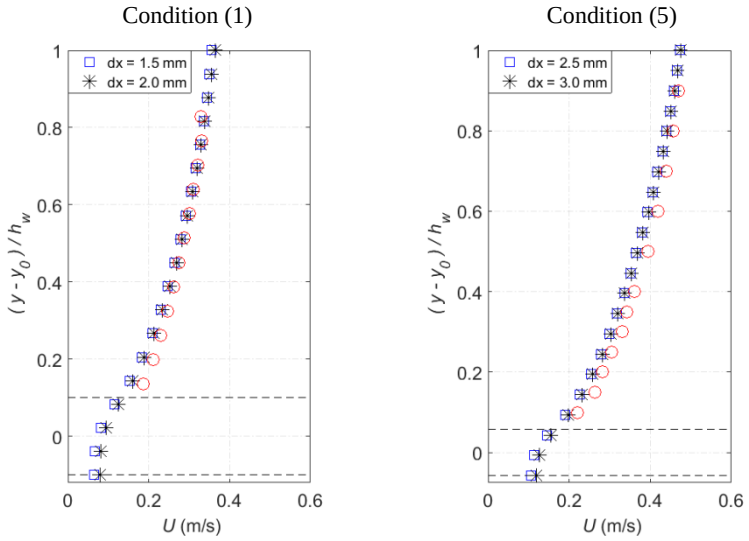

Figure 5.18 (a) Comparisons between experimental (red circles) and SPH time-averaged velocity profiles for two different particle sizes.

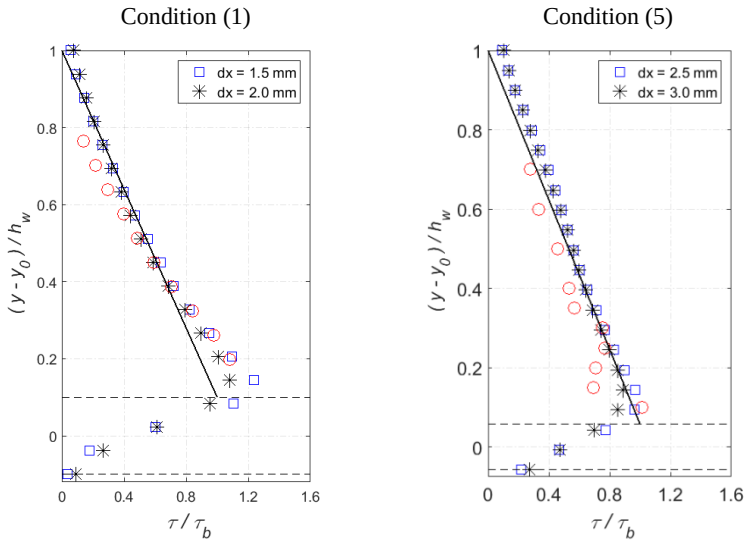

Figure 5.18 (b) Comparisons between experimental (red circles), analytical Equation (4.6) (black solid lines) and SPH time-averaged shear stress profiles for two different particle sizes.

5.3.3 Spatial pattern of the flow in the lateral direction

The spatial patterns of some hydrodynamics variables over the flume cross section and from the bottom of the roughness to the free surface are plotted in Figures 5.19 ~ 5.22 for flow condition 1, 2, 5 and 8, respectively. These patterns were obtained by averaging the flow field over time t = 0.2 s. This period was found to be sufficiently long to resolve strong secondary flow patterns for the four flow condition. The spatial averaging resolution was used as $\Delta y = \Delta z = 0.0025$ m for condition 1 and 2, and $\Delta y = \Delta z = 0.005$ m for condition 5 and 8. The mean streamwise U, vertical V and lateral W velocity patterns were all normalized by the maximum cross sectional streamwise velocity $U_{\max}$. Whereas the shear stress pattern was normalized by the average bed shear stress calculated as $\tau_b = \rho g(H - h_d)S_0$. From these patterns, it is apparent that the secondary flows are formed throughout the entire width of the flume cross section and are scaled with the flow depth. The indicated rotational sense of

these currents corresponds to the patterns of vertical (V) and lateral (W) mean velocities. Regions of upflow ($V > 0$) and downflow ($V < 0$) are approximately separated by lateral distance of $0.9H \sim 1.2H$ in the lateral direction. The vector fields show that the strongest cells occur near each side wall transporting high flow momentum from the free surface toward the channel bed, and causing the mean streamwise velocity to slightly bulge towards the side wall corners. For condition 1 and 2 (shallower), the secondary flows become weaker in regions away from the sidewalls. The secondary flow velocity was calculated as $U_s = \sqrt{\overline{V}^2 + \overline{W}^2}\,/\,\overline{U}$, where $\overline{U}$, $\overline{V}$ and $\overline{W}$ are the mean cross sectional streamwise, vertical and lateral velocities, respectively. It was found that as the aspect ratio decreases from condition 1 ~ 8, the secondary flow velocity becomes larger ranges from 1.2 % ~ 2.0 % of $\overline{U}$.

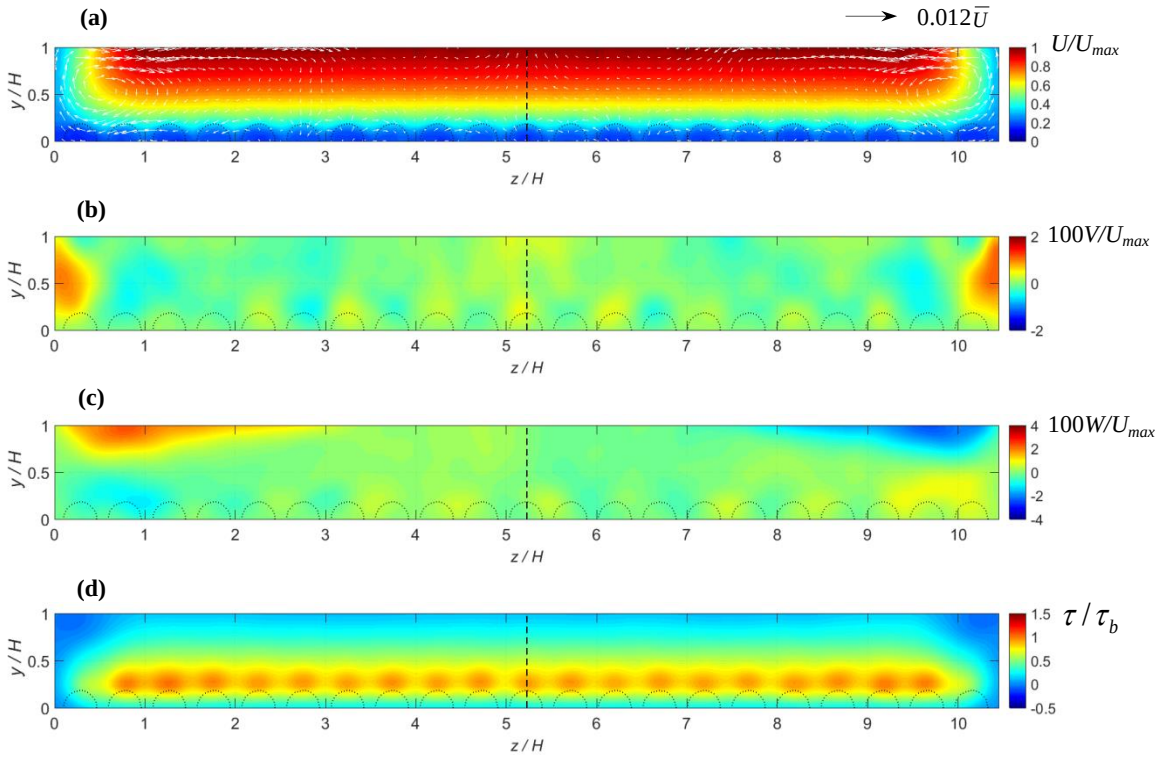

Figure 5.19 Cross sectional distribution of some hydrodynamic variables computed for condition 1 including the roughness elements;(a) normalized mean streamwise velocity with vector field; (b) normalized mean vertical velocity; (c) normalized mean lateral velocity; (d) normalized shear stress, (dash lines: flume centreline).

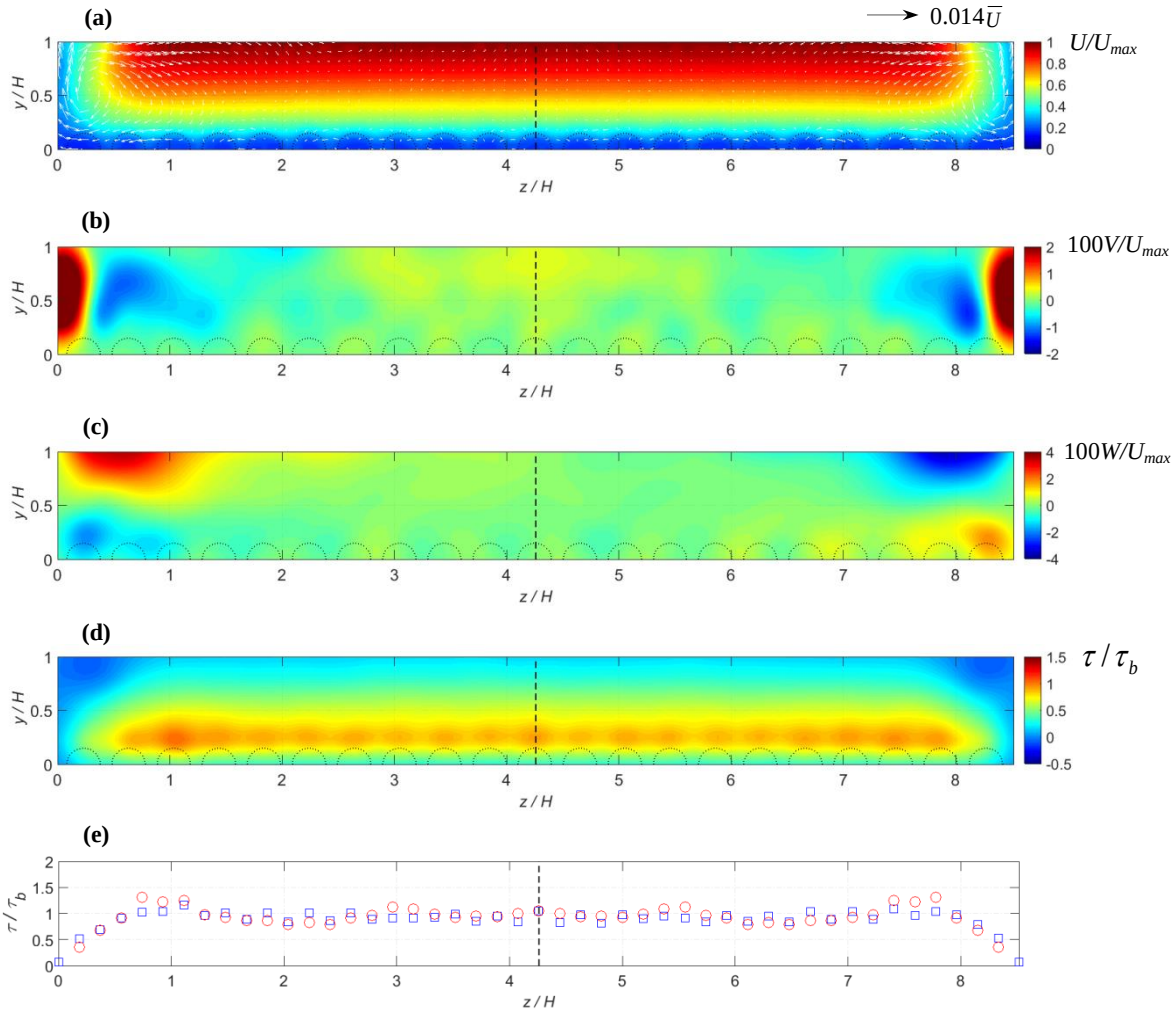

Figure 5.20 Cross sectional distribution of some hydrodynamic variables computed for condition 2 including the roughness elements;(a) normalized mean streamwise velocity with vector field; (b) normalized mean vertical velocity; (c) normalized mean lateral velocity; (d) normalized shear stress; (e) measured and computed bed shear stress, (circles: exp data; squares: SPH; dash lines: flume centreline).

The cross sectional distribution of the computed shear stress reveals a maximum value being on the top of the roughness element (where the streamwise velocity gradient dU/dy is higher), and is gradually decreasing towards the free surface and both side walls. Negative shear stresses were observed in small regions just below the water surface and next to both side walls indicating a strong secondary flow cell. Additionally, the lateral distribution of the measured and computed bed shear stresses

for condition 2 and 8 were compared as shown in Figures 5.20(e) and 5.22(e), respectively. The comparison generally shows a satisfactory agreement such that they increase from minimum at the side walls to a peak values 30 % ~ 50 % greater than τ_b. To quantify the accuracy of the proposed model in predicting the bed shear stress, the mean square error percentage MSEP between the measured and computed lateral bed shear stresses was calculated and it remains below 4.0 % for condition 2 and 8.

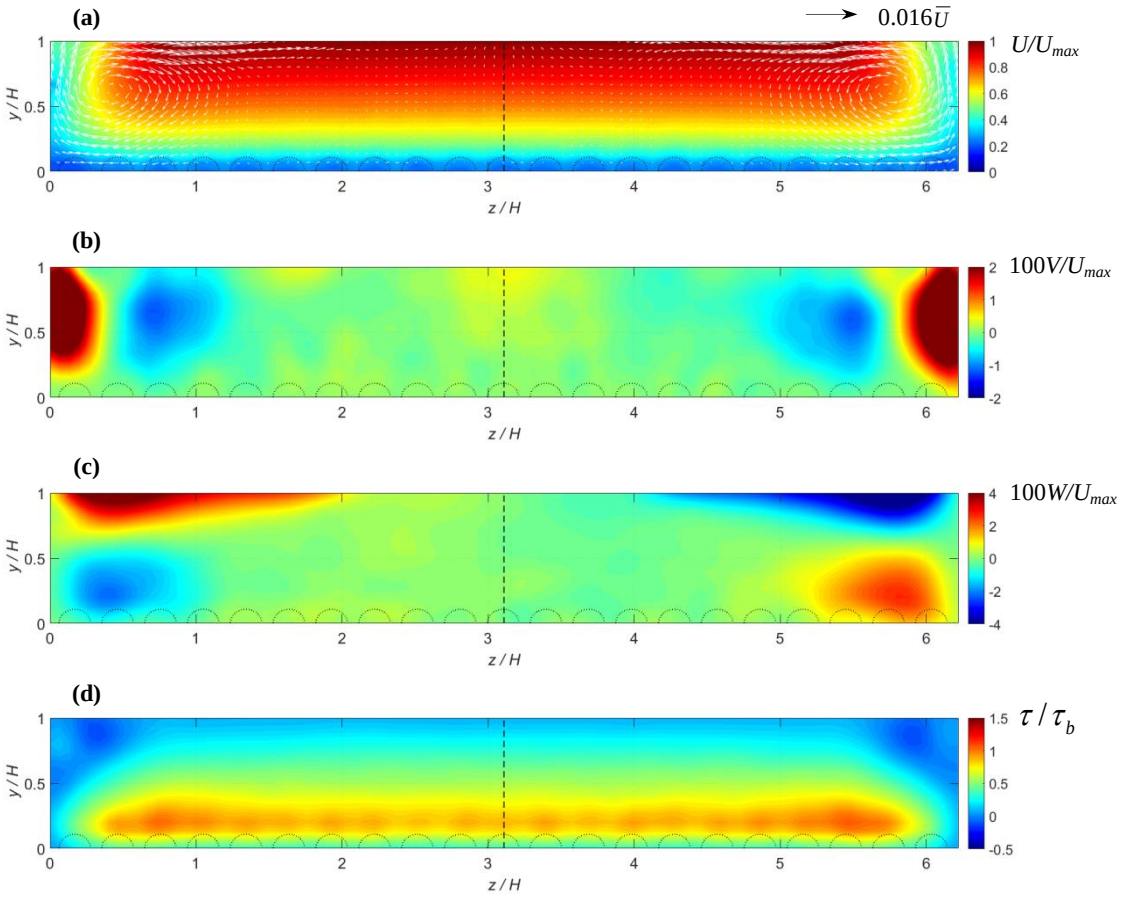

Figure 5.21 Cross sectional distribution of some hydrodynamic variables computed for condition 5 including the roughness elements;(a) normalized mean streamwise velocity with vector field; (b) normalized mean vertical velocity; (c) normalized mean lateral velocity; (d) normalized shear stress, (dash lines: flume centreline).

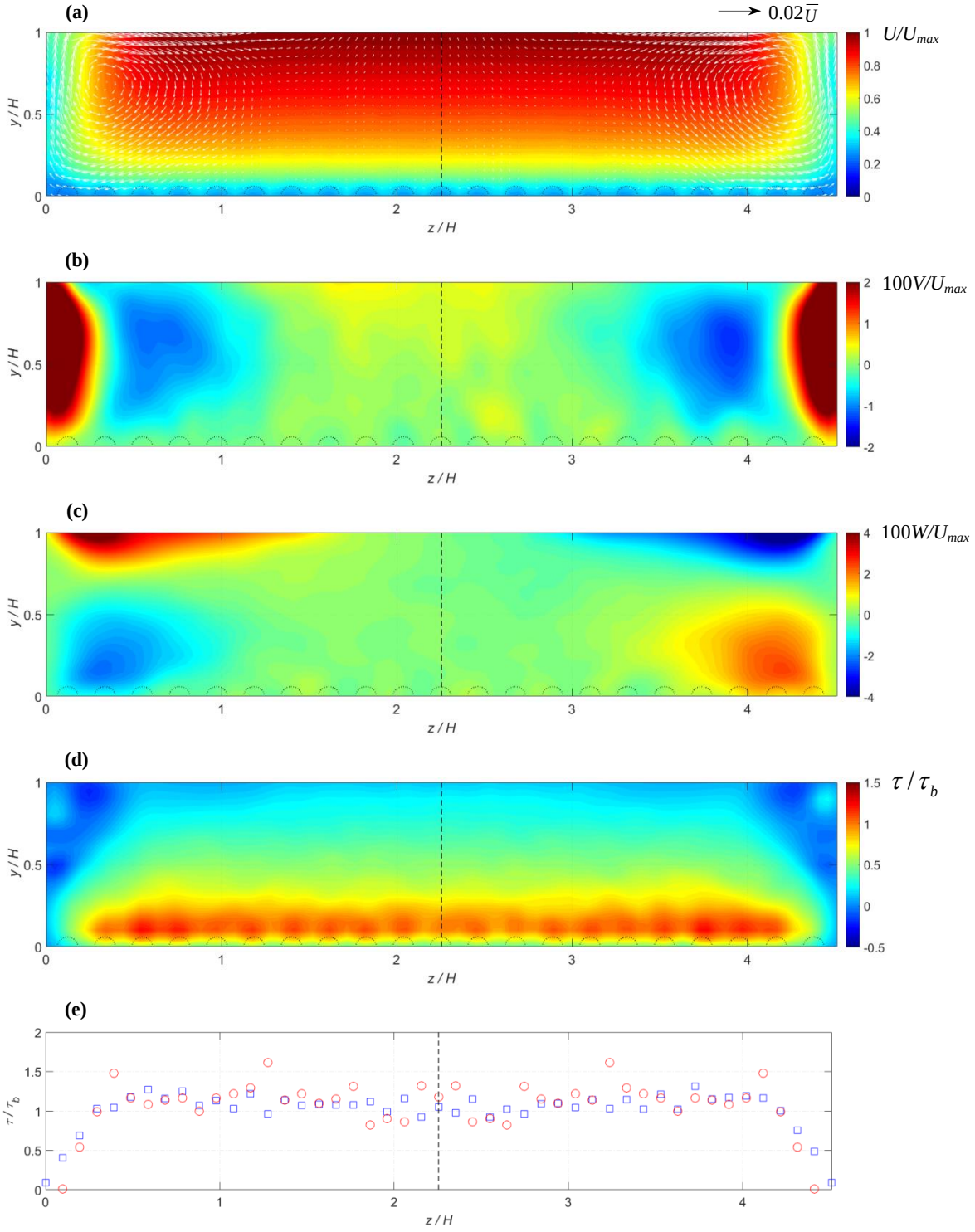

Figure 5.22 Cross sectional distribution of some hydrodynamic variables computed for condition 8 including the roughness elements;(a) normalized mean streamwise velocity with vector field; (b) normalized mean vertical velocity; (c) normalized mean lateral velocity; (d) normalized shear stress; (e) measured and computed bed shear stress, (circles: exp data; squares: SPH; dash lines: flume centreline).

To further evaluate the accuracy of the newly developed 3D SPH model, the vertical profiles of the time averaged streamwise velocity and shear stress at the upflow ($V > 0$) and downflow ($V < 0$) zones were computed and compared with the experimental data for condition 2 and 8. Figure 5.23 presents the lateral profiles of the measured and computed time averaged streamwise velocity for condition (2).

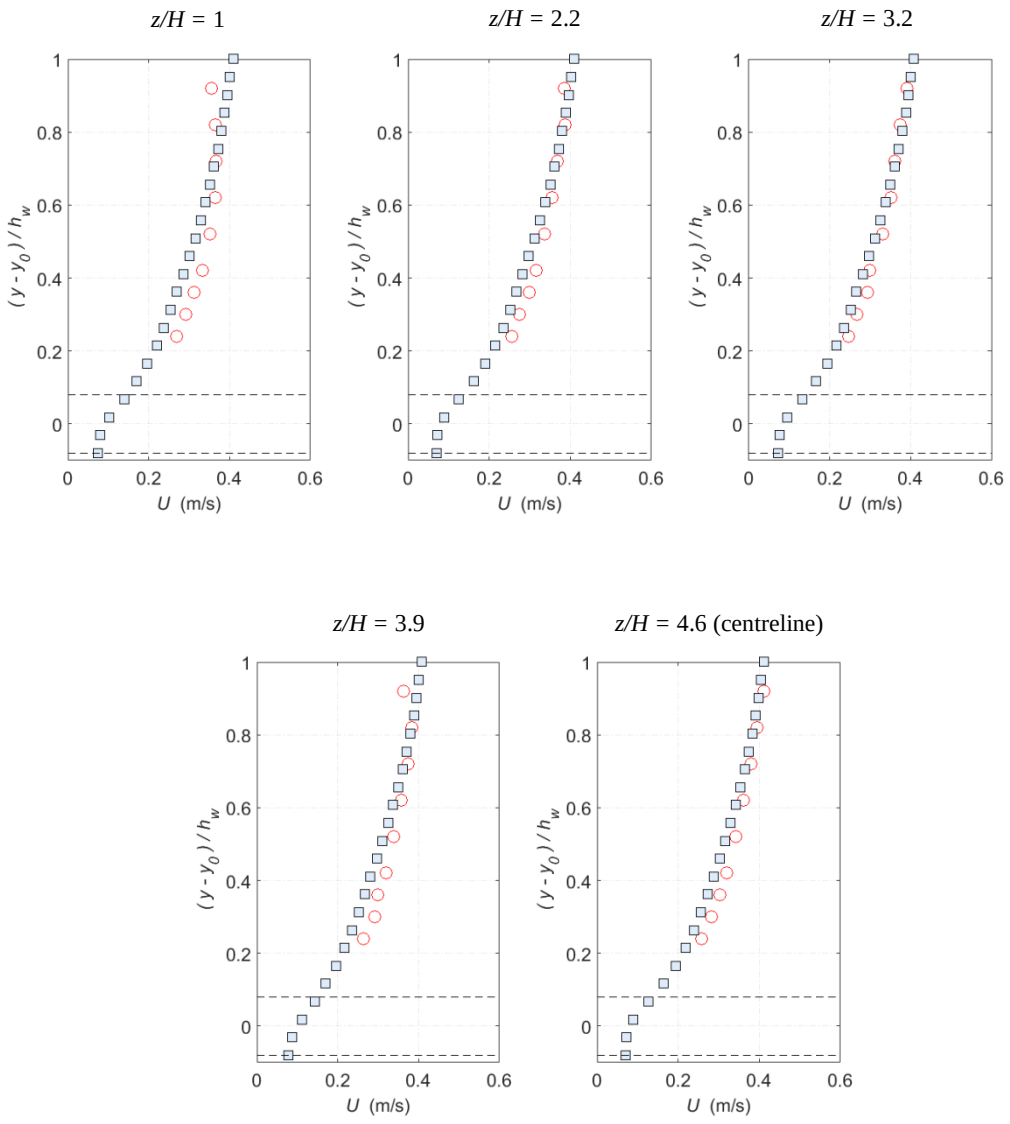

Figure 5.23 Comparisons of the lateral profiles of time averaged streamwise velocity between experimental and SPH results for condition 2 (circles: exp data; squares: SPH; dash lines: roughness top and bottom).

It can be seen that among all the compared profiles, the SPH model slightly under predicts the time averaged streamwise velocity. The MSEP between the measured and computed velocities and their gradients were calculated and plotted in Figure 5.24. It reveals that the error in *U* increases up to 2.0 % in the near bed region for all lateral profiles, while the largest error in *dU/dy* (around 15.0 %) occurs in the middle region of the flow. In the upper flow region $(y - y_0)/h_w > 0.6$, the largest error in *U* occurs in the lateral profile close the sidewall ($z/H = 1$) reaching approximately 2.0 %. This is due to the difficulty in simulating the velocity dip phenomena for this shallower condition (2), whereas the experimental velocity profile at $z/H = 1$ indicates that the velocity dip phenomena exist.

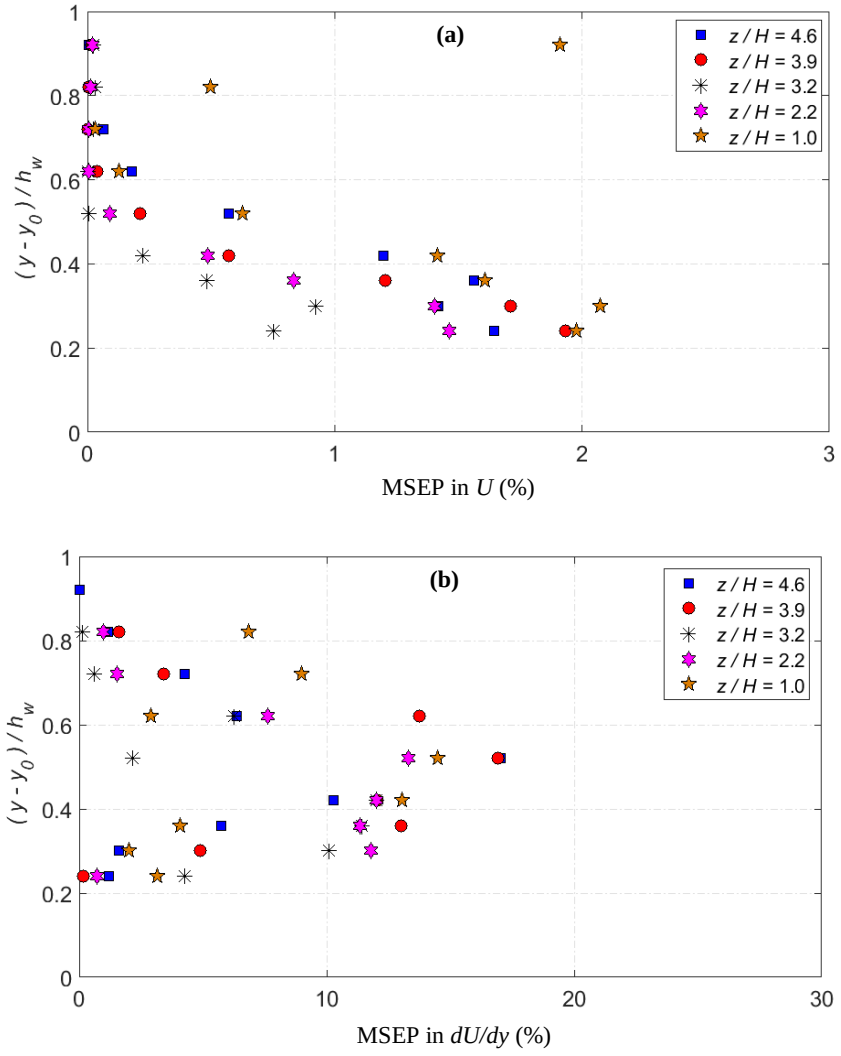

Figure 5.24 Mean square error percentage (MSEP) of (a) the streamwise velocity, (b) the streamwise velocity gradient for different lateral profiles (condition 2).

The computed lateral profiles of shear stress presented in Figure 5.25 are in good agreement with the measured and analytical profiles. However, there is a large deviation between the measured and predicted bed shear stress in region close to side wall ($z/H=1$), which was found to be approximately 22.0 % of τ_b .

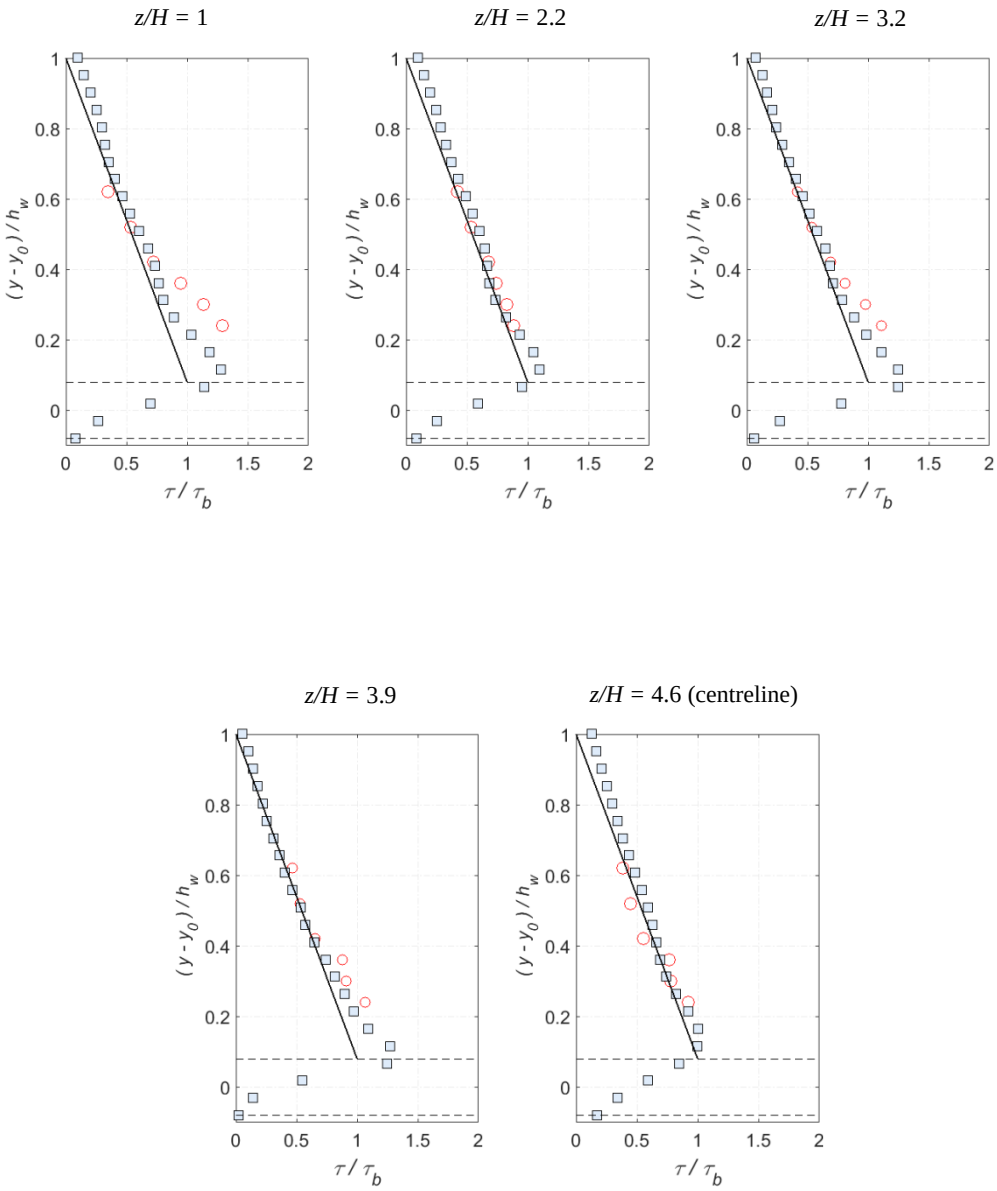

Figure 5.25 Comparisons of the lateral profiles of time averaged shear stress between experimental, analytical and SPH results for condition 2 (circles: exp data; squares: SPH; solid black lines: analytical (equation 4.6); dash lines: roughness top and bottom).

Figure 5.26 presents the lateral profiles of the measured and computed time averaged streamwise velocity for condition 8. Again a satisfactory match between the measured and computed time averaged streamawise velocity has been obtained in region away from the sidewalls. Close to the sidewall ($z/H=0.4$), the computed velocity profile becomes smaller than the measured one between $0.3<(y-y_0)/h_w<0.8$, while both profiles agree well in the near bed region and close to water surface. The MSEP in U is presented in Figure 5.27, which shows that the computed profile at $z/H=0.4$ exhibits the poorest prediction with a maximum error around 3.0 % in the middle region of the flow. This could be attributed to that the computed secondary flow was not strong enough to bulge the streamwise velocity as observed in the measured profile. This perhaps suggests that the selection of the parameter γ which controls the lateral mixing length variation in equations 5.4 and 5.5 was small, and thus generates weak secondary flows. Using a bigger value of γ results in smaller mixing length at $z/H=0.4$, and thus the flow momentum becomes higher there.

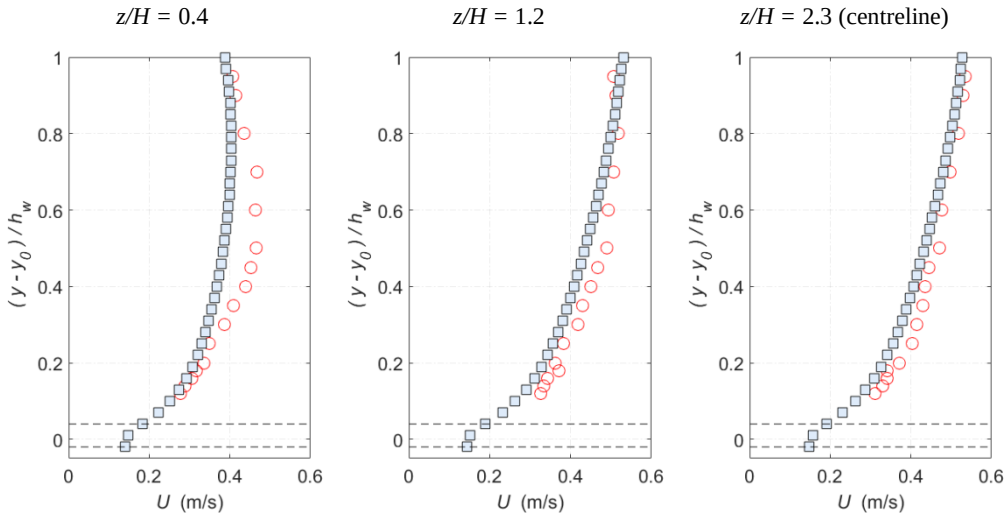

Figure 5.26 Comparisons of the lateral profiles of time averaged streamwise velocity between experimental and SPH results for condition 8 (circles: exp data; squares: SPH; dash lines: roughness top and bottom).

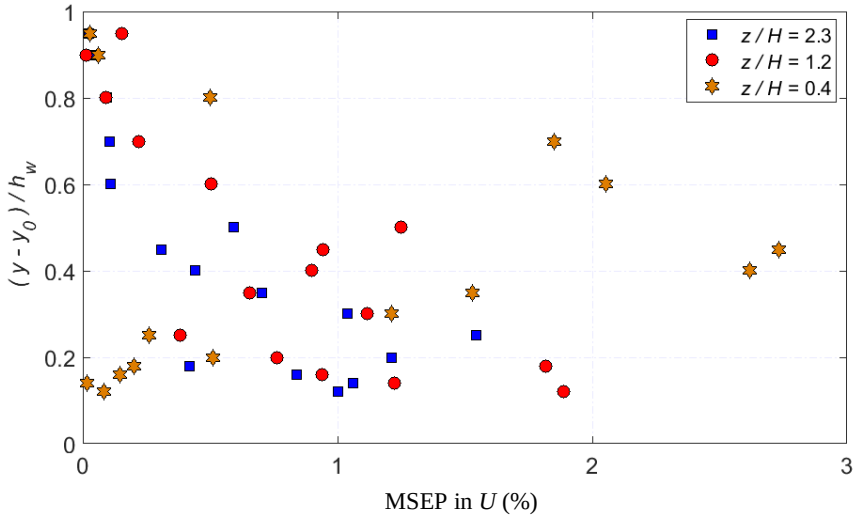

Figure 5.27 Mean square error percentage (MSEP) of the streamwise velocity for different lateral profiles (condition 8).

Additionally, the comparison of the shear stress profiles for condition 8 is plotted in Figure 5.28. It generally reveals a satisfactory agreement between the three lateral profiles. Again the maximum deviation in bed shear stress was observed in region close to the side wall ($z/H = 0.4$), which is about 26.0 % of τ_b. It is also worth noting that the measured and computed shear stress profiles at $z/H = 0.4$ become smaller than the analytical solution in the upper flow region $(y - y_0)/h_w > 0.25$, this is indeed due to the secondary flow momentum that moves from free surface towards the bed. Also the measured shear stress profile becomes zero at $(y - y_0)/h_w \geq 0.6$, whereas the computed shear stress profile becomes close to zero at $(y - y_0)/h_w \geq 0.85$. This clearly indicates that the predicted secondary flows are slightly weaker than that observed in the experiments. By using a larger value of γ, the mixing length in equations 5.4 and 5.5 becomes smaller which then results in a decrease in the shear stress in the upper flow region. Also due to the higher flow momentum transferring from free surface towards the bed, the near bed velocity gradient *dU/dy* becomes higher and thus produces larger bed shear stress.

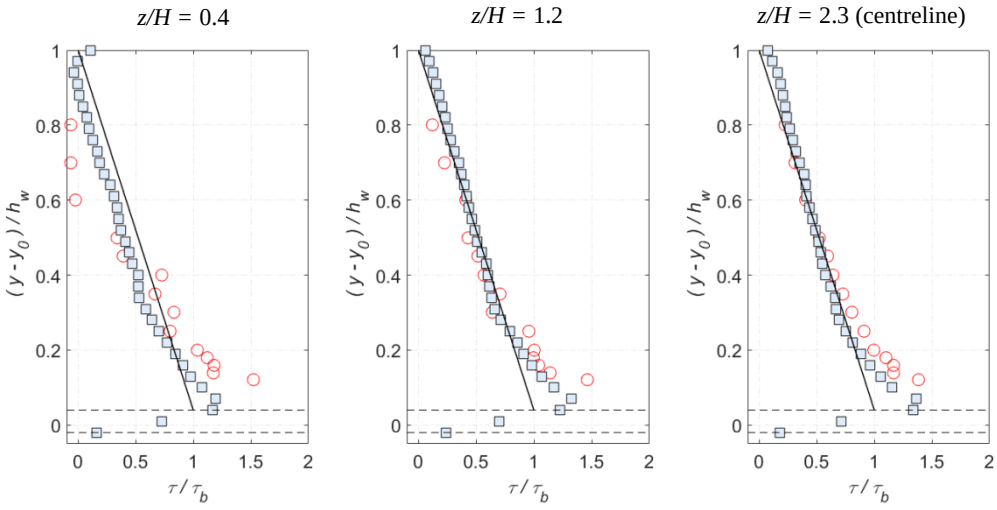

Figure 5.28 Comparisons of the lateral profiles of time averaged shear stress between experimental, analytical and SPH results for condition 8 (circles: exp data; squares: SPH; solid black lines: analytical (equation 4.6); dash lines: roughness top and bottom).

5.4 Water Surface Pattern

This section will examine the newly developed 3D SPH model in predicting the mean flow depth by comparing the predicted data with the experimental observations. The model will also be used to attempt to simulate the dynamic behaviour of the free surface and its interaction with the underlying flow.

5.4.1 Water surface identification

Similar to the 2D SPH model, the water surface elevations were extracted from the SPH particle data using the principle of the divergence of particle position (Equation 2.60). In the current 3D model, it was found that when the kernel is fully supported, the particle divergence $\nabla.\mathbf{r}$ is approximately equal to 3.0. At the free surface a value of $\nabla.\mathbf{r}$ = 1.5 was found to give the highest standard deviation of the free surface. Therefore $\nabla.\mathbf{r}$ = 1.5 was used to computed the instantaneous water surface elevations in the streamwise and lateral directions as following.

The free water surface is divided into mesh-grid points in the streamwise and lateral directions, and these grid points are equally separated by a distance $\Delta x = \Delta z = 5\,\text{mm}$. This gives a total number of 93 grid points along the lateral direction and 25 ~ 60 grid points in the streamwise directions. At each grid point *(x,z)*, several vertical locations were defined below and above the initial water surface level using a spacing of Δy = 0.01 mm. The particle divergence $\nabla.\mathbf{r}$ (Equation 2.60) was then computed at each of these locations. The vertical location which corresponds to the value closest to $\nabla.\mathbf{r}$ = 1.5 was taken as the instantaneous water surface elevation. This computation was performed over time t = 3.0 s resulting in a total of 3/0.02 = 150 sets of time series. The probability density function (PDF) of the water surface fluctuations computed by the above procedure is presented in Figure 5.29 for condition 1, 2, 5 and 8. The computed PDF's closely follow the Gaussian distribution (the red-solid lines in Figure 5.29). It is also worth noting that the computed standard deviation σ varies for each flow condition, such that it increases as the flow becomes deeper, which agrees with the experimental observations (see Figure 3.11). Here, it should be noted that the proposed 3D SPH model still predicts the standard deviation of water surface fluctuations smaller than that in the experiments. Also the standard deviation of the water surface fluctuations predicted by 3D model is smaller than that computed from 2D model. Since different sound speed value was used for each model ($c_0 = 60\,\text{m/s}$ for 2D model, and $c_0 = 20\,\text{m/s}$ for 3D model), these findings would suggest that the sound speed has an influence on the computed water surface fluctuations.

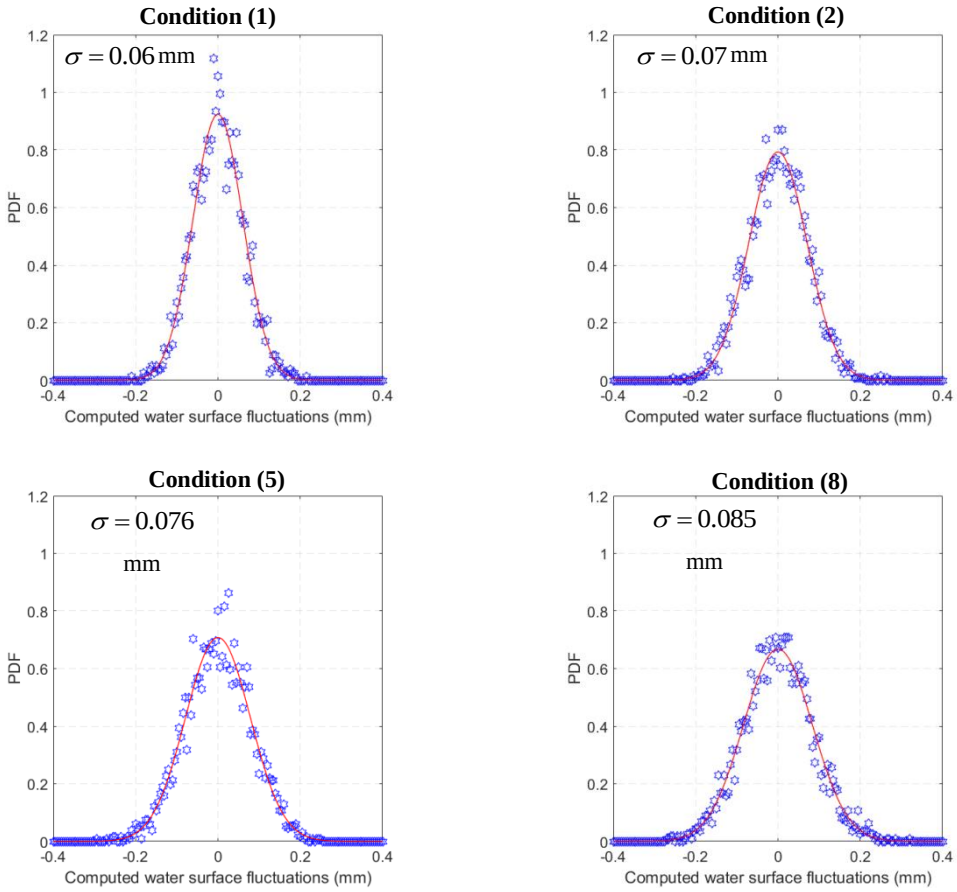

Figure 5.29 Probability density function (PDF) of the computed water surface elevations for flow conditions 1, 2, 5 and 8.

As far as the author is concerned, the possible reasons as to why the 2D and 3D models were not able to predict larger water surface fluctuations are:

(1) In the current SPH models, the drag force was used to model the effect of the rough bed rather than modelling the actual roughness geometry. This treatment may have disregarded some impact of the flow dispersion along the flow depth and hence the effect of this on the water surface fluctuations could be reduced.

(2) In SPHysics code which is based on the use of weekly compressible SPH approach, the computed pressure at the free surface is not precisely zero, due to the use of an artificial sound speed in Equation 2.45. This may influence the results when computing the instantaneous water surface elevations using the particle divergence $\nabla.\mathbf{r}$ (Equation 2.60). Therefore the sound speed value used in the 3D model may have dampened the free surface fluctuations.

(3) The use of density filtering operations in the current model to deal with numerical noise may also contribute to damping of the free surface fluctuations.

(4) Also it might be possible that in order to predict the water surface fluctuations more accurately, the computational particle size should be much smaller than the experimental water surface fluctuation size and thus the influence of the kernel averaging domain is minimized.

(5) Using smaller computational particle size means that smaller turbulent flow structures are resolved and their influence of the free surface might be observed as well.

5.4.2 Spatial distribution of the computed mean water level

The time averaged water surface elevations at each grid point were computed and plotted in Figure 5.30 for conditions 1, 2, 5 and 8. In regions very close to the side walls and the inflow and outflow boundaries (where the kernel is truncated due to the insufficient number of neighbouring particles), the computed water elevations were noisy and therefore they were removed from the plots. These contour plots shows that the mean water surface elevations are almost symmetrical in both sides of the flume without any significant numerical noise. A lateral variation of the mean water surface elevations can be observed across the flume width. For the four simulated flow conditions, the maximum mean water surface elevations occur in regions close to both sidewalls where strong secondary flow cells were observed in the previous section. Far away from both sidewalls, the variation in the mean water surface elevations becomes very small. The difference between the maximum and the minimum free surface elevations among the four conditions remains less than dx (where dx is the initial partial size).

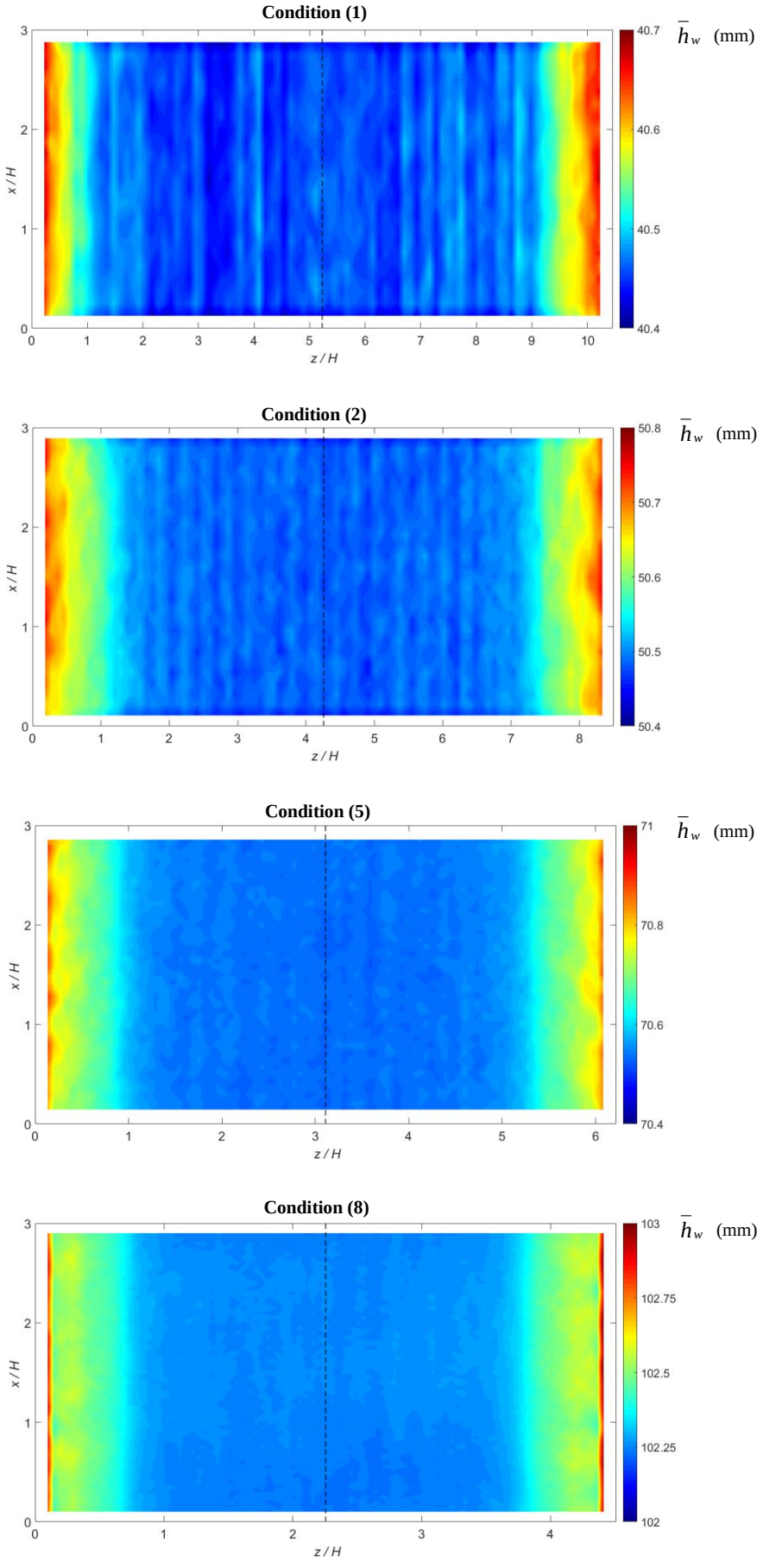

Figure 5.30 Contour plots of the computed mean free surface elevations for condition 1, 2, 5 and 8, (dashed lines: flume centreline).

Figure 5.31 presents a comparison of the computed mean water surface elevations along the flume centreline (along the black-dashed lines in Figure 5.30) with the experimental data. It reveals that the measured and predicted mean water depths are in good agreement with a maximum deviation approximately 2.0 % of the uniform flow depth.

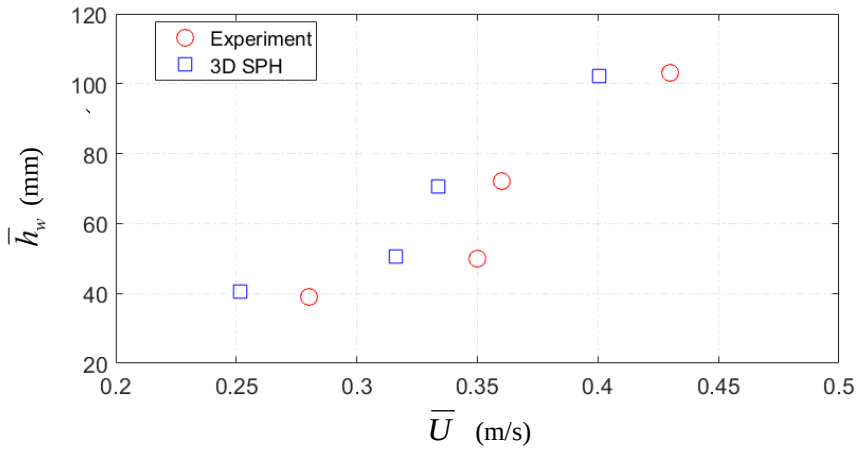

Figure 5.31 Comparisons of time-averaged water surface level vs depth averaged velocity between experimental and 3D SPH results for flow conditions 1, 2, 5, and 8.

Additionally, the mean water surface elevations measured by the two lateral wave probe arrays were compared with the computed data as presented in Figure 5.32. It shows that the experimental data collected by the two lateral arrays agree normally within 5.0 %, 5.0 %, 2.0 % and 3.0 % of the uniform flow depth for conditions 1, 2, 5 and 8 respectively. While the average errors between the predicted and measured data are 4.0 %, 5.0 %, 3.0 % and 4.0 % of the uniform flow depth for conditions 1, 2, 5 and 8, respectively.

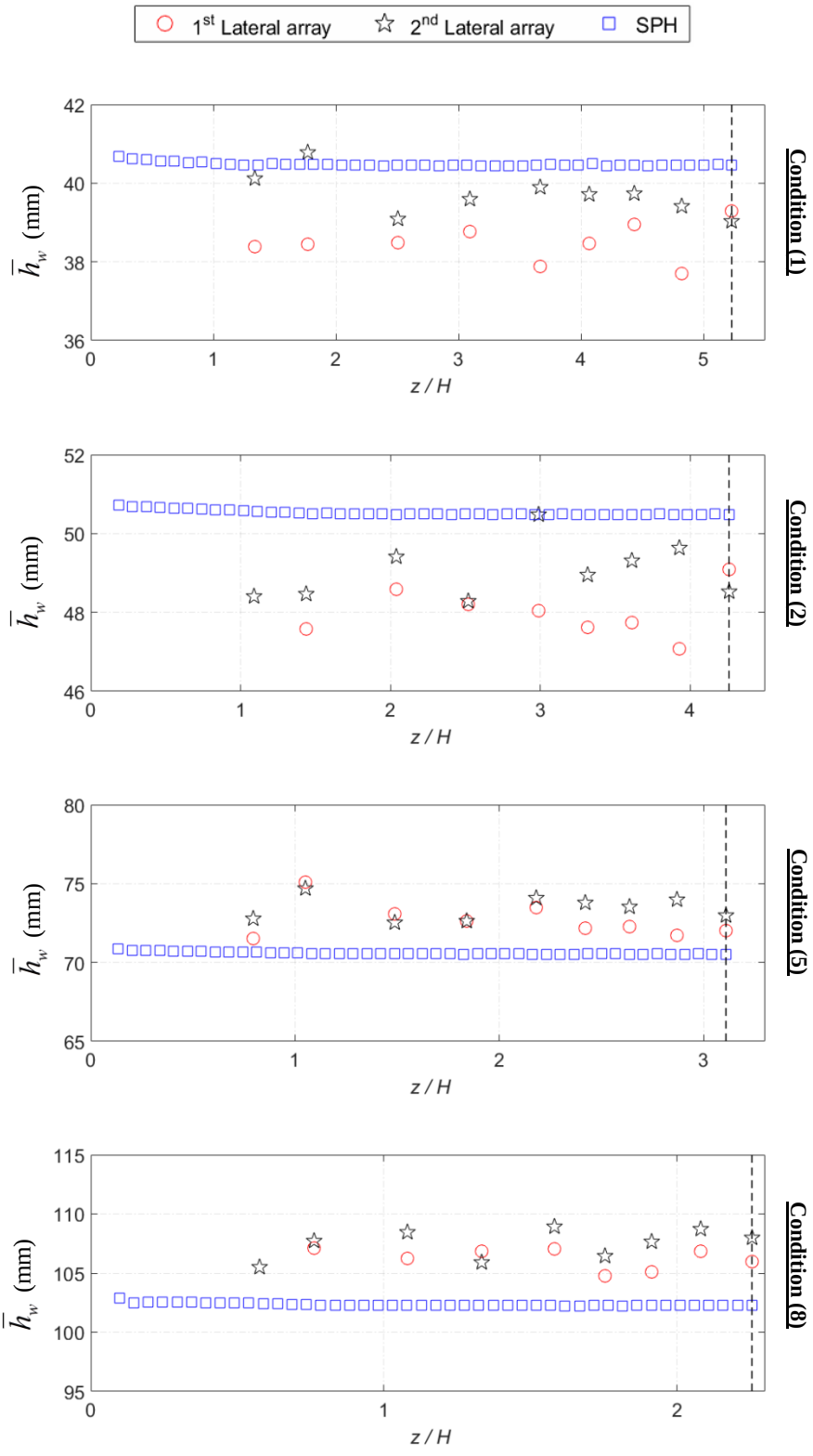

Figure 5.32 Comparisons of time-averaged water surface levels between experimental and 3D SPH results for flow conditions 1, 2, 5, and 8, (dashed lines: flume centreline).

5.4.3 Water surface pattern in the longitudinal direction

This section looks at the dynamic behaviour of the water surface along the flume centreline which is similar to procedure done in section 4.6.2. For each flow condition, the instantaneous water surface fluctuations h'_w at different streamwise locations were computed over t = 3.0 sec. The spatial-temporal field of the measured and computed instantaneous water surface fluctuations h'_w for the four simulated flow conditions are plotted in Figure 5.33 for a comparison. The black-dashed lines in Figure 5.33 represent the depth averaged streamwise velocity $\overline{U}$ listed in Table 3.1. The plots reveal that the water surface fluctuations have spatial patterns travelling with almost same orientation angles over the space and time. It can be visually judged that the slope of these patterns is very close to the depth averaged streamwise velocity $\overline{U}$. The plots also show that as the flow depth increases from condition 1 ~ 8, the spatial period of the water surface oscillations becomes longer. All of these findings are consistent with Fujita *et al.* (2011), Horoshenkov *et al*. (2013) and Nichols *et al*. (2016). It should be noted that using a much more refined particle size, longer simulation time and longer flume length would allow for more accurate water surface patterns to be simulated.

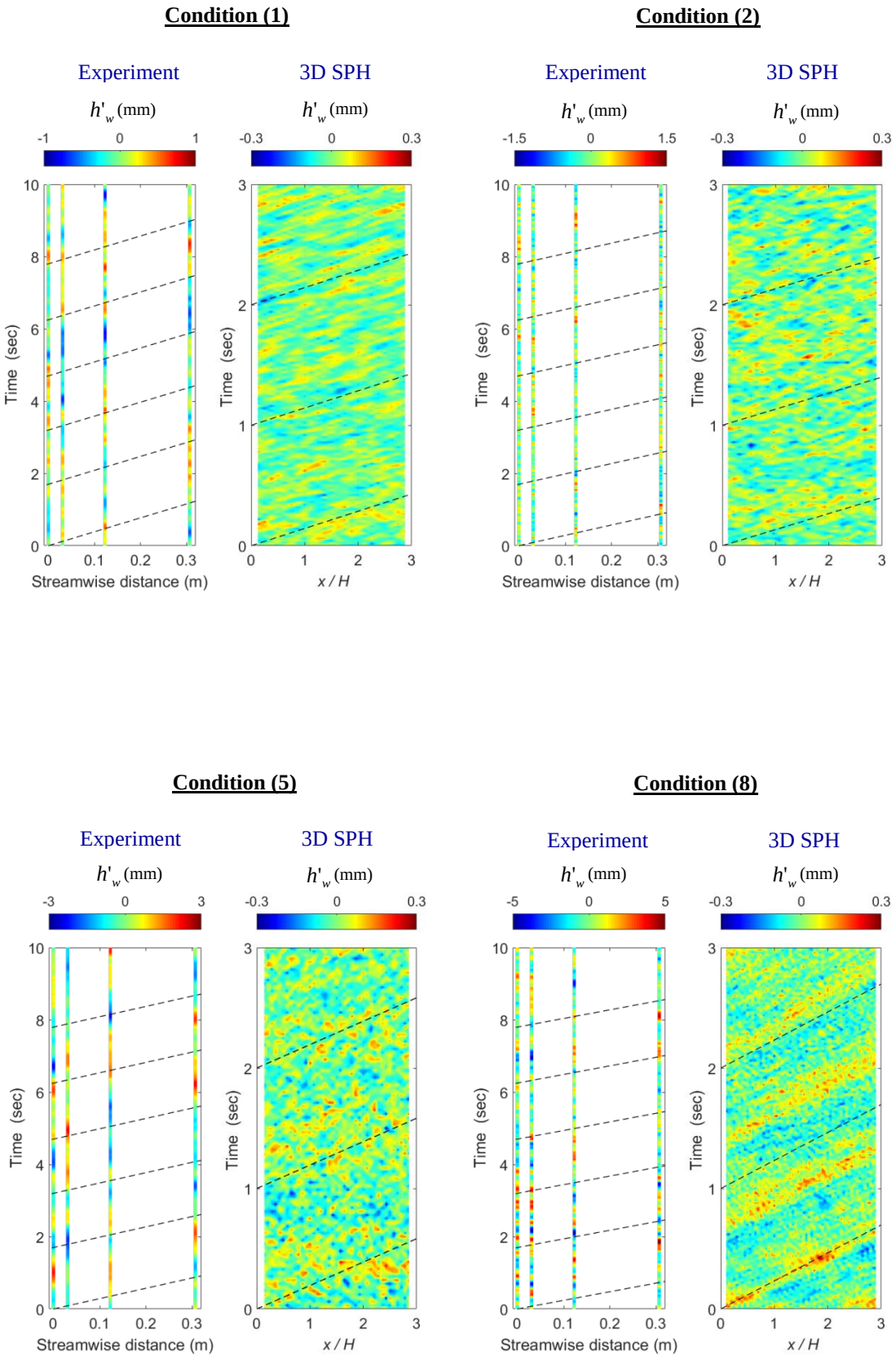

Figure 5.33 Comparisons of water surface dynamic patterns between experimental data and 3D SPH results for flow conditions (1), (2), (5) and (8) in Table 3.1.

5.4.4 Cross correlation analysis of the free surface fluctuations

This section aims to estimate the advection speed of the computed water surface fluctuations using the cross correlation analysis. In this case, the computed free surface fluctuations along the flume centreline were cross correlated using Equation 4.7 in order to obtain the extreme value (maximum or minimum). Figure 5.34 presents the contour plots of the computed space-time correlation function for the flow condition 1, 2, 5 and 8. It can be seen that the extreme value has a unity at time lag $\tau_l = 0$ and at spatial lag $x_l = 0$, then it becomes smaller as both time lag and the spatial lag increase. Now, it is possible to estimate the advection speed of the water surface as $U_{wave} = x_l / \tau_l$. It can be seen that the advection speed of the water surface (the white-dashed lines in Figure 5.34) is slightly less than the depth averaged velocity (the black-dashed lines in Figure 5.34) for the four flow conditions. The maximum deviation between the two velocities was observed in conditions 1 and 2 and it stays below 16 %. Figure 5.35 presents a comparison of the experimental and numerical temporal cross-correlation functions against the normalized spatial lag x_l / H for flow conditions (1), (2), (5) and (8). The experiment data were obtained by cross correlating the first three streamwise probes SP1 ~ SP3 giving a number of four unique pairs. While, the SPH data are the extreme values that are located along the white-dashed lines in Figure 5.34. In general though, the computed cross correlation function shows exponential decay in water surface pattern for the four flow conditions. A weak oscillatory component was observed for flow condition 1 and 2 (shallower) showing behaviour similar to their experiments. For conditions 5 and 8, the behaviour of the computed cross correlation function dose not fluctuate as observed in the experiments. This is probably due to that the particle size used in these two deeper conditions which is around 65 % bigger than the particle size used

for the shallower conditions. This indicates that the ability of the SPH model to simulate spatial patterns is dependent on the vertical resolution of the water surface predictions. It should also be noted that the spatial distribution of the wave probes is also poorer in tests 5 and 8.

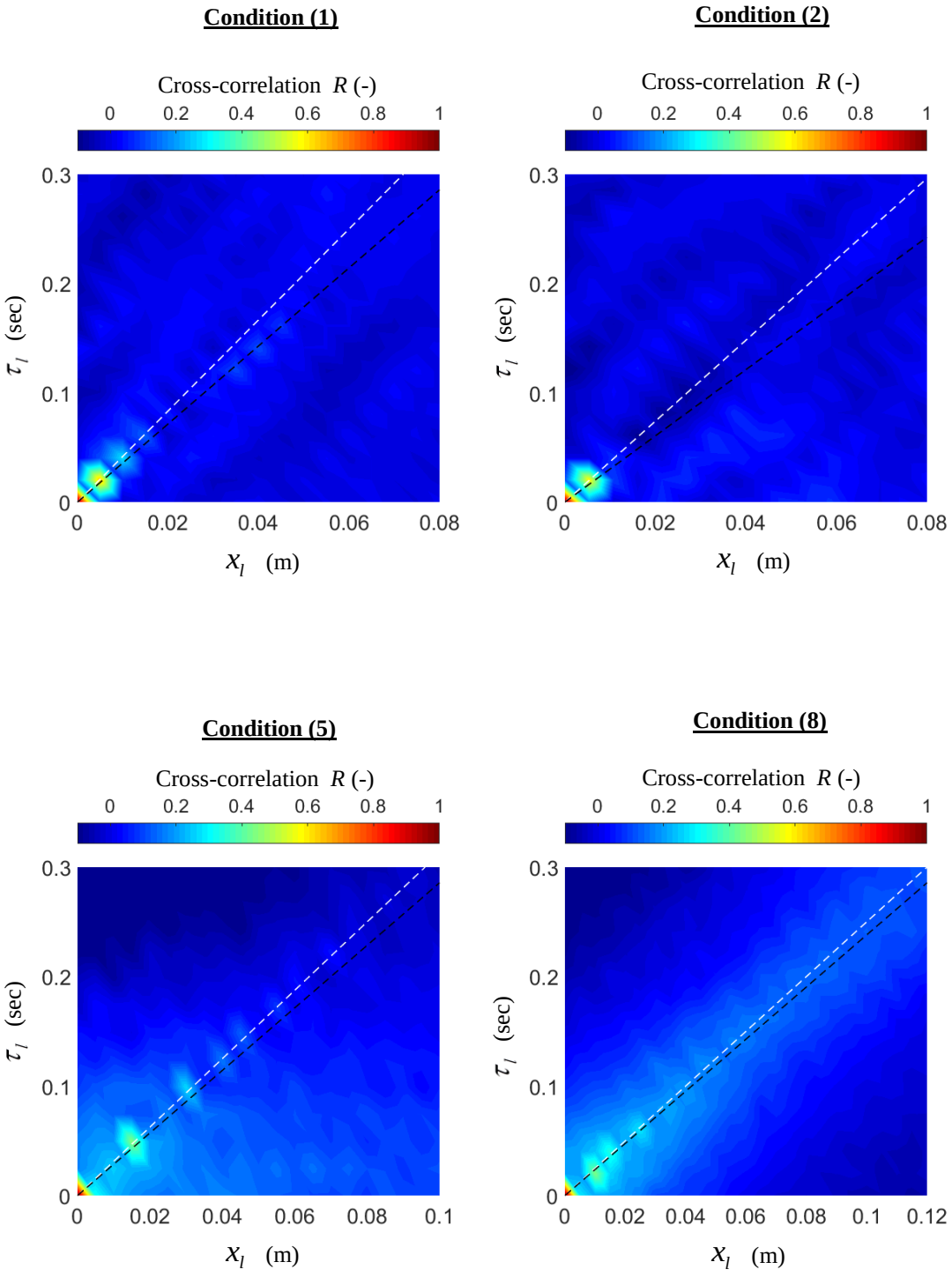

Figure 5.34 Space-time correlation function of the computed water surface fluctuations for flow conditions 1, 2, 5 and 8.

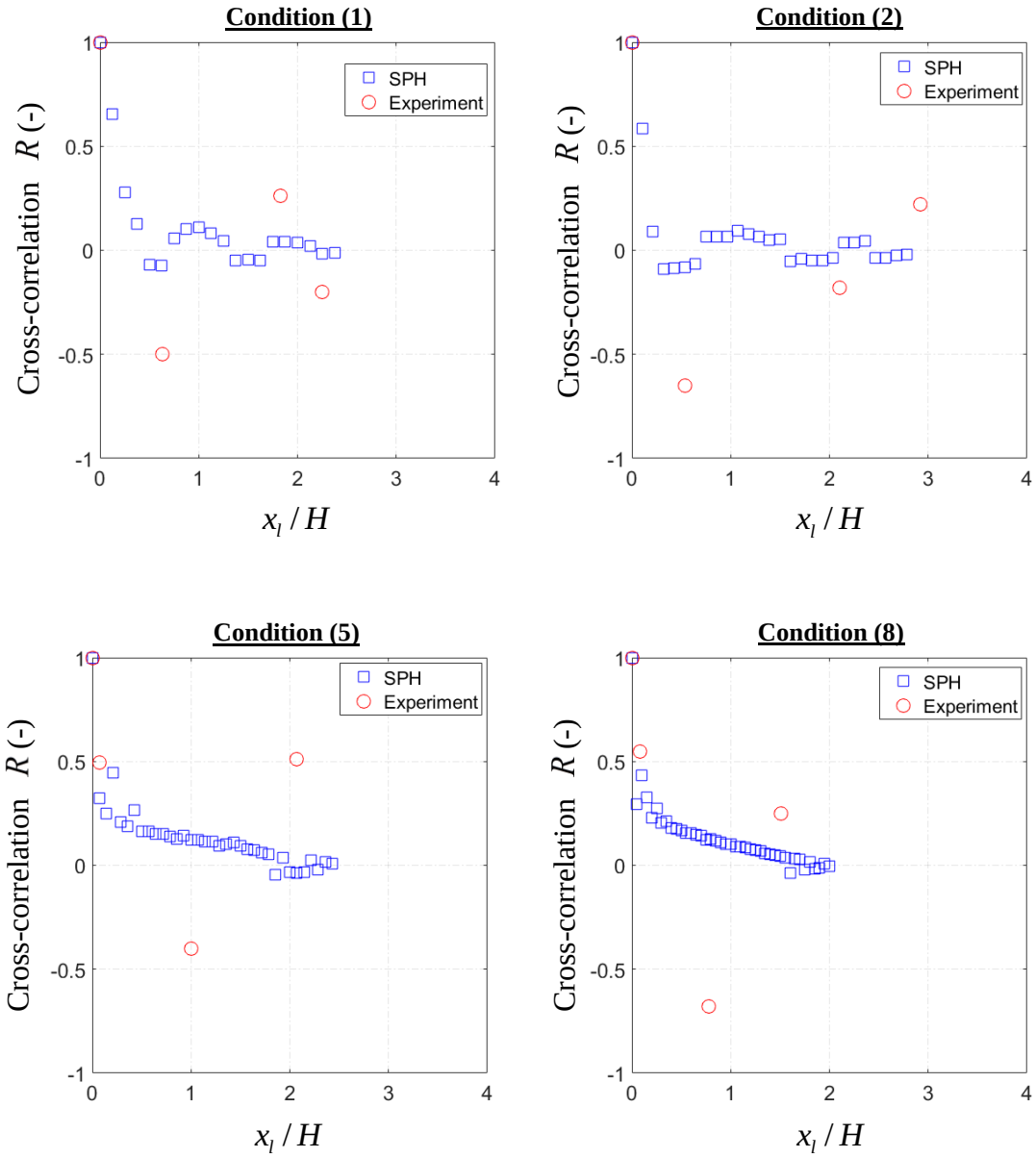

Figure 5.35 The experimental and numerical SPH temporal cross-correlations for flow conditions 1, 2, 5 and 8.

5.4.5 Correlation function of the underlying vertical flow velocity

In the previous section, it has been shown that the proposed 3D SPH model can initially simulate the free surface behaviour which was found to be closely related to the underlying main flow velocity. This section applies the spatial correlation function to the computed vertical velocity along the flume centreline and throughout the flow

depth. The implementation of this technique was similar to that used in the 2D model (see section 4.6.4). The spatial correlation function of the computed vertical velocity fluctuation is presented in Figure 5.36 for condition 1, 2, 5 and 8.

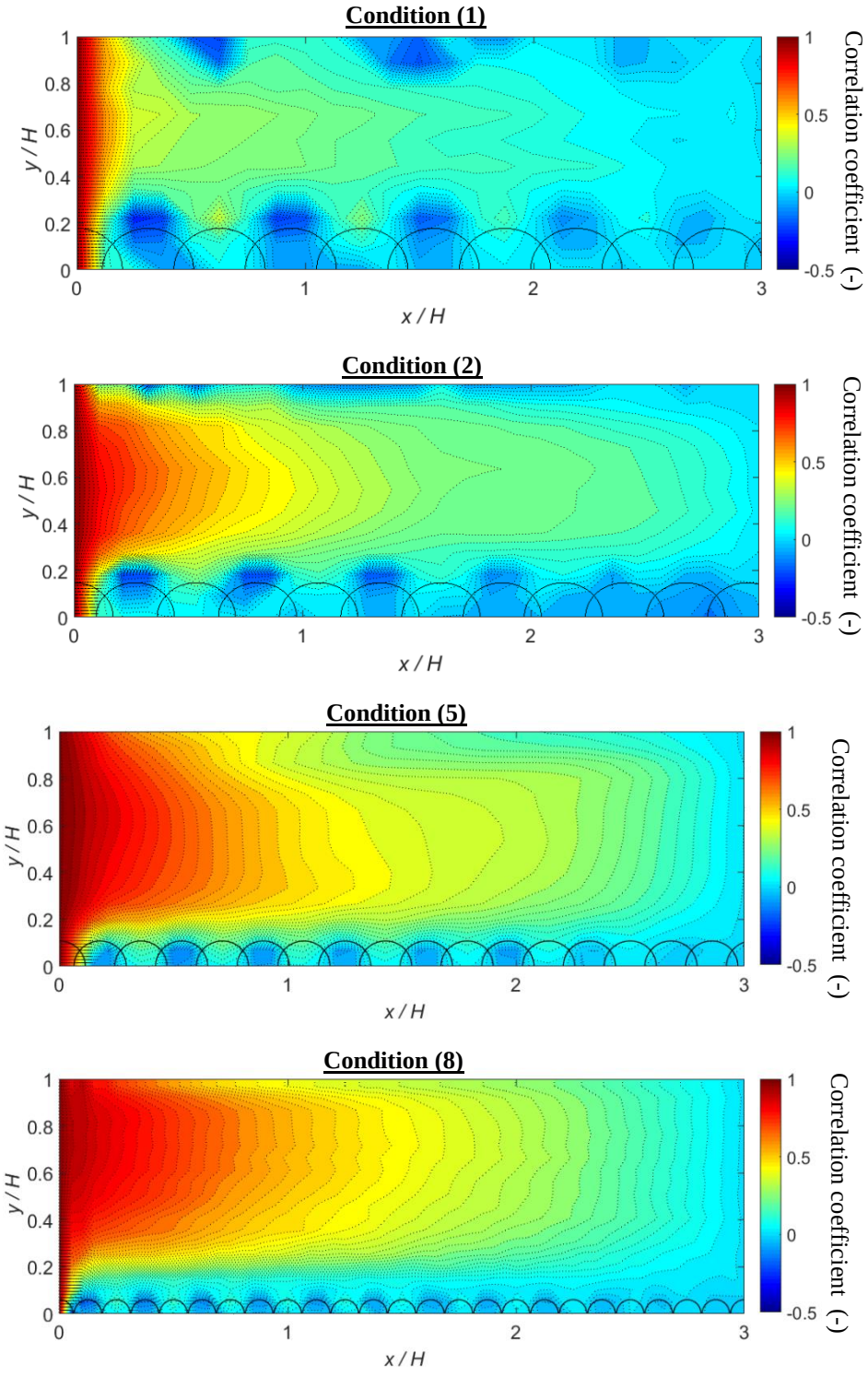

Figure 5.36 Computed spatial correlation function of the vertical velocity fluctuation over the flow depth for flow conditions 1, 2, 5 and 8.

It is apparent that the influence of the bed roughness which causes the spatial correlation plots to bulge upwards. In the middle region of the flow, the spatial correlation function declines linearly such that it reaches zero correlation at shorter distance of x/H as the flow depth becomes shallower. The spatial correlation function at the free surface exhibits an oscillatory component for condition 1 and 2 (shallower). On the other hand, the correlation functions at the free surface for condition 5 and 8 (deeper) show almost linear decay. These behaviours are in reasonable agreement with those observed in the free surface (see Figure 5.35). The deepest zero correlation at the free surface which determines the influential depth, reaches approximately y/H = 0.84 for flow condition 1. All of these numerical observations suggest that the SPH approach is capable in simulating the dynamic behaviour of free surface flows.

5.5 3D SPH Model Conclusions

This chapter has described the 3D numerical model used to investigate its potential in simulating turbulent free surface flow over rough bed. The numerical program is based on the open source code 3DSPHysics (http://www.sphysics.org). Improvements were made on the turbulence modelling, rough bed and smooth sidewalls treatments within the code. A modified sub-particle-scale (SPS) eddy viscosity model is proposed to address the 3D turbulence effect and drag force equations in the streamwise and lateral directions were included into the momentum equations to account for the effect of rough bed and smooth sidewalls. Because the turbulent flow is in a uniform steady condition, the inflow/outflow boundary was simply treated using the periodic open boundary provided by SPHysics, (Gómez-Gesteira *et al.*, 2012).

The proposed 3D numerical model was shown to be capable in simulating stable secondary flow patterns across the flume width for different flow conditions. The lateral distribution of bed shear stress has been validated against the experimental measurements with a maximum mean square error of 4.0 %. The comparison between the measured and computed profiles of streamwise velocity and shear stress at the flume centreline are in satisfactory agreement. It reveals that the error in *U* is around 0.2 % in the upper region of the flow, while in the near bed region this error becomes larger reaching up to 4.5 % for the shallowest flow condition. Among all compared profiles the maximum error in *dU/dy* was observed in the middle flow region and it remains less than 20.0 %. When the bed roughness height h_d was reduced by 6.0 % for condition 1, the maximum errors in *U* and *dU/dy* have also been minimized from 4.5 % and 15.0 % to less than 1.5 % and 10.0 %, respectively. Profiles close to the sidewall experience the largest error in the steamwise velocity and bed shear stress up to 3.0 % and 26.0 %, respectively. This was attributed to the selection of the parameter γ which defines the lateral variation of the mixing length. Thus using a bigger value of γ would generate stronger secondary flows and thus the velocity dip phenomenon is expected to occur. The sensitivity analysis using different particle size with 3D mixing length model has shown that the convergence behaviour can well be achieved. The predicted and measured mean water depths agreed to within 2.0 %. The cross correlation analysis has shown that both the measured and computed free surface fluctuations exhibit an oscillatory component for the shallower flow conditions. For the deeper flow conditions, the model was not able to show this behaviour. This was attributed to some numerical parameters such as computational particle size or speed of sound used in this model. The computational particle size used for deeper flow conditions was 65 % bigger than the size used for shallower flow conditions. This has perhaps influenced the accuracy in simulating their water surface

behaviour. The maximum error between the estimated celerity of the free surface pattern and the depth averaged velocity was found to be approximately 16.0 %. The computed spatial correlation of the vertical velocity at the flume centreline has also revealed that the free surface has an influence on the sub surface vertical velocity experienced down to approximately y/H =0.84. All of these numerical findings provide evidence that SPH model has the capability in simulating such flows if a suitable SPH particle size is selected.

CHAPTER 6 2D & 3D SPH Modelling Comparison

6.1 Introduction

In this chapter the numerical results computed by the newly proposed 2D and 3D SPH models are compared along with the experimental data measured at the flume centreline. Discussion of the results is made and the capabilities and limitations of each model will be highlighted.

6.2 Sub-Particle-Scale (SPS) shear stress

It was previously shown in this thesis that the shear stress computed by the original Sub Particle Scale (SPS) in 2D SPH model, was found to be much smaller than the experimental observations. This was attributed to several reasons, one of which is that in 2D model, the effect of the 3D uniform flow is neglected. In the 3D model, the velocity gradients appearing in Equation 5.3 will be influenced by the existence of the secondary flows presented in the previous chapter. Thus larger SPS shear stresses would also be expected. To investigate this, the SPS shear stress was computed from 2D and 3D models for flow condition 5 using same particle size (dx = 0.0025 m), and the result is presented in Figure 6.1. As might be expected, the 3D model predicts larger shear stress in the near bed region approximately $0 \le (y - y_0)/h_w < 0.4$ due to the 3D uniform flow effect. Just above the roughness top (the black-dashed line in Figure 6.1), the 3D SPS shear stress has become almost 2.25 times the value observed in the 2D model. Whereas in the upper region $0.4 \ge (y - y_0)/h_w \le 1$, both profiles are almost converged.

Although the 3D model was able to predict larger bed SPS shear stress, the value is still much smaller than the observed average bed shear stress about $\tau_{sps}/\tau_b = 5\times10^{-3}$. Also both profiles of SPS shear stress do not seem to decrease linearly towards the free surface.

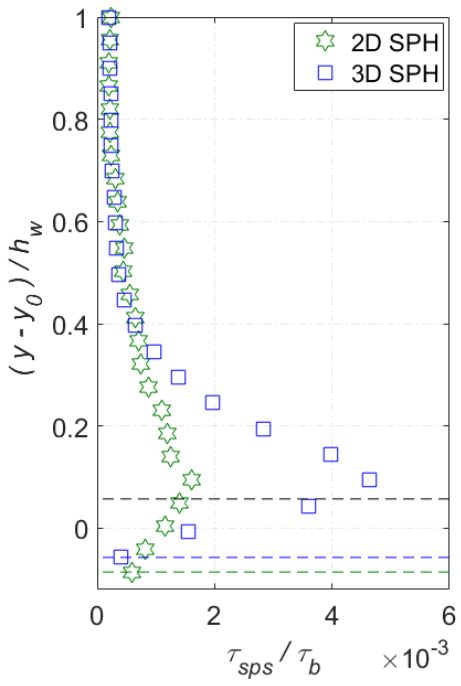

Figure 6.1 Comparisons between two shear stress profiles computed from 2D and 3D SPH models using original SPS turbulence model of Gotoh *et al.* (2001)

The reason as to why the original 2D and 3D SPS model did not provide large shear stress in the current application could be attributed to that the magnitude of the relevant processes in turbulent open channel flows and coastal hydrodynamics are different. In turbulent open channel flow the bed roughness is a much more dominant factor which produces many energetic flow structures throughout the flow depth. In order to resolve these turbulent structures by the original SPS model, the physical rough bed which causes more flow dispersion throughout the flow depth should be modelled. In this thesis, the effect of rough bed was microscopically modelled using a

drag formula neglecting the flow dispersion caused by rough bed elements. This treatment may have resulted in missing part of the turbulent structures. Also the density filter as well as the kernel averaging schemes used in the current models may contribute to this issue. Turbulent flow structures results in local pressure fluctuations and as the density filter removes pressure fluctuations, this could potentially suppress smaller turbulent structures. The density filter is needed in order to achieve numerical stability so cannot be removed. Currently because it is difficult to model the physical rough bed as it requires a much more refined particle size to be used, the missing part of turbulent structures was accounted for by modifying the turbulent eddy viscosity v_t based on Smagorinsky in Equation (4.1) with a mixing length model which more physically represents the turbulent eddies' size and motion in open channel flow with a fixed boundary.

To check the modified 2D and 3D SPH models in terms of turbulence prediction, the turbulent spectra of the measured and modelled streamwise and vertical velocities have been studied for flow condition 2. This was performed at a vertical location $(y-y_0)/h_w = 0.24$. The results are presented in Figure 6.2 which shows the comparisons of the measured and modelled data along with the Kolmogorov's $-5/3$ law. It can be visually judged that there is a loss of energy in the simulated data in frequencies in the 3 ~ 10 Hz range. Above a frequency of 10 Hz, the expected energy loss with frequency is not observed. This mismatch between the measured and simulated spectra could be attributed to the computational particle size used, as well as the density filter applied to the current model. More-in-depth studies are needed to investigate this issue.

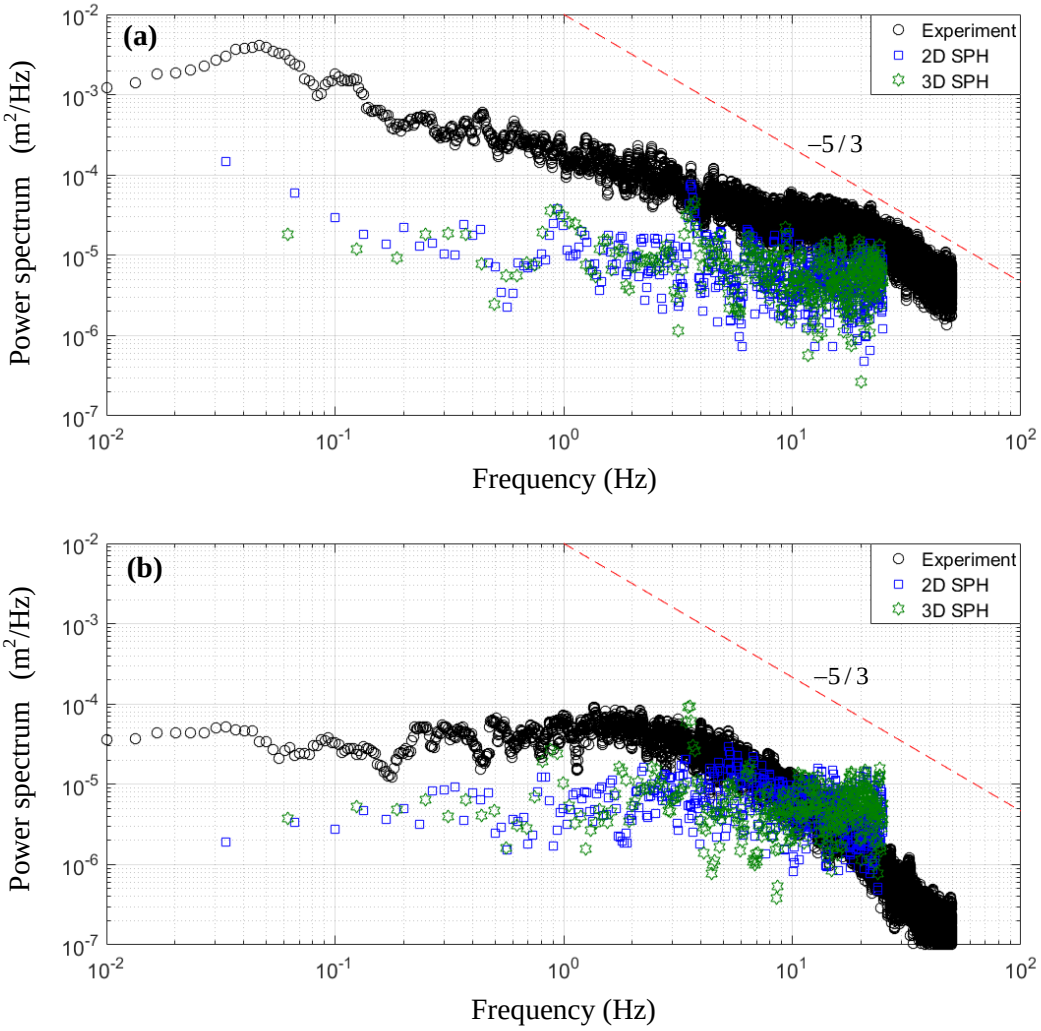

Figure 6.2 Measured and modelled power spectrum of (a) streamwise velocities; (b) vertical velocities for flow condition 2 (dash red-lines: Kolmogorov's $-5/3$ law).

6.3 Streamwise velocity profiles

The measured and computed streamwise velocity profiles at the flume centreline are presented in Figure 6.3. The black, green and blue dashed lines are corresponding to the roughness top, roughness bottom in 2D model and roughness bottom in 3D model, respectively. As mentioned before, the roughness height h_d in the 3D model was chosen to be slightly smaller than that used in the 2D model in order to obtain the best match with the experimental profiles. This selection actually makes physical sense because in the 3D flow, the flow momentum is removed in the streamwise and lateral

directions due to the presence of obstacles. When the flow is 2D, the flow momentum is only removed in the streamwise direction. Therefore it is expected that using smaller roughness height in the 3D model would provide better match with the experimental profiles. Nevertheless, the selection of the roughness height in both models is still within the range of $0.15D \sim 0.35D$ widely reported in literature (Einstein & El-Samni, 1949; Bunco & Partheniades, 1971; Grass, 1971; Cheng & Clyde, 1972 ;Nakagawa *et al.*, 1975; Bayazit, 1976). For the four simulated flow conditions in Figure 6.3, the velocity profiles predicted by 2D and 3D models almost overlap in the upper region of the flow approximately $0.6 \geq (y - y_0)/h_w \leq 1.0$. In this region the maximum MSEP was found to be less than 0.2 % for both models (see Figures 4.8(a) and 5.14(a)). In the inner flow region $0 \leq (y - y_0)/h_w < 0.6$, the velocity profiles of the 2D model show better agreement with the experiments with a maximum MSEP being less than 1.0 %. On the other hand, the 3D model velocity profiles experience slower velocity resulting in a maximum MSEP of 4.5 % for flow condition (1). This shows that the proposed roughness bed in 3D model removes more flow momentum near the bed although same drag coefficient $C_d = 0.8$ was used in both models. Additionally, the 2D model profiles reveal that the largest errors in the velocity gradient *dU/dy* occur very close to the bed reaching approximately 12.0 %, while the 3D model profiles exhibit larger errors in *dU/dy* in the middle region of the flow which was around 20.0 %. The larger errors in *U* and *dU/dy* quantified from 3D model were attributed to the roughness height h_d used being slightly larger. When h_d is reduced by 6.0 % for flow condition (1), the maximum MSEP in *U* and *dU/dy* were minimized to 1.5 % and 10.0 %, respectively. It is also believed that these errors might be minimized by selecting slightly smaller roughness height for the other flow conditions.

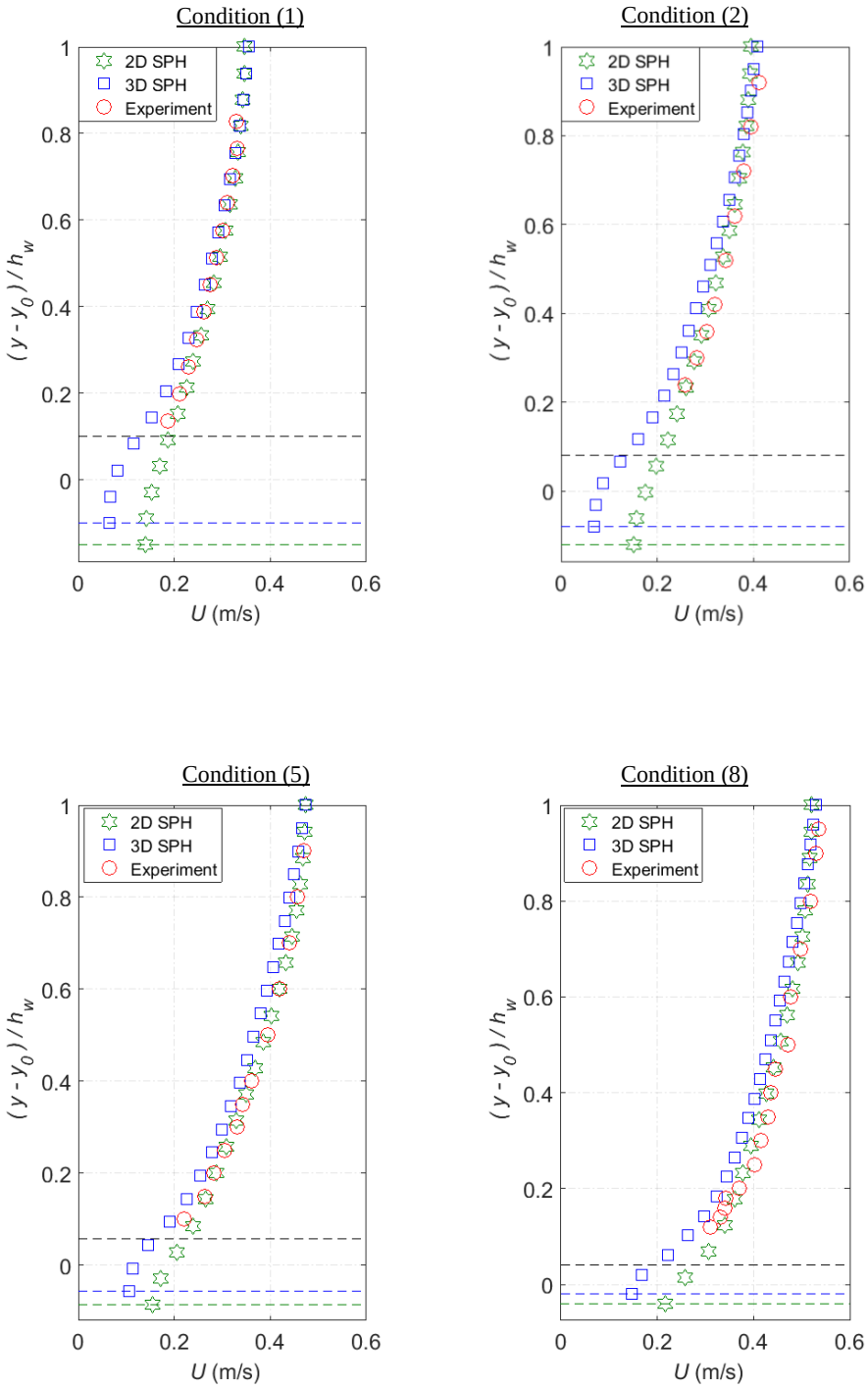

Figure 6.3 Comparisons between 2D SPH, 3D SPH and experimental time-averaged velocity profiles at the flume centreline for condition 1, 2, 5 and 8.

Another factor which plays important role in predicting more accurate results is the selection of the initial computational particle size. It is recommended that the diameter of the influence domain ($4h$) should be smaller than the physical mixing

length l_m. In the near bed region $0 \le (y - y_0)/h_w < 0.25$, l_m is approximately defined as $l_m = \kappa y$, which means that l_m at the roughness top could be approximated as $l_m = \kappa h_d \approx$ 0.003 m ~ 0.004 m. This size is almost two times smaller than $4h$ (4×1.5×0.0015 = 0.009 m). Thus the selection of the computational particle size may also have influenced the results especially in regions close to the bed where the velocity gradient is higher.

6.4 Shear stress profiles

Shear stress is an important factor considered in this research study. The shear stress profiles at the flume centreline computed by the modified 2D and 3D models are plotted together with the measured profiles in Figure 6.4 for a comparison. It generally shows that the 3D shear stress profiles are in better agreement with the experimental and analytical profiles. This indicates that the newly developed 3D bed roughness elements can sufficiently reflect the effect of the physical roughness size. It also shows that the use of the proposed 3D mixing length model can well represent the transformation of the bed roughness effect along the flow depth. On the other hand, the 2D model reveals that the shear stress profiles are under predicted for the four flow condition, and the match with the experimental and analytical profiles becomes worst for the shallower flow conditions. This is perhaps due to insufficient drag force which produces smaller velocity gradient in the roughness interface and thus producing smaller shear stress. This can also be observed in Figure 6.3 that the 2D velocity profiles exhibit smaller velocity gradient compared with the experimental and 3D profiles. The maximum value of bed shear stress predicted by 2D model varies between $0.7\tau_b$ ~ $0.8\tau_b$, while the maximum value of shear stress predicted by 3D model is within $1.0\tau_b$ ~ $1.35\tau_b$.

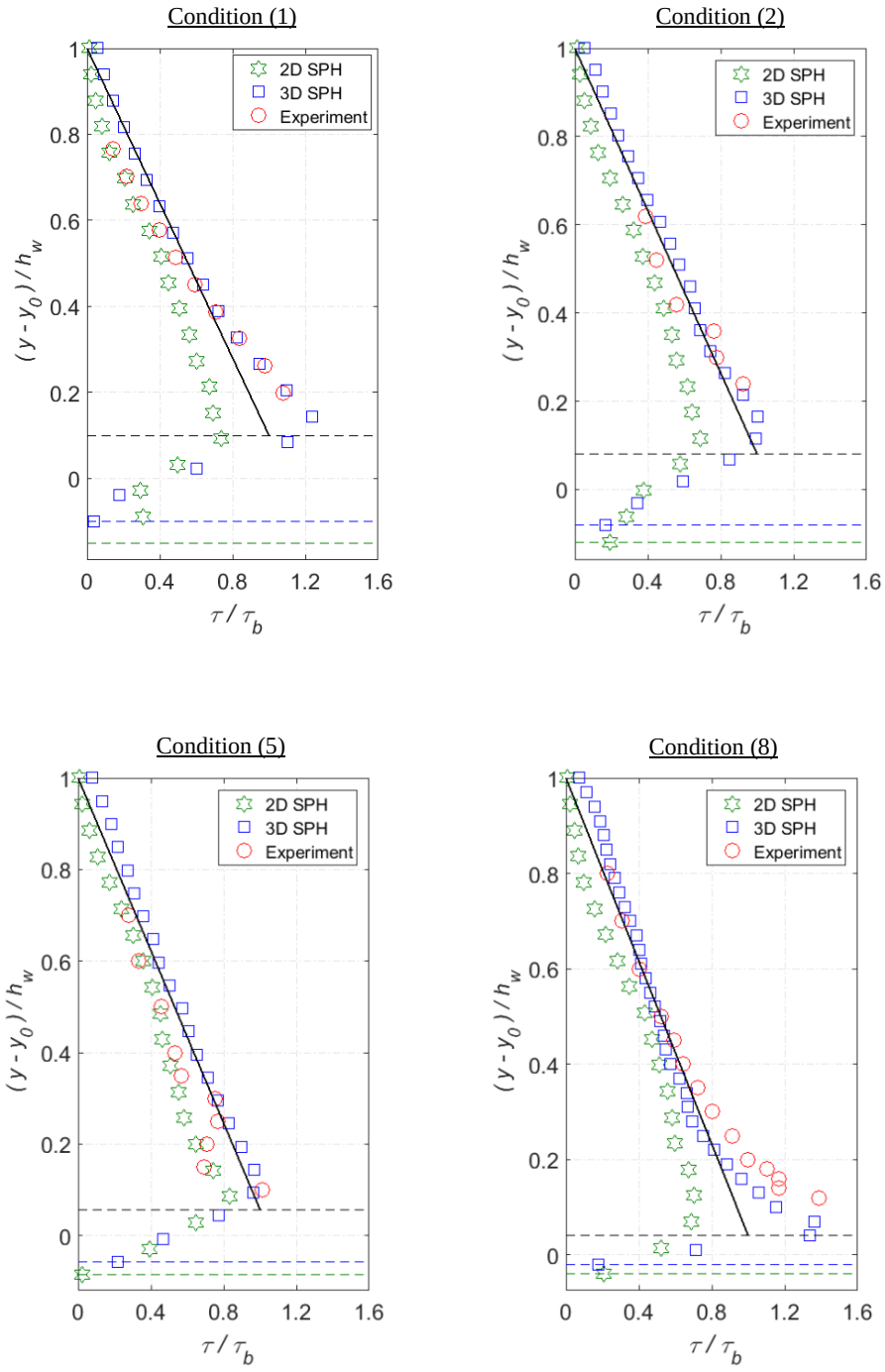

Figure 6.4 Comparisons between 2D SPH, 3D SPH and experimental time-averaged shear stress profiles at the flume centreline for condition 1, 2, 5 and 8, (black sold lines: analytical solution (Equation 4.6)).

6.5 Free surface behaviour

As well as studying the underlying turbulent flow structures, the dynamic behaviour of the free surface and its interaction with the underlying flow were also studied in 2D and 3D models. The proposed 2D model shows that as the flow depth increases from

flow condition 1 ~ 8, the computed time-averaged water surface level becomes more less than the measured time-averaged water surface level. The maximum deviation was observed in condition 8, which was about 5.0 % of the uniform flow depth. This under prediction could also be one of the reasons to why the 2D bed shear stress discussed in the previous section becomes around 25.0 % smaller than τ_b. On the other hand, a better agreement between the predicted and measured time-averaged water surface elevations has been achieved by the 3D model with a maximum deviation approximately 2.0 % of the uniform flow depth. This shows that the combination of the proposed bed and sidewall roughness described in Chapter 5 gives almost the correct mean flow depth. Additionally, it was found that the probability density function (PDF) computed by the two models follows the Gaussian distribution. However, the water surfaces fluctuations computed by 2D and 3D models were found to be much smaller than the measured data for the four flow conditions. It was also found that the 3D free surface fluctuations are smaller than that in 2D model. This was attributed to the fact that the sound speed c_0 value influences of the free surface fluctuation magnitude, since different sound speed were used as $c_0 = 60$ m/s in 2D model and $c_0 = 20$ m/s in 3D model. In the 3D model it was not possible to use a bigger value of c_0 due to the CPU constraint, and thus it is recommended to check the performance of the 3D model under bigger values of c_0. Despite the fact that the 3D model was not able to predict larger water surface fluctuations, it is worth noting that the predicted water surface standard deviation increases as the flow depth also increases (see Figure 5.29). This tendency is consistent with the experimental PDF's presented in Figure 3.11. Whereas this is not the case with the 2D model which shows that the water surface standard deviation is almost constant for different flow conditions. This perhaps due to that fact that the

flow in 2D model is restricted in the lateral direction which then may results in random free surface fluctuations size. In the 3D model, the simulated secondary flow has been found to vary within $0.012\overline{U}$ ~ $0.02\overline{U}$ such that it becomes larger as the flow becomes deeper. Thus it could be argued that the effects of these secondary flows on the free surface also result in different water surface fluctuations for different flow conditions. In additional to this, both models were able to simulate almost similar spatial pattern of water surface fluctuations as observed in the experiments (see Figures 4.18 and 5.33). The gradient of these patterns was approximately found to be related to the depth averaged flow velocity. This was further examined using the cross correlation technique which measures the amplitude of the coherence and variance in water surface fluctuations at different locations. In 2D model, it was found that the error in estimating the celerity of the computed free surface patterns increases as the flow depth becomes shallower reaching up to 27.0 % of the depth averaged velocity. Similar tendency was also observed in the 3D model with less error being 16.0 % of the depth averaged velocity. The computed 2D and experimental cross correlation functions, however, were found to behave in a similar way (see Figure 4.19). In the 3D model, the computed and measured cross correlation functions reveal a good agreement for condition 1 and 2 (shallower), while for condition 5 and 8 (deeper) the computed correlation functions do not fluctuate (see Figure 5.33). For these two deeper conditions, the computational particle size was used as dx= 2.5 mm, which is 65 % bigger than the size used for the shallower conditions. This particle size gives a kernel of influence ($4h$ = 4×1.5×2.5 = 15.0 mm) that is 15.0 % larger than the distance between two wave probes (13.0 mm) in the experiment. This perhaps could be one reason why the correlation functions do not fluctuate for the deeper flow conditions. It could also be attributed to the value of sound speed being smaller than the value used for the 2D model, which may have

dampened the free surface fluctuations. The influence of the speed of sound can clearly be seen by comparing the 2D and 3D correlation functions of the shallower flow conditions since same spatial resolution was used in both models. It shows that a smaller value of sound speed dampens the magnitude of the cross correlations functions.

The cross correlation analysis was further used to examine the interaction between the free surface and the vertical velocity throughout the flow depth. The most interesting observation in both models was the behaviour of the spatial correlation of the vertical velocity fluctuation at the free surface. It was shown that the spatial correlations of the vertical velocity fluctuation have spatial periods that are closely match the spatial periods of their free surface. The depth of influence was estimated as the distance corresponding to the deepest zero correlation of the vertical velocity fluctuation. It was found that the influential depth experiences down to a depth of approximately $y/H = 0.93$ and $y/H = 0.84$ in the 2D and 3D models, respectively. The influence depth becomes slightly larger in the shallower flow conditions. One argues that this could be the reason as to why shallower flow conditions experience larger error in estimating the speed of the free surface patterns demonstrated in the previous section.

The comparisons in sections 6.3, 6.4 and 6.5 have shown that the 3D model is more accurate in predicting the flow velocity and shear stress, as well as simulating the dynamic behaviour of the free surface. It has been shown that the profiles of velocity and shear stress computed by 3D model are in better agreement with both the experimental and analytical profiles. This is due to the inclusion of new roughness treatment of the bed and both sidewalls, and also due to the developed mixing length model applied across the channel. When the bed roughness height in 3D model was

slightly reduced, the difference between 2D and 3D models in predicting the streamwise velocity was found to be very small. However, 2D model was found to under predict the shear stress profiles quite significant. It has also been shown that the dynamic behaviour of the free surface could be more accurately simulated by the 3D model although smaller sound speed was used.

6.6 CPU time

The 2D and 3D SPH numerical simulations in the current research have been performed on PC with an Inter® Core(TM) i7-4770 CPU 3.4 GHz and 32.0 GB of RAM running a 64-bit version of windows. Table 6.1 presents a comparison of the total CPU time required for flow conditions 1, 2, 5 and 8 in 2D and 3D models.

Table 6.1 Comparison of total CPU time between 2D and 3D SPH models.

Flow condition			**(1)**	**(2)**	**(5)**	**(8)**
2D SPH	Total simulation time (130 sec)	Total number of particles	4123	5054	6916	9177
	$C_{CFL} = 0.15$ $c_0 = 60$ m/s	Total CPU time (days) `	5.0	6.0	8.0	11.0
3D SPH	Total simulation time (6.0 sec)	Total number of particles	800000	953000	506000	980000
	$C_{CFL} = 0.15$ $c_0 = 20$ m/s	Total CPU time (days)	60.0	70.0	40.0	80.0

CHAPTER 7 **Final Conclusion & Future Work**

7.1 Introduction

The aim of this research was to develop 2D and 3D numerical models based on Smoothed Particle Hydrodynamics (SPH) approach that could be used to predict the flow velocity, shear stress and free surface behaviour in turbulent open channel flows over rough fixed bed. To validate these numerical models, experimental measurements of flow velocity and free surface elevations were carried out for a range of steady uniform flow conditions which cover a range of Froude Numbers. Here the results of the newly developed 2D and 3D numerical models and their comparison with the experimental measurements will be summarized and recommendations for future work will be addressed.

7.2 Summary of 2D SPH numerical findings

- The proposed 2D model shows a reasonable performance in predicting the streamwise velocity U and velocity gradient dU/dy in the upper region of the flow. In the near bed region, the model prediction becomes poor showing a maximum square error of 2.5 % and 12.0 % for U and dU/dy, respectively.

- The vertical profiles of the measured and computed shear stress based on the mixing length approach show that there is a large deviation in region just above roughness top. The computed bed shear stresses were found to be around 25.0 % smaller than the averaged measured bed shear stress τ_b.

- The sensitivity analysis using two different SPH particle sizes (0.5 mm difference) shows the convergence of the 2D numerical model.

- The comparison between the measured and predicted time averaged water depths is in good agreement. The quantified error was found to increase as the flow becomes deeper reaching up to 5.0 % of the uniform flow depth.

- Although the computed water surface fluctuations were found to be smaller than the experimental observations, the proposed 2D model was able to simulate the spatial patterns of the free surface fluctuations. These patterns exhibit positive and negative elevations that are travelling with almost same orientation angles over time and space. The slope of these patterns was found to be related to the mean bulk flow velocity.

- The computed and measured cross-correlation functions of the water surface fluctuations for different time lags τ_l were found to behave in a similar way. It was also found that the error in estimating the celerity of the computed free surface patterns increases approximately from 6.0 % ~ 27.0 % of the depth averaged flow velocity as the flow depth becomes shallower.

- The spatial correlation function of the vertical flow velocity over the flow depth has shown that the sub-surface flow is affected by the dynamic behaviour of the free surface down to a depth of approximately $y / H = 0.93$.

7.3 Summary of 3D SPH numerical findings

- The comparison between the computed 2D and 3D shear stress profiles based on the original Sub Particle Scale (SPS) model was presented. It has revealed that the 3D SPS shear stress becomes approximately 2.25 times larger than the 2D SPS shear stress in region close to the bed. In the upper flow region, both 2D and 3D SPS shear stress profiles almost overlapped.

- Both 2D and 3D SPS bed shear stresses were found to be much smaller than the value of τ_b, approximately $\tau_{SPS} = 0.005\,\tau_b$. This was attributed to that the SPS model does not provide the correct shear mechanism in open channel flows over rough boundaries with higher Reynold Number. When the turbulent eddy viscosity was modified with a mixing length approach which represents a more physically turbulence damping mechanism, much more realistic shear stress profiles were obtained.

- The spectra of the simulated streamwise and vertical velocities has shown that there is a loss in turbulent energy in 3 ~ 10 Hz frequency range. Above 10 Hz the higher frequency velocity fluctuations do not show a reduction in the turbulent energy. This pattern was attributed to the averaging effect of the particle size as well as the density filter used in the current SPH models.

- The proposed 3D model was found to under predict the flow velocity in the near bed region resulting in a maximum square error of 4.5 %, while the maximum error in the velocity gradient occurs in the middle flow region reaching to around 20.0 %. When the bed roughness height was slightly reduced by 6.0 %, the maximum errors in the velocity and its gradient were

minimized approximately to 1.5 % and 10.0 %, respectively. This clearly demonstrates the importance of accounting for the bed roughness.

- The sensitivity analysis using two different SPH particle sizes (0.5 mm difference) has shown that the vertical profiles of streamwise velocity and shear stress are almost converged.
- The 3D model was also able to simulate the secondary flow patterns such that the secondary flows become stronger as the aspect ratio decreases. The comparison between the measured and predicted bed shear stress distributions reveal a good agreement with a maximum mean square error stays below 4.0 % of the averaged measured bed shear stress τ_b .

- The computed and measured lateral profiles of steamwise velocity reveal a satisfactory match. Profiles close to the side wall experience the poorest agreement. This was attributed to the selection of the parameter $\gamma = 0.5$ (which controls the lateral distribution of the mixing length) was not appropriate. It is expected that using bigger value of γ would generate stronger secondary flows near the side walls and thus the velocity dip phenomenon starts to appear.

- The lateral profiles of the computed, measured and analytical shear stress were found to be in a better agreement. The computed bed shear stress was in the range of $1.0\,\tau_b \sim 1.35\,\tau_b$.

- The comparison between the measured and predicted mean water depths shows a good agreement with a maximum square error of 2.0 %. This

indicates that the developed combination of the bed and sidewall roughness provides almost the correct water depth.

- Similar to 2D model, the 3D model was able to reasonably simulate the spatial pattern of the free surface which was found to be in relationship with the depth averaged flow velocity. It was estimated via the use of the cross correlation analysis that the celerity of the free surface patterns agreed to within 16.0 % of the depth averaged velocity.

- The spatial correlation analysis of the vertical flow velocity over the flow depth and at the flume centreline has initially shown a clear link between the sub-surface flow and the water surface in region down to a depth of approximately $y / H = 0.84$.

7.4 Summary of experimental findings

- Velocity time series in the vertical direction at the flume centreline were measured using a 3D Acoustic Doppler Velocimetry (ADV) for all flow conditions listed in Table 3.1. The obtained vertical profiles of shear stress, streamwise and vertical turbulent intensities confirm the achievement of uniform flow conditions as previously drawn by researchers.

- The lateral bed shear stress distributions which was calculated as $\tau = -\rho\overline{u'v'}$, reveal undulating patterns with an amplitude of 20 % ~ 50 % of the mean bed shear stress ($\tau_b = \rho u^{*2}$) for flow condition 2 (shallower) and flow condition 8 (deeper). These lateral patterns of bed shear stress suggest that the secondary flows exist across the flume width. The suggested number of

upwelling and downwelling regions which are associated with lower and higher bed shear stresses, agree well with the previous observations reviewed in the literature.

- At the upwelling and downwelling regions, velocity time series were also measured along the water column and lateral profiles of time-averaged streamwise velocity and shear stress were obtained for condition 2 and 8. It was found that condition 2 (shallower) exhibits a little variation in the lateral profiles, while a larger variation in the lateral profiles was observed in condition 8 (deeper). This suggests that secondary flows become stronger as the aspect ratio decreases. In these two flow conditions, the velocity dip phenomenon was observed in region close to side wall.

- The temporal changes in the water surface elevations were measured using the conductance wave probe technique for condition 1, 2, 5 and 8 listed in Table 3.1. These measurements were taken in different streamwise locations at the flume centreline and at two different lateral locations. It has been found that the probability density function (PDF) of the instantaneous water surface elevations closely follow the Gaussian distribution. The standard deviation of the water surface was found to increase as the flow becomes deeper.

- All of these experimental findings were used to support the development of the 2D and 3D SPH numerical models.

Based on the newly developed 2D and 3D SPH numerical findings, it could be generally concluded that both modified 2D and 3D models were found to be capable of predicting time-averaged flow quantities. 3D model is more accurate in predicting the time-averaged flow velocity, shear stress and free surface behaviour. However, performing such a 3D SPH simulation is more computational expensive. If the flow in nearly 2D and the bed roughness and sidewalls are symmetrical, then the 2D model would be sufficient to predict the velocity profile at the flume centreline. The 2D model was not able to show the change in the water surface standard deviation for different flow conditions. Therefore, it is recommended that water surface dynamic behaviour should be studied using the 3D model since it provides results that are more consistent with the experimental observations.

The following section addresses the need for further investigations in order to improve the current numerical models.

7.5 Recommendations for future work

- The instruments used in the current research to measure the flow velocity and water surface elevations can only collect data with low spatial resolution. Implementation of more widespread techniques such as Particle Image Velocimetry (PIV) would provide more information over a flow field at many points. Thus a full image of comparison between experimental and numerical simulations could be obtained.

- Although the bed roughness height used in the proposed 2D and 3D models is within the range provided in literature, it is necessary to calibrate this variable for more different flow conditions so that a relationship between this roughness height and flow parameters could be obtained.

- The parameter γ which defines the lateral distribution of the mixing length should be calibrated more accurately. The calibration should be supported by measuring the velocity profiles and lateral bed shear stress distribution in region close to the sidewall for more different flow conditions.

- The dynamic behaviour of the free surface patterns have been simulated successfully by the proposed 3D model. However, the model was not able to predict larger free surface fluctuations. This was attributed to several reasons such as the value of speed of sound and the spatial resolution used in this model. Therefore, it is recommended to check the model accuracy in predicting larger fluctuations for bigger speed of sounds and smaller particle size. It was not possible to examine the influence of these two parameters as they lead to computational cost that is much more than those listed in Table 6.1.

- It is also recommended to check the capability of the SPH model in predicting the time-averaged quantities for free surface turbulent flows over different geometry such as vegetation and porous beds.

- The numerical findings herein show that for the bed treatment used that the original SPS turbulence model using a fixed Smagorinsky constant cannot simulate the appropriate shear flow mechanism. Thus it is recommended to investigate the original SPS model but by introducing the bed drag by simulating the actual rough bed geometry. Simulating an actual rough bed geometry would cause additional flow dispersion throughout the flow depth, and may result in larger shear stresses being resolved.

References

Abbs, T.J., Kells, J. A., and Katopodis, C., (2007) . A Model Study of the Hydraulics Related to Fish Passage Through Backwatered Culverts. *Proceedings of the 18th CSCE Hydro Technical Conference.*

Absi, R., (2011). An ordinary differential equation for velocity distribution and dip-phenomenon in open channel flows. *Journal of Hydraulic Research*, IAHR, 49 (1), 82–89.

Albayrak, I. and Lemmin, U., (2011). Secondary Currents and Corresponding Surface Velocity Patterns in a Turbulent Open-Channel Flow over a Rough Bed. *Journal of Hydraulic Engineering*, 137 (11), 1318–1334.

Anderson, S., and Lohrmann, A., (1995). Open water test of the Sontek acoustic Doppler velocimeter. *Proc., IEEE Fifth Working Conf. on Current Measurements*, IEEE Oceanic Engineering Society, St. Petersburg,Fla.,188–192.

Barkdoll, B., (2002). Discussion of Mean flow and turbulence structure of open-channel flow through non-emergent vegetation,' by F. Lopez,and M. H. García. *Journal of Hydraulic Engineering*, 127 (5), 392–402.

Barr, D. I. H., (1963), Tables for the Hydraulic Design of Pipes, Sewers and Channels. *Hydraulic Research Station*, Wallingford, UK

Bayazit, M., (1976). Free Surface Flow In A Channel Of Large Relative Roughness, *Journal of Hydraulic Research*, 14(2), 115–126.

Berlamont, J., Trouw, K. and Luyckx, G., (2003). Shear Stress Distribution in Partially Filled Pipes. *Journal of Hydraulic Engineering*, 129 (9), 697–706.

Biferale, L., Cencini, M., Lanotte, A. and Vergni, D., (2003). Inverse velocity Statistics in two-dimensional turbulence. *Physics of Fluids*, 15 (4),1001–1019.

Bigillon F., Nino Y. and Garcia M., (2006). Measurements of turbulence characteristics in an open-channel flow over a transitionally-rough bed using particle image velocimetry, *Experiments in Fluids*, 41(6), 857–867.

Blanckaert K., Duarte A. and Schleiss A. J. (2010). Influence of shallowness, bank inclination and bank roughness on the variability of flow patterns and boundary shear stress due to secondary currents in straight open-channels. *Advances in Water Resources*, 33, 1062–1074.

Brederode, V. A. S. L. DE and Bradshaw, P., (1974). A note on the empirical constants appearing in the logarithmic law for turbulent wall flows. *I.C. Aero Rep*. 74-03, Imperial College of Science and Technology, London.

Brunn, S., Cutter, S. and Harrington, J., (2004). *Geography and Technology*. New York:pringer.

Buffin-Bélanger, T., Roy, AG., (1998). Efects of pebble cluster on turbulent structure of a depth-limited flow in a ravel-bed river, *Geomorphology*, 25, 249–267.

Buffin-Bélanger, T., Roy, A. G. and Kirkbride, A., (2000). On large-scale flow structures in agravel-bed river. *Geomorphology*,32, 417–435.

Bunco, R., H., and E., Partheniades (1971). Turbulence Characteristics in Free Surface Flows over Smooth and Rough Boundaries, *Journal of Hydraulic Research*, 9(1), 43–69.

Cardoso, A. H., Graf, W. H. and Gust, G. (1989). "Uniform flow in smooth open-channel." *Journal of Hydraulic Research*, IAHR, 27(5), 603–616.

Carvalho, E., Maia, R., and Proença, M. F. (2010). Shear Stress Measurements over Smooth and Rough Channel Beds. *Proceedings of the 5th River Flow Conference.*

Chanson, H., (1997). Air-water flows in partially-filledconduits. *Journal of Hydraulic Research*, 35 (95), 591–602.

Cheng, ED., H. and Clyde, C., D., (1972). Forces on Large Roughness Elements in Turbulent Open Channel Flow, Sedimentation (Einstein).

Cheng, N. S., (2007). Power-law index for velocity profiles in open channel flows. *Adv. Water Resour*. 30, 1775–1784.

Chern, M. and Syamsuri, S. (2013). Effect of corrugated bed on hydraulic jump characteristic using SPH method. *Journal of Hydraulic Engineering*. 139(2), 221–232.

Chiu, C., (1989). Velocity distribution in open channel flows. *Journal of Hydraulic Engineering*, ASCE, 115(5), 576–594.

Chiu, C.-L., and Abidin Said, C. A., (1995). Maximum and mean velocities and entropy in open channel flow. *Journal of Hydraulic Engineering*, ASCE,121(1), 26–35.

Chiu, C. and Tung, N., (2002). Maximum Velocity and Regularities in Open-Channel Flow. *Journal of Hydraulic Engineering*, 128 (2002), 390–398.

Chow, V., C., (1959). *Open-Channel Hydraulics*. McGraw-Hill Book Co., New York, USA.

Christodoulou, G., (2014). Equivalent Roughness of Submerged Obstacles in Open-Channel Flows. *Journal of Hydraulic Engineerin*g, 140(2), 226–230.

Colagrossi, A. and Landrini, M. (2003). Numerical simulation of interfacial flows by smoothed particle hydrodynamics. *J. Comput. Phys*., 191 (2), 448–475.

Colebrook, C. F., (1939). Turbulent flow in pipes, with particular reference to the transition region between smooth and rough pipe laws. *Journal of Institution of Civil Engineers*, London. 11, 133–156.

Coles, D., (1956). The law of the wake in turbulent boundary layer. *J. Fluid Mech.*,1, 191–226.

Coles, D., (1968). The Young Person's Guide to the Data, *Computation of Turbulent Boundary Layer: AFOSR-IFP-Stanford Conference*, Vol. II, 1–45

Cooper, J. R., S. J. Tait, and K. V. Horoshenkov, (2006). Determining hydraulic resistance in gravel-bed rivers from the dynamics of their water surfaces, Earth in the conterminous United States, *J. Hydrol*., 93, 313–338.

Cooper, J. R., and S. J. Tait (2008). The spatial organization of time averaged streamwise velocity and its correlation with the surface topography of water-worked gravel bed, Acta-Geophys., 56(3), 614–641, doi:10.2478/s11600-008-0023-0

Czernuszenko, W., and Rylov, A. A., (2000). A generalisation of Prandtl's model for 3D open channel flows. *Journal of Hydraulic Research*, 38(3), 173–180.

Dabiri, D., (2003). On the interaction of a vertical shear layer with a free surface. *J. Fluid Mech,*. 480, 217–232.

Dalrymple, R. A. and Knio, O., (2001). SPH modelling of water waves, *Proc. Coastal Dynamics*. 779–787, Sweden.

Dalrymple, R. A. and Rogers, B. D., (2006). Numerical modelling of water waves with the SPH method. *J. Coastal. Eng*., 53(2–3), 141–147.

De Padova, D., Mossa, M., Sibilla, S. and Torti, E., (2013). 3D SPH modelling of hydraulic jump in a very large channel. *Journal of Hydraulic Research.* 51 (2), 158–173.

Džebo, E., Žagar, D., Cetina, M., Petkovšek, G., (2012). Simulation of dam-break flow in channel expansion with coupled 2-D/3-D SPH model. *Proc. of 7th Int. SPHERIC Workshop*, Prato, 403–408.

Džebo, E., Žagar, D., Cetina, M., Petkovšek, G. (2013b). Reducing the computational time of the SPH method with a coupled 2-D/3-D approach. *J. Mech. Eng.* 59(10), 575–584

Džebo, E., Žagar, D., Krzyk, M., Četina, M. and Petkovšek, G., (2014). Different ways of defining wall shear in smoothed particle hydrodynamics simulations of a dam-break wave. *Journal of Hydraulic Research*, 52, 453–464.

Ead, S. A., Rajaratnam, N., Katopodis, C., and Ade, F., (2000). Turbulent Open-Channel Flow in Circular Corrugated Culverts, *Journal of Hydraulic Engineering*,126(10), 750–757.

Einstein, H. A. and EL-Samni, E. S. (1949). Hydrodynamic Forces on a Rough Wall, *Review of Modern Physics*., 21(3), 520–524.

Einstein, H. A., and Li, H., (1958). Secondary currents in straight channels. Transactions - American Geophysical Union, 39(6): 1085–1088.

Farhadi, A., Ershadi, H., Emdad, H. and Rad, E. G., (2016). Comparative study on the accuracy of solitary wave generations in an ISPH-based numerical wave flume. *J. Applied Ocean Res.*, 54,115–136.

Fedderico, I., Marrone, S., Colagrossi, A., Aristodemo, F., Antuono, M., (2012). Simulating 2D Open-channel Flows through an SPH model, *European Journal of Mechanics*,34, 35–46.

Finnigan, J., (1985). Turbulent transport in flexible plant canopies. B. A. Hutchinson and B. B. Hicks, eds., *The forest-atmosphere interactions*, Reidel: Dordrecht, 43–480.

Fornberg, B., (1988). Steady viscous flow past a sphere at high Reynolds number, *J. Fluid Mech.*, Vol. 190, 471–489.

Fujita, I., Furutani, Y. and Okanishi, T., (2011). Advection features of water surface profile in turbulent open-channel flow with hemisphere roughness elements. *Vis. Mech Proc.* 1(4), doi:10.1615/VisMechProc.v1.i3.70.

Garcia, C., Cantero, M., Nino, Y. and Garcia, M., (2005). Turbulence Measurements with Acoustic Doppler Velocimeters. *Journal of Hydraulic Engineering*, 131 (12), 1062–1073.

Gingold, R. A. and Monaghan J. J., (1977). Smoothed particle hydrodynamics: theory and application to non-spherical stars. Mon. *Not. R. Astron. Soc*. 181, 375–389.

Gómez-Gesteira, M. and Dalrymple, R. A., (2004). Using a three-dimensional Smoothed Particle Hydrodynamics method for wave impact on a tall structure. *J. Waterways, Ports, Coasts, and Ocean Engineering, ASCE*. 130(2), 63–69.

Gomez, D. L., (2007). The hydraulic jump: a test case for the SPH model. *Proceedings of the 32nd IAHR Congress*, Venice, Italy, 2007.

Gomez-Gesteira, M., Rogers, B. D., Crespo, A. J. C., Dalrymple, R. A.,Narayanaswamy, M. and Dominguez, J. M., (2012a). SPHysics - development of a free-surface fluid solver - part 1: theory and formulations. Computers and Geosciences.

Gotoh, H., Shibahara, T. and Sakai, T., (2001). Sub-Particle-Scale turbulence model for the MPS method — Lagrangian flow model for hydraulic engineering. *J. Comp. Fluid Dyn.* 9(4), 339–347.

Gotoh, H. and Sakai, T., (1999). Lagrangian simulation of breaking waves using particle method. *J. Coast. Eng.*, 41 (3 & 4), 303–326.

Godley, A., (2002). Flow measurement in partially filled closed conduits. *Flow Measurements and Instrumentation*, 13 (2002), 197–201.

Graf, W, H. and Altinakar, M. S., (1998). *Fluvial Hydraulics–Flow and Transport Processes in Channels of Simple Geometry*. John Wiley & Sons.

Grass , AJ, (1971). Structural features of turbulent flow over smooth and rough boundaries. *J. Fluid Mech*., 50(2), 233–255.

Grass l, H., (1976). The dependence of the measured cool skin of the ocean on wind stress and total heat flux. *Boundary Layer Meteorology*, 10, 465–475.

Handler, R., Smith, G. and Leighton, R., (2001). The thermal structure of an air–water interface at low wind speeds. *Tellus*, 53 (2001), 233–244.

Hinze, J.O., (1975). *Turbulence*. New York: McGraw-Hill.

Hornung, H.G, Willert, C., Turner , S., (1995). The flow field downstream of ahydraulic jump, *J.Fluid Mech*., 287(1995), 299–316.

Horoshenkov, K. V., Nichols, A., Tait, S. J. and Maximov, G. A. (2013). The pattern of surface waves in a shallow free surface flow. *J. Geophysical Res, Earth Surface*. 118(3), 1864 – 1876.

Horriike, H., Kondo, H., Nakamura, H., Miyamoto, S., Yamaoka, N., Matsushita, I., Ida, M., Ara, K. Muroga, T. and matsui, H., (2007). Free-Surface Fluctuation at High Speed Lithium Flow for IFMIF. International Atomic Energy Agency, *21st Fusion Energy Conference.*

Hu, X. Y. and Adams, N. A., (2007). An incompressible multi-phase SPH method. *J Comput Phys*. 227 (1), 264–278.

Hu, Y. F., Wan, W. Y., Cai, F. K., Mao, G., and Xie, F., (2008). Velocity distribution in narrow and deep rectangular open channels. *Journal of Zhejiang University (Engineering Science)*, 42(1), 183–187.

Jamshidnia, H., Takeda, Y. and Firoozabadi, B., (2010). Effect of standing baffle on the structure of flow in a rectangular open channel. *Journal of Hydraulic Research,* 48 (3), 400–404.

Järvelä, J., (2002). Flow resistance of flexible and stiff vegetation: a flume study with natural plants. *Journal of Hydrology.*, 269(1-2), 44–54.

Kahler, C., McKenna, R. and Scholz, U., (2005). Wall-shear-stress measurements at moderate Re-numbers withsingle pixel resolution using long distance μ-PIV – an accuracyassessment, *6th International Symposium on Particle Image Velocimetry Pasadena, California, USA, September 21-23*, 1–5.

Kamphuis, J., W., (1974). Determination of Sand Roughness for Fixed Beds, *Journal of Hydraulic Research*., 12(2), 193–203.

Khayyer, A. and Gotoh, H., (2010). On particle-based simulation of a dam break over a wet bed. *J. Hydraul. Res*. 48 (2), 238–249.

Kirkgöz, M.S., Ardiclioglu, M., (1997). Velocity profiles of developing and developed open channel flow. *Journal of Hydraulic Engineering*, 123, 12, 1099–1105.

Kironoto BA, Graf WH., (1995). Turbulence characteristics in rough nonuniform open channel flow. *Proceedings of the Institution of Civil Engineers-Water Maritime and Energy*. 112, 336–348.

Komori, S., H. Ueda, F. Ogino & T. Mizushina, (1982). Turbulence structure and transport mechanism at the free surface in an open channel flow. *Int. J. Heat and Mass Transfer*, 25, 513–522.

Koshizuka, S., Nobe, A., Oka, Y., (1998). Numerical analysis of breaking waves using the moving particle semi-implicit method. *Int. J. Numer. Meth. Fluids*. 26(7), 751–769.

Kotey, N. A., Bergstrom, D. J. and Tachie, M. F., (2003). Power laws for rough wall turbulent boundary layers, *Physics of Fluids* 15 (6), pp. 1396-1404.

Krynkin, A., Horoshenkov, K. V., Nichols, A., & Tait, S. J., (2014). A non-invasive acoustical method to measure the mean roughness height of the free surface of a turbulent shallow water flow. *Review of Scientific Instruments*, 85(11), 114902. doi:10.1063/1.4901932

Kumar, S., Gupta, R. and Banerjee, S., (1998). An experimental investigation of the characteristics of free-surface turbulence in channel flow. *J. Phys. Fluids.*, 10(2), 437–456.

Kundu, S., and Ghoshal, K., (2012). An analytical model for velocity distribution and dip-phenomenon in uniform open channel flows Int. *J. Fluid Mech*. Res., 39, 381–95.

Kurose, R. and Komori, S., (2001). Turbulence structure over a particle roughness.*International J. Multiphase Flow*, 27(4), 673–683.

Lane, S. N., Biron, P. M., Bradbrook, K. F., Butler, J. B., Chandler, J. H., Crowell, M. D., McLelland, S. J., Richards, K. S., and Roy, A. G., (1998). Three-Dimensional Measurements of River Channel Flow Processes Using Acoustic Doppler Velocimetry. *Earth Surface Processes and Landforms*, 23, 1247–1267.

Lee, E.-S., Moulinec, C., Xu, R., Violeau, D., Laurence, D. and Stansby, P., (2008). Comparisons of weakly compressible and truly incompressible algorithms for the SPH mesh free particle method. *J. Comp. Phys*., 227, 8417–8436.

Lemmin, U., and Lhermitte, R., (1999). Discussion of 'ADV measurements of turbulence: Can we improve their interpretation?' by V. I. Nikora, and D. G. Goring. *Journal of Hydraulic Engineering*, 125 (9), 987–988.

Li, X., Dong, Z., Chen, C., (1995). Turbulent flows in smooth-wall open channels with different slope. *J. Hydraulic Res*., 33(3), 333–347.

Li, S. and Liu, W., (2004). *Meshfree Particle Methods.* New York: Springer.

Lohrmann, A., Cabrera, R., and Kraus, N. C., (1994). Acoustic-Doppler Velocimeter (ADV) for Laboratory Use. *Fundamentals and Advancements in Hydraulic Measurements and Experimentation Proceedings, sponsored by the Hydraulics Division/ASCE, August 1-5*, 1994, Buffalo, New York.

López, D., Marivela, R. and Garrote, L., (2010). SPH model applied to hydraulic structures: a hydraulic jump test case. *J. Hydrual. Res*. 48 (Extra Issue), 142–158.

Lu, J., Hong, J, Wang, C., Lee, K. and Yang, H., (2003). Measurement and simulation of turbulent flow in a Steep open-channel with smooth boundary. *Journal of the Chinese Institute of Engineers*, 26 (2), 201–210.

Luo, T. F., and Lü, H. X., (2006). Discussion of velocity profile in open channel with U-shaped cross-section. *Journal of Irrigation and Drainage*, 25(2), 12–14.

Magoules, F., (2011). *Computational Fluid Dynamics.* New York: CRC Press.

Mathieu, J. and Scott, J., (2000). *An Introduction to Turbulent Flow.* Cambridge: Cambridge University Press.

Meister, M., Burger, G. and Rauch, R., (2014). On the Reynolds number sensitivity of smoothed particle hydrodynamics, *J. Hydrual. Res*. 52(6), 824–835.

McLelland, S. J., Ashworth, P. J., Best, J. L. and Livesey, J. R., (1999). Turbulence and secondary flow over sediment strips in weakly bimodal bed material. ASCE, Journal of Hydraulic Engineering 125(5), 463–473.

Michael Meister, Gregor Burger & Wolfgang Rauch (2014) On the Reynolds number sensitivity of smoothed particle hydrodynamics, Journal of Hydraulic Research, 52(6), 824–835.

Miraghaie, R., Lopez, M. and Hirsa, A., (2003). Flow induced patterning at the air–water interface. *Physics of Fluids*, 15(6), 45–48.

Monaghan, J. J., (1992). Smoothed Particle Hydrodynamics. *Annu. Rev. Astrophys*, 30, 543–574.

Monaghan, J. J. and Kos, A., (1999). Solitary waves on a cretan beach. *J. Waterways Port, Coastal Ocean Eng*. 1111, 145–54.

Monaghan, J. J., (2012). Smoothed Particle Hydrodynamics and its Diverse Applications. *Annual Review of Fluid Mechanics*, 44,323–346.

Nakagawa, H., I. Nezu & H. Ueda, (1975). Turbulence in open channel flow over smooth and rough beds. Proc. Of Japan Soc. Civil Engrs., 241, 155–168.

Nakayama, A. and Yokojima, S., (2001). Direct numerical simulation of the fully developedopen-channel flow at subcritical Froude numbers. *DNS/LES Progress andChallenges*, 3rdAFOSRInt' Conference Arlington, Texas 2001, 569–576.

Naot, D. and Rodi, W., (1982). Calculation of secondary currents in channel flow, *J. Hydr. Engrg.*, ASCE, 108(8), 948–968.

Nezu, I. (1977a). Turbulent structure in open channel flow. Ph. D Thesis presented to Kyoto University, Kyto, Japan.

Nezu, I., and Nakagawa, H., (1984). Cellular secondary currents instraight conduit. *J. Hydr. Engrg.*, ASCE, 110(2), 173–193.

Nezu, I., and Rodi, W., (1986). Experimental study on secondary currentsin open channel flows, in *Proceedings of the 21st Congress*, 2, 115–119.

Nezu, I., and Nakagawa, H., (1993). *Turbulence in Open-Channel Flows*. Rotterdam: A. A. Balkema.

Ng, T., Lawrence, C. and Hewitt, G., (2001). Gravity-driven laminar flow in a Partially-filled pipe, *Chemical Engineering*, 79, Part A, 499–511.

Nichols, A., Tait, S. and Horoshenkov, K., (2010). *Remote Characterisation of Shallow flows from the 'fingerprint' of the free surface.* Yorkshire: Yorkshire Water Department.

Nichols, A. , Tait, S. J., Horoshenkov, K. V., & Shepherd, S. J., (2016). A model of the free surface dynamics of shallow turbulent flows, *Journal of Hydraulic Research*, 54 (5), 516–526.

Nikora, V. and Goring, D., (2000). Flow Turbulence over Fixed and Weakly Mobile Gravel Beds. *Journal of Hydraulic Engineering*, 126(9), 679–690.

Nikora, V., Goring, D., McEwan, I. and Griffiths, G., (2001). Spatially Averaged Open Channel Flow Over Rough Bed. *Journal of Hydraulic Engineering*,127 (2), 123–133.

Nikuradse, (1933). Stromungsgesetz in rauhren rohren, vDI Forschungshefte 361 (English translation: Laws of flow in rough pipes). Tech. Rep. NACA Technical Memorandum 1292. National Advisory Commission for Aeronautics, Washington, DC, USA (1950).

Nino, Y. & Garcia, M. H., (1996). Experiments on particle-turbulent interactions in the near-wall region of an open channel flow: implications for sediment transport: *Journal of Fluid Mechanics*, 326, 285–319.

Onate, E., Idelsohn, S., Zienkiewicz, O. C., Taylor, R. L., (1996). A Finite Point Method in Computational Mechanics. Applications to Con vective Transport and Fluid Flow. Internat. *J. Numer. Methods Engrg*., 39, 3839 – 3866.

Papanicolaou, A., N., Tsakiris, A., G., & Kramer, C., M., (2010). Effects of relative submergence on flow and sediment patterns around clasts. *Proceedings of the 5th River Flow Conference.*

Pechlivanidis, G., Keramaris, E., Pechlivanidis, I. and Samaris, G., (2012). Measuring the Turbulent Characteristics in an Open Channel using the PIV Method. *Global NEST Journal*, 14 (3), 378–385.

Perry, A., E., Schofield, W. H., and Joubert, P., (1969). Rough wall turbulent boundary layers. *Journal of Fluid Mechanics*, 37, 383–413.

Petkovšek, G., Džebo, E., Cetina, M., Žagar, D., (2010). Application of non discrete boundaries with friction to smoothed particle hydrodynamics. *J. Mech. Eng*. 56(5), 307–315.

Pope, S.B., (2000). *Turbulent Flows.* Cambridge: Cambridge University Press.

Prandtl, L., (1952), Uber die ausgebildeteTurbulenz, *ZAMM*, 5, 136–139.

Raupach, M. R., Antonia, R. A., and Rajagopalan, S., (1991). Roughwall turbulent boundary layers. *Appl. Mech. Rev.*, 44 (1), 1–25.

Raupach, M. R., and Shaw, R. H., (1982). Averaging procedures for flow within vegetation canopies. *Boundary-Layer Meteorology*, 22, 79–90.

Rodi, W., (2017). Turbulent modelling and simulating in hydraulics: A Historical Review. *Journal of Hydraulic Engineering*, 03117001.

Rodriguez, J. F., and M. H. Garcia, (2008). Laboratory measurements of 3-D flow patterns and turbulence in straight oen channel with rough bed, *J. Hydraul. Res*., 46, 454–465, doi:10.3826/jhr.2008.2994.

Roy, AG, Biron, P & De Srres, B 1996, 'On the Necessity of Applying a Rotation to Instantaneous Velocity Measurements in River Flow', *Earth Surface Processes and Land Forms*, 21, 817–827.

Ruppert-Felsot, J., Praud, O., Sharon, E. and Swinney, L., 2005. Extraction of coherent structures in a rotating turbulent flow experiment. *Physical Review E 72*, 016311 (2005), 1–14.

Savelsberg, R. & van de Water, W., (2006). Measurement of the gradient field of a turbulent free surface. *J. Exp in Fluids.*, 41, 629–640.

Savelsberg, R. & van de Water, W., (2009). Experiments on free-surface turbulence. *J. Fluid Mech.*, 619, 95–125.

Schlichting, H. and Gersten, K., (2000). *Boundary Layer Theory*. Berlin: Springer.

Schmeeckle, M., W. Nelson, J., M., and Shreve, R., L., (2007). Forces on stationary particles in near-bed turbulent flows. *Journal of Geophysical Research*, 112:F02003.

Seckin, G., Seckin, N, and Yurtal, R., (2006). Boundary shear stress analysis in smooth rectangular channels. *Canadian Journal of Civil Engineering*, 33 (2006), 336–342.

Shakibaeinia, A. and Jin, Y. C., (2010). A weakly compressible MPS method for modeling of open-boundary free surface flow. *Int. J. Numer. Methods Fluids.* 63(10), 1208–1232.

Shamloo, H., Rajaratnam, N. & Katopodis, C., (2001). Hydraulics of simple habitat structures, *Journal of Hydraulic Research*, 39(4), 351–366

Shao, S. D., Gotoh, H. and Memita, T., (2003). Simulation of wave overtopping on partially immersed breakwater by SPH model, *Proceedings of Second International Conference of Asian and Pacific Coast, APAC2003*, Japan.

Shi, J., Thomas, T. G. and Williams, J. J., (2000). Fee-surface effects in open channel flowat moderate Froude and Reynold's numbers. *J. Hydraulic Research*, 38(6), 465–474.

Shvidchenko, B. and Pender, G., (2001). Macroturbulent structure of open-channel flow over gravel beds, *Water Resources Research*, 37 (3), 709–719.

Smolentsev, S. and Miraghaie, R., (2005). Study of a free surface in open channel water flow in the regime from "weak" to "strong" turbulence. *Int. J. Multiphase Flow*. 31, 921–939.

Smutek, R., (1969). Discusion on ' Measurement of turbulence in water' by Richardson & McQuivey. *J. Hydraulics Div., ASCE*, 95: HY-1 : 519–523.

Stansby, P., (2003). A mixing-length model for shallow turbulent wakes. *J. Fluid Mech.* 495,369–384.

Stoesser, T., Fohlich, J. and Rodi, W., (2003). Identification Of Coherent Flow Structures In Open Channel Flow Over Rough Bed Using Large Eddy Simulation. *Proc. 30th IAHR Thessaloniki, Greece, 25.-31.8.2003,* 1–8.

Tabeling, P., (2001). Two-dimensional turbulence: a physicist approach. *Physics Reports,* 362 (2002), 1–62.

Tamburrino, A. and Gulliver, J. S., (1998). Measurements of free-surface turbulence in an open-channel flow. *Submitted to Jour. Hydraulic Engineering.*

Tamburrino, A. and Gulliver, J. S., (1999). Large flow structures in a turbulent open channelflow. *IAHR J. Hydraulic Research* 37(3), 363–380.

Tamburrino, A. and Gulliver, J., (2002). Free-Surface Turbulence and Mass Transfer in a Channel Flow, *AIChE Journal*, 48 (12), 2732–2743.

Tan, SK., Cheng, N-S., Xie, Y. & Shao, S., (2015). Incompressible SPH simulation of open channel flow over smooth bed. *Journal of Hydro-environment Research*, 9(3), 340–353.

Tominaga, A., Nezu, I., Ezaki, K., and Nakagawa, H., (1989). "Three-dimensional turbulent structure in straight open channel flows. " *Journal of Hydraulic Research*, 27(1), 149–173.

Tritton, D. J., (1988). *Physical Fluid Dynamics*, Clarendon, Oxford, UK.

Tsubaki, R. and Fujita, I., (2005). Stereoscopic measurement of a fluctuating free surface with discontinuities, *Meas. Sci. Technol*, 16, 1894–1902.

Vanoni, V. A., (1941). ”Velocity Distribution in Open Channels,” *Civil Engineering, ASCE*, 11(6). 356–357.

Venditti, J. G. and Bennett, S. J., (2000). Spectral Analysis of Turbulence Flow and Suspended Sediment Transport over Fixed Dunes. *Journal of Geophysical Research,* 105 (22), 35–48.

Vermaas, D. A., Uijttewaal, W. and Hoitink, A. J. F., (2011). Lateral transfer of streamwise momentum caused by a roughness transition across a shallow channel, *Water Resources Research*, vol. 47 (W02530).

Violeau, D. and Issa, R., (2007). Numerical modelling of complex turbulent free surface flows with the SPH method: An overview. *Int. J. Numer. Meth. Fluids*. 53(2), 277–304.

Violeau, D., (2012). *Fluid Mechanics and the SPH Method: Theory and Applications*.Oxford: Oxford University Press.

Vlaskamp, J. H. A., (2011). *An Experimental and Numerical Investigation into the Vertical Dependence of Taylor-Columns Generated by a Rotating Disc*,Warwick: The University of Warwick.

Von Kármán, T., (1930). MechanischeÄhnlichkeit und Turbulenz.*Nachrichten v. d. Gesellschaft der WissenschaftenzuGöttingen Math. Phys. Klasse*, 58–76.

Voulgaris, G., and Trowbridge J., (1998). Evaluation of the acoustic Doppler Velocimeter _ADV_ for turbulence measurements. *Journal of Atmospheric and Ocean Technology*, 15 (1), 272–288.

Wang, Z. Q., and Cheng, N. S., (2005). Secondary flows over artificial bed strips. *Advances in Water Resources*, 28(5), 441–450.

Wren, D., Bennett, S., Barkdoll, B. and Kuhnle, R., (2000). Studies in Suspended Sediment and Turbulence in Open Channel Flows. *Agricultural Research Service, Research Report No. 18*, 1–133.

Xie, Z., Lin, B. and Falconer, R., (2013). Large-eddy simulation of the turbulent structure in compound open-channel flows. *Advances in Water Resources*, 53 (2013), 66–75.

Yagawa G., Yamada T., (1996). Free mesh method: a new meshless finite element method. *Comput. Mech*, 8, 383–386.

Yalin, M. S., (1992). River Mechanics. Pergamon Press, Oxford.

Yang, S., Tan, S., and Lim, S., (2004). ”Velocity Distribution and Dip-Phenomenon in Smooth Uniform Open Channel Flows.” *J. Hydraul. Eng.*, 130(12), 1179–1186.

Yang, S., (2010). Depth-Averaged Shear Stress and Velocity in Open-Channel Flows. *Journal of Hydraulic Engineering,* 136 (11), 952–958.

Yang, S.., Tan, S. K. and Wang X. -K., (2012). Mechanism of secondary currents in open channel flows, *Journal of GeophysicsResearch*, 117, 1–13. DOI:10.1029/2012JF002510.

Yen, B., C., (1991). ‘‘Hydraulic resistance in open channels.’’ in Channel Flow Resistance: Centennial of Manning’s Formula, B. C. Yen, ed., Water Resource Publications, High lands Ranch, Colo., 1–135.

Yen, B. (2002). ‘‘Open Channel Flow Resistance’’. *Journal of Hydraulic Engineering*., 128(1), 20–39.

Yue, W., Lin, C. and Patel, V. C., (2005). Large eddy simulation of turbulent open channel flow with free surface simulated by level set method. *Phys. Fluids*17, 025108.

Zanoun, E., Durst, F., Bayoumy, O. and Salaymeh, A., (2007). Wall skin friction and mean velocity profiles of fully developed turbulent pipe flows. *Experimental Thermal and Fluid Science*, 32 (1), 249–261.

Zeng, C. and C.W., (2012). Modelling flows over gravel beds by a drag force method and a modified S–A turbulence closure. *Advances in Water Resources*, 46 (2012), 84–95.

Zhang, X. and Cox, C. S., (1994). Measuring the two-dimensional structure of a wavy water surface optically: a surface gradient detector. *Exps. Fluids*, 17, 225–237.